EPFL

Thèse n° 10 500

Precision luminosity measurement at hadron colliders

Présentée le 31 mai 2024

Faculté des sciences de base
Laboratoire de physique des hautes énergies LS
Programme doctoral en physique

pour l'obtention du grade de Docteur ès Sciences

par

Joanna Malgorzata WANCZYK

Acceptée sur proposition du jury

Prof. J. H. Dil, président du jury
Prof. L. Shchutska, Dr A. E. Dabrowski, directrices de thèse
Dr J. Wenninger, rapporteur
Dr R. Hawkings, rapporteur
Prof. M. Seidel, rapporteur

École polytechnique fédérale de Lausanne

2024

Tam, gdzie wszystko można zdobyć bez trudu, wszystkie wartości giną.
Nie ma wiedzy bez wyobraźni i nie ma wyobraźni bez wiedzy.
Poznanie jest zdobyciem pewności w jakiejkolwiek kwestii.
Człowiek stawia hipotezy zawsze, nawet kiedy się ma na baczności, nawet kiedy o tym nie wie.
— Stanisław Lem

Acknowledgements

Firstly, I would like to express my gratitude to my supervisors, Anne Dabrowski and Lesya Shchutska, for giving me the invaluable opportunity to conduct this study. Thank you Anne for being always ready to come to my aid during challenging situations. This project was commonly funded by CERN organization and CHART project for which I am profoundly grateful.

I wish to convey my appreciation to Taiana Pieloni for introducing me into the world of the beam-beam interactions through all our human-human interactions driven by the coffee potential. Thank you for all the fruitful and stimulating discussions, your mentorship has been instrumental in my professional growth. I would also like to extend the gratitude to Claudia Tambasco for helping me to start the COMBI simulation endeavours. I was fortunate to meet so many inspiring female role models.

I would like to thank David Stickland for sharing his enthusiasm, and expertise in the luminosity measurement. For constantly positive attitude, sharing the motivation and providing the invaluable connections to other experts. For many enriching and thought-provoking conversations; your guidance has played a pivotal role in advancing my professional development.

I am extremely grateful to Witold Kozanecki, for being the genuine mentor and generously sharing his expertise. I am thankful for the invaluable guidance that has not only enhanced the quality of my work but also underscored the significance of a comprehensive understanding.

I am grateful to the manuscript reviewers, Jorg Wenninger and Richard Hawkings, for providing valuable feedback, as well as Werner Herr for proofreading and helping me shape some of the chapters.

I would like to thank all the knowledgable, friendly, and supportive colleagues. To Andres Delannoy, Francesco Romeo, Georg Auzinger, Jonas Rubenach, and Mykyta Haranko for sharing the adventure and hardship of detector assembly, operations, and the live problem-solving. I would like to especially thank Moritz Guthoff for his selfless advice and discussions that enabled me to become the BCM1F expert. I extend my gratitude to Sophie Mallows for her perfect coffee break timing, and to Olena Karacheban for fostering the most pleasant working atmosphere imaginable. I really appreciated working in the CMS collaboration - in

the environment of shared expertise and scientific responsibilities.

I would like to acknowledge all the people who helped with preparing and carrying out the beam-beam experiment. I am very thankful for all valuable insights and discussions with Xavier Buffat, Rogelio Thomas, and Georges Trad.

I express my sincere gratitude to all my friends, especially the fellow PhD students, for sharing all the joys and challenges of this journey.

I would like to express my deepest appreciation to my family, for the unconditional support regardless the distance. I am extremely lucky to have your love, encouragement, and understanding which have always been the pillars that sustained me. I believe you all shaped me and you are always a part of anything I do. To my husband Marcin, the most patient and loving person on the Earth. Thank you for keeping the guard on my sanity, all this work would have not be possible without you.

Lausanne, March 3, 2024 J. W.

Abstract

This thesis links two realms of particle accelerator dynamics and precision particle physics. The achievement of precise luminosity measurement at hadron colliders is enabled with dedicated luminometers. For the Run 3 period, the luminometer upgrade was planned for the Compact Muon Solenoid (CMS) experiment at the Large Hadron Collider (LHC). The intricacies of the process of preparation, installation, and commissioning of the upgraded Fast Beam Conditions Monitor (BCM1F-μTCA) are described in this thesis. Its design was optimized based on analysis of the performance of the Run 2 version of BCM1F with the main changes being the utilization of silicon sensors and real-time and dead-time free pulse shape analysis in the back-end electronics. The BCM1F-μTCA optimization and resulting performance are studied in detail.

The most common and most precise way of obtaining the absolute calibration of the luminosity at the hadron colliders is the van der Meer (vdM) method. However, it requires careful consideration and correction for the accelerator-related systematic effects. While numerous particle accelerator effects have previously been studied in detail, their direct impact on the precision luminosity calibration was neglected for a long time. Notably, the historically disregarded beam-beam interaction is now recognized as a significant factor. The first correction models underestimated the optical effect induced by the beam-beam-interaction by a factor 2 to 6, which led to the overestimation of the full beam-beam correction by about 1%. This prompted an extended effort to recognize and quantify different ingredients of the beam-beam-related systematic uncertainty on the luminosity calibration. The development of the new correction model has started, originally aiming to parametrize the beam-beam effects on luminosity in the simplest case of a single interaction point. The main objective was to provide per-bunch corrections based on its properties.

This study aimed to extend the correction model with a further level of complexity - multi-collision effects. The investigation into additional contributions to the systematic uncertainty arising from beam-beam interaction is presented, considering the crossing-angles in the vdM scans as well as the sensitivity to the phase advances between the collision points. The multi-particle simulation studies are complemented with a dedicated beam-beam experiment at the LHC that was designed to provide the first statistically significant measurement of the beam-beam effects on luminosity. The beam-beam effects were studied depending on the strength of the interaction, as a function of separation steps when scanning the beams, as well as depending on the number of collisions.

The detailed detector studies led to a minimized integration systematic uncertainty on the

Abstract

BCM1F-μTCA measured integrated luminosity in 2022. The absolute luminosity scale calibration of this data set with the vdM method was performed, and the beam-beam effects were among the largest calibration corrections. The corresponding overall systematic uncertainty was estimated, profiting from the detailed studies on the beam-beam interaction effects. This work culminates in an unprecedented precision of the CMS preliminary luminosity calibration, with a projection towards achieving the ultimate precision below 1%.

Keywords — Collider, luminosity, luminosity measurement, luminosity calibration, vdM, beam-beam, beam dynamics

Résumé

Cette thèse fait le lien entre les domaines de la dynamique des accélérateurs de particules et de la physique des particules de précision. Lors de la troisième phase d'exploitation du Large Hadron Collider (LHC), une mise à niveau des luminomètres de l'expérience Compact Muon Solenoid (CMS), délivrant des mesures précises de luminosité, a été mise en oeuvre Les subtilités du processus de préparation, d'installation et de mise en service du sytème de monitorage rapide de conditions de faisceau (BCM1F-μTCA), amélioré lors de cette phase, sont décrites dans cette thèse. Sa conception a été optimisée sur la base de l'analyse des performances atteintes lors de la précédente phase d'exploitation du système BCM1F, les principaux changements étant l'utilisation de capteurs au silicium et l'analyse de la forme des impulsions libres en temps réel et en temps mort dans l'électronique back-end. L'optimisation du systeme BCM1F-μTCA et les performances qui en résultent sont présentées en détail.
La méthode la plus courante et la plus précise pour obtenir un étalonnage absolu de la luminosité dans les collisionneurs de hadrons est la méthode van der Meer (vdM). Cependant, elle nécessite un examen attentif et une correction des effets systématiques liés à l'accélérateur. En effet, bien que de nombreux de ces effets ont déjà été étudiés en détail, leur impact direct sur l'étalonnage précis de la luminosité a longtemps été négligé. En particulier, l'interaction faisceau-faisceau, est désormais reconnue comme un facteur important. Les premiers modèles de correction sous-estimaient d'un facteur duex à six l'effet optique induit par l'interaction faisceau-faisceau. Cela a incité à déployer des efforts considérables pour reconnaître et quantifier différents ingrédients de l'incertitude systématique liée au faisceau sur l'étalonnage de la luminosité. Le développement du nouveau modèle de correction a commencé, visant à l'origine le paramétrage des effets faisceau-faisceau sur la luminosité dans le cas le plus simple d'un seul point d'interaction. L'objectif principal était de fournir des corrections par paquet en fonction de ses propriétés.
Cette étude vise à étendre le modèle de correction avec un niveau de complexité supplémentaire : les effets multi-collisions. L'étude des contributions supplémentaires à l'incertitude systématique résultant de l'interaction faisceau-faisceau est présentée, en considérant les angles de croisement dans les balayages vdM ainsi que la sensibilité aux avances de phase entre les points de collision. Les études de simulation multiparticules sont complétées par les données d'une expérience faisceau-faisceau dédiée au LHC, conçue pour fournir la première mesure statistiquement significative des effets faisceau-faisceau sur la luminosité. Ces effets ont été étudiés en fonction de la force de l'interaction, des étapes de séparation lors du balayage des faisceaux, ainsi que du nombre de collisions.
Les études détaillées des détecteurs ont conduit à une mesure de l'incertitude systématique d'intégration minimisée sur la luminosité intégrée mesurée par BCM1F-μTCA en 2022. L'étalonnage de l'échelle de luminosité absolue de cet ensemble de données avec la méthode vdM a été effectué, et les effets faisceau-faisceau figuraient parmi les corrections d'étalonnage les plus importants. L'incertitude systématique globale correspondante a été estimée, en profitant des études détaillées sur les effets d'interaction faisceau-faisceau. Ce travail aboutit à une précision sans précédent sur l'étalonnage préliminaire de la luminosité délivrée dans le détecteur CMS, avec une projection vers une précision ultime inférieure à 1%.

Contents

List of acronyms

Symbols

μTCA Micro Telecommunications Computing Architecture.

A

AC Alternating Current.
ADC Analog-to-Digital Converter.
ADT The LHC Transverse Damper.
ALICE A Large Ion Collider Experiment.
AMC Advanced Mezzanine Card.
AOH Analogue Opto-Hybrid.
ASIC Application-Specific Integrated Circuit.
ATLAS A Toroidal LHC Apparatus.

B

BB Beam-Beam.
BBQ Base-Band Tune Measurement System.
BCID Bunch Crossing Identification Number.
BCM1F Fast Beam Conditions Monitor.
BCML Beam Conditions Monitor for Losses.
BGI Beam Gas Imaging.
BHM Beam Halo Monitor.
BIB Beam-Induced Background.
BLM Beam Loss Monitor.
BPM Beam Position Monitor.
BPTX Beam Pickup Timing for eXperiments.
BRAN Beam RAte of Neutrals.
BRIL Beam Radiation, Instrumentation, and Luminosity.
BRILDAQ BRIL data acquisition system.
BSRL Beam Synchrotron Radiation Telescope - Longitudinal.
BSRT Beam Synchrotron Radiation Telescope - Transverse.
BX Bunch crossing.

C

CEPC Circular Electron-Positron Collider.
CERN European Laboratory for particle physics.
CLIC The Compact Linear Collider.

CMS Compact Muon Solenoid.
COMBI COherent Multibunch Beam-beam Interactions.
CP Collision Point.
CVD Chemical Vapor Deposition.

D

DA Dynamic aperture.
DAQ Data acquisition.
DCCT DC current transformer.
DESY Deutsches Elektronen-Synchrotron.
DG Double Gaussian.
DIP Data Interchange Protocol.
DOH Digital Opto-Hybrid.
DOROS Diode ORbit and Oscillations System.
DSR Double Storage Ring.
DT Drift Tubes.

E

EIC Electron-Ion Collider.

F

FBCM Fast Beam Conditions Monitor.
FBCT Fast Beam Current Transformer.
FCC Future Circular Collider.
FIFO First in, first out.
FLUKA A simulation code used to simulate radiation levels.
FMC FPGA Mezzanine Card.
FPGA Field-programmable gate array.
FPIX Forward Pixel.
FWHM Full width at half maximum.

G

GLIB Gigabit Link Interface Board.

H

HERA Hadron–Electron Ring Accelerator.
HF Hadronic Forward Calorimeter.
HFET HF E_T sum algorithm.
HFMM Hybrid Fast Multipole Method.
HFOC HF occupancy algorithm.
HL-LHC High Luminosity LHC.
HV High Voltage.

I

ILC International Linear Collider.

IP Interaction Point.
IR Interaction Region.
ISR Intersection Storage Rings.

L

LEMMA Low EMittance Muon Accelerator.
LHC Large Hadron Collider.
LOD Linear Orbit Drift.
LR Long-range.
LS Lumi Section, approx. 23.3s.
LUCID The ATLAS Luminosity Detector.

M

MADX Methodical Accelerator Design.
MAP Muon Accelerator Program.
MIP Minimum Ionizing Particle.
MPI Message Passing Interface.
MPV Most Probable Value.

N

NSIP Non-scanning Interaction Point.

O

OMC Optics Measurement and Corrections.
OMS Online Monitoring System.

P

PCB Printed Circuit Board.
PCC Pixel Cluster Counting.
pCVD Polycrystalline chemical vapor deposition.
PLL Phase-locked loop.
PLT Pixel Luminosity Telescope.
PLUME Probe for LUminosity MEasurement.
PMI Air-filled ionization.
PMT Photomultiplier Tube.

Q

QCD Quantum chromodynamics.
QED Quantum electrodynamics.

R

RAMSES Radiation Monitoring System for the Environment and Safety.
RF Radio Frequency.
RHIC Relativistic Heavy Ion Collider.

RHU Realtime Histogramming Unit.
ROD Residual Orbit Drift.

S

SBIL Single-bunch instantaneous luminosity.
SG Single Gaussian.
SLAC Stanford Linear Accelerator Center.
SM Standard Model.
SND Scattering and Neutrino Detector.
SNR Signal-to-noise ratio.
SPD Silicon Pixel Detector.
SPS The Super Proton Synchrotron.
SSR Single Storage Ring.

T

TCDS Trigger Control and Distribution System.
TDR Technical Design Report.

U

USC CMS service cavern.

V

vdM van der Meer scan.
VELO VErtex LOcator.
VGI Vacuum pressure gauges.
VME Versa Module Eurocard.

W

WCT Wall Current Transformer.
WS Wire Scanner.

Z

ZDC Zero Degree Calorimeters.

Large Hadron Collider and beyond Part I

The first colliders were built as discovery machines. Aimed to provide access to high energies:

$$E_{cm} = \left[2E_1E_2 + (m_1^2 + m_2^2)c^4 + 2\sqrt{E_1^2 - m_1^2c^4}\sqrt{E_2^2 - m_2^2c^4}\cos\phi \right]^{1/2}, \quad (1)$$

where E_1, E_2 and m_1, m_2 and energies and masses of the two colliding beams at crossing angle ϕ. The collider era started with lepton machines when AdA facility was built [1]. This first hadron collider, the Intersecting Storage Ring (ISR), was built only a decade later at CERN, paving the way towards the S$p\overline{p}$S first and then the Large Hadron Collider [2] that is currently setting the energy frontier. The list of all past and current existing hadron colliders is presented in Tab. 1 - two out of six ever-existing hadron colliders are currently in operation. Many notable discoveries have been made throughout the colliders' history. Starting with the Touschek effect in the first lepton collider, studying interactions of various particle types, measurements confirming QED and QCD theory, discovering all the pieces of the Standard Model (SM), including heavy leptons and quarks, the W, Z, and Higgs bosons. It was followed by traces of the charge-parity (CP) violation, at the turn of the new millennium, indicating that the model is not complete. Its theory was brought into light in the attempts of cosmology to explain the dominance of matter over antimatter in the present universe and in the study of weak interactions in particle physics.

Apart from fundamental physics studies, this fast development over the last century was followed by a lot of technological advances. These have a contribution to everyday life: Internet (www), hadron therapy, complex materials of various uses (energy, photonic, biocompatibility, composite structures), semiconducting devices including advanced imaging, integrated circuits, and high field magnets.

There are two types of colliders: storage rings and linear colliders (or actually the linear collider). In the former, the beams are continuously circulated and meet each other at every turn in the accelerator at defined locations called interaction points (IPs), while the latter is a single pass machine, and beams are discarded after a collision. The beams in storage rings can be circulated in a single ring (SSR), in case one of the beams consists of the antiparticles of the other beam, or in double rings for other cases (DSR).

Period	**Location**	**Name**	**Machine Type**	**Particle Types**	**Max.** E_{cm} [GeV]
1971-1984	CERN, Europe	ISR	DSR	pp	63
1981-1984	CERN, Europe	S$p\overline{p}$S	SSR	$p\overline{p}$	630
1987-2011	Fermilab, USA	Tevatron	SSR	$p\overline{p}$	1960
1992-2007	DESY, Germany	HERA	DSR	$e^{\pm}p$	320
2000-now	Brookhaven, USA	RHIC	DSR	Heavy ions	200/u
2001-now				pp	500
2008-now	CERN, Europe	LHC	DSR	pp	13600
2010-now				Heavy ions	13600/u

Table 1: List of all existing hadron colliders [3].

The productivity and performance of a collider are measured in terms of the integrated luminosity. On the side at the experiments, it is the metric of the amount of collected data, expressed in terms of the recorded luminosity. The latter depends on the availability of the subsystems that allow to reconstruct events.

Large Hadron Collider

The Large Hadron Collider (LHC) [2] is the largest experiment in the world, in terms of the area with the accelerator circumference of 27 km, as well as in terms of the collaboration, involving thousands of people around the globe from around 240 institutes and universities. It hosts four main experiments along the ring located at the so-called interaction regions (IRs), where the two beams circulating in opposite directions cross each other. There are two general-purpose detectors ATLAS [4] and CMS [5], designed with the primary aim of discovering the Higgs boson. The LHCb [6] detector was designed for precise measurement of CP violation and rare decays of charged and beauty hadrons, and the dedicated heavy-ion detector ALICE [7] focuses on strongly interacting matter. Additionally, smaller experiments are also present at the LHC, with the latest two that started to operate recently in 2022: FASER [8] and SND@LHC [9].

Since the beginning of its operation in 2008, the LHC and its experiments have built a great legacy. The Standard Model of particle physics has been confirmed with high accuracy, up to the unprecedented energy level of $\sqrt{s} = 13.6$ TeV. The last missing particle was discovered at ATLAS and CMS experiments, proving the existence of the Higgs boson in 2012. At that point, the LHC's initial goal was achieved, considering the exploratory possibilities, and evolving into a powerful tool towards the legacy precision measurements.

Until the end of 2023, the LHC delivered a total of 237 fb^{-1} integrated luminosity, with expectations of another $\sim$ 200 fb^{-1} within Run 3, which is currently scheduled until the end of 2025. In terms of instantaneous luminosity, the LHC can operate currently above twice its design value, up to $\sim$ 2.5×10^{34} cm^{-2}s^{-1}. However, the further operation in Run 3 is foreseen at lower peak instantaneous luminosity as the trigger systems of the high-luminosity experiments are currently unable to process the corresponding number of pp interactions per bunch-crossing, $\sim$ 75 are predicted for the indicated peak luminosity results. The data processing capacity of the detectors is planned to be increased with major subsystem upgrades in the next shutdown period scheduled between 2026 and 2028. The overview of the LHC performance is shown in terms of CMS-measured delivered luminosity for the pp collisions, shown per year of operation in Fig. 1. Many of the precision measurements of the Standard Model physics require high precision in the luminosity measurement. Currently, there are analyses where it is the largest single contribution to the final systematic uncertainty. This is the case for example in the W [10] and Z [11] boson studies, as well as top quark [12, 13], and the Higgs boson [14] production cross section measurements. The luminosity precision is predicted to become even more significant in the High-Luminosity LHC (HL-LHC) era [16]. Major upgrades are planned, that will enable the LHC and experiments to operate for the next decade, currently planned up to 2041, with the prediction of reaching 3000 fb^{-1} of total integrated luminosity at each of the high-luminosity experiments (ATLAS and CMS). The larger data sample will enable more precise studies or rare processes, but it will still depend on the systematic uncertainty in the luminosity determination. Another goal is to achieve the unprecedented peak instantaneous luminosity of $\mathscr{L}_{peak} = 5 \times 10^{-34}$ cm^{-2}s^{-1}. Several advancements are planned that extend the capabilities of accelerator technology beyond its current boundaries. These include novel technology and physical processes for beam collimation, and 100-meter-long high-power superconducting links with minimal energy dissipation [17]. The increase in the instantaneous luminosity is planned to be achieved thanks to the high brightness achieved in the injector chain. The intensity of the proton bunches will be increased to 2.2×10^{11} and reduced transverse beam size of ~ 6.6 μm at the IP. The reduced beam size is achieved thanks to a more powerful focusing new triplet magnets system, enabling to reach $\beta^* = 0.15$ m. To avoid multiple beam-beam collisions left and right of the IP the LHC operates at a finite crossing angle. The reduced overlap of the two beams coming

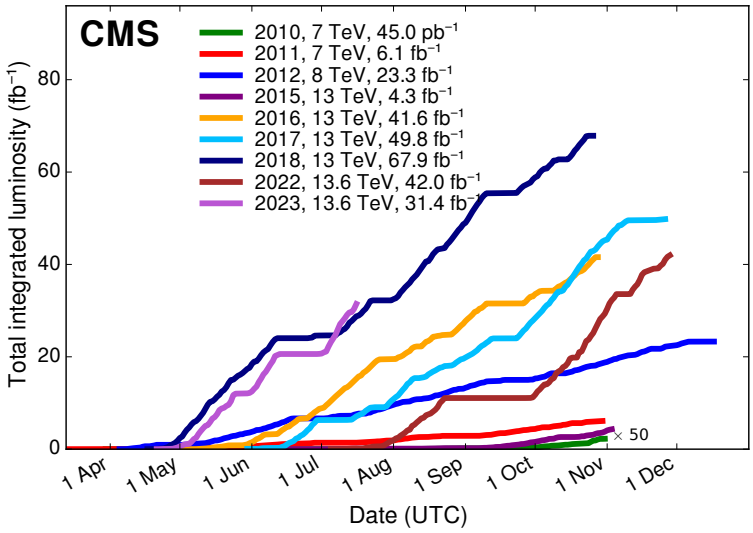

Figure 1: LHC delivered luminosity versus time per each year of nominal pp operation, at different center of mass energies [15].

from such an operational set-up will be canceled thanks to two techniques: applying β^* leveling [18] and/or a beam rotation with superconducting crab cavities just before the collision. The goal is to maximize the overlap of the two beams and therefore the luminous region. This upgrade is a catalyst for the development of new technologies including focusing magnets for ATLAS and CMS, crab cavities, and collimators. Limitations to bunch intensity due to e-cloud and resulting heat load, which are an issue at the LHC, are planned to be mitigated with in situ surface treatment [19].

Future colliders

Since the era of particle colliders began, the pieces of the Standard Model have been collected. From probing the structure of ubiquitous proton to the discovery of the long-awaited Higgs boson, with abundant and diverse measurements on the way. Nevertheless, there are still many unanswered questions about the Universe and observed anomalies. This causes suspicion in the high-energy physics community in physics Beyond the Standard Model.

The construction of the first Electron-Ion Collider (EIC) at the Brookhaven Laboratory (US) is approved. It is aimed at studying the strong force, quarks, and gluons with a polarised electron beam. It is expected to be operational in the next decade (around 2033) [20].

Based on the multi-dimensional achievements of the hadron colliders, the discussion on the future machines is ongoing. The conceptual studies are in progress for a diverse range of possible lepton colliders or hadron colliders as the Higgs factories (FCC-ee, FCC-hh, FCC-eh, CLIC (CERN), CEPC, SppC (China), ILC (Japan), C^3 (SLAC)). The possibility of building a muon collider is under study (International Muon Collider Collaboration, MAP (US), LEMMA (IT)), which for a long time was assumed to be impossible due to the extremely short muon lifetime.

Outline of the thesis

This thesis is composed of three main parts, followed by the general conclusion section.

In the first part, the luminosity is defined (Chapter 1), and the overview of the absolute scale calibration is presented, including the most precise van der Meer (vdM) method. The basic formalism is introduced that is relevant for the following parts. Additional possible complications in physics data-taking conditions are summarized. Chapter 2 begins with the basics of luminosity counting and the discussion of the detector-related systematic effects. The LHC instrumentation relevant to the luminosity measurement is introduced, and it is followed by a summary of the luminosity measurement strategies of each of the main experiments. The main section in this chapter is devoted to one of the CMS luminometers - the Fast beam conditions monitor (BCM1F), as it includes all the detector-related work performed within this project. This includes hardware preparation and installation within the CMS volume, followed by the commissioning of the upgraded detector and the new backend system. The studies related to the detector optimization and performance are presented, with examples of possible measurements next to the luminosity. The chapter includes the outlook toward the HL-LHC era in terms of luminosity and LHC instrumentation upgrades.

Among the biases to the luminosity calibration, the electromagnetic interactions of the two colliding beams have been identified as the major contributor. Part II starts with Chapter 3 which includes a subset introduction of the beam dynamics relevant to understanding the beam-beam interaction. A linearized model is derived to describe the beam-beam interaction-induced effects on the luminosity calibration with the van der Meer method. The model limitations are highlighted, supporting the need for multi-particle tracking and numerical luminosity calculation. This approach is further employed in Chapter 4, devoted to the studies on the beam-beam related systematic effects for the vdM calibration. These studies are a part of the collaborative effort to derive the precise corrections for the beam-beam effects and estimations of various contributions to the related systematic uncertainty. Results of this study have been published in [21]. The extension of the correction model is presented from the single-collision to the real-scenario multi-collision characterization, leading to a significant increase in the final correction. Further, systematic uncertainty contributions are defined from the residual crossing-angle during the vdM scans as well as the sensitivity to the phase advance between the collision points. Chapter 5 describes the experiment at the LHC, that was designed to validate the above-mentioned simulation studies. The first measurement of the beam-beam effects on the luminosity is presented.

Lastly, Part III establishes the connection between the two previous parts. The absolute luminosity calibration is performed for the BCM1F-μTCA on its first Run 3 data set. The calibration and integration systematic uncertainties are discussed in separate sections, highlighting the excellent BCM1F-μTCA performance. Moreover, the investigation into the non-linearity inherent in the detector's response is presented through the application of specialized beam-beam corrections in a novel approach. The last section includes a discussion on the overall systematic uncertainty with an outlook towards the legacy results.

1 Luminosity formalism

There are two key particle collider parameters that define its efficiency as well as the discovery potential. Firstly, the available center of mass energy $\sqrt{s}$ for probing normally unreachable scales, which is maximized in the collider geometry with both beams being accelerated in opposite directions. Secondly, the instantaneous luminosity $\mathscr{L}_{\text{inst}}$ that defines the number of observable events at a given time. It is the proportionality factor between the particle rate R and the production cross section for a given event σ_{ev} [22]:

$$R = \mathscr{L}_{\text{inst}} \cdot \sigma_{\text{ev}}. \tag{1.1}$$

Thus the instantaneous luminosity unit is $\text{cm}^{-2}\text{s}^{-1}$. The collection of data extends in time, and ultimately, the total integrated luminosity has to be evaluated to define the total number of events observed:

$$\mathscr{L}_{\text{int}} = \int_0^T \mathscr{L}_{\text{inst}}\, dt. \tag{1.2}$$

This is especially important for rare events with a small production cross section. Their observation with a large statistical sample is only possible within the limited time of an accelerator operation when the integrated luminosity is maximized. For the integrated luminosity, the unit of the inverse barn is used, defined as $b = 10^{-28}$ m^2, which links it to the production cross sections typically expressed in barns. If the Standard Model Higgs boson production cross section is considered [23], and the total CMS integrated luminosity shown in the previous Section, there have been more than 12 million Higgs bosons produced (or twice that in both ATLAS and CMS). There is also a slight distinction between the delivered luminosity from the accelerator and the recorded luminosity by the experiments. The experiments require stable conditions and a complex setup including multiple systems so that the events can be recorded, and only these events can be used in the following analyses.

Luminosity is defined directly from the beam parameters. In general terms, it is obtained by integrating over the particle density distribution in all directions, and including the time variable $s_0 = c \cdot t$ to describe the movement of the beams across each other, which describes the distance to the central collision point (IP):

$$\mathscr{L}_{\text{inst}} = K \cdot N_b N_1 N_2 f_{\text{rev}} \int\int\int\int_{-\infty}^{+\infty} \rho_1(x, y, s, -s_0)\rho_2(x, y, s, s_0)\, dx\, dy\, ds\, ds_0, \tag{1.3}$$

where K is the kinematic factor of the two beams moving against each other with a speed close to the speed of light, N_b is the number of bunches within the beam, N_1 and N_2 are the number of charges per bunch within each of the beams, f_{rev} is the revolution frequency as controlled by the radio-frequency

(RF) accelerating cavities. For the beams colliding centrally $K = 2$ with factorizable density distributions ρ in all planes, the overlap integral can be defined as:

$$\mathscr{L}_{\text{inst}} = 2N_b N_1 N_2 f_{\text{rev}} \int\int\int\int_{-\infty}^{+\infty} \rho_{1,x}(x)\rho_{1,y}(y)\rho_{1,s}(s-s_0) \\ \rho_{2,x}(x)\rho_{2,y}(y)\rho_{2,s}(s+s_0)\, dx\, dy\, ds\, ds_0. \tag{1.4}$$

In this chapter, the luminosity formulas are derived for various machine configurations and beam parameters. Gaussian particle distributions are used in all three dimensions as described in the following section, as a natural choice. In section 1.3.5 the significance of this choice is discussed. In the following sections including the simulation results, no assumption on the particle density distribution is needed when the luminosity is evaluated, as it is calculated numerically. The luminosity formulas for Gaussian beams are used to validate the numerical implementation and to understand the dependence on measurable parameters. In real scenarios, Eq. (1.3) is extended to include the possibility of each bunch having an independent number of charges and density distribution parameters. This can be obtained by dropping the N_b factor in the expression and making a sum over the Single Bunch Instantaneous Luminosity, commonly abbreviated to SBIL. In this case, N_1 and N_2 as well as the transverse bunch sizes are dependent on the specific bunches crossing each other.

1.1 Luminosity definition from beam parameters

To obtain a closed formula, it is possible to assume beams have typically Gaussian distributions:

$$\rho_{\text{beam, i}}(i) = \frac{1}{\sqrt{2\pi}\sigma_i} \exp\left(-\frac{i^2}{2\sigma_i^2}\right), \tag{1.5}$$

where i can be any of the transverse x, y or longitudinal $s \pm s_0$ planes, and σ represents the RMS width of that distribution $\sigma^2 = \frac{1}{2}\langle i^2 \rangle$ and thus is commonly referred to as the bunch size. Inserted into eq. 1.4, with the simplifying assumption of geometrically equal beams ($\rho_{1,i}(i) = \rho_{2,i}(i)$), the integral becomes:

$$\mathscr{L}_{\text{inst}} = \frac{2N_b N_1 N_2 f_{\text{rev}}}{(\sqrt{2\pi})^6 \sigma_x^2 \sigma_y^2 \sigma_s^2} \int\int\int\int_{-\infty}^{+\infty} e^{-\frac{x^2}{\sigma_x^2}} e^{-\frac{y^2}{\sigma_y^2}} e^{-\frac{s^2}{\sigma_s^2}} e^{-\frac{s_0^2}{\sigma_s^2}}\, dx\, dy\, ds\, ds_0. \tag{1.6}$$

Performing the integration (using Eq. A.1), it is possible to obtain the common luminosity expression for the Gaussian beams:

$$\mathscr{L}_{\text{inst}} = \frac{N_b N_1 N_2 f_{\text{rev}}}{4\pi\sigma_x\sigma_y}. \tag{1.7}$$

It is commonly expressed using the convoluted beam widths Σ_i, which corresponds to the integral without the assumption on the symmetry of the two beams in transverse planes:

$$\mathscr{L}_{\text{inst}} = \frac{N_b N_1 N_2 f_{\text{rev}}}{2\pi\Sigma_x\Sigma_y} = \frac{N_b N_1 N_2 f_{rev}}{2\pi\sqrt{\sigma_{1,x}^2 + \sigma_{2,x}^2}\sqrt{\sigma_{1,y}^2 + \sigma_{2,y}^2}}. \tag{1.8}$$

It is worth noting that this expression does not depend on the bunch length σ_s, and it is only true in case of the uncorrelated density distributions.

The formula in Eq. 1.7 is commonly used to estimate the luminosity from the beam parameters in the assumption that the beam profiles remain Gaussian. It is not used in the precision studies that aim to

understand effects at the 0.1% level. For these studies, the numerical luminosity estimation is used instead, based on the true particle distributions and performing the integration, according to Eq. (1.3). It can be used with any original particle distribution and allows for understanding the changes to the distribution, for example coming from the beam-beam interaction. Nevertheless, the formulas presented in this chapter for the simplest Gaussian distributions are vital in the benchmarking phases of the numerical calculations.

Bunch transverse sizes at the collision points

The rms width of a bunch, $\sigma_{x,y}$ which represents its size is the product of the optical β function and the geometrical beam emittance. The first represents the focusing strength provided by the quadrupole magnet system that confines and squeezes the transverse dimensions of the beams along the accelerator. It is one of the Courant-Snyder (Twiss) parameters that describe the evolution of the phase space ellipse in a periodic beam line. The second is a property of a charged particle bunch, and it refers to the area occupied by that bunch in position-and-momentum phase space. In the case of zero dispersion, as it is by design at the interaction points, the bunch σ is given by the following expression:

$$\sigma = \sqrt{\beta^* \times \epsilon_g}. \tag{1.9}$$

where β^* is the optical function at the interaction point, while ϵ_g is the geometrical beam emittance. The latter depends on the bunch energy and the normalized bunch emittance ϵ_n:

$$\epsilon_g = \frac{\epsilon_n}{\gamma \beta_{\text{rel}}}, \tag{1.10}$$

where β_{rel} and γ are the relativistic factors. The normalized emittance is a constant during the acceleration process, thus causing the RMS bunch size to decrease. Such an effect is known in accelerator physics as adiabatic damping.

1.2 Absolute luminosity scale calibration

The measurement of the luminosity from the beam parameters is limited by the precision of the beam instrumentation. Namely, the precise estimation of the per bunch currents and colliding bunch-pair overlap are required. The latter is further complicated by the fact that it cannot be measured precisely outside of the collision region, as it depends on the local lattice properties including imperfections as well as the effects of the beam-beam interaction (this is discussed separately in Chapter 3).

Therefore, the beam-separation scans at the IPs are used to define the overlap area and achieve better precision. This calibration method, known with the name of van der Meer method [24], is discussed in the next Sec. 1.2.1. It is followed by the summary of other possible calibration methods in Sec. 1.2.2.

1.2.1 van der Meer method

If a constant offset Δ_i is added to a coordinate in a transverse plane $i \in x, y$, the integral in Eq. 1.6 will be reduced by an extra exponential factor W:

$$\mathscr{L}_{\text{inst}} = \frac{N_b N_1 N_2 f_{\text{rev}}}{4\pi\sigma_x\sigma_y} \cdot W, \qquad W = e^{-\frac{\Delta_i^2}{4\sigma_i^2}}. \tag{1.11}$$

This formula can be used to calculate the luminosity at each separation step during a separation scan at the IP. It is important to notice that it is a Gaussian distribution with a width of $\sqrt{2}\sigma_i$. This formalism enables the measurement of the transverse beam width at the IP by performing a separation scan and measuring the luminosity at each of these steps. In case of non-equal beam sizes for the colliding pair more general form is used:

$$\mathscr{L}_{\text{inst}} = \frac{N_b N_1 N_2 f_{\text{rev}}}{2\pi\Sigma_x\Sigma_y} \cdot W, \tag{1.12}$$

where W is the reduction factor that depends on the offset between the beams and convoluted beam width:

$$W(\Delta_i, \Sigma_i) = e^{-\frac{\Delta_i^2}{2\Sigma_i^2}}. \tag{1.13}$$

The method of performing a separation scan for the beam size measurement was used for the first time at the CERN Intersection Storage Rings (ISR) [24]. This technique was named after its pioneer - Simon van der Meer, who is also well known for the invention of the stochastic cooling of particle beams, for which he was awarded the Nobel Prize. It was extended in [25] for the measurement on the absolute luminosity scale. It is referred to as the van der Meer (vdM) method and is applied as the main calibration technique by all the LHC experiments. During these scans, the detector-specific constant is measured that relates the observed rate to the absolute instantaneous luminosity computed from measured beam parameters at one point in time. Under the assumption of uncorrelated x and y planes, the transverse convolved bunch widths Σ_x, Σ_y can be extracted from the measured beam-separation dependence of the collision rate R:

$$\Sigma_x = \frac{1}{\sqrt{2\pi}} \frac{\int R(\Delta_x, 0) d\Delta_x}{R(0,0)}, \qquad \Sigma_y = \frac{1}{\sqrt{2\pi}} \frac{\int R(0, \Delta_y) d\Delta_y}{R(0,0)}. \tag{1.14}$$

The above definition using the integral avoids the assumption made in Eq. (1.11) on the shape of the transverse distributions. In reality, the term 'specific luminosity' is used instead - which is the measured collision rate normalized to the colliding bunch-pair intensities to remove the dependence on the change of the current with time. This is equivalent, based on the direct proportionality of measured rate and luminosity Eq. (1.1). The total rate R^{vis} measured by a detector is primarily defined from Eq. (1.1), but also depends on detector-intrinsic features: position, geometry, sensor, and system efficiencies. Thus, it is dependent on the luminometer-specific constant σ_{vis} :

$$R^{\text{vis}} = \mathscr{L}_{\text{inst}} \sigma_{\text{vis}}. \tag{1.15}$$

The combined information from the vertical and horizontal scans (from Eq. (1.14)), bunch intensities $N_{1,2}$, and the rate at the peak $R^{\text{vis}}(0,0)$ allow to calculate the instantaneous luminosity from the measured bunch parameters. Thus the luminometer-specific visible cross section is obtained:

$$\sigma_{\text{vis}} = \frac{R^{\text{vis}}(0,0)}{N_1 N_2} 2\pi\Sigma_x\Sigma_y. \tag{1.16}$$

Subsequently, this calibration constant is used to measure the luminosity directly from the detector rate, at any beam conditions:

$$\mathscr{L}_{\text{inst}} = \frac{R}{\sigma_{\text{vis}}}, \tag{1.17}$$

where $R = \mu^{\text{vis}} f_{\text{rev}}$ is the observable rate of hits, events, tracks, clusters, etc. The typical cross section unit of a barn is also used, with common values from ~ 0.1 mb and much higher for high occupancy luminometers.

Special conditions required for dedicated vdM calibration fills to maximize the measurement precision are discussed in Sec. 4.1. The calibration is performed regularly, typically every year to minimize the bias from long-term changes in the detector performance.

Extended scan programs to study systematic effects

Multiple scans are performed within the vdM fill to study the systematic effects during the calibration process. This includes:

- multiple pairs of standard full separation vdM scan pairs in the two transverse planes. Typically, 25 steps each 60 s long are used within the transverse separation ranges of $\langle -6\sigma; 6\sigma \rangle$ in each plane. Any variation in the results within these scans indicates the uncorrected systematic effects.
- Super-separation scans - separating the beams fully at the IP allows to study the sensitivity of a detector to the beam-induced backgrounds.
- Beam-imaging is performed by scanning the transverse profile of one beam using the other beam. Thus the separation is applied to one of the beams while the other is stationary. Such a scan has to be repeated separately for each of the beams.
- Constant-separation scans are performed to understand the length scale of the nominal separation applied using the corrector magnets. The beams are moved to maximum absolute displacement in multiple steps while keeping a constant distance between the two beams.
- Diagonal scans are separation scans at 45°, thus the movement of the beams is applied in both transverse directions at the same time. A variation of this scan is also possible at different angles.
- Constant-offset scans are standard vdM scans with additional offset in the non-scanning plane.
- 2D scans are also performed with the full transverse distributions scanned at once. This is particularly useful for the non-factorization analysis as the full luminous area can be studied.

The example use of such an extended scan program is presented in Part III for the 2022 vdM calibration at the CMS experiment.

1.2.2 Other methods

The Beam Gas Imaging (BGI) method [26] allows for the reconstruction of the luminous region based on the spatial distribution of beam-gas vertexes data. The measured luminous region combined with any detector measurement can be used to infer the luminosity and thus to find the absolute luminosity scale. A high-precision vertexing detector is necessary to obtain an accurate reconstruction.

This method was pioneered by LHCb with a dedicated gas-injection system, achieving comparable precision to the vdM method [27].

The optical theorem can be used to extract simultaneously the total pp cross section and the luminosity. It follows from the general law of scattering theory and the conservation of probability in quantum mechanics. Elastic pp scattering at small angles can be used to measure the luminosity if combined with measurement of the total pp interaction rate or the elastic scattering in the Coulomb-interference region [28].

The indirect luminosity measurement is also possible using a reference physics process. This requires precise knowledge not only of the relevant cross section but also of the acceptance and efficiency of the relevant subdetectors. In e^+e^- colliders the Bhabha scattering process is commonly used as the cross section theoretical error is below 0.05% [29]. At the hadron colliders, the cross section predictions have significantly worse accuracy in the order of 1%. Commonly, Z boson counting is used currently reaching the 2% precision [30].

1.3 Physics operation conditions

Maximizing the total integrated luminosity implies that the operating conditions of a collider have to be pushed to their limits. From the simplest definition of luminosity with the beam parameters (Eq. 1.7), it is clear that it can be maximized by maximizing the machine revolution frequency, number of bunches, per bunch charge, and minimizing the transverse overlap area at the IP. The first two parameters are limited by the machine design. Specifically, by the machine radius ρ, according to $f_{rev} = \frac{\beta_{rel}c}{2\pi\rho}$ and the frequency of the cavities that define the harmonic number h of a synchrotron, and thus the number of available potential buckets for a bunch: $h = \frac{f_{RF}}{f_{rev}}$. Additionally, the end of the orbit has to have empty space whose length corresponds to the rise time of the kicker magnet, which ensures the possibility of a safe beam dump. The maximum charge is limited by multiple factors. With increasing current, the strength of beam-beam interactions increases, both at the IP and all other long-range interactions in the common vacuum chamber - these effects are discussed in detail in chapter 3. The influence on the collimation and machine protection has to be considered, including the total beam power stored in the machine and the resulting heat load. Special injection schemes are used to reduce the losses, instabilities, and e^--cloud. The transverse area limit is defined from the emittance that depends on the performance of the injector chain, and β^* that is defined from magnetic lattice as described further in Sec. 1.3.4. On the side of experiments, the pile-up limitation has to be considered, in terms of the maximum number of events that can be processed at the same time.

1.3.1 Crossing-angle

The angle in one of the transverse planes is commonly applied to avoid unwanted collision in the common vacuum chamber around the IP. To obtain the luminosity formula in this case, the coordinates have to be rotated before performing the integral over the density distributions. The new coordinates are obtained by transforming both beams in a symmetric way, by the half crossing-angle $\phi/2$, but in the opposite directions. Assuming the crossing-angle is applied in the horizontal plane, the new

coordinates become:

$$x_1 = x\cos\frac{\phi}{2} - s\sin\frac{\phi}{2}, \quad s_1 = s\cos\frac{\phi}{2} + x\sin\frac{\phi}{2},$$
$$x_2 = x\cos\frac{\phi}{2} + s\sin\frac{\phi}{2}, \quad s_2 = s\cos\frac{\phi}{2} - x\sin\frac{\phi}{2}. \tag{1.18}$$

The constant in Eq. 1.4 has to be complemented with the updated kinematic factor $2\cos^2\frac{\phi}{2}$, and the overlap integral for the Gaussian bunch distribution takes a different form:

$$\mathscr{L}_{\text{inst}} = \cos^2\frac{\phi}{2}\frac{N_b N_1 N_2 f_{\text{rev}}}{4\pi^2\sigma_x^2\sigma_y\sigma_s}\int\int_{-\infty}^{+\infty} e^{-\frac{x^2\cos^2\phi/2 + s^2\sin^2\phi/2}{\sigma_x^2}} e^{-\frac{x^2\sin^2\phi/2 + s^2\cos^2\phi/2}{\sigma_s^2}} dx\, ds. \tag{1.19}$$

The final luminosity formula becomes extended with direct dependence on the bunch length and the crossing angle:

$$\mathscr{L}_{\text{inst}} = \frac{N_b N_1 N_2 f_{\text{rev}}}{4\pi\sigma_y}\frac{\sigma_s\cos^2\frac{\phi}{2}}{\sqrt{(\sigma_x^4+\sigma_s^4)\sin^2\phi/2\cos^2\phi/2 + \sigma_x^2\sigma_s^2(\sin^4\phi/2 + \cos^4\phi/2)}}. \tag{1.20}$$

Typically in hadron machines, very small crossing-angles are used, and the transverse sizes are a few orders of magnitude smaller than the longitudinal size. By allowing the multiplication of these two terms to disappear ($\sigma_x^n\sin^m\phi/2 \approx 0$), the formula is simplified:

$$\mathscr{L}_{\text{inst}} = \frac{N_b N_1 N_2 f_{\text{rev}}}{4\pi\sigma_x\sigma_y}\cdot S, \quad S = \frac{1}{\sqrt{1+\frac{\sigma_s^2}{\sigma_x^2}\tan^2\phi/2}} \tag{1.21}$$

where S can be easily interpreted in this form as the geometrical reduction factor that diverges from 1 with applied crossing-angle. Its dependence on the full crossing-angle in the physics conditions is shown in Fig. 1.1. Qualitatively, the geometrical transformation causes the beams to overlap at an effectively wider area:

$$\sigma_{\text{eff}} = \sigma_x/S = \sigma_x\sqrt{1+\frac{\sigma_s^2}{\sigma_x^2}\tan^2\phi/2}, \tag{1.22}$$

which reduces significantly the luminosity.

1.3.2 Emittance scans

The crossing-angle is necessary in one of the transverse planes during the operation with closely spaced bunches to reduce the impact from the long-range interactions. Therefore, the formula presented in Sec. 1.2.1 has to be extended with the crossing angle dependence for the purpose of describing the luminosity scans. These operational scans are regularly performed at the LHC for the emittance measurement and detector stability tracking. Integration over Gaussian density distributions including the coordinate transformation [Eq. (1.18)] as in Eq. (1.19) with an additional bunch centroid displacement

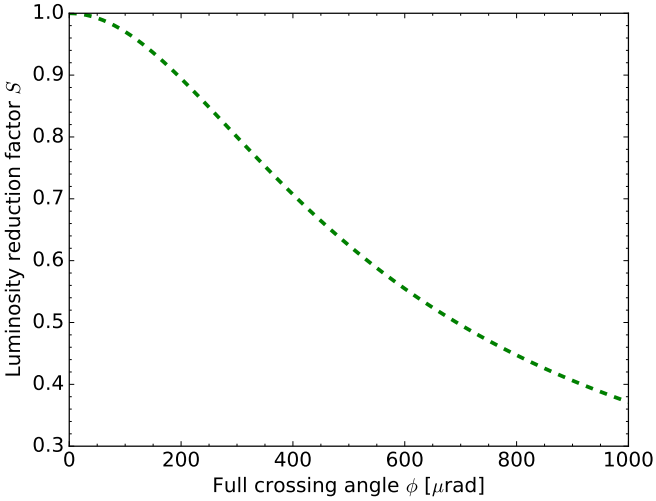

Figure 1.1: The luminosity reduction factor S as a function of the full crossing-angle for typical physics conditions with $\sigma_x = 15\ \mu m$ and $\sigma_s = 7.5$ cm in head-on configuration.

in a transverse plane, and using the same approximation ($\frac{\sigma_x^2}{\sigma_s^2} \approx 0$), results in the following formula:

$$\begin{aligned} \mathscr{L}_{\text{inst}} &= \frac{N_b N_1 N_2 f_{\text{rev}}}{4\pi\sigma_x\sigma_y} \cdot S \cdot W \cdot \exp\left(\frac{B^2}{A}\right), \\ A &= \frac{\sin^2\frac{\phi}{2}}{\sigma_x^2} + \frac{\cos^2\frac{\phi}{2}}{\sigma_s^2}, \qquad B = \frac{\Delta_x \sin\frac{\phi}{2}}{2\sigma_x^2} \end{aligned} \tag{1.23}$$

When compared to Eq. 1.12 and 1.21 it can be noticed that the presence of both crossing angle and displacement results in an additional exponential mixing factor, which is only present for the scanning direction in the crossing-angle plane (x plane used in the example). It can be shown that Eq. (1.23) is equivalent to the standard separation dependence formula in Eq. (1.12), if the effective overlap width is used that includes the crossing-angle and bunch length dependence, introduced in Eq. (1.22).

The widths extracted from the separation scans are the measure of the convoluted width of the two colliding bunches:

$$\sigma_{\text{av}} = \sqrt{\frac{\sigma_{B1}^2 + \sigma_{B2}^2}{2}}, \tag{1.24}$$

Then the normalized emittance can be estimated from:

$$\epsilon_n = \frac{\sigma_{\text{av}}^2}{\beta^*}\gamma\beta_{\text{rel}}, \tag{1.25}$$

after extracting the bunch length and the crossing-angle dependence from the measured σ_{eff} from the scan performed in the crossing-angle plane direction. Thus, the measurement precision in the crossing-angle plane is limited by the precision of bunch length and crossing-angle measurements.

The introduction of the crossing-angle couples one of the transverse planes to the longitudinal plane.

Therefore, the transverse displacements induce changes to the overlap of the two bunches in the longitudinal plane. This can be observed by the changes to the luminous region.

As the real overlap area is extracted in emittance scans, the vdM method can be applied to measure the σ_{vis} directly with Eq. (1.16). However, it is challenging to comprehend the systematic effects as thoroughly as in the dedicated vdM fills. These scans are typically much shorter (10 s/step), and usually performed over a narrow beam separation range ($\sim 3.5\,\sigma$), which has an impact on the precision of the extracted widths.

1.3.3 Luminosity optimization

From the perspective of machine performance, it is alluring to drive the new milestones of achieving the highest possible instantaneous luminosity. On the other side, for the experiments, it is crucial to be able to collect as much interesting data as possible. This is achieved, in most cases, by maximizing the total integrated luminosity, or by optimizing the luminosity to the desired number of proton-proton interactions occurring at the same time (pile-up).

LHC example

At the LHC, the peak luminosity exceeded already its design value. Since the beginning of its operation, there was a lot of effort put into optimizing the luminosity.

In Run 3, the leveling scheme was commissioned, which was designed to keep the instantaneous luminosity flat, instead of starting each fill from the highest possible value. It was done, by allowing the machine parameters to change at the IP [31]. The β^* and crossing-angle values are set to moderate values at the beginning of each fill, and reduced in steps, causing a change in the luminous region that results in a gradual increase in the luminosity.

Another way of recovering the luminosity is the use of "crab" crossing scheme [32]. This method allows to recover the geometric factor resulting from the need of beams crossing at an angle at the IP, by transversely deflecting them with cavities to recover the angle just before they arrive at the collision point. This method is under study at CERN SPS as one of the solutions for the HL-LHC.

1.3.4 Hour-glass effect

The β function is a property of the magnetic lattice of an accelerator and is dependent on the longitudinal position s. As described in the previous section, at the IP it is minimized to β^* . This is obtained by a complex magnetic structure including a quadrupole triplet. As a result, the β-function can get approximately 10^4 bigger at the quadrupoles, which creates a limit coming directly from the physical aperture for the minimum possible β^* at the IP. At the experimental area, β-function has a quadratic dependence on distance s from the IP:

$$\beta(s) = \beta^* \left(1 + \left(\frac{s}{\beta^*}\right)^2\right). \tag{1.26}$$

Thus, in the case of the small values of β^* , there is an increase of the transverse beam size along the distance from the IP (assuming no dispersion):

$$\sigma(s) = \sqrt{\beta(s) \cdot \epsilon} = \sigma_s \cdot \sqrt{1 + \left(\frac{s}{\beta^*}\right)^2}, \tag{1.27}$$

with ϵ corresponding to the bunch emittance, and σ_s to the minimum transverse bunch size calculated from β^* . It becomes significant with β^* approaching the bunch length σ_s. Example is shown in Fig. 1.2, with β-functions shown along the bunch length in range $\langle -6 \times \sigma_s, +6 \times \sigma_s \rangle$, and using an example bunch length of $\sigma_s = 7.5$ cm. The above-described dependence causes some of the particles to collide

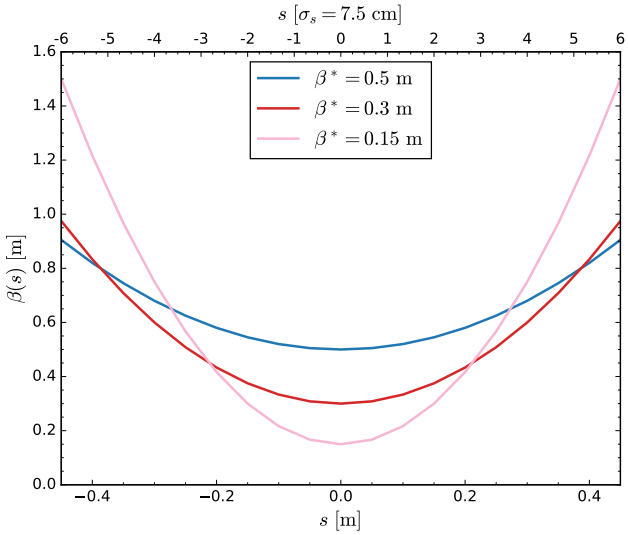

Figure 1.2: β-function around the interaction region (IP at $s = 0$) with low minimum β^* values. The parabolic change of β-function causes changes in the transverse beam sizes dependent on the distance from the IP. Because of the visible shape, this effect is known as the hourglass effect.

at increased transverse bunch size, and hence the area, therefore reducing the resulting luminosity. It is calculated using the general formula from Eq. (1.19) with transverse density distribution dependent on non-constant bunch size as in Eq. (1.27). This leads to the formula that cannot be solved analytically:

$$\mathscr{L}_{\text{inst}} = \cos^2\frac{\phi}{2}\frac{N_b N_1 N_2 f_{\text{rev}}}{4(\sqrt{\pi})^3\sigma_x^*\sigma_y^*}\int_{-\infty}^{+\infty}\frac{1}{1+(s/\beta^*)^2}\frac{1}{\sqrt{\sigma_s^2\cos^2\frac{\phi}{2}+(\sigma_x^*)^2\sin^2\frac{\phi}{2}(1+(s/\beta^*)^2)}} \times \exp\left(-s^2\left(\frac{\sin^2\frac{\phi}{2}}{(\sigma_x^*)^2(1+(s/\beta^*)^2)}+\frac{\cos^2\frac{\phi}{2}}{\sigma_s^2}\right)\right)ds. \tag{1.28}$$

The numerical implementation has to be used to study the impact of the hourglass effect on the luminosity. The example solutions are shown in Fig. 1.3. The above-mentioned reduction is shown, which is typically much smaller than the geometrical crossing-angle reduction but becomes more significant for extreme β^* values. In the presence of crossing-angle the bunch distribution overlap area can be augmented at a specific configuration which is also shown in Fig. 1.3, where the factor increases above 1. The plotted factor does not include the geometrical crossing-angle reduction.

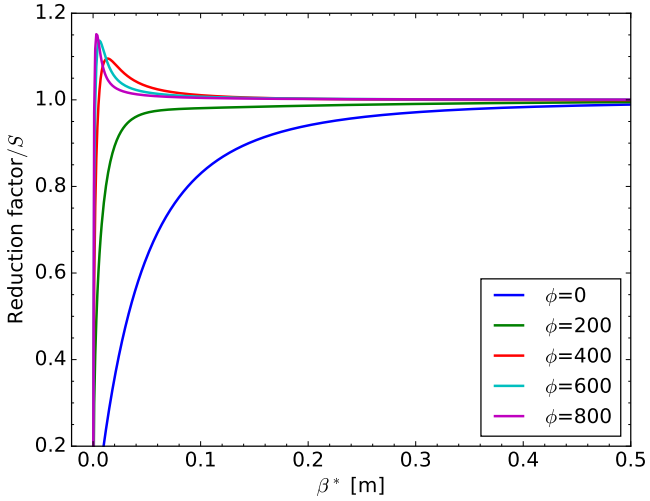

Figure 1.3: Luminosity reduction factor from the hour-glass effect (excluding the static crossing-angle-related factor S) at the head-on configuration as a function of β^* , for different crossing-angles ϕ [μrad].

1.3.5 Other potential challenges

In this section, other possible complications are listed that can contribute to the beam-related systematic effects or can have an impact on the luminosity measurement but are not discussed in the following chapters.

Non-gaussian profiles

Gaussian function is a good approximation for the spatial bunch density distributions at the LHC. However, it was observed that the tails of the transverse profiles are more populated than what is expected from the normal distribution. Various models are used by the experiments to describe the true bunch shape (for example [33, 34]). It has also an impact on the evaluation of the beam-beam effects as the generated field depends on the transverse charge distribution (discussed in Sec. 3.2.1). The example of how different generated kicks depend on the charge distribution as a function of amplitude within a bunch is shown in Fig. 1.4, for extreme cases. For more realistic scenarios with small deviations from the perfect Gaussian profiles, for example double- or q-Gaussian, the possible range of the bias needs to be evaluated with dedicated study beyond the scope of this thesis.

Luminous region displacement

As discussed in sec. 1.3.2, the luminous region is always displaced in the configuration with crossing angle and separation. However, this displacement can be also a result of the optics imperfections, causing the waist of the β-function to be shifted. In that case $d\beta^*/ds \neq 0$ at the IP, and thus the effective beam size is bigger than the design value, causing a reduction in luminosity.

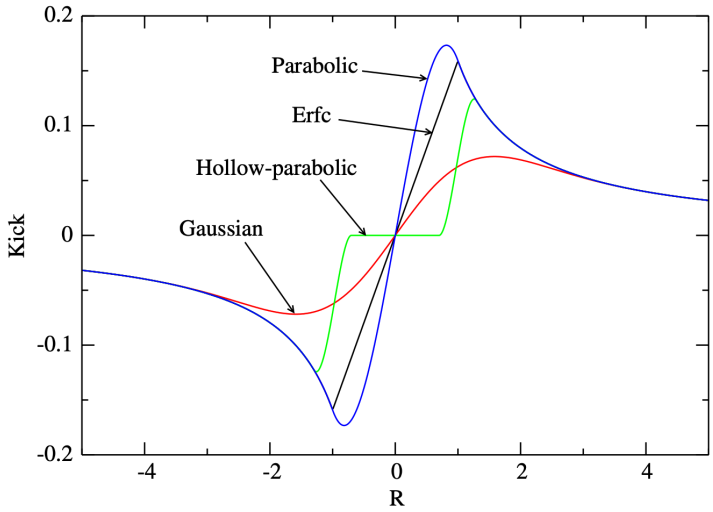

Figure 1.4: Incoherent transverse kick on a proton for different electron-bunch charge distributions [35]. An equal amount of charges was used for all distributions.

Non-zero dispersion

Particles in a bunch have intrinsically spread in momenta, which will cause them to move on an alternative (dispersive) orbit, as shown in Fig. 1.5. The lattice design and optimizations are aimed at

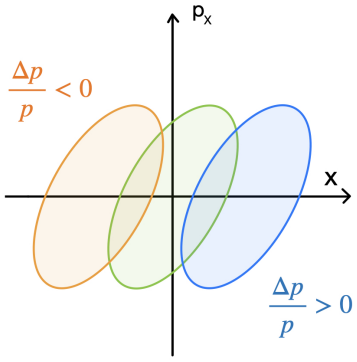

Figure 1.5: Dispersive orbits or particles with various momentum spread $\frac{\Delta p}{p}$ causing the beam size change in the presence of dispersion D^*.

minimizing dispersion at the IPs D^*. However, these are designed for specific configurations, and any change, for example, crossing angle or separation bump can modify the dispersion function. Non-zero dispersion can be also introduced by lattice imperfections. In that case, the effective beam size is increased, causing a reduction in the luminosity:

$$\sigma = \sqrt{\beta^* \, \epsilon + \left(D^* \frac{\Delta p}{p} \right)^2}, \tag{1.29}$$

where $\Delta p / p$ is the relative momentum spread.

Linear and non-linear lattice elements

The colliders are based on the linear elements, as the beam movement can be converged with dipoles and quadrupoles. In reality, the operation of a machine requires multiple higher-order elements and additionally the unwanted lattice errors (e.g. tilted quadrupoles) are present. Their presence breaks the independence of the horizontal and vertical motion and creates linear and non-linear coupling between the two transverse planes. This introduces an additional angle between beams, that would disappear in the case of a perfectly symmetric machine. However, in the two-ring collider, each beam is exposed to different magnetic perturbation terms leading to lattice resonances. These resonances will modify the particles equilibrium orbits and the overall focusing changing the single particle betatron frequencies [36].

Crab cavities

As mentioned in Sec. 1.3.3 crab cavities are considered as one of the luminosity optimization tools for the HL-LHC. The idea of removing the crossing angle at the collision is prone to deterioration resulting from the non-linear rotation. This imperfection is difficult to avoid, as the cavity has a finite frequency generating a sinusoidal field limited by the size of the cavity. Thus the deformation caused by the cavities can lead to a reduction of luminosity and changes to the luminous region when compared to the case of an ideal cavity designed to obtain zero crossing angle equivalent luminosity. This could also potentially lead to additional systematic effects if the crab cavities have to be used during the vdM calibration, i.e. coupling between all three planes. Additional tune shift is also expected from the impedance of crab cavities.

2 Luminosity measurement

The real-time luminosity measurement is pivotal for optimizing the operational scenarios of both the LHC and experiments. It determines the delivered luminosity, a critical parameter that underpins many of the physics goals of the experiments. As the LHC enters Run 3 and it is getting ready for Phase-2 (HL-LHC), the demands for precision in luminosity measurements have grown significantly. In many cases, achieving the desired level of physics precision hinges on achieving highly accurate luminosity measurements. Experience gained during Run 2 has highlighted the need for an overall luminosity systematic precision of approximately 1%. To meet this target, it has become evident that a combination of multiple detector systems with different systematic uncertainties, along with the development of sophisticated methods and algorithms, is necessary. These tools will not only facilitate the measurement of luminosity but also work to minimize the various components of systematic uncertainties associated with different detector types.

This chapter starts with an introduction to luminosity counting and the detector-related systematic effects that can deteriorate the direct measurement (Sec. 2.2). Further, the overview of the LHC instrumentation relevant to the luminosity measurement is presented (Sec. 2.3). The four main LHC experiments, where beams are colliding have independent and diverse approaches to the luminosity measurement. These are summarized separately for low luminosity experiments, in Sec. 2.6 and 2.5. The measurement is more demanding in high-luminosity (high pile-up) general-purpose experiments. The ATLAS instrumentation used in the luminosity measurement is summarized in Sec. 2.4, and more focus is put on the CMS approach (Sec. 2.7) and improved strategy for HL-LHC era. One of the CMS standalone luminometers - BCM1F is discussed in more detail in Sec. 2.8, as it was upgraded for the Run 3 with the aim of improving the luminosity measurement. The detector assembly, calibration, installation, and commissioning were a significant part of this thesis. The performance in Run 3 is discussed in detail and its absolute luminosity scale calibration is presented in Chapter III. The future CMS luminometer, FBCM, is planned to use the same sensors as the current BCM1F. Thus, the latter gives an insight into the performance of the future luminometry.

2.1 Luminosity counting algorithms

Direct instantaneous luminosity measurement relies on counting an observable that is proportional to the luminosity. Any observable with high statistical significance can be used to measure the luminosity. For example number of hits, tracks, charge clusters, trigger primitives, events, transverse energy E_{T} sum, etc. The zero-counting algorithm is commonly used to infer the average count, based on

the Poisson distribution, as shown in the following section. This method provides the luminosity measurement at any conditions, according to Eq. (1.17). The absolute calibration is necessary to define the detector specific σ_{vis} , as discussed in Sec. 1.2.1. Linear dependence between luminosity and the measurement is required. This is not guaranteed, especially in the high pileup conditions, as discussed further in Sec. 2.2.1. The long-term stability is crucial for good precision in the integrated luminosity measurement. This includes detector efficiency changes with radiation exposure but also involves the reliability of the detector and constant availability.

2.1.1 Zero-counting

In the zero-counting algorithm, the average number of hits is calculated based on the zero-hit probability. Assuming that the number of hits within a bunch-crossing follows a Poissonian distribution, the probability p of n hits is described by:

$$p(n) = \frac{\mu^n e^{-\mu}}{n!}, \tag{2.1}$$

where μ is the average number of hits (occupancy). It can be defined in the simplest form from counting 'zeros', denoting bunch-crossings that produced no hits:

$$p(0) = e^{-\mu}, \quad \rightarrow \quad \mu = -\ln[p(0)]. \tag{2.2}$$

This method requires the assumption that the probability of multiple hits per bunch-crossing is negligible. The zero-probability can be calculated from the difference between the probability sum (1) and the probability of any number of hits different than 0:

$$\mu = -\ln[p(0)] = -\ln[1 - p(n \neq 0)]. \tag{2.3}$$

Thus, the mean number of hits can be determined from the measured hit count r per bunch crossing:

$$\mu = -\ln\left[1 - \frac{r}{N_{\text{bc}}}\right], \tag{2.4}$$

where N_{bc} denotes the total number of bunch-crossings, and the fraction of counts per bunch-crossing is further referred to as $f_r = \frac{r}{N_{bc}}$. The total rate per second R is defined by multiplication by the LHC frequency f_{rev}.

The interesting part of the process becomes counting whether hits are present or not. As the number of bunch-crossings (trials) becomes large and given that the probability of a hit f_r (success) is small, the Poisson distribution becomes a special case of the binomial distribution. Thus, the error on the hit count can be defined from either:

$$\sigma_{\text{poiss}}(r) = \sqrt{r}, \quad \sigma_{\text{binom}}(r) = \sqrt{\frac{f_r(1-f_r)}{N_{bc}}}. \tag{2.5}$$

These expressions can be propagated using the non-linear relation in Eq. (2.4) to define the statistical error on the mean number of hits:

$$\sigma_{\text{poiss}}(\mu) = \frac{\sqrt{r}}{1-f_r}, \quad \sigma_{\text{binom}}(\mu) = \sqrt{\frac{f_r}{N_{bc}(1-f_r)}}. \tag{2.6}$$

The comparison of the two formulas as a function of the occupancy, in terms of relative error is shown

in Fig. 2.1. The presented occupancy range is representative of Run 3 conditions, corresponding up to SBIL ≃ 8.6. The estimated per-channel statistical error in the figure is rather significant, but not representative of the final luminosity measurement. The reduction of this error with channel averaging and time integration is presented further in Sec. 2.8.7.

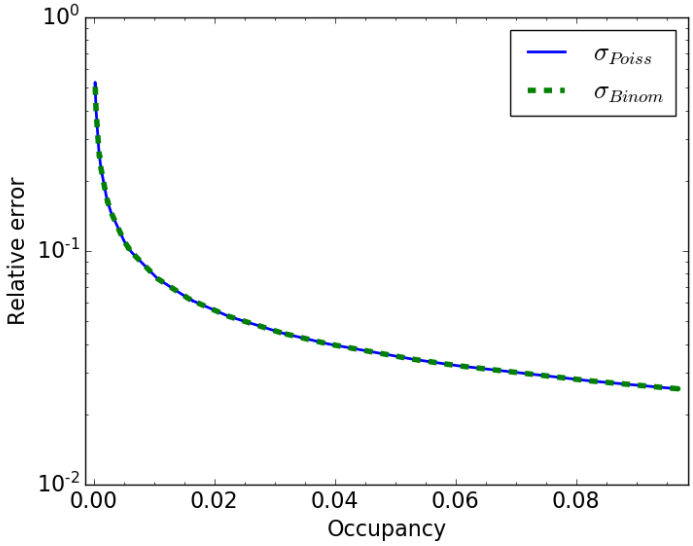

Figure 2.1: Relative error on the occupancy as calculated using the two possible estimators in Eq. (2.6). The smallest possible time-granularity is used, equal to ≃ 1.46 s.

Poisson fit

It is also possible to fit the Poisson distribution to the hit spectrum. This method is expected to be robust for high-efficiency counters, thus reducing the impact of the saturation effects. However, the knowledge of the detector response to a single pp interaction is needed.

2.2 Detector related systematic effects

The measured mean number of hits μ can be biased with detector-specific effects. Two types of corrections are typically applied, according to the formula:

$$\mu_{\text{corr}} = p_0\mu + p_1\mu^2, \tag{2.7}$$

where p_0 is the offset parameter and p_1 is the extra non-linearity slope. In the case of an ideal luminometer, p_0 is equal to 1, and the non-linearity slope p_1 disappears to 0.

2.2.1 Linearity

Numerous factors can contribute to inefficiencies in experimental systems, potentially affecting the accuracy of the measurement. These include zero-starvation and saturation effects at high pile-up,

accidental events, and activation-induced and electronic system inefficiencies. Thus, the non-linearity can cause an over- or under-estimation of the instantaneous luminosity, which is correspondingly described by a positive or negative slope with μ. This response non-linearity propagates further to the integrated luminosity, affecting the absolute measured value. It is interesting to compare the linearity between detectors in absolute terms of slopes with respect to pile-up or single-bunch luminosity. The non-linearities need to be monitored during operation as these are expected to evolve with accumulated fluence and resulting in overall system degradation. Typically, the non-linearity measurement is based on cross-detector comparisons which require assumption on one of the systems being very linear. However, this method becomes completely insensitive in case the compared systems are co-linear. This generates the need for a reference-detector-independent non-linearity measurement.

Non-linearity measurement and cross-checks are further discussed on the BCM1F-μTCA example in Sec. 7.3. Furthermore, the preliminary example of the independent non-linearity measurement is presented.

2.2.2 Stability

The stability includes multiple factors that change the detector response temporarily as well as the long-term components as a function of the radiation damage from the integrated absorbed dose and high heavy particle fluence. It is studied during the data-taking and the corrections are applied with reference to the absolute luminosity scale calibration in the vdM scans. The response differences need to be recognized, for example filling pattern dependence, which can be minimized in a well-designed luminometer. The timing of the detector has to be well synchronized with the collision signal to avoid the spillover outside of the 25 ns boundary to the subsequent BCID. The temporary changes in efficiency are inevitable, and while these can average out when a small subset of a luminometer is affected, there is a possibility of a significant global efficiency change. This requires particular attention in case the integrated luminosity sample includes single periods with major contributions to the total integrated luminosity, denoting long high-luminosity fills, which in Run 3 reached the maximum of delivered luminosity above 1fb^{-1} per fill. Studying the systematic effects is of paramount importance, the appropriate models are needed to correct for the long-term changes due to accumulated irradiation in both the active detector material and the signal read-out chain.

The stability monitoring was studied in detail for BCM1F-μTCA and it is presented in Sec. 2.8.5. The correction strategy and systematic uncertainty estimation for the 2022 data is presented in Sec. 7.2.

2.3 LHC Instrumentation

In this section, a small fraction of the LHC instrumentation is shortly described, which is relevant for luminosity determination. The bunch current and beam position measurements are crucial in the vdM luminosity calibration method, as discussed later in Part 6. The LHC luminometers are also introduced, however these can provide only a relative luminosity measurement.

2.3.1 Bunch current

The relative per-bunch current differences are obtained from the Fast Beam Current Transformers (FBCT) measurement [37]. Separate devices are used to measure turn-by-turn bunch intensities within

each beam. This measurement is also used to measure the bunch position within the orbit to verify the filling pattern and differentiate colliding bunches at different locations. There was a significant upgrade in 2017 from the original FBCT to the Wall Current Transformer (WCT) allowing to remove signal leakage to the next bunch from 5 to 0%. The acquisition system was also updated during Run 2 to tackle issues with even/odd bunch slot and filling scheme dependence, as well as the systematically over-estimated first bunch in a train. The FBCT bunch-by-bunch measurement precision is within 0.3%.

These are scaled to the total beam current measurement from much more accurate DC current transformers (DCCT) (also known as Beam Current Transformer - DC, BCTDC). The calibration is applied before each fill, which checks the response to the reference current and applies the offset correction. Over the years of operation the system proved to be very stable, $\leq 0.1\%$ variations were observed in Run 2. The measurement accuracy per beam was 0.2% (in terms of full confidence interval) [38], and it was further improved with the upgrade to 24 bits ADC.

In the case of both types of current transformers two fully independent systems (A and B) are used per beam. The first one is used for the primary measurement while the other is meant for testing and development purposes.

DCCT measurement is corrected for the measured 'ghost' and 'satellite' charge, which is measured by Beam Synchrotron Radiation - Longitudinal (BSRL, also known as LDM). It uses the time-correlated single photon counting method to measure the charge in each bucket. The 'ghosts' refer to a residual charge trapped in supposedly empty BCIDs that is below FBCT sensitivity, thus being invisible. The 'satellites' are charges captured in the RF buckets around the colliding bunch bucket (2.5 ns), within the same 25 ns BCID.

2.3.2 Beam position

The DOROS Beam Position Monitors (BPM), located in the quadrupole triplets are the closest BPMs to any IP, allowing for measuring the beam displacements in both transverse directions at the experiments. These are part of the Diode ORbit and OScillation (DOROS) system, designed to achieve a sub-micrometer orbit resolution [39]. They are commonly used in the vdM analysis with respect to measuring the linear and residual orbit drifts.

The DOROS BPMs are simple pickups providing the turn-by-turn measurement. Both beams are measured separately and the average of measurements on each side of the IP (left and right) is used to improve the accuracy. These measurements are also used to reconstruct the crossing-angle.

These BPMs are a subset of about a thousand BPMs present around the LHC, measuring the beam orbit which is crucial for the operation of the accelerator. Additionally, BPMs located in the LHC arcs adjacent to the IP are used to cross-check results from DOROS. These measurements have to be propagated to the IP through the intermediate lattice, resulting in worse precision.

For the HL-LHC era, a new system is being developed to replace the DOROS BPMs, to tune and monitor the crabbing process in the new crab cavities. It will allow the measurement of the per-bunch orbits for the first time, with unprecedented precision of sub-μm [40]. This upgrade will provide the possibility of applying the per-bunch orbit drift corrections in the vdM calibration, improving the per-bunch spread. It will also lead to the reduction of the orbit drift-related systematic uncertainties, which are currently based on the full beam orbit measurement. The multiple BPMs of two different types around the IP

will constitute a valuable tool in validating the corrections and assigned errors.

2.3.3 LHC luminometers

Since the beginning of the LHC operation, dedicated LHC luminometers have been in operation. Beam RAte of Neutrals (BRAN) detectors were designed to optimize the LHC luminosity at the high-luminosity interaction regions (IR) IR1 (ATLAS) and IR5 (CMS). These devices are fast ionization chambers, which are capable of bunch-by-bunch measurement, installed inside a neutral particle absorber, at 140 m from each of the IPs [41]. Apart from the luminosity measurement these devices aimed to reconstruct the crossing-angle applied at the IP. The BRANs proved to serve well for machine optimization purposes, but their performance suffered due to the high activation environment.

For Run 3 new monitors were installed around IR1 and IR5 which were also designed as prototypes for the HL-LHC era. The luminosity measurement is based on the Cherenkov radiation detected with PMTs, produced in fused silica rods by the showers coming from the neutral particle absorber. Good agreement with ATLAS and CMS online luminosity was found during the first year of operation in Run 3, within 5% [42].

2.4 ATLAS

This summary of the ATLAS [34] luminosity measurement strategy is based on the latest Run 2 luminosity measurement publication [34].

The LUCID2 Cherenkov light detector is the primary bunch-by-bunch ATLAS luminometer. It is placed at ±17 m from the IP, with 16 photomultiplier tubes (PMT) distributed around the beampipe at each side. Each PMT quartz window is coated with a Bismuth calibration source (Bi-207), that allows for gain monitoring. Several methods are used to combine the PMTs signal which is then used in the zero-counting algorithm to infer the average number of hits. The 'EventOR' method counts hit at any of the tubes but suffers zero starvation already at pileup 20-30. The 'hitOR' method uses the average count from all tubes providing the best measurement.

The secondary bunch-by-bunch measurement is provided by the Beam Conditions Monitor (BCM). It consists of 4 diamond sensors at each side of the IP, located in the inner ATLAS volume, at ±1.8 m. While it shows a very good performance in the vdM conditions, it does not work well in nominal physics conditions, suffering from the bunch position in the train-dependent effects.

The luminosity measurement is supplemented with the observables from the main ATLAS subsystems. The track counting from an offline measurement of the multiplicity of reconstructed charged particles (in random bunch-crossings) is used. The number of tracks is proportional to the pileup and is expected to be very linear. Several track-selection criteria are used to provide different sensitivity to pileup values. This measurement can resolve individual bunches but it is statistically limited. Moreover, the calorimeter currents are used for bunch-integrated measurement. These measurements are especially useful for the 'calibration transfer' performed once a year. It is essentially a linearity correction for LUCID, which is in order of 10% at $\mu = 40$, or in units per SBIL approximately 1.75% [Hz/μb].

2.5 ALICE

All ALICE [7] luminosity measurements are based on the event counting. Special trigger conditions are used depending on the colliding type. Two systems inside the ALICE detector volume are used, located outside of the Silicon Pixel Detector (SPD). This includes T0 composed of two circular arrays of Cherenkov radiators with 12 PMTs per side at 3.7 m and -0.7 m from the IP. The second system V0 composed of two scintillator arrays on opposite sides of the IP is installed next to T0. For the luminosity measurement at proton-proton (pp) and proton-ion (p-Pb) collisions, the T0 and V0 two sides coincidences are used. The V0 with multiplicity trigger can be also used in ion-ion (Pb-Pb) collisions. Additionally, the Neutron Zero Degree Calorimeters (ZDC) located at ±114 m are used for measurement at Pb-Pb collisions.

2.6 LHCb

LHCb [27] luminosity can be measured both directly with luminometers and indirectly from the event rate of theoretically well-known processes. Multiple direct measurements are used from the VErtex LOcator (VELO) of tracks, vertices, upstream hits, and backward tracks, as well as hits from Scintillating Pad Detector (SPD) pre-shower, transverse energy from calorimeters and muon counting. Zero-counting is used to measure the average event count. A new dedicated luminometer PLUME (Probe for LUminosity MEasurement) was developed for Run 3, based on Cherenkov light measurement. The LHCb is the only experiment to use another approach for the absolute luminosity scale calibration, next to the vdM scans method. The Beam-Gas Imaging (BGI) technique [26] is also used to reconstruct the beam profiles, based on the interaction vertices between the beams and residual or injected gas molecules. The combination of the two techniques proved to be very powerful in reducing the final systematic uncertainty on the luminosity measurement, reaching 1.16% in 2014 [27] on a subset of Run 1 data.

LHCb BGI technique is crucial for ghost and satellite charge measurement [43], which is used also by other experiments allowing to reduce the systematic uncertainty on the BSRL measurement.

Indirect measurements are used for the data-taking periods that do not have the fully calibrated luminosity. Luminosity can be inferred from the event rate of a theoretically well-known process, for example, W & Z bosons production or dimuon production via two-photon fusion. Precision is determined by the uncertainty on the cross section prediction and experimental uncertainties (efficiencies etc.). An example of such a measurement can be found in [44], with the high systematic uncertainty on luminosity of 6%. Furthermore, it has a significant impact on the final cross section $\sigma(X \to \mu^+\mu^-)$ uncertainty as the luminosity determination is highly correlated with the efficiency uncertainties.

2.7 CMS

At the CMS experiment [5], dedicated Beam Radiation Instrumentation and Luminosity (BRIL) project has the mandate of the beam-related measurements and simulations. The beam-induced radiation instrumentation plays a vital role in monitoring the radiation environment. It does so both in real-time and by measuring integrated fluence, with the primary objective of optimizing the protection and extending the lifetimes of the CMS detector systems. This is essential for maintaining the integrity and longevity of the experimental setup. The overview sketch of the dedicated luminosity, radiation,

beam background, halo, losses and timing instrumentation as well as incorporated CMS subsystems for the luminosity measurement is shown in Fig. 2.2. The Beam Pick-up Timing eXperiment (BPTX) detectors are used for the beam timing measurement, this signal is used by the CMS trigger system. Beam losses are measured at two different locations with pCVD diamond and sapphire-based Beam Conditions Monitors for Losses (BCML1 and BCML2) with beam abort functionality [45]. Beam-induced background (BIB) is measured by the Fast Beam Condition Monitor (BCM1F, presented in Sec. 2.8) in the inner part of CMS and by Beam Halo Monitor (BHM) [46] outside of the CMS endcaps. Radiation levels are additionally monitored with LHC Beam Loss Monitors and Radmons, as well as RAMSES Ionization chambers [47].

Four completely independent systems described in the following subsection are calibrated with the vdM method and are used for bunch-by-bunch luminosity measurement at any LHC conditions. Particular emphasis is directed towards the recently upgraded BCM1F system (as detailed separately in Sec. 2.8). The orbit-integrated luminosity measurement is additionally used to verify the stability and linearity. To sum up, CMS has in total 9 direct luminosity measurements in Run 3.

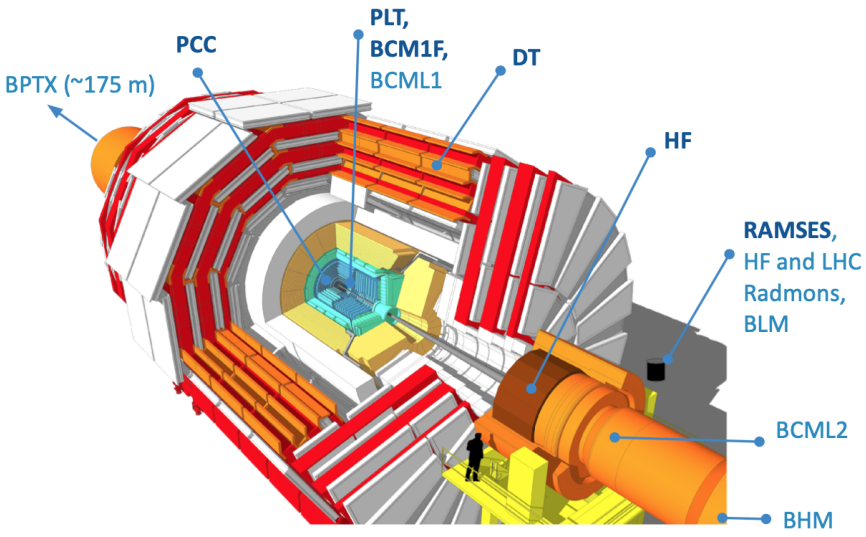

Figure 2.2: The sketch of CMS detector with BRIL-incorporated systems highlighted. The subsystems used for luminosity measurement are indicated with dark blue font.

Hadron Forward Calorimeter

The measurement of luminosity in the HF (Hadron Forward) region employs two specific HF rings. This selective approach is designed to ensure a relatively uniform distribution of data occupancy. It uses a dedicated readout system integrated into the HF calorimeter, as documented in [48]. Two distinct algorithms are used. The original method, known as HFOC (HF Occupancy Counting), relies on the concept of 'zero counting.' It monitors the proportion of bunch crossings in which no energy deposition surpasses a predetermined threshold within specified HF towers. This approach estimates the mean tower occupancy based on the fraction of bunch crossings with the energy depositions exceeding the threshold. A complementary method, known as HFET (HF Energy Transverse), was introduced in 2016. It is founded on the assumption that the measured sum of transverse energy is directly proportional to the luminosity. As of 2022, the primary algorithm of choice for luminosity measurement is HFET,

reflecting its enhanced reliability and performance.

Pixel Cluster Counting

Precise measurement of luminosity can be achieved by utilizing the CMS pixel system located at the heart of the CMS tracker volume. The pixel cluster counting (PCC) technique involves counting the average number of clusters generated within the pixel detector modules for zero-bias events. This method exhibits a high level of statistical precision, even in scenarios with a low pileup, owing to the substantial number of pixels integrated into the system. It served as the primary luminosity measurement tool during Run 1 and Run 2 [49]. For Run 3 several changes were made: replacement of the first BPIX layer, replacement of all DC-DC power converters, repair faulty power connectors and optical fibers, and upgrade FPIX electronics boards [5].

Pixel Luminosity Telescope

The Pixel Luminosity Telescope (PLT) is a specialized luminometer that employs silicon pixel sensors for its operation [50]. Its inaugural installation took place in January 2015 as a pivotal component of the Run 2 upgrades within the scope of the BRIL project. The PLT performed admirably throughout the entirety of Run 2 of the Large Hadron Collider (LHC), spanning from 2015 to 2018.

During the Long Shutdown 2 (LS2) period from 2019 to 2022, a new PLT unit was meticulously constructed and subsequently integrated into the LHC in July 2021, marking the commencement of LHC Run 3, slated for 2022 to 2025. The PLT configuration comprises a total of 48 silicon sensors arranged into discrete 'telescopes'. Each telescope encompasses three sensors spaced along the z-axis, aligned parallel to the beam line. This layout ensures that particles originating from the CMS interaction point (IP) traverse all three planes within the telescope. Importantly, the triple coincidence requirement effectively suppresses background noise and mitigates the influence of activated material within the detector.

Of the 16 PLT telescopes, eight are positioned on either side of the pixel endcaps, situated approximately 1.75 meters away from the IP. These telescopes form a circular arrangement around the beam pipe, operating at a pseudorapidity of approximately 4.2.

In the fast-or mode, if any pixels within a sensor register a hit above the prescribed threshold during a brief 25-nanosecond time interval, a solitary pulse is generated. While this signal inherently lacks intricate hit information, it can be efficiently extracted at the full bunch crossing frequency of 40 MHz. The subsequent readout hardware tallies the occurrences of 'triple coincidences', signifying events in which all three planes within a telescope concurrently record a signal. This tally serves as the basis for determining instantaneous luminosity.

Orbit-integrated luminosity

There are two additional systems used by CMS to validate the luminosity measurement: DT & RAMSES. The former, the Drift Tube (DT) system uses the observation of muon track stubs within the muon barrel track finder. The latter, RAMSES is a part of the central CERN radiation monitoring system, and for the relative luminosity measurement, the ionization chambers are used that are located the closest to the CMS volume (around the HF area) [51]. These are used in the mode of orbit-integrated data,

hence these cannot be independently calibrated in a precise way. Nevertheless, these systems are crucial in evaluating the stability and linearity of other luminometers.

Detector strategy for HL-LHC

The new system replacing the current Fast Beam Condition Monitor is being designed - FBCM, as the only CMS standalone luminometer. The current BCM1F is a prototype, using the same sensor technology. The low occupancy is planned to be maintained by moving the detector to a higher radial position around $r = 15$ cm, as shown in Fig. 2.3. This will result in a comparable linearity to BCM1F-μTCA at a much higher pileup (simulations were done up to PU = 200). An increased number of sensors is planned to minimize the statistical uncertainty (336 instead of 48). Upgraded CMS subsystems are

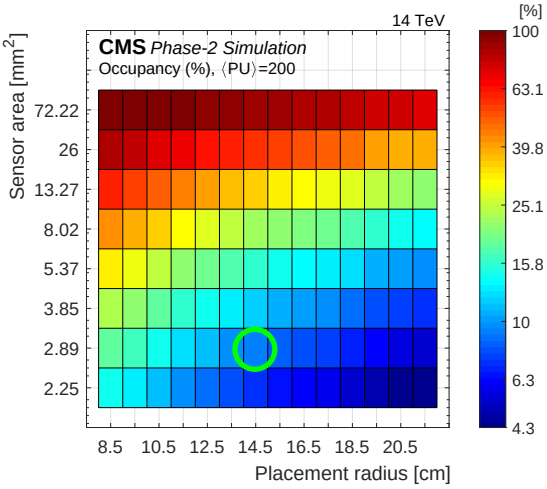

Figure 2.3: FBCM occupancy Phase 2 simulation at high pile-up - the choice of the radial location and sensor area is indicated with the green circle [16].

planned to be incorporated to improve the luminosity measurement. Apart from well-established HF algorithms, DT trigger primitives and outer tracker stubs are planned to be used for bunch-by-bunch measurement. The forward extension of the pixel detector data will be used to sample the random bunch-crossings. The detailed description of the CMS upgrades regarding the luminosity measurement in the HL-LHC era is described in BRIL TDR [16].

2.8 Fast beam conditions monitor (BCM1F)

The Beam Conditions Monitor (BCM1F) exists from the beginning of the LHC operation [52]. The original design employed sCVD (single-crystal Chemical Vapor Deposition) diamond sensors and it was meant for background measurement but the sensors turned out to have poor longevity. During Run 1 the performance was studied and the possibility of using it for luminosity measurement [53]. The major upgrade was performed for Run 2 [54] with dedicated PCB, sensors, and dedicated fast ASIC [55]. A lot of effort was put into the detector performance studies [56].

During Run 2, the BCM1F consisted of multiple sensor types. At the beginning, in 2016-17 still, single-crystal diamonds (sCVD) were used. These had to be exchanged for the last year of the Run and the

combination of different sensor types was used, including poly-crystalline diamond (pCVD), and Silicon sensors. Notably, Silicon sensors exhibited superior characteristics in terms of signal-to-noise separation and response linearity. The diamond sensors' performance suffered due to the charge trapping, contributing to the orbit integrated rate. Two types of non-linearities were observed, as a function of prompt radiation (pile-up) as well as the total integrated luminosity, due to the radiation-induced degradation [57, 45].

The Fast Beam Condition Monitor (BCM1F) underwent a comprehensive upgrade in preparation for the exacting conditions anticipated during LHC Run 3. This comprehensive refurbishment occurred during the Long Shutdown 2 (LS2) period. The key transformation involved the adoption of radiation-resistant sensors using acceptor-doped (p-type) silicon. To ensure optimal performance throughout Run 3, an innovative three-dimensional (3D) printed titanium active cooling loop was incorporated. One of its notable features is its sub-bunch crossing (BX) precision, which allows for the measurement of beam-induced background radiation. The complete detector comprises four C-shaped components (Fig. 2.4), amounting to a total of 48 channels.

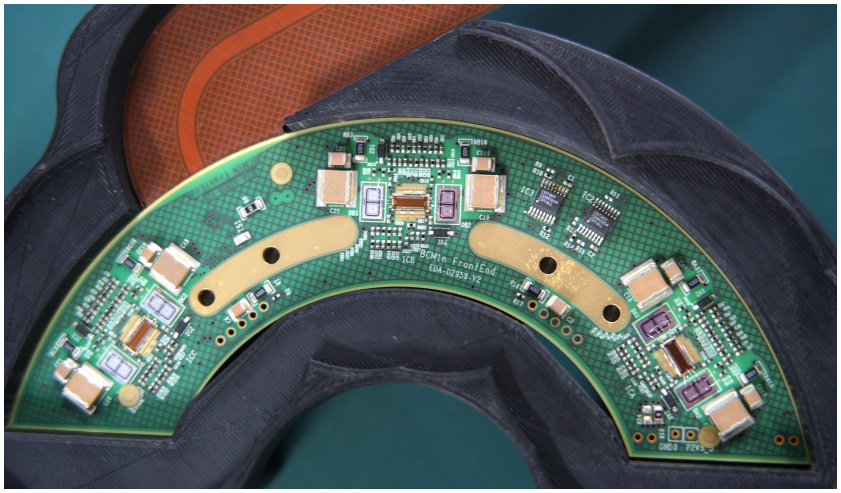

Figure 2.4: Picture of the Run 3 BCM1F C-shape.

These C-shaped pairs are positioned in a ring configuration around the beam pipe with sensors placed at different azimuthal positions, approximately 7 cm from the beam pipe. It is strategically installed at $z = \pm 1.8$ m from the IP on either end of the CMS detector. This distance is optimal for separating background and collision products, based on the signal arrival time. The single-beam induced background (BIB) arrives ~ 12.5 ns before the collision products signal, which is also half-distance between the consecutive bunches in a train. The analog signals detected by the sensors are shaped and then converted into an optical signal on the front-end within the analog optical hybrids (AOH). In the back-end, the signal is split into two readout systems, one VME and one μTCA-based. The overview system diagram, encompassing both the front-end and the back-end, is visually represented in Fig. 2.5. Detailed discussions regarding each component can be found in subsequent sections. The BCM1F operates independently as a dedicated luminometer, distinct from all central CMS services. This is further explained in the next section (see Sec 2.8.3).

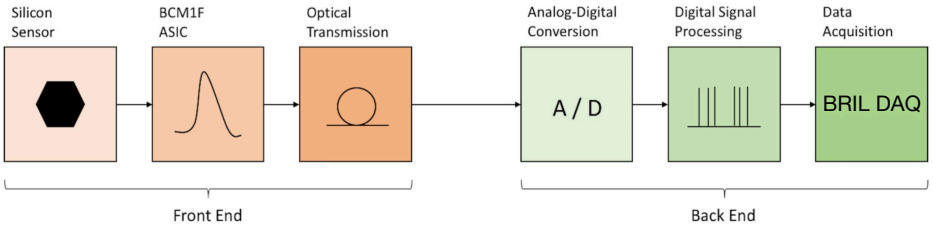

Figure 2.5: Diagram of the BCM1F detector architecture [58].

2.8.1 Front-end electronics

Each C-shape is a single flex-rigid printed circuit board, which includes all front-end components: double silicon diodes, ASIC chips, and optoelectronics readout.

The new sensors were produced as a part of the CMS Phase 2 Outer Tracker sensor production [59]. They were prepared as double silicon sensors (see Fig. 2.6), each with an active area of 1.7×1.7 mm^2, and active thickness of 290 μm. The diodes are operated under reverse bias with high voltage to generate a depletion zone free of charge carriers and reduce the leakage current (using the negative polarity). As the latter is dominated by thermally generated $e^- h^+$ pairs, it is minimized with the sensor cooling. Any ionizing particles passing the active sensor material generate $e^- h^+$ pairs in the depletion zone, which drift to the opposite electrodes with the velocity proportional to the applied electric field, creating the current. The sensors are A/C-coupled to protect the amplifier from the leakage current, which can increase after irradiation. The grounded guard ring is used for a well-defined active area, whose positive impact on the signal-to-noise ratio (SNR) was proven during the LS2 test beam [58]. The dedicated cooling is supplied to the pads located next to the sensors, aimed to minimize the

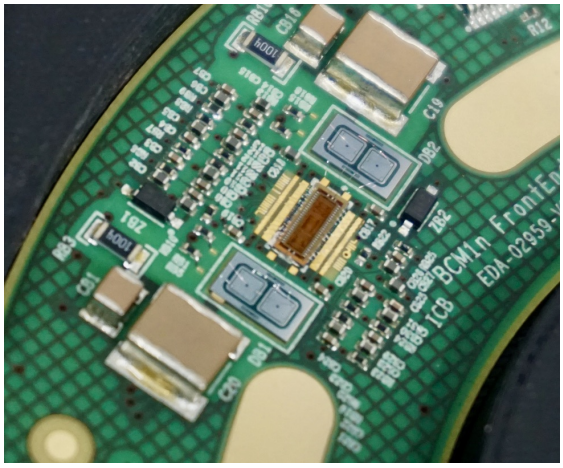

Figure 2.6: Picture of the BCM1F Run 3 sensors mounted on the C-shape (green). The connection of two double-pad sensors is visible to a common ASIC chip (in the middle).

radiation damage effects by operation and $-20°$. The high rates of neutrons and charged hadrons are expected in the BCM1F area as a consequence of irradiation generated from the high-energy colliding beams. These particles can interact with atoms of detector material causing permanent defects. These create new energy levels in the band gap between the valence and conduction bands. This leads to multiple effects: the change of the full depletion voltage by the modification of the effective doping

concentration, trapping of charge carriers, and the increase in the leakage current.

The detected signal is shaped with the fast asynchronous ASIC from the Run 2 design [55], implemented in radiation-hard IBM 130 nm process. It provides a short peaking time (FWHM<10 ns), narrow Gaussian-like pulses (see testing results in Fig. 2.8b), and thus sub-bunch timing resolution. The optical readout is fixed on a separate board connected with a short flex cable to the C-shape. It uses analog-opto-hybrids (AOH), which convert the current into infrared light at a wavelength of 1310 nm. It is placed at a larger distance from the IP, to reduce the radiation exposure, as the AOH laser diodes can suffer from the effects of radiation damage, which results in lower efficiency of signal propagation. The AOH bias current setting needs to be monitored with automated regular scans, and in case of damage, the new higher set-point is suggested that needs to be adjusted by the operator. These are set with the digital opto-hybrid (DOH). The signal is then propagated with long fibers from the CMS experimental cavern to the separate shielded underground cavern, where all the back-end systems are located.

The sensor selection process involved testing at DESY, with a preference for sensors exhibiting the highest quality. The qualification was based on I-V and C-V characteristics, sensor pad, and guard ring leakage current, guard ring breakthrough voltage, full depletion voltage around −260 V, capacitance after full depletion, and coupling capacitance [60]. The C-shape PCBs were fabricated simultaneously, and subsequently, the sensor bonding was performed at CERN. It was followed by detector-quadrant testing with internally generated test pulses as well as with a radiation source (Sr-90 with $\beta(e^-)$ decay at 0.546 MeV). The scheme of the laboratory setup is presented in Fig. 2.7. It included a low voltage supply for the active components (amplifiers, AOHes, and DOHes), and high voltage was supplied to the sensors. The test pulses (6 fC height) were generated internally in the ASIC chip by supplying the extra input signals. The amplitude and periodic strobe signals were implemented on the external Arduino circuit. An example of such a test pulse is shown in Fig. 2.7, which was read out at 0.5 GHz sampling frequency. The front-end stability was tested with the test pulse input charge, giving the

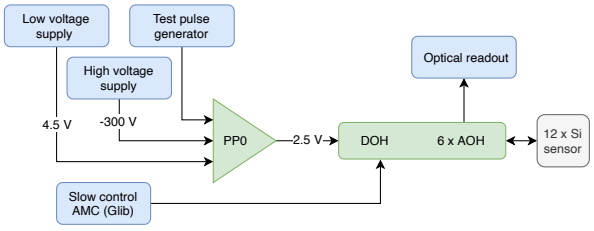

(a) Laboratory testing setup for the BCM1F C-shapes.

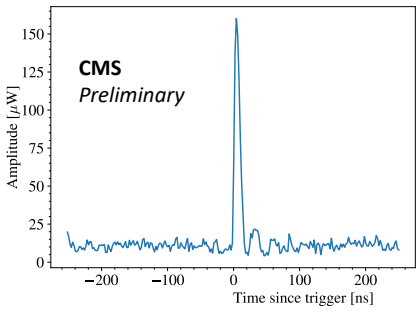

(b) Self-triggered response of BCM1F frontend to the externally generated test pulse.

Figure 2.7: The scheme of laboratory setup (left) and an example of raw test pulse (right).

calibration factors for the measured pulse heights in the order of $1.2 \times 10^4 e^-/100$ mV. The detector signals full width at half maximum (FWHM) timing distributions were in agreement with the design value: a mean around 10 ns for all channels was obtained (example channel in Fig. 2.8b). Additionally, the amplitude spectra of source hits indicated a favorable signal-to-noise ratio (SNR), as shown for example channel in Fig. 2.8a. As it shows the charge deposited in a thin layer, it can be qualitatively described with the Landau distribution, and the accurate model for the experimental spectra can be developed with detailed detector-specific effects [61]. This was not done for BCM1F as its performance

is not linked to the precise measurement of the deposited energy. Before these tests, during LS2, a dedicated test beam was used to verify the new design with A/C coupling on an early version of the sensors [58]. The new cooling system effectiveness was tested on the spare C-shape by supplying the coolant to the pads and measuring the temperature with incorporated Pt1000 temperature sensors.

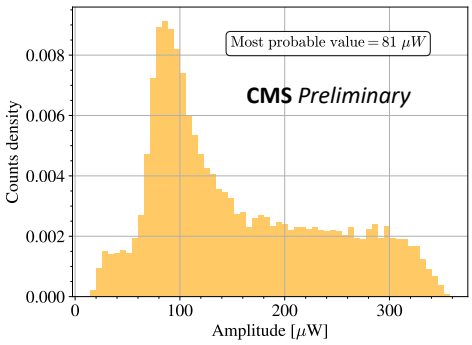

(a) Distribution of the detected signal amplitudes coming from Sr-90 beta source, with its most probable value. 25000 triggers were used.

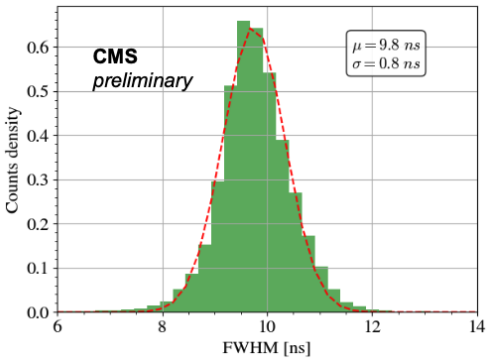

(b) Distribution of the full width of radiation source pulses at half amplitude maximum.

Figure 2.8: Laboratory tests results for the BCM1F front-end.

The assembly and qualification of the detector quadrants are followed by integration into a common carriage with the Pixel Luminosity Telescope (PLT) and Beam Conditions Monitor for Losses (BCML1). The installation took place in July 2021 and commissioning was done during the first 2021 LHC pilot beam test at the injection energy of 450 GeV. The snapshots of this process are shown in Fig. 2.9.

(a) Integration of the BCM1F quadrant into a carbon fiber carriage (black). In the bottom right corner the new titanium cooling circuit is visible.

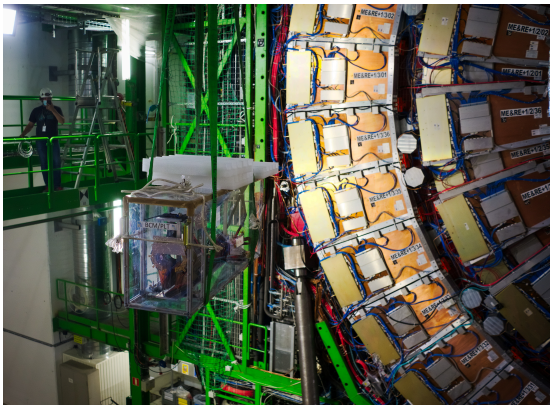

(b) Transport of the BCM1F detector for the installation inside the CMS volume.

Figure 2.9: BCM1F assembly, integration and installation processes.

2.8.2 Back-end electronics

The optical signal is converted into an 8-bit-equivalent electric signal at the ARx12 optical receiver situated in the CMS service cavern (USC). This location provides shielding from the prompt radiation exposure in the experimental cavern. Subsequently, the signal is duplicated and propagated into two distinct back-end systems: one based on VME and one on μTCA technology. The former is the baseline system, operating since 2012. The latter is the new system introduced as an upgrade for the long-lasting VME discriminator with the Realtime Histogramming Unit (VME RHU). Detailed descriptions of these two systems are provided in subsequent subsections. In the following BCM1F sections, the presented data is based on the new μTCA-based back-end.

VME discriminator + Realtime Histogramming Unit

Within the VME system, the incoming pulses are sampled and discriminated with a constant threshold discriminator. This unit employs a leading-edge discriminator module (CAEN V895 [62]) equipped with a fixed threshold. It generates a logical output from the identified hits, which is directed towards the Realtime Histogramming Unit (RHU) [63] (located in the upper right part of Fig. 2.5). The RHU creates an LHC orbit occupancy histogram with a fine granularity of 6.25 ns (equivalent to 4 bins per bunch crossing). It was designed to operate with no dead time. Given that the counts are based on 5-nanosecond discriminator pulses, the system faces a limitation in distinguishing piled-up pulses. In cases where the signal persists above the threshold beyond this duration, some pulses may not be counted, resulting in a degree of inefficiency. The VME system can also operate in a level-triggered mode where it continually counts signals that remain above the threshold, instead of relying on the leading-edge discrimination. However, this mode can pose challenges when single hits produce a longer signal response than a single RHU bin, potentially leading to the counting of a single hit multiple times. Thus, the number of real events can effectively be obscured. It's important to note that this mode was originally designed to facilitate time-over-threshold measurements.

μTCA: FMC digitizer + GLIB peak finding and histogramming

This system comprises an FPGA Mezzanine Card (FMC) 8-bit digitizer featuring a sampling frequency of 30×40.08 MHz = 1.2024 GHz, AC coupling of the analog-to-digital converter (ADC) inputs, and a phase-locked loop (PLL) mechanism for synchronization with the LHC bunch clock (left part of the scheme in Fig. 2.10) [64]. The core functions of peak detection and histogramming are executed within the Xilinx Virtex-6 FPGA, integrated into the Gigabit Link Interface Board (GLIB) (middle part of the scheme in Fig. 2.10), which is a double width Advanced Mezzanine Card (AMC). The communication between software and firmware is done through the IPbus protocol, via IP address assigned to each of the GLIBs. In the current system, 10 GLIBs are available in two separate μTCA crates per detector side, allowing for the read-out of 40 channels. To maintain the sample structure the data are streamed into a FIFO that transmits all 30 samples per bunch crossing. Two orbit signals are available: the central CMS Trigger Distribution and Control System (TCDS) [5] signal and the direct LHC orbit signal coming from the FMC. In the normal configuration, both clock and orbit are taken from the FMC, while the TCDS signal is used to define the corresponding nibble, run, and fill identifiers. This is done to avoid using the TCDS timing since it might not always be synchronized to the actual machine clock, which changes slightly depending on the beam energy (in the order of a few Hz). The timing interface to the TCDS and clock distribution is done by AMC13. Compared to the VME RHU, this system offers improved time resolution, capable of detecting hits with the sample resolution of 5/6 ns. Similar to the old system, the

orbit occupancy histogram is constructed based on the arrival times, but with also enhanced resolution of 6 bins per bunch-crossing. A derivative-based peak finder algorithm has been implemented allowing for resolving double hits [65]. This feature is particularly important for preserving the linearity of the system response at high pile-up conditions. Moreover, the derivative threshold enables the distinction between sudden electronic noise spikes and pulses generated by a traversing particle through the active material of the detector. The full configuration of the new system was finalized only after the beginning of LHC Run 3 data collection. More details are described in the following section 2.8.2. Since then, the system has demonstrated remarkable reliability throughout the year 2023.

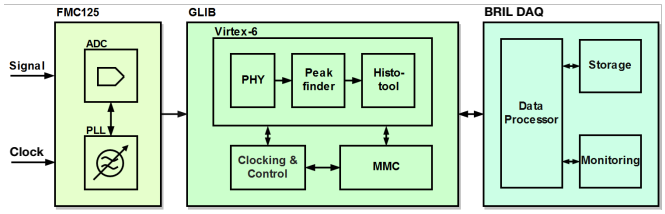

(a) Diagram of the BCM1F-μTCA Back-end [65].

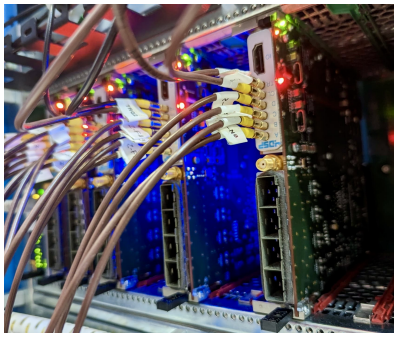

(b) Picture of one of the μTCA crates with GLIB cards and input signals [66].

Figure 2.10: BCM1F-μTCA back-end.

Derivative based peak finding algorithm

The BCM1F uTCA back-end electronics offer the potential for sophisticated data processing and improved general performance. The novel peak detection algorithm uses a derivative-based threshold, which is designed to differentiate the overlapping pulses to maintain detection efficiency even at high pileup conditions. It is not influenced by any constant (DC) component while mitigating low-frequency signals, such as baseline shifts. Nonetheless, a straightforward derivative threshold does have the drawback of potentially including high-frequency noise with pronounced gradients as genuine signals. These components are further suppressed by applying low pass filtering techniques. The choice of the window size was adjusted to the signal bandwidth and the desired amount of noise reduction, providing linear differentiation. The implementation and simulation performance studies for this method are shown in [65]. This methodology is implemented by calculating the derivative using the smooth noise-robust differentiator, utilizing a window size of $N = 7$ samples:

$$\mathrm{SNRD} = \frac{5(x_1 - x_{-1}) + 4(x_2 - x_{-2}) + x_3 - x_{-3}}{32h}, \tag{2.8}$$

where x_i represents the sample with index i around the sample where the SNRD is calculated, and h is the distance between samples. The peak detection is based on the derivative threshold level crossing (example shown in Fig. 2.11). The sharp leading edge of the pulse, shaped with the front-end ASIC results in the steep gradient that is possible to detect.

There are three algorithm parameters that need to be adjusted carefully to optimize the peak detection performance:

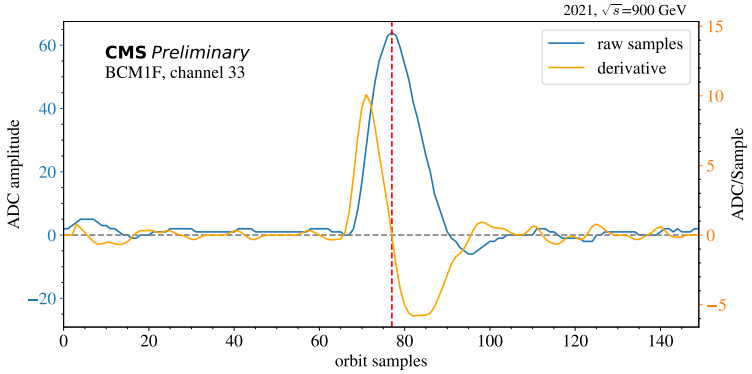

Figure 2.11: BCM1F uTCA sampled hit signal (blue), overlaid with the corresponding derivative (orange). The detected peak at derivative zero-crossing is marked with red line.

- derivative threshold (ddt) - is based on the gradient of fast raising edge of the signal pulse generated with particle hits. This threshold is expected to be more effective than the simple amplitude threshold, as the ASIC shapes the pulses with a constant raising edge. This implies that the threshold has to be adjusted to the channel signal amplitude. The rough estimation of this threshold, or rather its maximum, can be done using the test pulse amplitude. The final value cannot be based on the MIP-equivalent amplitude, as the lower momentum particles would be cut off. Nonetheless, it provides a good separation from the low amplitude Gaussian-like electronic noise. To separate the pulses, the signal derivative level-crossing is used. In the simplest case shown in Fig. 2.11 the 0-derivative crossing at the raw signal maximum could be used the separate the pulse. However, in the case of stacked pulses, it is also possible that there is a single signal maximum (0-crossing), thus a level-crossing can also be used to differentiate the pulses. The example is shown in Sec. 2.8.4.

- amplitude threshold (dat) - is set as a secondary threshold, checked only after the ddt is crossed. It is aimed at rejecting the fast and small pulses that are unlikely to originate from the particle hit. The amplitude is calculated from the integral over the samples between the derivative level-ascent to the level-descent zero-crossing. This method of obtaining the pulse amplitude makes it insensitive to the baseline shifts, as it does not require any baseline subtraction.

- peak isolation or time over the threshold (tot) - it is the last step that checks the samples around the peak to guarantee that it is a true peak. It defines the number of preceding and succeeding points that have to have a smaller derivative value than the peak.

Due to the differences in the sensors' signal paths, the optimization has to be done separately for each of them. These parameters need to be checked regularly after the irradiation, and adjusted as the detector signal degrades. The complete data flow within the peak finding algorithm discussed above is shown schematically in Fig. 2.12.

The electronic random noise is also separated based on the low value of the maximum derivative, which is intrinsic to the channel performance, as well as by applying the amplitude cut-off.

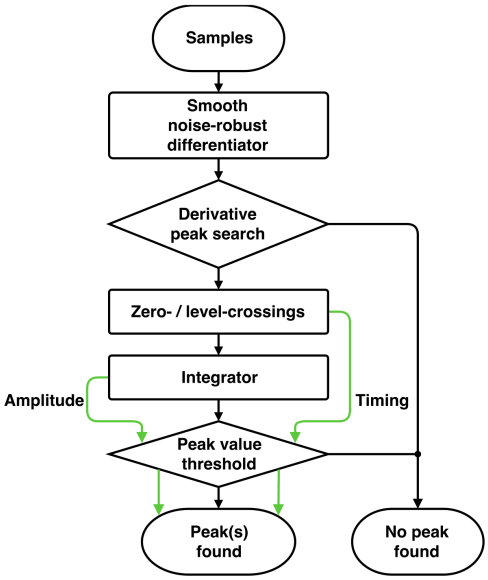

Figure 2.12: Peak finding algortihm flow chart [65].

2.8.3 Data acquisition and processing

The acquisition of data is managed by the dedicated BRIL DAQ software [66], which operates independently of the central CMS DAQ system. Its architecture is presented schematically in Fig. 2.13. This software is built upon the publisher-subscriber concept and does not involve event building. Its architecture encompasses three core components: sources, processors, and central processors, which collectively enable efficient data handling. The orbit signal and data identifiers including fill, run, and nibble numbers are distributed from the TCDS to each of the data source. The source and processor data are published on the central eventing bus, for further utilization by other processors or storage. The eventing bus also includes data exchange with the LHC via Data Interchange Protocol (DIP bridge). This provides the availability of the live LHC beam instrumentation data, as well as communication flags between LHC Operations and the Experiment. The central service encompasses data quality monitoring (Web monitor), storage service, and data publication to the LHC and the central CMS Online Monitoring System (OMS).

The BCM1F-μTCA source is used to configure the firmware and adjust the per-GLIB timing (discussed further in Sec. 2.8.4). Configuration involves three essential settings that require optimization for the peak-finding algorithm: derivative threshold, amplitude threshold, and counts over the threshold, as detailed in Sec. 2.8.2. The source publishes the histograms to the central eventing bus. Subsequently, the data are manipulated in an asynchronous way within the data processor application. It can subscribe to any relevant topics available on the eventing bus. The raw data histograms are passed to the queue, and various methods are invoked for data processing, shown in the scheme in Fig. 2.14. As it is an object-oriented software, the online data are handled efficiently, allowing for multiple independent parallel algorithms for each observable. Additionally, for BCM1F-μTCA the LHC-published beam topic is necessary. It is provided by the FBCT (described in Sec. 2.3) and includes the measured filling scheme with information about the filled bunches within each of the beams, as well as measured per bunch charge. The former is used to define the colliding (contributing to luminosity) and non-colliding bunches (contributing to the background). The latter is used for the background normalization.

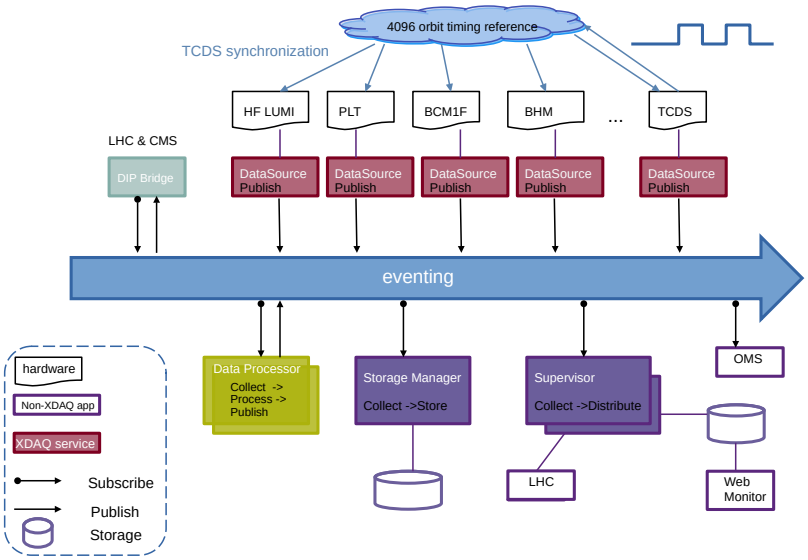

Figure 2.13: BRIL DAQ architecture scheme [66].

Furthermore, the vdM-related LHC topics are used, including the flag giving the information that the scan has started along with its properties.

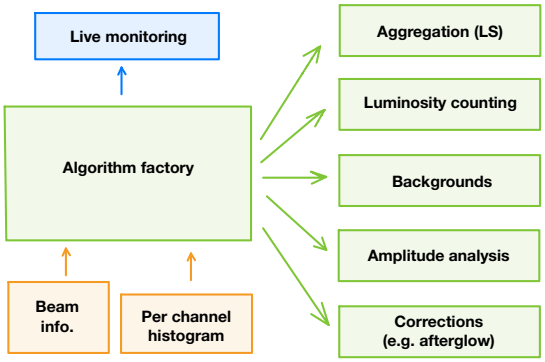

Figure 2.14: BCM1F-μTCA online processor functionality scheme, the object-oriented processing possibilities are shown in green.

The primary function of the processor is the source data aggregation, so that it is available in various time intervals, not only per four luminosity nibbles 'NB4' (4×4096 LHC orbits ≈ 1.46 s) but also per so-called luminosity section 'LS' (equivalent to $16 \times$NB4 ≈ 23.3 s). The luminosity and background measurements are discussed in detail separately in the following sections (Sec. 2.8.7 and 2.8.8). Additionally, the amplitude analysis was implemented, including the operations on the raw ADC pulse amplitude heights. Firstly, the aggregation of data per LS is performed for increased total count, as lower data integration can lead to poor spectra description. The main features of the spectrum are extracted: the total number of hits, the amplitude of the most probable value (MPV), minimum amplitude (after

applying thresholds), and maximum amplitude. An additional feature of extracting the test pulse height is also implemented, which is evoked only outside of the beam presence (based on the beam mode). Albedo (more commonly called afterglow) algorithm is implemented as a separate class, the need for this correction is discussed further in Sec. 2.8.5.

The application has also a very useful feature for detector debugging of providing the online monitoring of all the processor variables with live webcharts.

2.8.4 Detector optimization

BCM1F has been operating since the beginning of LHC commissioning for the Run 3, measuring collision products at a center-of-mass energy of 13.6 TeV. During this time, the detector configuration was optimized. This included the study of per-channel performance and its optimal configuration as well as the per-channel timing alignment.

Front-end parameters

The initial high voltage (HV) setpoint for the sensors was −350 V, and it was decreased to −400 V after the first ~ 10 fb^{-1} of delivered luminosity. This was based on the HV scan results, an example channel is shown in Fig. 2.15. The change in the depletion zone and charge collection caused by long-term irradiation was observed. This degradation was expected from the p-type sensor, which has the characteristic of ever-increasing depletion voltage with irradiation [67], in contrast to the n-type sensor where the depletion voltage first decreases and then the type inversion occurs. This is a result of irradiation-induced point defects, that can combine with impurities in the silicon lattice. As a result, there is an increase in impurities that behave like acceptors.

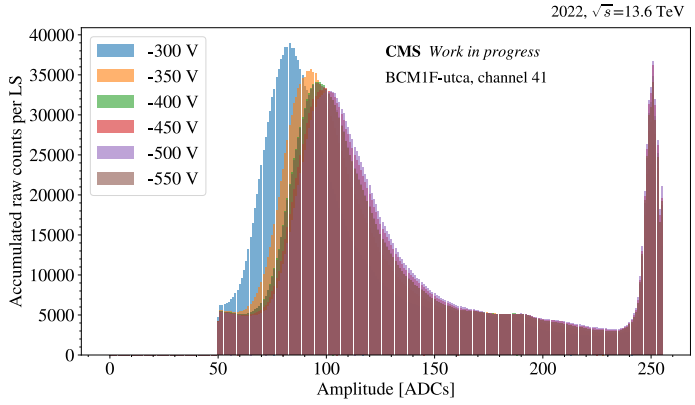

Figure 2.15: Amplitude spectra of a BCM1F sensor produced by the 6.8 TeV proton colliding beams, at different high voltages applied. The pedestal cut-off is visible with missing data (<50), and saturated signal at high amplitudes (~ 250).

Another front-end parameter that needs to be adjusted is the AOH bias. The AOHes come from original CMS Tracker production, thus tests were required to guarantee the linear response as a function of the bias setting. Regular scans are made during the operation to check the setting, as the optical signal of the AOH degrades with irradiation. The baseline position change is measured at each bias setting.

The example results for one of the BCM1F channels are shown in Fig. 2.16. The recommended bias current for the laser diode should be as low as possible to preserve the signal bandwidth, but above the baseline noise (indicated by the flat response for low-bias settings).

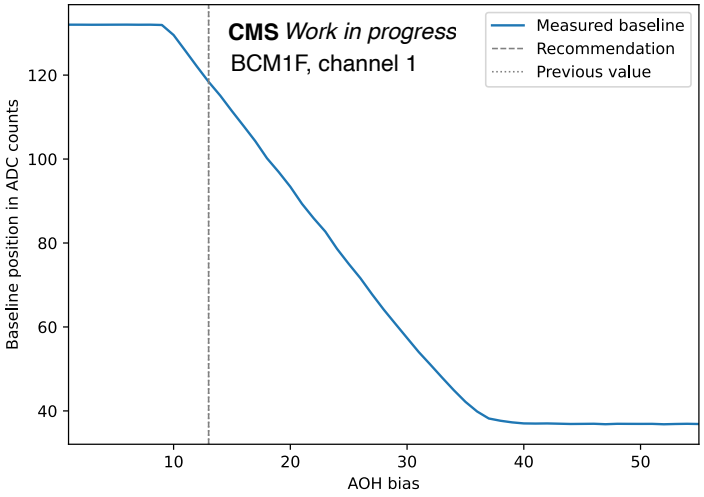

Figure 2.16: Example results of the AOH bias scan for one of the BCM1F channels [66]. The recommended lowest possible setting is indicated with the gray vertical line.

Back-end parameters

As described in Sec. 2.8.2, the peak finder algorithm requires per-channel optimization. In the commissioning period of the new firmware, the back-end was running in the two modes of using the simple amplitude threshold for half of the channels and the derivative threshold for the other channels. The test-bench implementation with ModelSim simulation of the peak finder algorithm was used to find the initial thresholds. The sweep over the derivative threshold (ddt) for various amplitude thresholds (dat) was made, and both test pulse and 2021 LHC test beam raw data were used in the simulation. The thresholds were fine-tuned with respect to the amplitude spectrum of each sensor, to ensure good noise and signal separation with the real beam signal. The performance of the two peak finding modes was compared with the first colliding beams in the LHC 2021 test beam. It was confirmed that at low pile up they yield very similar results. The derivative threshold is set to the lowest possible level and is expected to remain constant unless major degradation of the sensor or signal transmission occurs. This was confirmed throughout the 2022 and 2023 operations.

The example of setting the derivative threshold (green curve) is shown in Fig. 2.17, for a problematic channel. The raw pulse is distorted with the extreme baseline noise, which for the peak finder algorithm appears as two stacked-up pulses. Thanks to the shaper the real pulse has a faster raising edge than the baseline noise, thus the derivative threshold is effective. However, due to the baseline distortion, the threshold is crossed twice - red curves indicate two recognized pulses. Nevertheless, for most of the channels, the signal does not include this extreme noise component (as shown in Fig. 2.11), thus providing high efficiency in the signal and noise distinction. The multiple peak recognition is in use, even though the probability is very small (0.01% for double hits at the highest Run 3 pile-up).

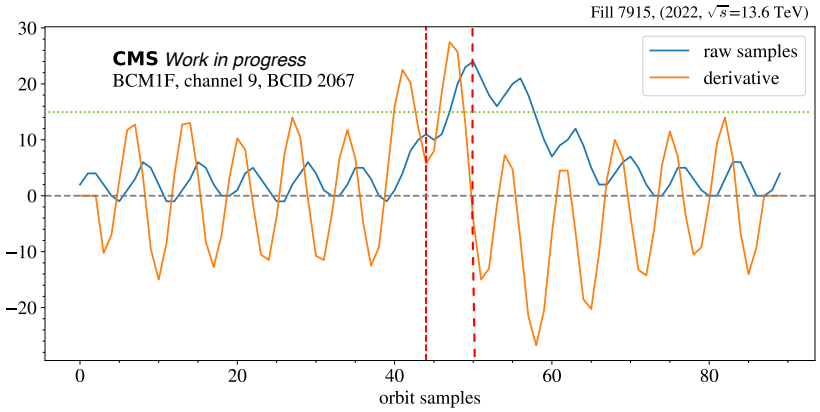

Figure 2.17: Double pulse detection example (indicated with vertical red dashed lines) in case of stacked pulses. The derivative threshold level is indicated with a horizontal green dashed line.

Timing alignment

The timing of the full system is of paramount importance for the detector's performance. The primary difference in timing comes from the separate readout of different lengths on the two sides of the CMS. Furthermore, per-channel NIM cables with various delays are used in the back-end between the optical receiver (OR) and the μTCA crate. This timing needs to be adjusted in the BCM1F-μTCA -source application. There are three types of orbit delay types available, implemented per GLIB:

- Coarse delay, equal to the bunch-crossing time - 25 ns steps [0:4095], delays all 30 samples. Implemented from the delay of the synchronized orbit signal.
- Fine delay - 3.33 ns steps [0:63], delays 4 samples. Implemented as the delay of the CDC align signal (300 MHz data clock).
- Ultra-fine delay equals to single sample delay - 0.83 ns steps [0:15]. Implemented in the ADC configuration register.

The rough timing adjustment is primarily done with the test pulse signal, which is sent at the end of the LHC orbit where no filled bunches are foreseen, to allow for the rise-time of the beam-dump kicker magnet (commonly called the abort gap). For the precise timing alignment, on the single μTCA -histogram bin level, the real beam signal is necessary. For Run 3, the first LHC circulating beams were used to perfect the timing on all channels. It was verified further with the first single-bunches collisions, showing that 90-95% of the signal is aligned in a single histogramming bin.

An example accumulated full orbit occupancy histogram with raw counts is shown in Fig. 2.18: results from a single channel are shown using data collected over around 20 min and normalized to the fixed time interval of a lumi-section (LS). At the very beginning of the orbit, occupancy corresponding to a bunch with a low occupancy signal is visible, which is caused by non-colliding bunches. It is followed by multiple bunch-trains including 36 bunches each, regularly separated by 7 or 31 Bunch IDs (BCIDs). There are 2 individual colliding bunches present giving much narrower occupancy spikes around BCIDs 56 and 2726. The total of 2450 colliding bunches are shown in this Figure. Since the data were accumulated over a long time, afterglow tails are visible after each set of regular bunch trains, with an

increased hit count observed due to the activated detector material. The correction for this effect is described in the following section 2.8.5.

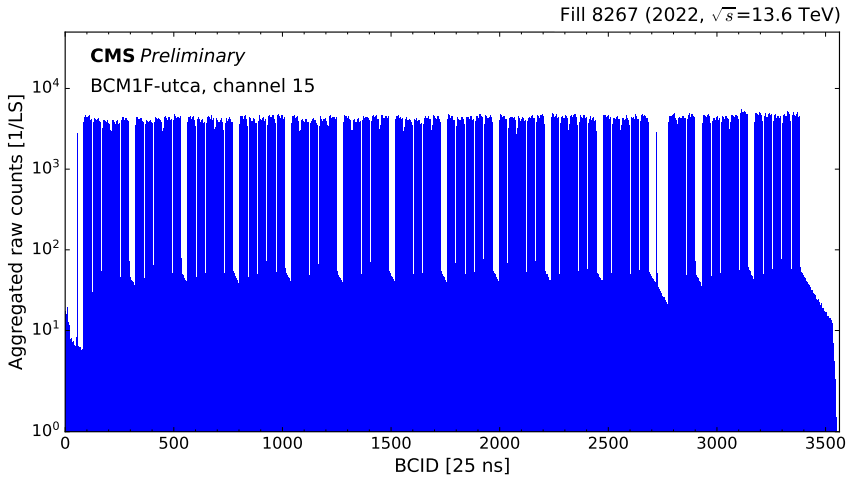

Figure 2.18: Example raw BCM1F-μTCA counts per-channel, per lumi-section (LS 23 s), over the full LHC orbit. Single-channel data, aggregated over 20 minutes and normalized per lumi-section (LS), is shown. In the very beginning of the orbit, low intensity signal is visible which is caused by the beam-induced background signal from non-colliding bunches, followed by a single colliding bunch and multiple bunch trains. Afterglow tails are visible after each set of bunch trains.

2.8.5 Detector performance

The above-described detector configuration allows for the online measurement with limited data quality. In this section, the offline analysis is discussed, which includes data subset selection from studying the detector performance, as well as the application of corrections.

Channel selection

Several channels showed different forms of problematic behavior resulting in a reduced data quality for the average luminosity. In raw data reprocessing all the underlying problems are recognized. It can be related to the intrinsic difference in each of the sensor, or optical and electrical lines, which were reused from the Run 1 system or impairment caused in the transportation and installation process. In consequence, some of the data might need dedicated corrections or simply rejected in case the inefficiency is problematic to model. In case of the 2022 dataset, 32 best channels out of all 48 channels have been included in the overall luminosity measurement both for RHU and μTCA . The subset of channels is slightly different for the two types of data. The inefficiencies in the early detector-running period typically arise from the front-end issues. These were not present in the testing and assembly period, and originate from the course of the detector transport to the CMS cavern and its installation. Due to schedule constraints imposed by the experiment and the LHC, there was no time to exchange the affected C-shape. Excessive noise or low signal reduces the signal-to-noise ratio. It can lead to additional non-linearity of the system. One of the main problems in the 2022 operation was the availability of the channels. After a few months of stable operation in the high radiation environment

(equivalent to 10 fb^{-1} of total delivered luminosity) the sensors started to develop excessive leakage current in the conditions with prompt radiation. This could be noticed from increasing sensor current, commonly crossing the trip threshold of 100 μA. The extra current had an impact on the output signal but was effectively suppressed with the derivative-based algorithm. To mitigate the problem of disappearing signal from a channel after a trip, the auto-masking algorithm was implemented in the online processor, as well as in the reprocessing scripts. It checks the luminosity measured by each sensor with respect to all channels' averages with a customizable threshold.

The signal baseline can be used to study the stability of the full electronic signal path. Its derivative is shown for two example channels (Fig. 2.19) - the first one (Fig. 2.19a) is recognized as a good channel due to the low and constant derivative. In the second example (Fig. 2.19b), the baseline gradient is much steeper and has a wide distribution over time, which indicates noise contribution. It is assumed, that some of the channels suffer from the induced capacitance from the surrounding detector parts, causing the baseline to include the 175 MHz component (visible in the raw data in Fig. 2.17). Unfortunately, due to the detector location with no access during the Run, there are no means to verify this hypothesis. This constant frequency component could be filtered out at the hardware level.

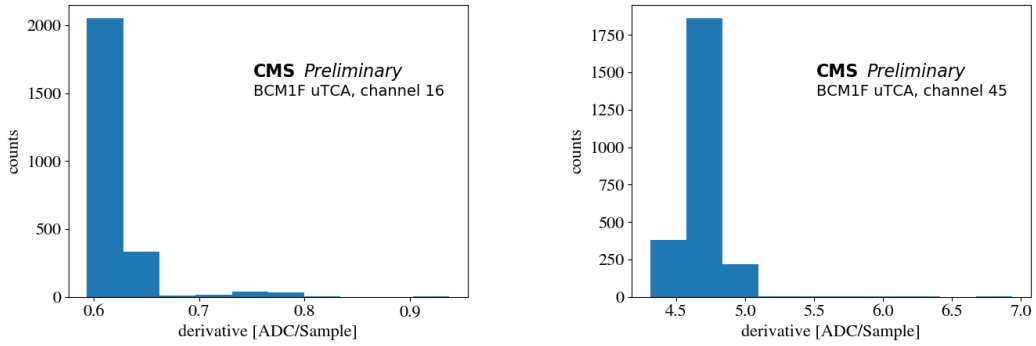

(a) good

(b) noisy

Figure 2.19: Distribution of maximum baseline derivative per orbit are shown for (2.19a) a good and (2.19b) a noisy BCM1F-μTCA channels. This derivative corresponds to the maximum slope gradient of the raw pulse rising edge shown in Fig. 2.11. The noisy channel has a high frequency noise contribution which results in the higher derivative values.

The example amplitude spectra for a good BCM1F channel at high energy collision conditions, built using the new peak finder is shown in Fig. 2.20. The low amplitude Gaussian noise contribution was cut out with operational thresholds. The spectrum is a skewed Landau distribution with the most probable value (MPV) corresponding to the energy loss of the minimum-ionizing particle. As the data were collected for 10 h, higher charge deposition peaks are also observed, which correspond to the deposit of multiple MIP charges.

Afterglow correction

The BCM1F is constructed using exceptionally lightweight components, strategically positioned just behind the PLT and Pixel Barrel. This design minimizes the activation of the detector materials and its

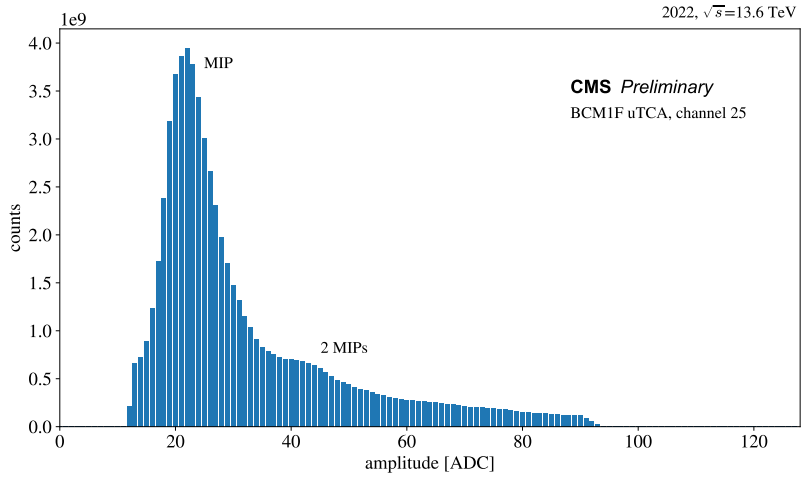

Figure 2.20: BCM1F-μTCA per-channel amplitude spectrum measured for high energy pp collisions. The distribution is cut at the amplitude threshold of 11. Data was collected for 10 h during fill 8118. The signal amplitude spectrum was built using the derivative-based peak finding algorithm. The main peak at 22 ADCs corresponds to the minimally ionizing particle (1 MIP) signal and that around 44 ADCs to 2 MIPs.

surrounding area. Nevertheless, as discussed in the previous section, the activation decay is observed in the accumulated data histograms appearing as an exponential tail that succeeds the bunch-train-induced signal. Each of the BCM1F sensors is exposed to radiation levels of a similar magnitude, as they are symmetrically situated around the beam pipe at the equidistant radius.

To correct for this signal contamination the correction model is derived based on the single bunch detector response. Two fills were used for this purpose (7921 and 8479) - one of the first and last fills of 2022. In both cases, there was a minimum number of colliding bunches present, however, in fill 8479 only one of them was separated enough to avoid including the preceding afterglow tail in the fitting model. To form the model, the entire fill data (order of a few hours) is summed and the histogram is normalized to the colliding bin signal. To mitigate the bias from the noise, it is subtracted from the data by calculating the noise level in an empty part of the orbit where the afterglow has declined significantly enough. Additional hits from the beam-induced background (BIB) of non-colliding bunches are filtered out. The data are separated into two components:

- short-term (< 100 ns) including the timing misalignment of the channels, resulting in a residual signal spillover, extracted from averaged data,
- decay tail (~ 10 μs) which is fitted with an exponential function.

The model describes the hit probability in the bunch crossings after a colliding bunch pair, and is shown in Fig. 2.21. The fractions were checked to be stable across a wide SBIL range $2-8$ [Hz/μb], measured within the data used for the correction model. The time component was extracted from the fit and is equal to $\tau = 1/b = 2.04$ μs. It was checked to be stable across a long time (~ 10 h in fill 7921). This constant is not straightforward to link to any of the predicted isotopes from the previous activation studies. The corresponding half-life is more common for the heavy isotopes which are unlikely to be produced in the BCM1F area, dedicated simulations are needed. Simulations performed in the

past indicate the contribution from scattered particles on heavier CMS components [68]. However, the measured constant is very close to the muon lifetime, which could potentially be indicated as the background source.

The fast component of the afterglow correction depends on the sensitivity of each of the sensors contributing to the final average signal. Thus, the correction model must be rebuilt for the subset of channels employed in the final measurement, to ensure optimal precision.

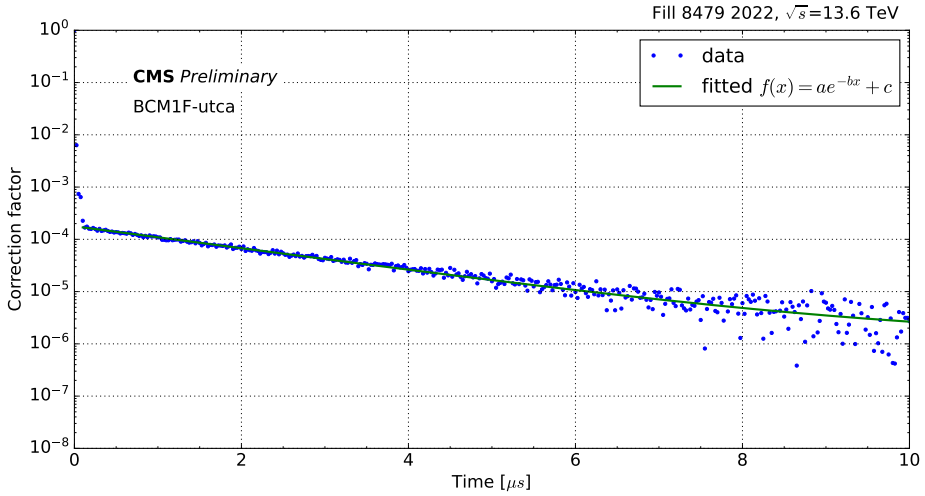

Figure 2.21: Run 3 afterglow correction model based on single colliding bunch data. BCM1F-utca raw data was aggregated over many orbits (~ 20 min) and normalized to the collision counts (thus, the correction factor for first BCID is set to 1). The fast component (< 100 ns) is extracted from averaged data, as it caused by the timing misalignment of all channels, which results in a residual signal spillover. The constant decay tail (~ 10 us) is fitted with an exponential function. This correction is applied to each per bunch data.

The correction algorithm iterates over all the colliding bunches, computing the contamination of the subsequent bunches based on the afterglow model and subsequently subtracting these hits. Thus, the total correction depends on the train length as well as the total number of bunches in the orbit (due to the tail component). This dependence is shown in Fig. 2.22 - the correction factor is shown for three consecutive trains of bunches, each including 36 bunches with 25 ns spacing. The corrected histogram typically retains a non-zero baseline, which is removed by computing the baseline within the abort gap.

The correction is currently applied only at the reprocessing step of the data processing. Its impact on the measured collision rate is illustrated in Fig. 2.23. The corrected rate data have no afterglow contribution, which can be assessed qualitatively from observing measured rates very close to zero for empty bunch slots between the colliding bunch trains. The systematic uncertainty of this correction for the 2022 data set is discussed in Sec. 7.1.

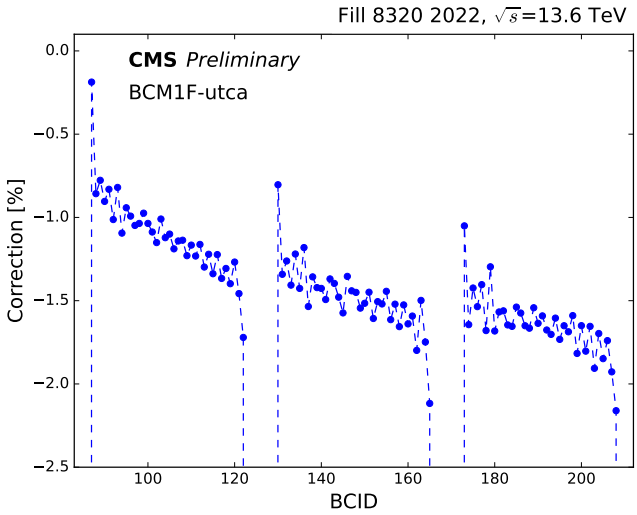

Figure 2.22: The BCM1F-μTCA afterglow correction as a function of the position in a train for an example nominal physics fill (8320). The total correction is calculated by comparing the measured single bunch rate after applying the afterglow correction factor to all colliding BCIDs with reference to the non-corrected rates.

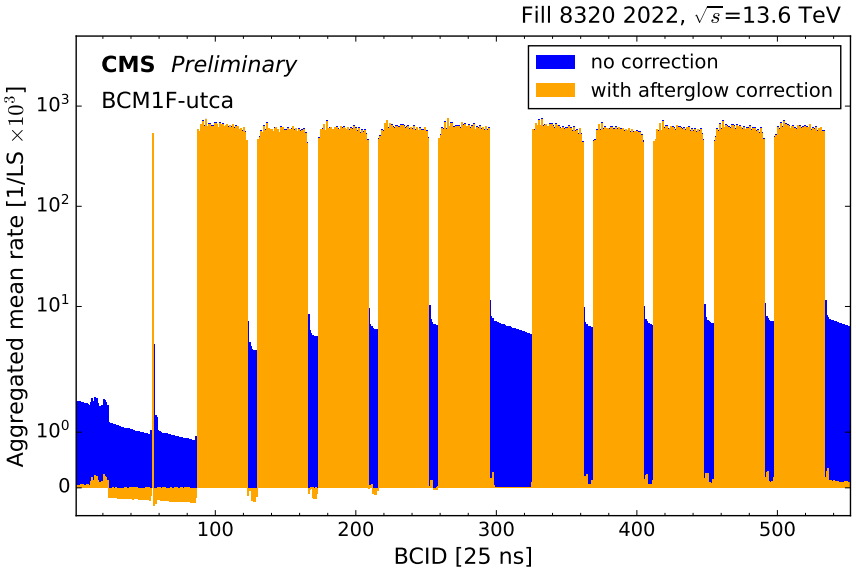

Figure 2.23: The raw rates measured by BCM1F-μTCA as a function of bunch crossings in the LHC orbit. Data are shown without (blue) and with the afterglow corrections (orange), both aggregated over 200 LS ($\approx$ 78 min), normalized per LS and scaled by 10^3 to enhance the visibility of the correction efficiency in the BCIDs outside of the colliding ones.

Signal efficiency changes

During operation time, and thus exposure to the prompt radiation, the traces of detector efficiency degradation can be observed. Multiple methods are available to track these long-term effects.

The amplitude analysis feature of the BCM1F-μTCA processor provides the crucial metrics. The test pulse signal is sent regularly to measure the combined effect of changes to the electronic and optical paths. The MPV of the beam amplitude spectra can be observed in time to track the overall changes, including the silicon sensors. The total number of hits can be used to compare per-sensor efficiencies and their evolution with time.

The overview of the MPV changes on four example BCM1F-μTCA channels during the 2023 proton-proton data-taking period is shown in Fig. 2.24. It is clear that the efficiency changes are not consistent across the channels. Three out of four presented channels were very stable at the beginning of the 2023 operation during the first 6 fb^{-1}, while the efficiency of the last one (ch39) was steadily decreasing. Later in the year, some stable periods and degradation slopes are observed, independently for each channel. These values can be used in the reprocessing to correct for the per-channel efficiency changes (available for all of the channels). The data are normalized with reference to the vdM calibration period (marked with the vertical gray dashed line) to indicate the efficiency differences before and after obtaining the absolute luminosity calibration.

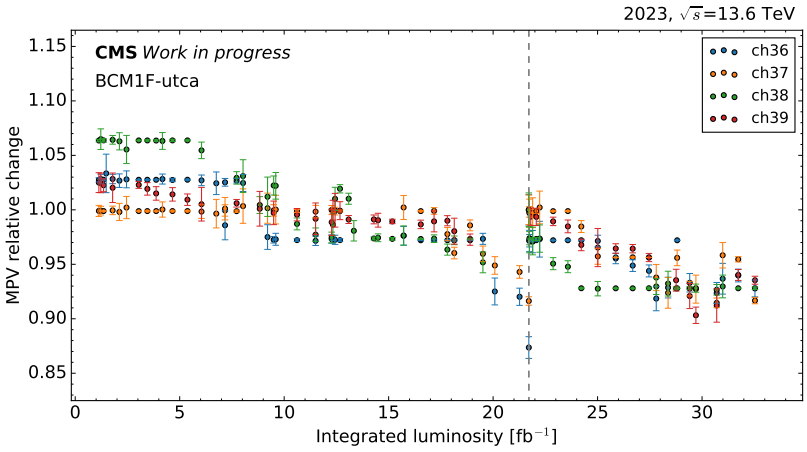

Figure 2.24: The relative change in the most probable value (MPV) of the amplitude spectra for four example BCM1F-μTCA channels during 2023 data-taking. The values are normalized to the MPV measured during the vdM period, indicated by the gray dashed line.

Additionally, the stability correction can be extracted by observing how the emittance scan results change over the operating period. This method was used in the reprocessing of 2022 data, as the amplitude analysis feature was not deployed at that time. This stability measurement is discussed in detail in Sec. 7.2.

Anomaly detection

Additionally, the possibility of validating the detector performance was studied using the artificial neural network model. It was built to detect BCM1F-μTCA data anomalies in a semi-automatic way, based on autoencoders.

The model was trained on the sample of the Run 3 fills including all the per channel BCM1F-μTCA rates, available at the time (2022). In total 50 fills were used, divided in half into training and testing data

sets. The training data were validated manually to guarantee high-quality training with no anomalies included. The data processing included normalization of the data (between 0-1), and the principal component analysis was performed [69]. The Mahalanobis distance was chosen as it takes into consideration the distribution of the data points, as an accurate metric to define the anomalies. Based on this distance the anomaly threshold is set, thus it is a semi-automatic way of finding anomalies.

The trained model was able to recognize and learn the typical features of the data such as optimization and emittance scans or luminosity leveling, which can cause problems when a simple rate comparison between the channels is made. After the single channel anomalies are detected, the improved reconstruction of the luminosity is made. This was a proof-of-concept study. However, the implementation within the data acquisition system requires more sophisticated model training and deployment, so that it can be used in online processing.

2.8.6 Linearity

The BCM1F-μTCA response linearity was already studied at the design phase. The front-end provides a very fast signal response with no dead-time. The size of the sensor was optimized for a low hit probability, to avoid zero-starvation. The low occupancy is crucial to preserve the linearity of the zero-counting algorithm. The improvements for preserving the linearity resulting from the new peak finder algorithm were also discussed in Sec. 2.8.2. The measured occupancy as a function of SBIL is shown in Fig. 2.25, the luminosity reduction was achieved by separating the beams. The linearity of the detector response is highlighted with the fitted linear function to measured occupancy. The maximum SBIL in the figure corresponds to a pile-up close to 60. Even at this point, the low hit probability is measured, below 0.1. Thus, the probability of double hits in a single bunch-crossing is below 0.01.

The linearity measurement cross-checks are shown in Sec. 7.3 for the 2022 dataset, confirming the excellent performance of BCM1F-μTCA .

2.8.7 Luminosity measurement

The single bunch instantaneous luminosity (SBIL) measurement is based on the sum of counts within a colliding BCID. The corresponding six orbit histogram bins that belong to that bunch crossing are aggregated, and a zero-counting algorithm (explained in Sec. 2.1.1) is then employed. At this step, the afterglow correction can be applied. The raw rate is saved separately ('bxraw') and the per-channel calibration constant is used to define the luminosity ('bx'). These steps are performed for each of the channels and the average data are also produced (correspondingly 'avgraw' and 'avg'). The iteration over all LHC BCIDs is performed, to calculate the total instantaneous luminosity. The per-channel luminosity data are only published during the separation scans so that each of the BCM1F-μTCA channels can be calibrated separately and can be treated as independent luminometers. These per-channel calibration constants are used as efficiency factors for the final average measurement, based on the assumption that each of them should measure the same luminosity:

$$\mathrm{SBIL} = \frac{\sum_i^N \mathrm{SBIL}_i}{N}, \tag{2.9}$$

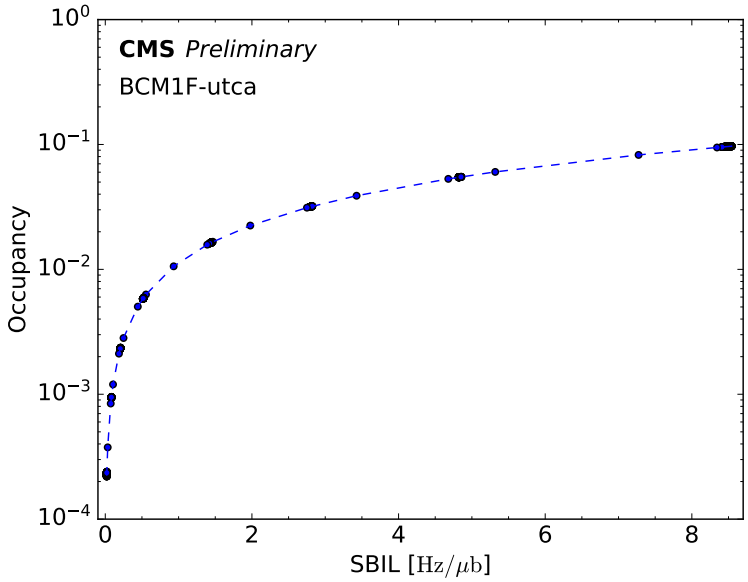

Figure 2.25: The BCM1F-μTCA measured average mean number of hits (from zero-counting algorithm) per single BCID as a function of SBIL (dots) during a separation scan. The data are fitted with a linear function (dashed line) to show the linear response. The maximum SBIL in the plot corresponds to pile-up close to 60.

where i indicates the channel number. Thus, the spread in the rate across the channels is removed from the average measurement:

$$\overline{\mu} = \frac{\sum_i^N \frac{\overline{\sigma_{\text{vis}}}}{\sigma_{\text{vis},i}} \mu_i}{N}. \tag{2.10}$$

An example measurement of these efficiency factors, during an early Run 3 emittance scan, is shown in Fig. 2.26. The standard deviation of all channels was measured as 8%.

The efficiency factors can be alternatively estimated from the total per-channel rates, for example within an entire fill, compared to all channels rate average.

This approach leads to the reduction of the final statistical error. This is shown in Fig. 2.27, based of Eq. (2.6). For the vdM conditions when the rate occupancy is very low, the typical integration time of the vdM scan steps is 60 s. This changes the error from 3.5% on a single channel to approximately 0.5% if all of the BCM1F-μTCA channels are used. In the nominal physics conditions, the rate occupancy is much higher, thus the integration steps can be as short as 10 s. The single channel statistical error is much lower, equal to 1.25%, and reaches 0.2% when all channels are averaged. The extended integration time can give further statistical error reduction, the vdM-equivalent integration time would lead to a relative error of less than 0.1%.

Due to front-end problems (discussed in Sec. 2.8.4), a special feature was implemented for auto-masking of under-performing channels. The rejection condition is based on the per-channel luminosity, ensuring it is within the acceptable distance from the average luminosity. It uses an adjustable threshold which can be changed or switched off directly from processor configuration, and is only active during

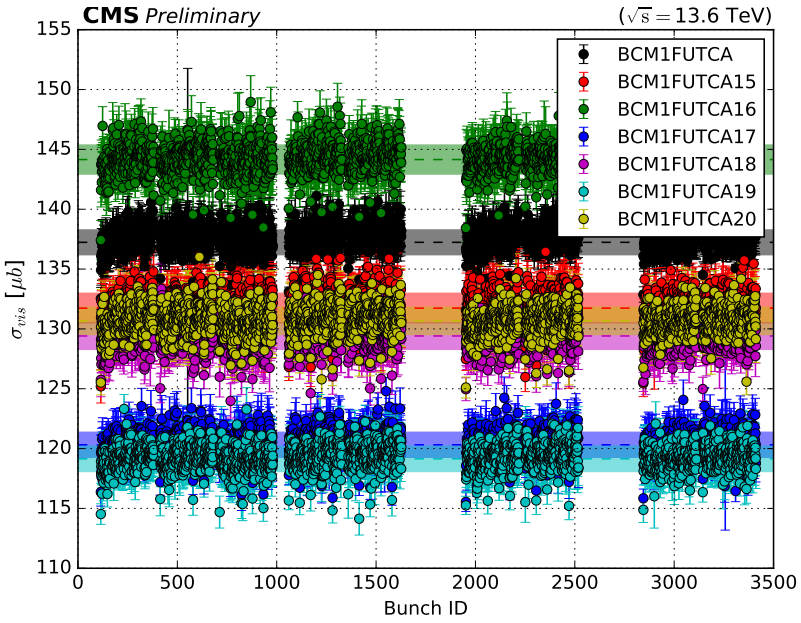

Figure 2.26: Calibration constant σ_{vis} measured for each of the filled bunches, shown for six example channels compared to all BCM1F-μTCA channels average in black. Preliminary measurement from an emittance scan in fill 8113 is shown - single gaussian fit was used without any corrections.

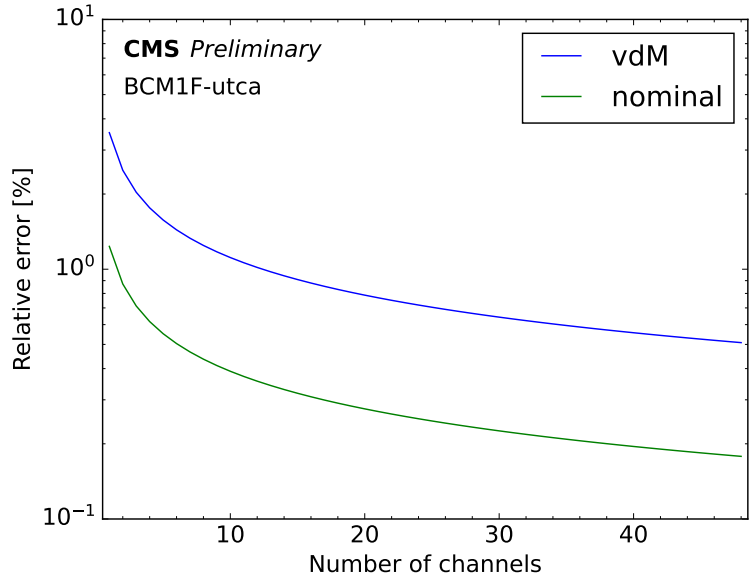

Figure 2.27: Statistical error on the BCM1F-μTCA measured per-bunch luminosity as a function of number of channels for the vdM conditions (SBIL $\simeq$ 0.1 [Hz/μb], t_{int} = 60 s), and for the nominal physics conditions (using average SBIL $\simeq$ 5.3 [Hz/μb], t_{int} = 10 s).

the Stable Beams mode.

2.8.8 Background measurement

The signals in the detector originating from beam-induced background particles are measured by different BCM1F channels, based on their location with respect to the CMS IP. This is shown schematically in Fig. 2.28, at the CMS the opposite sign is used for the longitudinal coordinate than at the LHC. The background signal is separated by the time of arrival. As shown in the scheme, each beam will first arrive at the detector location on each side of the IP (incoming direction), producing the background signal. Only after $\Delta t = 6.25$ ns the collision occurs. The second beam arrives on the other side of BCM1F after another Δt (outgoing direction), together with the collision products. The separation of the incoming background and collision products is only possible after the correct timing alignment is done. The synchronization of the BCM1F signals from different locations is adjusted for the simultaneous arrival of the collision products. This process was described in Sec. 2.8.4. The effectiveness of this method was shown during Run 2 [70].

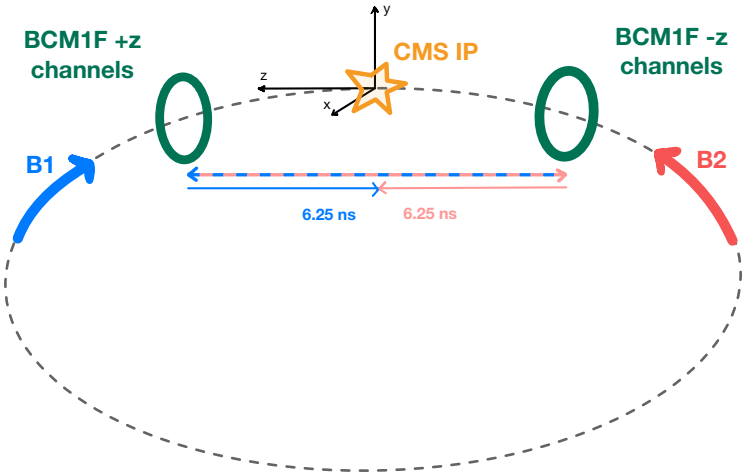

Figure 2.28: Scheme of the separate halves of the BCM1F detector located at different sides of the CMS IP. The time delay between the beam crossing the BCM1F area and the moment of collision is indicated, which is used for the background signal separation.

The example of the time structure of the BCM1F-μTCA histogramed LHC orbit, after the final alignment is shown in Fig. 2.29. In this example, two bunches are shown which were present at the LHC, circulating in opposite directions, at different BCIDs. The signal from each of these bunches is shown separately, BCID101 in the upper and BCID1001 in the lower plot. The measured background is shown in separate colors as measured on the $+z$ (BKG1) and $-z$ (BKG2) sides of CMS. The bunch circulation direction is defined by the time of arrival: BCID 101 signal is measured firstly at $+z$ and then at $-z$ (upper plot). The opposite is true for the second presented BCID in the lower plot: the signal is measured firstly at $-z$ and 12.5 ns later at $+z$. The outgoing background is always higher than the incoming background signal, after crossing the interaction point region. This is predicted with the CMS FLUKA model, due to secondary radiation from showering on the beampipe and components close to the beamline [66]. Therefore, each beam upstream channels average is used to estimate the incoming beam-induced background. Single bin signal before a bunch crossing (span of ~ 4 ns for BCM1F-μTCA) is used for the

measurement.

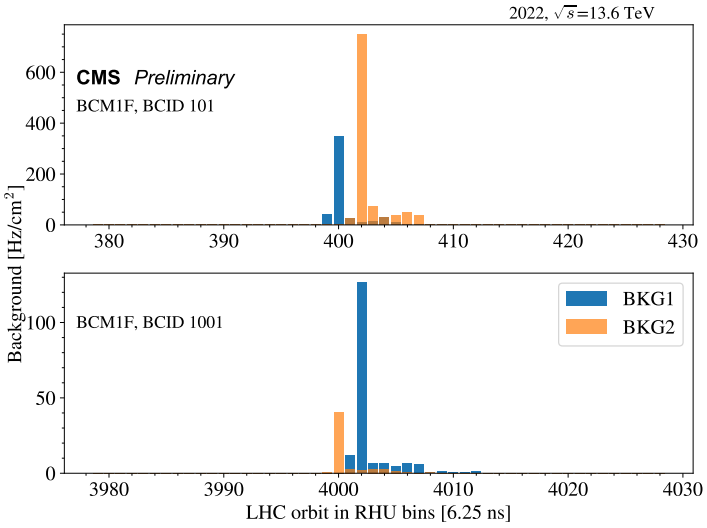

Figure 2.29: BCM1F average measured incoming and outgoing backgrounds for two individual nominal circulating bunches shown separately in the upper (BCID 101) and lower plot (BCID 1001). Background measured on the $+z$ side of CMS is marked in blue (BKG1), while the measurement from the $-z$ side is marked in orange (BKG2).

There are two types of backgrounds calculated per beam - from the signal generated by the non-colliding bunches, as well as from the sum of non-colliding bunches and 'leading' bunches signal. The 'leading bunches' are defined as the first bunches in a bunch train, with an additional condition on the distance from the preceding train, of 30 BCIDs. This is done to minimize the impact of the detector materials activation by prompt radiation on the beam background measurement. The afterglow contribution is estimated from the 20 preceding bins (~ 84 ns) and removed from the background signal. The total rate is normalized to the sensor active area to represent the occupancy and the NB4 integrated measurement is further normalized by the time corresponding to the number of orbits used so that the units are natural [Hz/cm^2]. The backgrounds are further normalized to the total charge of the bunches contributing to each of the backgrounds. BCM1F-μTCA also publishes per-bunch backgrounds separately, that are available for more sophisticated offline analyses. An additional example of the background measurement for colliding beams is shown in Sec. 6.1 in the vdM conditions, where the background contribution is much more significant than in the physics operation.

Based on the BCM1F measurements the beam conditions are assessed to guarantee safe operation for the other CMS subsystems. The beam-induced backgrounds measured using BCM1F are sent to the LHC as real-time feedback of the beam conditions prevalent close to the CMS experiment, throughout the full machine cycle (Fig. 2.30).

2.8.9 Beam properties measurement in transverse scans

As discussed in Sec. 1.2.1 and 1.3.2, the transverse beam separation scans can serve to measure the convoluted beam sizes Σ_x, Σ_y in a non-destructive way. In the process of fitting the rate curve during a scan, another parameter extracted from detector rates is the fit mean, which represents the

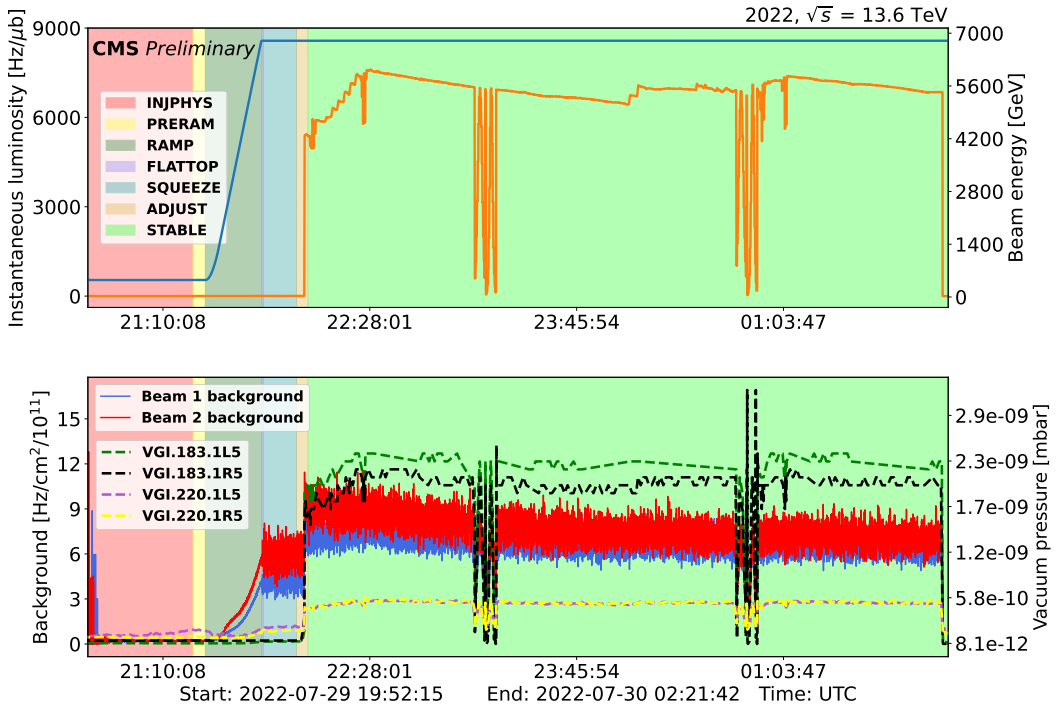

Figure 2.30: BCM1F measured B1 and B2 backgrounds (bottom figure) over the LHC beam mode cycle indicated with the background shades and listed in the top figure together with the beam energy (light blue curve) and BCM1F measured luminosity (orange curve). The readings from the vacuum pressure gauges (VGI) located close to the BCM1F at ±1.8 m and ±2.2 m are also shown.

displacement of the orbit. This parasitic measurement is very valuable, as it gives access to per-bunch displacements, which is not possible with the existing instrumentation, that integrates the entire orbit data. Examples of such measurements conducted by BCM1F-μTCA are shown in the following subsections.

Beam overlap measurement

Figure 2.31 shows the bunch overlap evolution during a fill with β^* -leveling in which the scans were performed after each β^* adjustment, from 60 cm to 42 cm. The overlap width decreases along these steps. During operation in the nominal conditions, a crossing angle ϕ is applied using the dipole corrector magnets to avoid long-range interactions. At CMS, it is applied in the horizontal plane $\{x\text{–}z\}$, hence the beam overlap includes the effect of this crossing angle (according to Eq. (1.22)). Thus, the effective overlap area is bigger in Fig. 2.31a. The statistical error on the measured Σ_x, Σ_y is estimated depending on the fit model. Typically it is similar to the one obtained for the peak rate, in the presented example it is below 0.1 %.

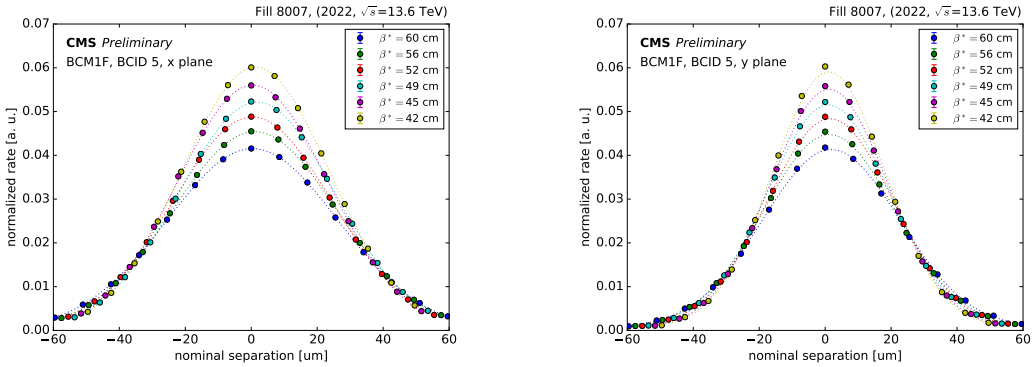

(a) Scan in x plane.

(b) Scan in y plane.

Figure 2.31: Evolution of beam overlap for various β^* steps during luminosity levelling. An example bunch is shown, for scans in both $\{x, y\}$ planes.

This measurement can be further used to estimate the convoluted emittance (Eq. 1.24). An example is shown in Fig. 2.32, for a special fill which included bunches with a wide range of normalized emittances: 1.85-5.15 μm in x and 1.79-5.59 μm in y. However, according to Eq. 1.22 precise measurements of the ϕ and σ_z are needed to preserve the small error. In the example, the nominal settings were used which can be affected by a significant systematic error. Additionally, in both planes, there is additional uncertainty from the limited knowledge on β^* with the dynamic effects. Nevertheless, the estimation is in agreement with expected emittances.

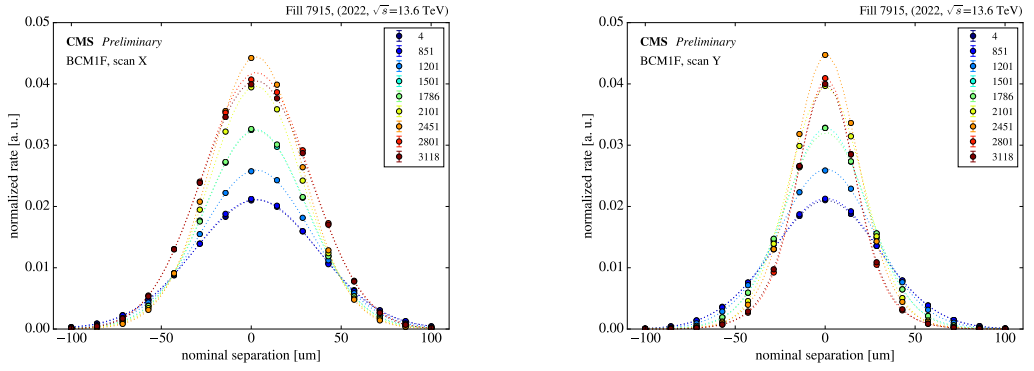

(a) Scan in x plane.

(b) Scan in y plane.

Figure 2.32: Beam overlap profile for 9 bunches with various emittances for both $\{x, y\}$ planes (left and right). In the legend the BCIDs are indicated, each of them was fitted with the double Gaussian function. The differences between bunches are more pronounced in the y plane - in this plane the overlap does not include the contribution from the crossing-angle and the bunch length at the CMS.

Orbit displacement measurement

The mean value is extracted from a Gaussian fit to the normalized rate over separation steps (as in Figs. 2.31 and 2.32). It indicates the per-bunch orbit offset, which is dependent on the number of parasitic collisions for a given filling pattern. An example of bunch train displacement structures measured by BCM1F for fill 8113 is shown in Fig. 2.33. It indicates the incredible accuracy of this method of ~ 0.1 μm, which is also below the limits of the current instrumentation. The plotted errors include only the statistical uncertainty from the fit.

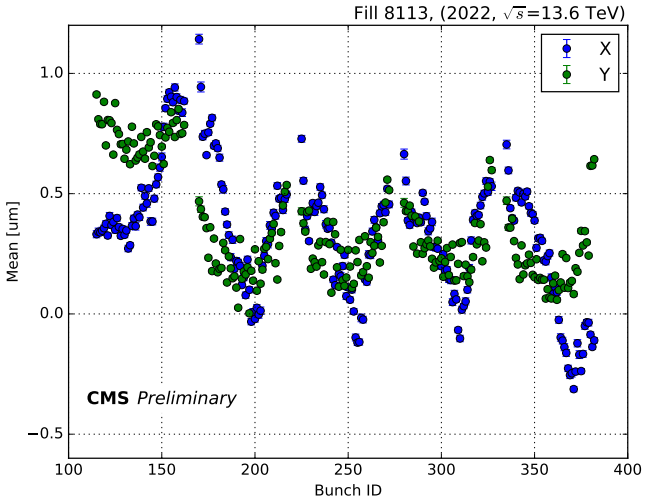

Figure 2.33: BCM1F measured per-bunch orbit displacement, during an emittance scan. The displacement in transverse direction is extracted from the Gaussian fit to the separation scan in given direction, as its mean. The zoom into a group of trains is shown with regular per-train structure in both $\{x, y\}$ planes, which is dependent on the number of Long-Range interactions per bunch.

Part II

Beam-beam interaction and its effect on luminosity

As the two particle beams are brought into collision, they interact electromagnetically implying a substantial force on one another. This force, known as the beam-beam interaction, can be derived from the electromagnetic field produced by the collection of charges within each bunch. The beam-beam interaction effects have been known as one of the main non-linearities and challenges in the operation of colliders, yet for a long time considered negligible when it comes to luminosity calibrations.

3 Beam dynamics

This section starts with relevant basics of beam dynamics, starting from the transverse linear motion in a circular particle accelerator. Next, the beam-beam interaction is defined (see Sec. 3.2). It is a common practice to distinguish the beam-beam effects into those affecting individual particles independently (incoherent effects) and those that impact the behavior of the particle bunches as a whole (coherent effects). This distinction is examined in detail in the subsequent subsections. For precise evaluation of the beam-beam effects, multi-particle simulations are conducted in this thesis, the COherent-Multibunch Beam-beam Interaction multiparticle code (COMBI) has been used. In Section 3.3 the important aspects of the code are introduced, crucial in obtaining the results presented in the following chapters. Further, the discussion delves into the implications of beam-beam interaction effects on luminosity curves during separation scans and other relevant observables (see Sec. 3.4). This is followed by a simplified analytical description of the vdM scans using transport matrices that are useful for qualitative understanding of the underlying phenomena (see Sec. 3.5) linked to the periodicity of the accelerator lattice and collisions.

3.1 Transverse motion

The equations of motion in the transverse planes in a circular periodic accelerator can be derived from a general equation of motion. A curved coordinate system around the reference orbit of a beam (x, y) is used [71] to describe the particle dynamics for the simple case of only linear field changes (i.e. quadrupole magnets):

$$x'' + K(s)x = \frac{1}{\rho(s)} \frac{\Delta p}{p_0}, \tag{3.1}$$

where $\rho(s)$ describes the radius of curvature, $K(s)x$ is the amplitude-dependent curvature that varies for different lattice elements, and $\frac{\Delta p}{p_0}$ is the deviation in the particle momentum.

In linear approximation, the principal trajectories of a particle in the accelerator can be found using transport matrices of all the lattice elements $(M_1 \ldots M_N)$:

$$M = M_N \ldots M_2 \cdot M_1, \tag{3.2}$$

where M gives the full turn map. The motion in each of these elements can be described with corresponding Hamiltonian H. Multiplying the symplectic solutions always gives another symplectic matrix which preserves the fundamental phase-space properties. Phase space refers to the combined space of

positions and momenta of particles (x, x', y, y'), and preserving its symplectic structure is crucial for maintaining the stability of a particle over multiple turns. The transport matrix between the arbitrary sections of the ring $(s_0 \to s)$ is described by:

$$M_i = \begin{pmatrix} \sqrt{\frac{\beta}{\beta_0}}(\cos\Delta\mu + \alpha_0 \sin\Delta\mu) & \sqrt{\beta\beta_0}\sin\Delta\mu \\ -\frac{1}{\sqrt{\beta\beta_0}}((\alpha-\alpha_0)\cos\Delta\mu + (1+\alpha\alpha_0)\sin\Delta\mu) & \sqrt{\frac{\beta_0}{\beta}}(\cos\Delta\mu - \alpha\sin\Delta\mu) \end{pmatrix}, \tag{3.3}$$

where α, β are the Courant-Snyder (Twiss) parameters describing the phase space ellipse [71], shown in Fig. 3.1, and $\Delta\mu$ is the phase change between the two sections:

$$\Delta\mu = \int_{s_0}^{s} \frac{ds}{\beta_i(s)}, \tag{3.4}$$

where $i \in \{x, y\}$ indicates the transverse plane. The Courant-Snyder parameters can be used to define the action variable (for example in the x plane) that is invariant under the transport along the beamline if no dispersive forces are present:

$$J_x = \frac{1}{2}\left(\gamma_x x^2 + 2\alpha_x x x' + \beta_x (x')^2\right). \tag{3.5}$$

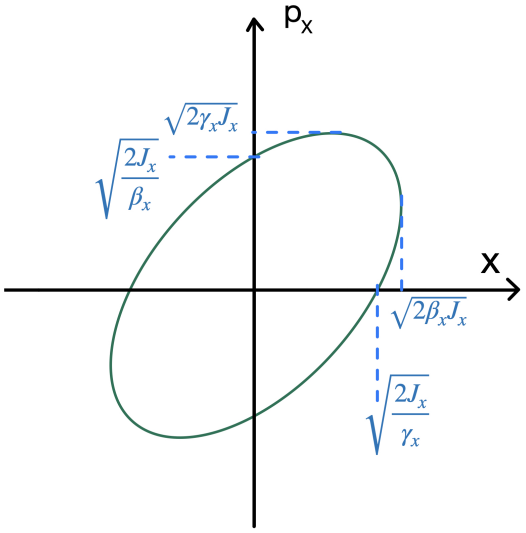

Figure 3.1: Phase space ellipse in a periodic beam line and its parameters. The area of the ellipse is $2\pi J_x$.

When propagating along a periodic lattice, the phase grows linearly, thus particles' motion resembles that of a harmonic oscillator. At a specific location, the phase space ellipse is sampled by a particle in consecutive turns through the ring, thus providing stable motion. The machine betatron tune is defined as the number of transverse oscillations in one revolution. It is defined by integrating over the lattice β-function:

$$Q_i = \frac{1}{2\pi}\int_{s}^{s+C} \frac{ds}{\beta_i(s)}, \tag{3.6}$$

where C is the circumference of the accelerator. Thus, the phase advance in the single revolution is equal to $\mu_i = 2\pi Q_i$. The betatron tune of a single particle within a beam depends on its off-momentum

coordinate $\Delta p/p_0$ due to chromaticity, on its betatron actions due to magnetic multipoles, and the mean field of the source beam in the beam-beam interaction.

If the symmetric point in the magnetic lattice is chosen, where $\alpha = -\frac{1}{2}\beta' = 0$ at the same location $\beta = \beta_0$, and the phase change over the full revolution is used $\mu = 2\pi Q$ that is related the machine tune Q, the complete turn transfer map is obtained:

$$M_{\text{turn}} = \begin{pmatrix} \cos 2\pi Q & \beta \sin 2\pi Q \\ -\frac{1}{\beta}\sin\ 2\pi Q & \cos 2\pi Q \end{pmatrix}. \tag{3.7}$$

In reality, betatron motion is coupled through the solenoidal and skew quadrupole fields. Solenoid fields are often present at the interaction points, for the purposes of the detector tracking systems. The latter is commonly present from the magnetic lattice errors, e.g. misalignment. The coupling of the transverse planes can be described by including extra terms in a 4×4 transport matrix with 16 parameters.

The betatron tunes of a machine are carefully adjusted to avoid the resonance condition:

$$nQ_x + mQ_y = l, \tag{3.8}$$

where n, m, l are integers. Tune modulations, for example from sextupole magnets, used to correct chromaticity, can drive nonlinear resonances and thus cause particle loss (see Fig. 3.2a). With these possibilities of driving the higher-order resonances, the resonance-free tune area becomes small, and the successful operation of a synchrotron becomes more challenging. However, with the chaotic movement caused by the higher order fields, the stable motion can be preserved by creating the empty resonance islands (see Fig. 3.2b). One of the strongest such non-linearities is the beam-beam interaction once the beams are brought into collisions. It is described in the following section.

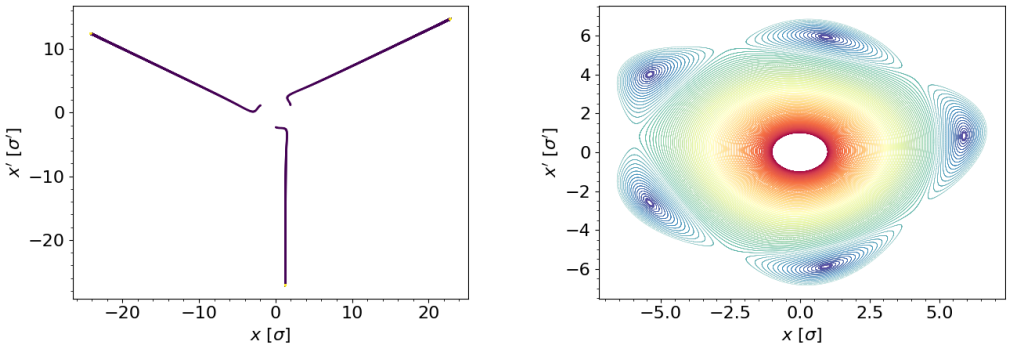

(a) Single particle resonant trajectory (3^{rd} order).

(b) Stable single particle trajectories while crossing 5^{th} order resonance

Figure 3.2: Phase space pictures for a particle undergoing a resonance (left) and multiple (100) trajectories for particles in the sextupole field with different amplitudes (right).

3.2 Beam-beam interaction

The particle beam in an accelerator is a collection of moving charges that represent an electromagnetic (EM) potential for any other charges. Thus, when brought into collision, the beam exerts forces on itself (space charge), as well as on the opposing beam. The electromagnetic interaction of the two colliding beams while crossing each other is called the beam-beam (BB) interaction. Typically very small fractions of the beams collide leading to intensity burn-off, while all the particles within a bunch distribution are distorted with these EM forces. This interaction can be approximated as an electromagnetic lens, but in a very non-linear form (with multipoles), and exact forces depending on the particle distribution.

The beam-beam interaction has been extensively studied in both lepton and hadron colliders [72, 73, 74, 75]. It caused operational challenges for LEP, exhibiting as the strongest non-linearity in the machine [76]. It is also expected to represent a major challenge and limitation for future colliders, as the beam-beam perturbation becomes stronger with higher intensity and smaller beams, that would be present in these high luminosity conditions.

3.2.1 Incoherent beam-beam force

The theoretical description of the single-particle dynamics is rather complete, and described in detail in many handbooks, for example [71, 77]. The problem becomes complex, when studying the full system of particles, e.g. LHC nominal bunch, consisting of the order of 10^{11} particles.

The electric potential Φ of a bunch can be obtained from the Poisson equation:

$$\nabla^2\Phi(x,y,z) = -\frac{\rho(x,y,z)}{\epsilon_0}, \tag{3.9}$$

where $\rho(x,y,z)$ is the bunch charge distribution and ϵ_0 is the vacuum permittivity. The former can have a very complicated shape but can be qualitatively approximated with a Gaussian charge distribution:

$$\rho(x,y,z) = \frac{Ne}{(2\pi)^{3/2}\sigma_x\sigma_y\sigma_z}\exp\left(-\frac{x^2}{2\sigma_x^2}-\frac{y^2}{2\sigma_y^2}-\frac{z^2}{2\sigma_z^2}\right), \tag{3.10}$$

with total charge $Ne = \int\int\int\rho(x,y,z)dxdydz$. The potential of this distribution can be found using Green's function for Laplace operator ∇^2, which takes the form:

$$G(x,y,z) = \frac{-1}{4\pi\sqrt{x^2+y^2+z^2}}, \tag{3.11}$$

and thus:

$$\Phi(x,y,z) = \frac{1}{\epsilon_0}\int\int\int G(x,y,z)\rho(x,y,z)dxdydz = \\ \frac{1}{4\pi\epsilon_0}\frac{Ne}{(2\pi)^{3/2}\sigma_x\sigma_y\sigma_z}\int\int\int\frac{\exp\left(-\frac{x^2}{2\sigma_x^2}-\frac{y^2}{2\sigma_y^2}-\frac{z^2}{2\sigma_z^2}\right)}{\sqrt{x^2+y^2+z^2}}dxdydz. \tag{3.12}$$

This formula is not trivial to solve. The electromagnetic field can be then computed:

$$\vec{E} = -\nabla\Phi(x,y,z) \tag{3.13}$$

The Lorentz force exerted on a particle by the opposing bunch at a radius r is:

$$\vec{F}_{\perp} = e(\vec{E} + \vec{v} \times \vec{B}) = e(E_r + \beta_{rel} c B_{\phi})\hat{r}, \tag{3.14}$$

where $\beta_{rel} = v/c$ is the relativistic factor and B_{ϕ} is the magnetic field component following from the moving charge in the electric field $\vec{B} = \vec{\beta_{rel}} \times \vec{E}/c$.

The closed expression for the electrical field of a two-dimensional Gaussian charge Q distribution, as derived in [78] is:

$$\begin{aligned} E_x &= \frac{Q}{2\epsilon_0\sqrt{2\pi(\sigma_x^2-\sigma_y^2)}}\Im\left[w\left(\frac{x+iy}{\sqrt{2(\sigma_x^2-\sigma_y^2)}}\right) - e^{\left[-\frac{x^2}{2\sigma_x^2}+\frac{y^2}{2\sigma_y^2}\right]} w\left(\frac{x\frac{\sigma_y}{\sigma_x}+iy\frac{\sigma_x}{\sigma_y}}{\sqrt{2(\sigma_x^2-\sigma_y^2)}}\right)\right], \\ E_y &= \frac{Q}{2\epsilon_0\sqrt{2\pi(\sigma_x^2-\sigma_y^2)}}\Re\left[w\left(\frac{x+iy}{\sqrt{2(\sigma_x^2-\sigma_y^2)}}\right) - e^{\left[-\frac{x^2}{2\sigma_x^2}+\frac{y^2}{2\sigma_y^2}\right]} w\left(\frac{x\frac{\sigma_y}{\sigma_x}+iy\frac{\sigma_x}{\sigma_y}}{\sqrt{2(\sigma_x^2-\sigma_y^2)}}\right)\right]. \end{aligned} \tag{3.15}$$

The formulas E_x and E_y differ only by the imaginary ($\Im$) or the real ($\Re$) part of the expression. The complex error function $w(z)$ needs to be evaluated numerically. The resulting force includes the radial component $r = \sqrt{x^2+y^2}$ and for the simplified round beams geometry, can be expressed as:

$$F_{\perp} = \pm\frac{Ne^2(1+\beta_{rel}^2)}{4\pi\epsilon_0 r}\left(1-\exp\left[-\frac{r^2}{2\sigma^2}\right]\right), \tag{3.16}$$

where the sign depends on if the force is seen by the same (+) or different (−) charge. In the following, the same charge case will be considered, with $v \to c$, and thus $\beta_{rel} \approx 1$. Its non-linear dependence on a particle at different amplitudes is shown in Fig. 3.3. The series expansion of the exponential in Eq. (3.16) gives an insight into the multiple-order effects of the beam-beam force. The main effects, resulting from the linear and quadratic field components are discussed in the following subsections.

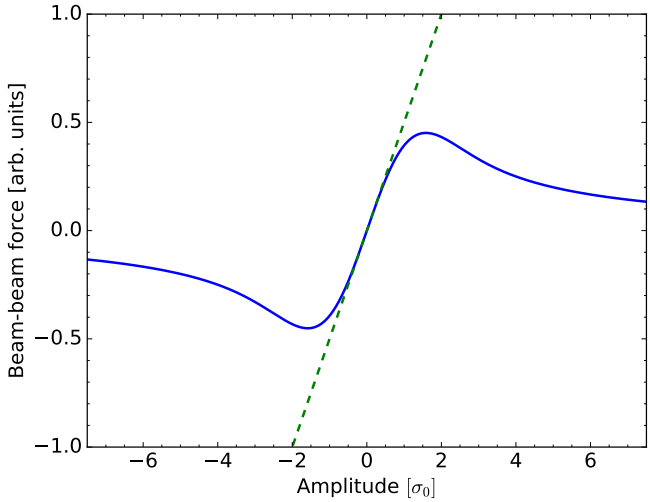

Figure 3.3: Beam-beam force of the source bunch on a particle in another beam as a function of its amplitude (blue), the linearized slope for small amplitude particles is indicated with a green dashed line.

The corresponding kick-angle $\Delta r'$ can be derived from the beam-beam force by the use of Newton's law:

$$\Delta r' = \frac{1}{mc\beta_{rel}\gamma}\int_{-\infty}^{\infty} F_{\perp}(r,t)\,dt, \tag{3.17}$$

where m is the particle mass, γ is the relativistic factor, and c is the speed of light. The radial kick on a single particle at a distance r induced by the source-field beam is:

$$\Delta r' = -\frac{2Nr_0}{\gamma r}\left(1-\exp\left[-\frac{r^2}{2\sigma^2}\right]\right), \tag{3.18}$$

by using the expression for the classical particle radius $r_0 = \frac{e^2}{4\pi\epsilon_0 mc^2}$.

Linearized beam-beam force

The Taylor expansion can be used to simplify the exponential formula in Eq (3.16), at small amplitudes, with $r \to 0$, it becomes:

$$F_{\perp} = \frac{Ne^2}{2\pi\epsilon_0 r}\left(1-\left[1+0\times r+\frac{-1}{2\sigma^2}\times r^2+...\right]\right) \approx \frac{Ne^2}{4\pi\epsilon_0\sigma^2}r. \tag{3.19}$$

The force becomes linear with r at small amplitudes and can be compared to the one exerted by a quadrupole magnet. The derivative of the linearized force can be related to the corresponding focal length $\frac{1}{f} = -\frac{\Delta r'}{r}$. Thus, this effect can be approximated as the β-beating at the IP and it is commonly referred to as the dynamic-β effect. It has a direct impact on the observed beam width, which is proportional to $\sqrt{\beta}$ (see Eq. 1.9).

Following the same steps for Eq. 3.18, the gradient of the force at the small amplitudes can be expressed as a linear dependence with r:

$$\lim_{r\to 0}\Delta r' = \frac{Nr_0}{\gamma\sigma^2}r. \tag{3.20}$$

This linearised slope is also indicated in Fig. 3.3 with the green curve. This is equivalent to a quadrupole with focal length as the proportionality factor. The tune change can then be defined using the thin lens approximation:

$$\Delta Q = \frac{1}{4\pi}\beta^*\left(-\frac{\Delta r'}{r}\right), \tag{3.21}$$

where β^* is the beta function at the location of the interaction. Combining this expression with Eq. (3.20), yields:

$$\Delta Q = \frac{Nr_0\beta^*}{4\pi\gamma\sigma^2} = \frac{Nr_0}{4\pi\epsilon_n} = \xi, \tag{3.22}$$

which is also known as the beam-beam parameter ξ. It is useful to expand this expression to non-round cases when the beam sizes are different in the two transverse planes $\sigma_x \neq \sigma_y$. The tune shift becomes plane-dependent and so does the beam-beam parameter:

$$\xi_{x,y} = \frac{Nr_0\beta^*_{x,y}}{2\pi\gamma\sigma_{x,y}(\sigma_x+\sigma_y)}, \tag{3.23}$$

thus the differences in the transverse emittances and β^* in the two planes have to be considered. This parameter is often used to quantify the strength of the beam-beam force, but it is important to emphasize that the beam-beam force does not depend on the local β^* but the tune shift does. This

derivation was done for small amplitude particles, thus it does not reflect the non-linear nature of the force at amplitudes greater than 1σ.

Beam-beam deflection

The derived force in Eq. (3.16) and kick in Eq. (3.18) can be also expressed separately for the two transverse directions. A constant displacement d can be added, as it is done in the separation scans or in the case of long-range interaction:

$$\Delta x' = -\frac{2Nr_0}{\gamma}\frac{x+d}{r^2}\left(1-\exp\left[-\frac{r^2}{2\sigma^2}\right]\right), \tag{3.24}$$

where $r=\sqrt{(x+d)^2+y^2}$, as the displacement is added in the horizontal plane. The equivalent definition follows in the vertical plane. The dipolar component of the beam-beam force is visible for well-separated beams $d \gg \sigma$:

$$\Delta x' \simeq -\frac{2Nr_0}{\gamma}\times\frac{1}{d}\left(1-\exp\left[-\frac{d^2}{2\sigma^2}\right]\left[1+O(r)+O(r^2)+...\right]\right), \tag{3.25}$$

thus each particle is displaced proportionally to d, independently of its amplitude.

Amplitude detuning

Additionally, the non-linear beam-beam force introduces non-linear detuning with respect to the particle amplitude. This amplitude-dependent change in the single particle oscillation frequency induces a spread in the tune for the collective of particles. In case this spread extends into the resonance tune values, it has the potential to make the particle motion unstable. Amplitude detuning is commonly described using the single-particle action variables J, which represent the invariant of motion. The quadrupolar component of the EM field generated by the source bunch changes as a function of the transverse separation during a scan as well as the transverse actions J_x, J_y. The resulting betatron tune shift is given by [79]:

$$\Delta Q_x(J_x,J_y) = -\xi_x\int_0^\infty \frac{1}{(1+t)^2}\exp\left(-\frac{J_x+J_y}{2\epsilon(1+t)}\right)\times\left[I_0\left(\frac{J_x}{2\epsilon(1+t)}\right)-I_1\left(\frac{J_x}{2\epsilon(1+t)}\right)\right] \times I_0\left(\frac{J_y}{2\epsilon(1+t)}\right)dt, \tag{3.26}$$

where I_0, I_1 are modified Bessel functions of the first kind, ϵ is the round-bunch emittance, and t is a bound variable. This amplitude-dependent tune shift can be also described in terms of the amplitude-dependent beta-function-beating. An example of this detuning is shown in Fig. 3.4 - the nominal betatron tunes were indicated with the red pentagon and the spread in the single particle tunes is indicated with different colors at the head on (blue) and separated collisions (green).

Other single-particle effects

The incoherent effects encompass several phenomena that are significant for the beam dynamics. Dynamic aperture (DA) defines the transverse region where particles within a beam remain stable.

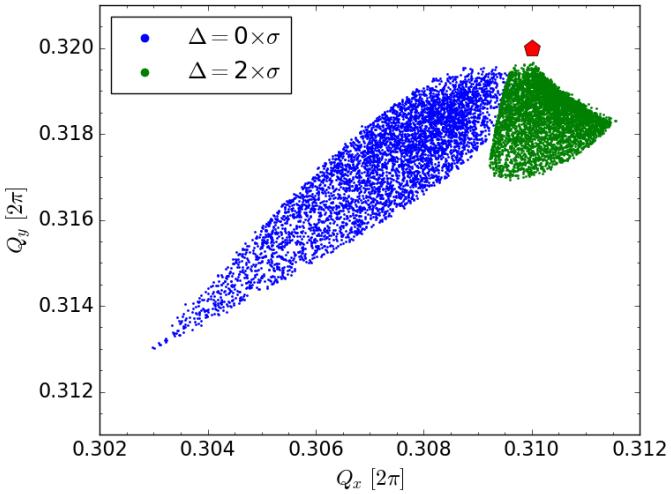

Figure 3.4: The single particle betatron tunes spread induced by head-on (blue) and separated (green) beam-beam interaction. The unperturbed tunes are indicated with the red pentagon.

When the motion of a single particle becomes chaotic or unstable, it can result in particle losses and a subsequent reduction in DA. This is possible to assess through the measurement of particle losses and the decreased beam lifetime. In a completely linear machine single particle probes the phase-space ellipse with the machine tune frequency $2\pi Q$. As the beam-beam interaction is non-linear, it leads to the formation of higher-order resonances, modifying the phase space structure as shown in Fig 3.5. This non-linear perturbation can be effectively treated as an additional non-linear lens, consequently modifying the optical properties of the machine.

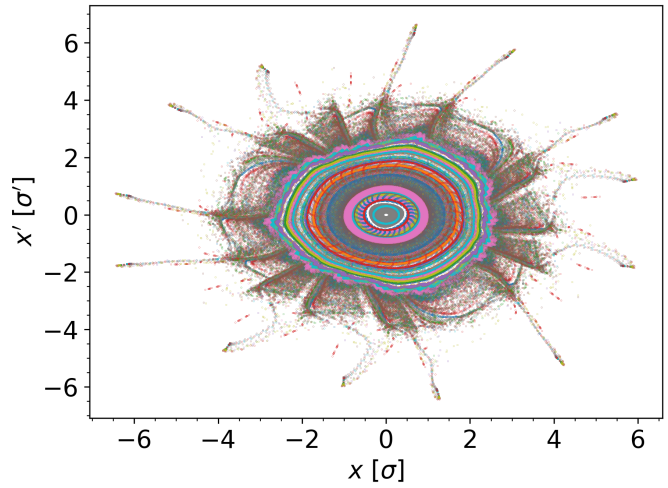

Figure 3.5: Phase space picture (x, x') of 100 random single particle trajectories with the beam-beam interaction. Different colors represent particles at varying initial amplitudes in x, x'.

3.2.2 Coherent beam-beam interaction

The beam-beam interaction couples the movement of the two beams, and thus it is important to study not only single particles but also the effect on the whole beam dynamics. This results in the bunch coupling and the appearance of the coherent modes, which may become unstable if their frequency is matched with the resonance frequencies, as well as effects on self-consistent orbits and beam emittance.

Coherent kick is obtained by integration of the single-particle kicks over the beam distribution:

$$\Delta x'_{coh}(x,y) = -\frac{2Nr_0}{\gamma}\frac{x}{x^2+y^2}\left(1-e^{-(x^2+y^2)/4\sigma^2}\right), \tag{3.27}$$

with gradients in both directions, assuming the scan is performed in x plane ($y=0$):

$$\frac{\partial \Delta x'_{coh}(x,y)}{\partial x} = -\frac{2Nr_0}{\gamma}\frac{e^{-x^2/4\sigma^2}}{2\sigma^2x^4}\left(x^4-2\sigma^2x^2(e^{x^2/4\sigma^2}-1)\right), \tag{3.28}$$

$$\frac{\partial \Delta y'_{coh}(x,y)}{\partial y} = -\frac{2Nr_0}{\gamma}\frac{e^{-x^2/4\sigma^2}}{2\sigma^2x^4}\left(2\sigma^2x^2(e^{x^2/4\sigma^2}-1)\right), \tag{3.29}$$

additionally:

$$\frac{\partial \Delta x'_{coh}(x,y)}{\partial y} = \frac{\partial \Delta y'_{coh}(x,y)}{\partial x} = 0. \tag{3.30}$$

At the small amplitude limit, similarly as for the single particle, the expression for the coherent beam-beam parameter is obtained:

$$\Xi = \frac{Nr_0\beta^*}{8\pi\gamma\sigma^2} = \frac{\xi}{2}, \tag{3.31}$$

which is equal to half of the single-particle beam-beam parameter.

In order to evaluate the collective effects of the two beams, the kick defined from the coherent force has to be used, Eq. (3.27). The one-turn map in the most basic scenario, where two symmetrical beams collide at a single interaction point, becomes [72]:

$$M_{\text{turn}} = \hat{U}(\mu_{\text{B1}},\mu_{\text{B2}})R(\Xi_{\text{B1}},\Xi_{\text{B2}}), \tag{3.32}$$

where $\hat{U}(\mu_{\text{B1}},\mu_{\text{B2}})$ is the block-diagonal 4×4 matrix including the transport of the two beams, as in Eq. (3.7):

$$\hat{U}(\mu_{\text{B1}},\mu_{\text{B2}}) = \begin{pmatrix} U(\mu_{\text{B1}}) & 0 \\ 0 & U(\mu_{\text{B2}}) \end{pmatrix}, \tag{3.33}$$

and R is the beam-beam kick matrix:

$$R(\Xi_{\text{B1}},\Xi_{\text{B2}}) = \begin{pmatrix} I-A(\Xi_{\text{B1}}) & A(\sqrt{\Xi_{\text{B1}}\Xi_{\text{B2}}}) \\ A(\sqrt{\Xi_{\text{B1}}\Xi_{\text{B2}}}) & I-A(\Xi_{\text{B2}}) \end{pmatrix}, \qquad A(\Xi) = \begin{pmatrix} 0 & 0 \\ 4\pi\Xi & 0 \end{pmatrix}. \tag{3.34}$$

In the above equation, the coupling between the two beams is present, via the off-diagonal forms, which propagates into the perturbed tunes. The mapping becomes unstable when μ_{B1} or μ_{B2} approaches half-integers or their sum approaches integer from the lower side. In case $\mu_{\text{B1}}=\mu_{\text{B2}}=\mu$, one can obtain the eigenvalues which indicate two distinct modes associated with in and out-of-phase motion of the two beams at the IP, shown in Fig. 3.6: σ-mode at the unaffected nominal tune and the π-mode

at $Q_\pi \simeq Q_0 - \xi$ (assuming identical beams). The system of the two beams is then coupled via the beam-beam force introducing the coherent oscillation modes. These modes are sensitive to differences in intensities, thus these frequencies change in case $N_{B1} \neq N_{B2}$. Even when steering clear of resonant conditions, the machine impedance can still induce instability via the coherent beam-beam modes, leading to mode coupling instability in the colliding beams. The coherent modes can be suppressed in configurations with multiple beam-beam interactions, by careful phase advance adjustment.

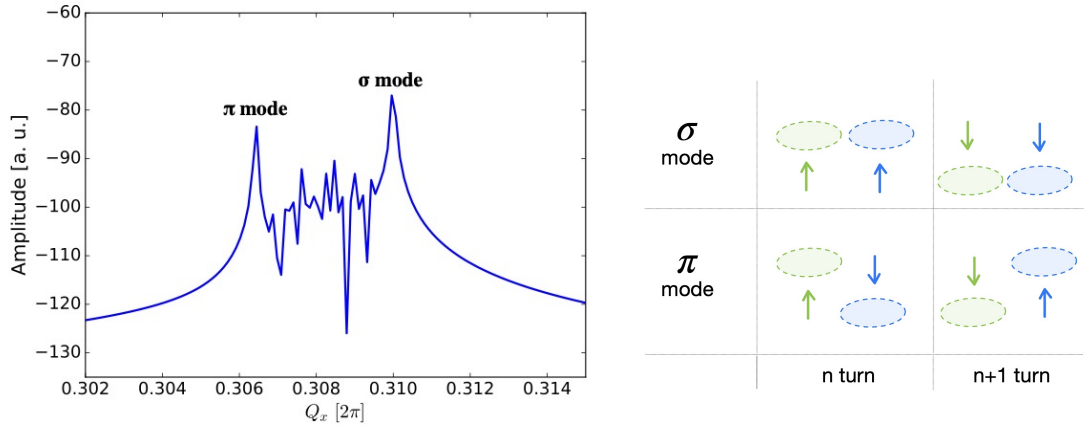

(a) The coherent spectrum

(b) Corresponding coherent modes

Figure 3.6: The coherent spectrum for two colliding bunches (left) with indicated coherent modes and the corresponding scheme of oscillating bunches in the coupled motion (right).

Another effect is the combined result of all the single particle kicks (described with Eq. (3.18)) in a bunch. In the case the symmetry in one of the transverse planes is broken by adding an offset, it results in the effect on the orbit, of the two beams mutually affecting each other centroid positions. This is discussed further in the following Sec. 3.4.1.

Lastly, in the filling schemes that maximize the total luminosity with a high number of bunches, the multi-bunch coupling has to be considered. It is the result of the long-range beam-beam interactions around the IP, within the common vacuum chamber of the IR. This is schematically shown in Fig. 3.7. Depending on the longitudinal spacing between the bunches, there can be up to ~ 30 such interactions around each of the IPs. A single long-range interaction resembles the separation steps considered for the case of separation scans, however, typically larger distances are used $\geq 10\,\sigma$ thanks to the crossing-angle at the IP. Additional interactions cause more coherent modes to be present in the frequency spectrum. The position of these modes also depends on the phase advances between the IPs and bunch properties. Due to the high complexity of this effect, it is only possible to study with COMBI simulation [77]. The introduction of the crossing-angle at the IP causes the coupling between the transverse and longitudinal planes. The beam-beam force varies over the bunch length which can lead to head-tail coupling within a single bunch [80].

3.2.3 Non-linearities

Beam-beam interaction is recognized to be the strongest source of the non-linearities in the collider. However, there are multiple effects that influence motion stability. One of them is the effect of Landau damping that is directly linked to the amplitude detuning described in Sec. 3.2.1. It causes the redistri-

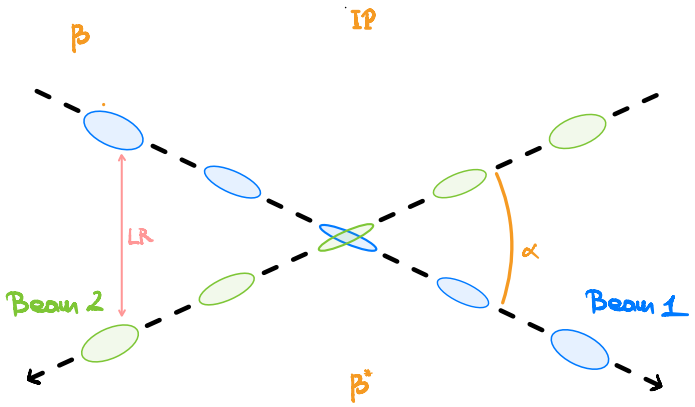

Figure 3.7: The scheme of the beam-beam interactions around the IR - head-on collision at full crossing angle α is shown, with two closest long-range (LR) interactions.

bution of particles within the frequencies of the incoherent spectrum, simply leading to the lack of instability. It is generated due to higher order fields from the beam-beam interaction, but can also be produced with the octupole magnets for particles in the transverse distribution tails. However, it was observed that the beam-beam interaction is significantly more efficient [81]. The stability is affected in the most significant way at small beam separation ($< 1\sigma$). Large tune spread from each collision (high ξ conditions) can cause a particle betatron frequency to cross the resonance condition. The stable motion might no longer be preserved, causing instability. This effect leads to particle losses as well as decoherence, which effectively leads to emittance growth.

As the high current beam propagates through the accelerator lattice it can also interact electromagnetically with the external environment. This effect is referred to as the beam coupling to machine elements impedance. The biggest sources include collimators, cavities, injection kickers, beam screens, and vacuum chambers. Apart from the interaction with electromagnetic fields, the beam can also generate electrons that in a chain reaction lead to the formation of e^--cloud.

3.3 Multi-particle tracking simulation with COMBI

The accurate and precise estimation of the beam-beam effects puts demanding requirements on the numerical models used. Multi-particle tracking approach enables self-consistent treatment providing the accurate description of the single-particle and collective effects. When studying the beam-beam effects for the precise estimation of the effects on luminosity, it is crucial to include the non-linear and multi-particle dynamics. The model can be optimized numerically with approximations for the charge distributions or the electromagnetic fields, which is feasible to limit the computing time and necessary resources.

The COherent Multibunch Beam-Beam Interaction code (COMBI) [77] is a strong-strong model, which describes the two colliding bunches using independent sets of macroparticles. The initial phase space density distributions can be arbitrary, typically the single Gaussian is used. This assumption is a good approximation for most of the studies included in this thesis unless stated otherwise.

The COMBI code uses one-turn map formalism with the possibility of including various actions. The simulation of multiple bunches, or trains within two separate beams is possible, based on the input filling scheme. The LHC arcs are modeled by applying a linear transfer map to the macroparticle coordinates, as shown schematically in Fig. 3.8. The phase advances precomputed by MADX are used, based on the nominal optical configuration used during vdM sessions at the LHC. The code has

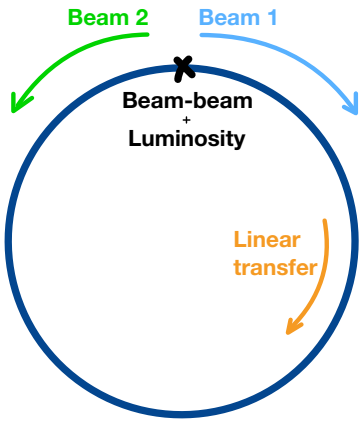

Figure 3.8: The scheme of COMBI actions describing the LHC ring.

been optimized to divide the bunches into separate processes, using the Message Passing Interface (MPI) [82]. CPU-extensive actions, for example, the luminosity calculation, also use the second level parallelization using OpenMPI [83, 84, 85]. These optimizations are implemented in a way that the interactions between bunches are possible. The beam-beam interaction can be included in the code by calculating the source field in multiple ways:

- using transverse phase space (x, p_x, y, p_y) as described in Chapter 3 (4D), with the so-called 'soft-Gaussian' approximation, which assumes Gaussian bunch distribution with variable parameters. This model does not include a description of the longitudinal plane. It is enough for most of the vdM-related studies, excluding the ones including the crossing-angle.
- using full 6D phase space $(x, p_x, y, p_y, z, \frac{dp}{p})$, implemented originally for studies of the mode

coupling instabilities. In this model, each particle coordinates are Lorentz boosted from the laboratory to a reference frame in which the crossing-angle appears cancelled. Next, the particle distributions are divided into slices along the length of each bunch. The kick experienced by each macroparticle in one beam is computed based on the statistical moments of the charge distributions in each slice of the opposing bunch [80]:

$$\begin{aligned} x^*_{\mathrm{BB}} &= x^* + S_z F^k_x(S_x, S_y, S_z), \qquad p^*_x = p^*_x - F^k_x(S_x, S_y, S_z), \\ y^*_{\mathrm{BB}} &= y^* + S_z F^k_y(S_x, S_y, S_z), \qquad p^*_y = p^*_y - F^k_y(S_x, S_y, S_z), \\ z^*_{\mathrm{BB}} &= z^*, \qquad \frac{dp^*}{p}_{\mathrm{BB}} = \frac{dp^*}{p} - F^k_z(S_x, S_y, S_z), \end{aligned} \tag{3.35}$$

where $(x^*, p^*_x, z^*, \frac{dp^*}{p})$ are the boosted coordinates, and S_z is the distance between the slice collision points and the IP at which (S_x, S_y) describe distances between the macroparticle and slice centroid, and (F^k_x, F^k_y, F^k_z) represent beam-beam integrated force components in each direction for slice k. The inverse Lorentz boost is applied at the end to restore the bunch coordinates. As it is a strong-strong model, the computation is repeated for the macroparticles in the other beam. There are two implementations available for this kick - one with full recalculation of the statistical moments after each slice-slice interaction. And the simplified one for faster calculations, calculates the statistical moments only at the start of the interaction (so-called 'Frozen model'). The transverse kick calculated in this way includes the dependence on the longitudinal position of a macroparticle, as shown in Fig. 3.9. This model was used to simulate vdM scans with crossing-angle and the physics LHC conditions as well as the HL-LHC configuration.

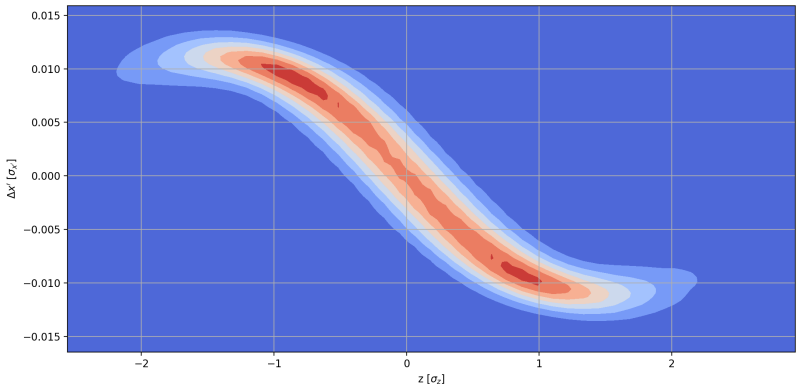

Figure 3.9: Dependence of the beam-beam interaction induced transverse momentum change on the longitudinal position in a bunch. In the example simulation following parameters were used: $\beta^* = 0.3\,\mathrm{m}$, $\xi = 3.3 \times 10^{-3}$, and $\phi = 400\,\mu\mathrm{rad}$

- by calculating the field directly from the charge distribution, using the Hybrid Fast Multipole Method (HFMM) [86]. It is used when the exact frequencies of the coherent modes and the frequencies of oscillations of individual particles in the beam need to be evaluated. For the luminosity-related studies, it was proved to give identical results as the 4D soft-Gaussian approximation [21].

The evolution of bunch parameters is computed turn-by-turn, by recalculating each macro-particle

trajectory, and then updating the field of the source bunch (interaction partner). This self-consistent treatment enables the possibility of studying the coherent beam-beam effects.

3.3.1 Numerical luminosity estimation

The calculation of the luminosity, or more precisely of the overlap integral (Eq. (1.3)), is based on a complete description of the macroparticle distribution in the two colliding bunches - no assumption is made about the transverse shape of the density distributions when evaluating the integral. It is calculated on a turn-by-turn basis, with the positions of all the macroparticles updated at each IP on every consecutive turn. Each step in a beam-separation scan is initialized and simulated separately, but the same simulation run is used for the luminosity normalization when comparing cases with and without the beam-beam interaction. This is necessary to remove the random seed error from the estimation of the beam-beam-induced changes.

The transverse distribution of the macroparticles, called $H^B_{x,y}$, is discretized, separately for the two beams B ($B = 1,2$), on a two-dimensional grid in the x-y plane. The number of cells in each grid is given by $N_{\text{cells}} = n \times m$, where n and m represent the number of bins in the x and y directions respectively. The grid boundaries are located at a distance $k_i \times \sigma^0_i$ ($i = x, y$) from the center of the grid, where σ^0_i is the initial, unperturbed nominal transverse beam size inferred from the input emittance and β^* values in the i plane; the scale factor k_i is typically set to 12 in both the positive and the negative direction along the x and y axes. The cell area is thus given by

$$\Delta S = \Delta x \times \Delta y = 2k_x\sigma^0_x/n \times 2k_y\sigma^0_y/m\,.$$

The separation between the two beams is taken into account when filling two-dimensional histograms of the macroparticle distributions.

With these definitions, the discretized macroparticle density distribution is given by:

$$h^B_{x,y} = \frac{H^B_{x,y}}{N_{\text{part}}\,\Delta S}\,,$$

where N_{part} is the total number of tracked macroparticles. The overlap density of the two bunches, i.e. the density distribution product in Eq. (1.3), is therefore represented by:

$$\lambda_{x,y} = h^1_{x,y} h^2_{x,y}\,.$$

The bunch luminosity can be calculated from the overlap integral I_{2D} as in Eq. (1.4):

$$\mathscr{L}_{\text{b}} = K \times N_1 N_2 f_{rev} I_{\text{2D}}, \tag{3.36}$$

where N_1 and N_2 are the bunch populations, and f_{rev} the revolution frequency, and kinematic factor $K = 2$ in the head-on configuration. The overlap integral is estimated by the two-dimensional trapezoidal method, with simplified integration in the longitudinal plane, assuming Gaussian distribution:

$$\begin{aligned} I_{\text{2D}} \quad = \quad & \frac{1}{2}\left[\frac{1}{4}\Delta x\Delta y\left(\lambda_{0,0} + \lambda_{m,0} + \lambda_{0,n} + \lambda_{m,n} + 2\sum_{i=1}^{m-1}\lambda_{i,0} + 2\sum_{i=1}^{m-1}\lambda_{i,n} + \right.\right. \\ & \left.\left. 2\sum_{j=1}^{n-1}\lambda_{0,j} + 2\sum_{j=1}^{n-1}\lambda_{m,j} + 4\sum_{j=1}^{n-1}\left(\sum_{i=1}^{m-1}\lambda_{i,j}\right)\right)\right]. \end{aligned} \tag{3.37}$$

The instantaneous luminosity in Eq. (3.36) is calculated at each turn, and the result is averaged over the total number of selected turns. Typically a few hundred turns are necessary for the result to stabilize. The reliability of this method was confirmed by benchmarking it against analytical calculations, with the beam-beam effects turned off.

Figure 3.10 shows the evolution of the σ_{vis} bias as a function of the number of macroparticles used in the simulation. The result converges to within 0.01% of its asymptotic value for 5×10^6 macroparticles. Most of the simulation results presented in this paper are based on 10×10^6 macroparticles per bunch, implying that the results are numerically stable at the 0.001% level.

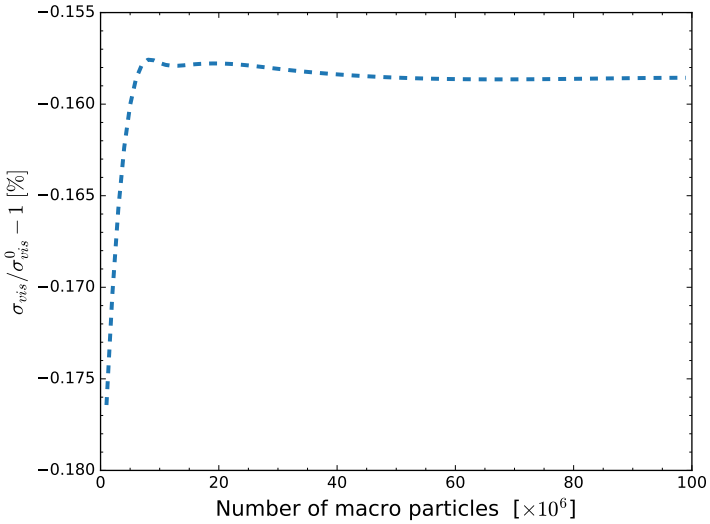

Figure 3.10: Visible cross section bias as a function of the number of macroparticles used to model the transverse-density distributions.

The uncertainty associated with statistical fluctuations in the discretization of the transverse-density distributions was evaluated separately and typically cancels out when computing luminosity ratios. It becomes significant only at large beam separation when the overlap integral is computed from a small number of macroparticles in the tails. At these scan points, however, the luminosity values are very small and therefore have a negligible impact on the estimation of the beam-beam bias factors.

3D integration

The integration in the above section assumes the full overlap of the two bunches in the longitudinal plane with a static distribution over the collision time. However, these assumptions are not valid when examining the effects of the 6D Gaussian kick, especially in scenarios involving a crossing-angle. To account for the overlap dependence on the crossing-angle, and thus coupling to the longitudinal plane, the coordinates of each macroparticle have to be transformed to the correct system. This is done by two rotations as in Eq. (1.18) and it is schematically shown for one of the bunches in Fig. 3.11 for the example crossing plane in $x-s$. The resulting change of overlap symmetry in the transverse planes $x-y$ is also shown, the dimension that includes the crossing-angle dependence is extended. The luminosity can be still evaluated from Eq. (3.36), since the transverse crossing plane includes the dependence on s from the rotation of coordinates, as shown schematically in Fig. 3.12. This integrator was implemented

as it gives a fast solution, but it has limited accuracy and can be used only for high β^* when the changes over collision time can be neglected.

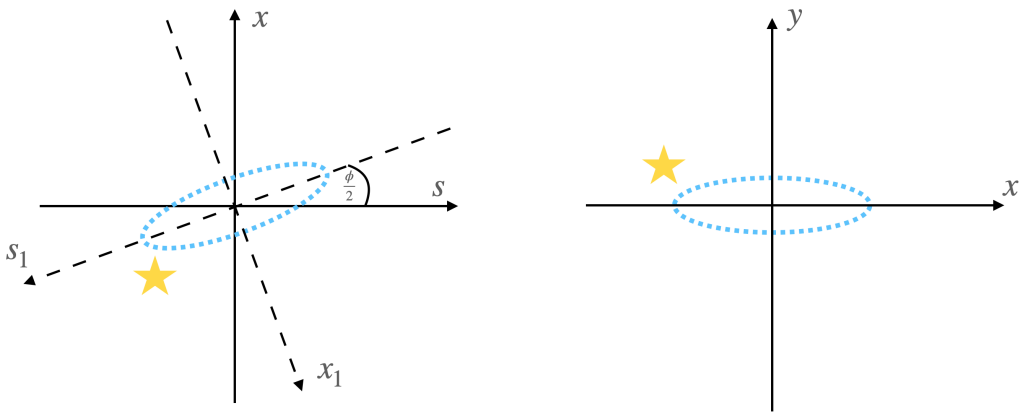

(a) $x-s$ (b) $x-y$

Figure 3.11: Rotation of the bunch coordinates (blue ellipse) in $x-s$ plane (left) by the half-crossing angle $\frac{\phi}{2}$. On the right the elliptical shape in $x-y$ plane is shown resulting from the crossing-angle rotation. The yellow star indicated the head of a bunch.

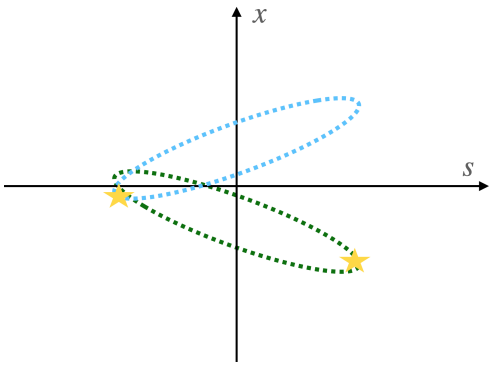

Figure 3.12: Overlap of the two bunches after rotation, in the separated case. The coordinates of the two bunches moving in opposite directions (indicated with starts) are schematically shown with blue and green ellipses.

4D integration

The following algorithm is employed to account for changes in the particle distribution over the collision time. The longitudinal distribution of each of the colliding bunches is divided into multiple slices, their number is denoted as N_s. The collision points (CP) of slice-pairs are then defined at both the centers and the edges of each slice within the distribution. This yields a total of $N_{CP} = 2N_s - 1$, as shown in a schematic example in Fig. 3.13 for the case where $N_s = 5$. The integration is carried out multiple times, separately for each slice-to-slice pair. The slice iteration and matching is conducted

separately at each CP, based on their longitudinal coordinates. This is based on the assumption that at each CP, different slice-to-slice pairs are possible. Similarly, as in the 6D soft-Gaussian kick calculation,

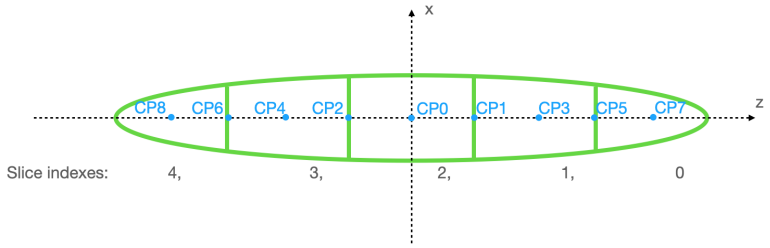

Figure 3.13: Scheme of the bunch distribution divided into $N_s = 5$ slices with their indexes, and the resulting definition of collision points.

the Lorentz boost is applied to the coordinates of each macroparticle in the bunch, moving them from the laboratory to a reference frame moving transversely to the propagation axis of the two bunches [80]:

$$\begin{aligned} x^* &= z\cos\alpha\tan\phi + x[1 + h_x^*\cos\alpha\sin\phi] + yh_x^*\sin\alpha\sin\phi, \qquad p_x^* = \frac{p_x}{\cos\phi} - h\cos\alpha\frac{\tan\phi}{\cos\phi}, \\ y^* &= z\sin\alpha\tan\phi + y[1 + h_y^*\sin\alpha\sin\phi] + xh_y^*\cos\alpha\sin\phi, \qquad p_y^* = \frac{p_y}{\cos\phi} - h\sin\alpha\frac{\tan\phi}{\cos\phi}, \\ z^* &= \frac{z}{\cos\phi} + h_z^*[x\cos\alpha\sin\phi + y\sin\alpha\sin\phi], \\ \frac{dp*}{p} &= \frac{dp}{p} - p_x\cos\alpha\tan\phi - p_y\sin\alpha\tan\phi - h\tan^2\phi, \end{aligned} \tag{3.38}$$

where ϕ is the half crossing angle, α is the angle between the crossing angle plane and the s,x plane, $(x, y, z, p_x, p_y, \frac{dp}{p})$ are the coordinates of the bunch in its own frame, and the Hamiltonians are given by:

$$h = 1 + \frac{dp}{p} - \sqrt{\left(1 + \frac{dp}{p}\right)^2 - p_x^2 - p_y^2},$$

$$h_{x/y}^* = \frac{p_{x/y}^*}{\sqrt{\left(1 + \frac{dp^*}{p}\right)^2 - (p_x^*)^2 - (p_y^*)^2}}, \qquad h_z^* = 1 - \frac{\frac{dp^*}{p} + 1}{\sqrt{\left(1 + \frac{dp^*}{p}\right)^2 - (p_x^*)^2 - (p_y^*)^2}}, \tag{3.39}$$

where notation x/y denotes either of the two transverse planes. In the new reference frame, the crossing-angle between the bunches is cancelled. Consequently, the location of CP is equidistant, defined from the boosted bunch distribution coordinates. To compute the luminosity at each CP, the coordinates have to be further transformed longitudinally to the location of the CP, where the slice-to-slice collision takes place (Fig. 3.14), thus all the other coordinates have to be recalculated. To determine the ranges for the overlap histogram, the extreme coordinates in the distribution are used, a measure taken to optimize the grid per slice. To ensure that the correct slices of the colliding bunches are matched at each collision point and to maintain their respective directions, the slice indexes are employed (from Fig. 3.13). All slice-to-slice contributions are summed up.

The accumulated luminosity from all the collision points gives the total luminosity estimation. It can be evaluated using the same equation (3.36), but using the above described 4D integral that includes

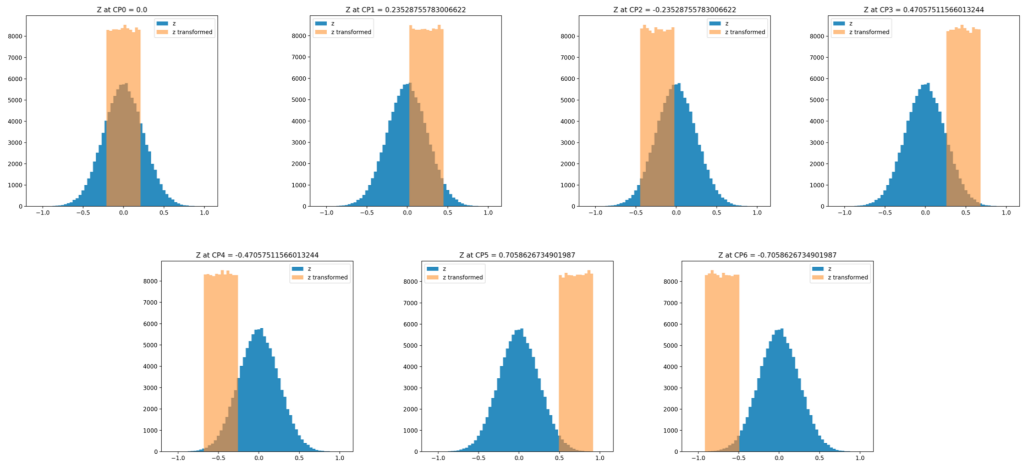

Figure 3.14: Distribution of single bunch longitudinal coordinates (blue) transformed to various CP locations, for $N_s = 5$. The transformed coordinates are shown in orange.

the 2D integral for each slice-slice interaction n_s at all collision points n_{CP}:

$$I_{4\mathrm{D}} = \sum_{n_{CP}}^{N_{CP}} \sum_{n_s}^{N_s} \Delta x_{n_{CP},n_s} \Delta y_{n_{CP},n_s} \sum_{j}^{m-1} \sum_{i}^{n-1} \lambda_{i,j,n_s,n_{CP}}. \tag{3.40}$$

The 4D luminosity integration enables studies related to the luminous region. An example of the separation scan is shown in Fig. 3.15, where the luminosity contributions are shown as a function of distance from the IP. Two cases are shown - without the crossing-angle and with $\phi = 400$ μrad. It is observed that when the angle and separation are present, the main contribution to the total luminosity is displaced from 0. The optimization is made to stop the calculation when the CP luminosity reaches zero contribution. Another optimization is possible to reduce the number of optimal slices if the unequal distribution of CPs is used, with higher density at the core of the distribution.

Another cross-check for the luminosity integrator performance is the observation of the hourglass effect. It is shown in Fig. 3.16 as a function of β^* , compared to the numerical solution of the analytical formula from Eq. (1.28). The geometrical crossing-angle reduction factor S contribution is removed. Again the two cases without and with the crossing-angle in the head-on configuration are considered. In the former, the reduction factor is reproduced already with $N_s = 15$, while for the case with crossing-angle more slices are needed for the precise evaluation.

For the HL-LHC equivalent case with β^* =0.15 m, the optimal performance, with estimation in agreement with analytical prediction, was reached at $N_s = 55$. The full separation scan results are shown in Fig. 3.17. The luminosity calculation can be verified with the analytical prediction for the high β^* =1.5 m case, however, it is not possible in the case of β^* =0.15 m configuration. The presented analytical prediction uses the evaluation of the hour-glass effect only in the head-on configuration, thus the new integrator gives an insight into the hour-glass effect at each separation step.

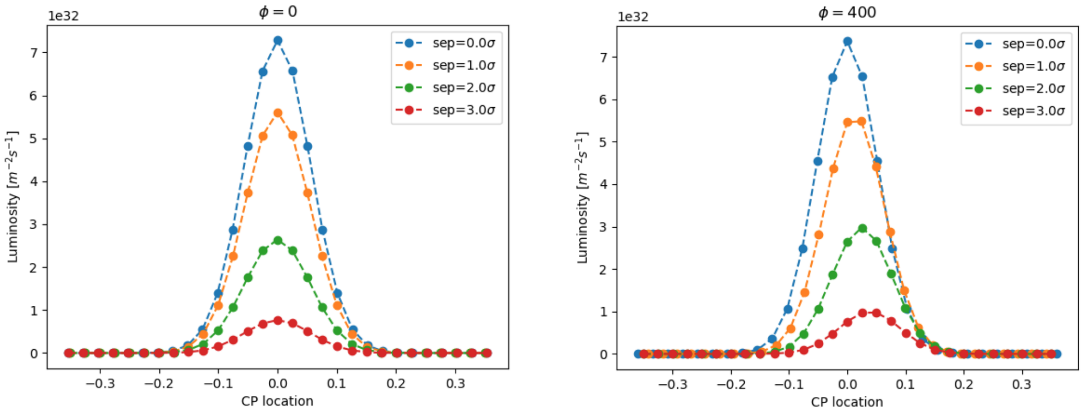

Figure 3.15: Example of luminous region displacement when crossing-angle and separation are present in the same plane (right-hand side), compared to separation with no crossing-angle (left-hand side). Each point is the luminosity calculated at a given CP, in this case $N_s = 15$.

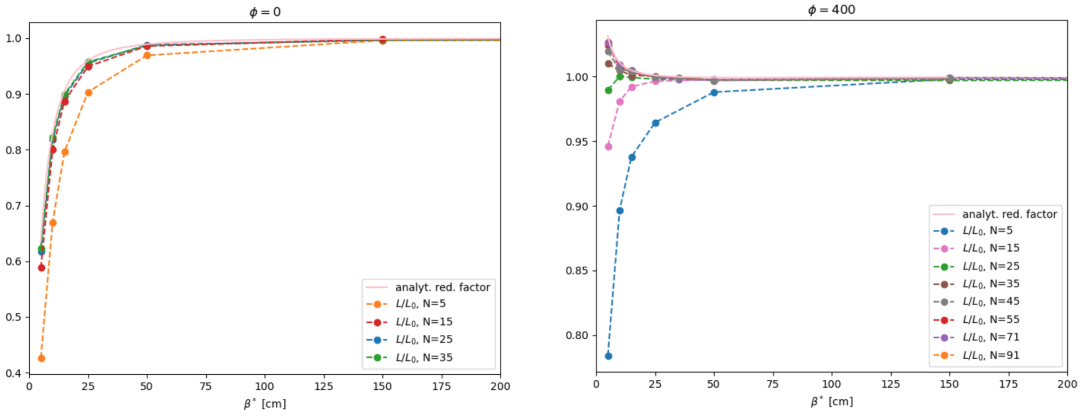

Figure 3.16: Convergence of the luminosity integrator depending on the number of slices towards the analytically predicted hour-glass effect factor (pink continuous line) - for the cases without (left) and with (right) crossing-angle.

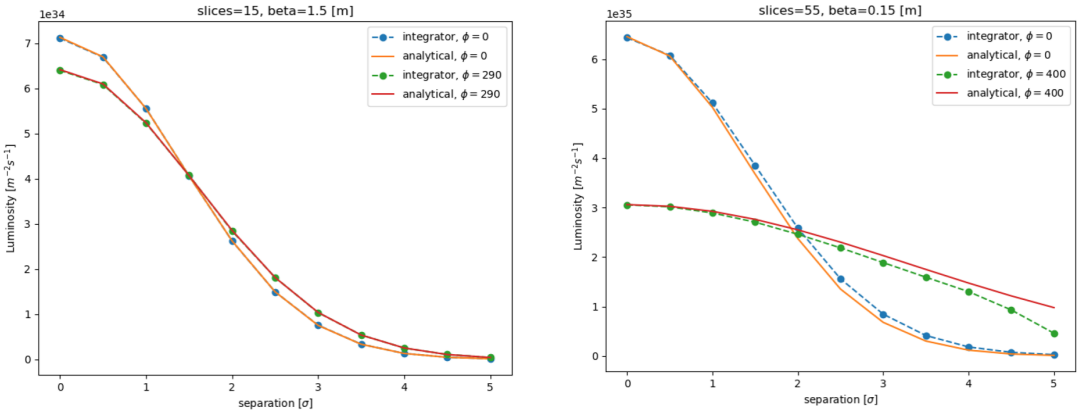

Figure 3.17: Luminosity estimation along the separation steps, for different β^* values and ϕ. The analytical estimation in the right-hand side plot includes the estimation of the hour-glass effect which is only possible at $\Delta = 0$, causing the difference with increasing separation. Only the numerical integration gives accurate results.

3.4 Beam-beam-induced bias on luminosity calibration

It is feasible to study the vdM calibration observables in terms of ratios, as in simulation it is possible to switch the beam-beam kick on and off. Thus, it is possible to estimate the relative effect caused by the beam-beam interaction. In the pursuit of disentangling luminosity bias effects, we employ an approach that hinges upon two separable components: the orbit effect induced by the beam-beam deflection, and the optical distortion. The separation of the full beam-beam effect into these components on the luminosity is shown in Fig. 3.18. In summary, the strategy for mitigating beam–beam-induced luminosity bias effects is anchored in an interplay of analytical calculations and precise simulations. The separate contributions are discussed further in the following sections.

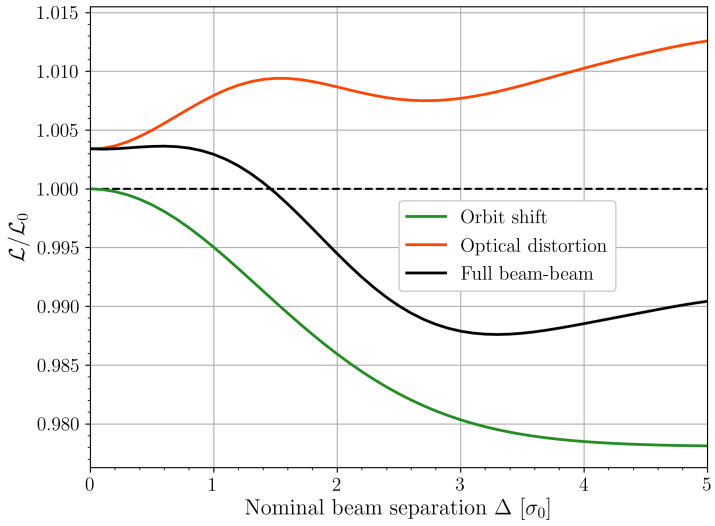

Figure 3.18: Beam-separation dependence, during a simulated horizontal vdM scan, of the luminosity-bias factor associated with the beam-beam orbit shift only (green), the optical distortions only (red), and their combination (black).

In the realm of studying the luminosity bias, the concept of reference normalization finds expression through two distinct yet interconnected terms. The first of these approaches, denoted as $\mathscr{L}_0$, encapsulates the luminosity computation untainted by any influence of the beam-beam interaction. This fundamental value can be derived from the beam parameters including a hypothetical beam size, that with reference to numerical simulations and its input parameters is referred to as σ_0. This approach disregards the presence of any beam-beam-related perturbations at all points within the accelerator.

Conversely, $\mathscr{L}_u$, representing the second approach, introduces a more intricate perspective. Here, the luminosity calculation remains unperturbed by the beam-beam effects at the primary scanning IP, preserving the exclusion of the main beam-beam perturbation. However, in a notable departure from the $\mathscr{L}_0$ methodology, $\mathscr{L}_u$ acknowledges the presence of beam–beam-induced distortions at other IPs within the accelerator. These other IPs are often referred to in the following text as the witness or observer IP. This recognition of beam-beam distortions at the witness IP serves to account for luminosity biases systematically, which is strictly connected to the separation scan. In case the approximation of beam-beam interaction acting as a quadrupole would be true, the additional head-on interactions should change the measured peak and convoluted bunch widths proportionally, without any bias to the calibration. However, as will be shown in Sec. 4.5 this statement does not hold. Additionally, the

$\mathscr{L}_u$ normalization removes the contribution from any numerical noise inherent to the simulation.

It is noteworthy that in cases involving a single IP, $\mathscr{L}_u$ seamlessly converges towards $\mathscr{L}_0$, as there exists no additional IP to introduce BB effects. In this context, the two methodologies coincide, simplifying the luminosity assessment.

3.4.1 Orbit effect

The orbit shift stems from the repulsive kick of the two bunches of the same charge, moving in opposite directions with an offset. It is a measurable effect, as the orbit centroid of each of the two colliding beams is changed in the opposite directions, increasing the distance between them. The precise calculation thereof is possible through analytical means using Eq. (3.15). Adding the information about the source bunch current N and its energy allows to calculate the deflection angle, as was derived in Sec. 3.2.1:

$$\theta_x = \frac{2Nr_0}{\gamma} E_x. \tag{3.41}$$

The deflection-induced offset at the IP increases slightly the beams separation, and can be evaluated from [87]:

$$\Delta_x^{\mathrm{BB}} = \frac{\theta_x \beta_x^*}{2\tan \pi Q_x}. \tag{3.42}$$

The same expressions are valid also in the other transverse plane y. A negligible approximation is made on the unchanged β^* and Q. The total distance between the two beams is then the sum of the nominal separation resulting from steering the beams apart, and the beam-beam interaction-induced offset. The example orbit effect for the vdM conditions is shown in Fig. 3.19, as a function of the increasing nominal beams separation. The calculation was found consistent with measurements [74, 88], although in many cases the absolute deflection amplitude had to be fitted due to the systematic effects. This analytical approach allows us to discern and account for the subtle effect on the orbit, for standard vdM conditions in the order of a few μm. However, it has an influential effect of reducing the observed luminosity (according to Eq. 1.12), which results in a significant correction of 1-2%.

3.4.2 Optical effect

Optical distortion arises from the electric field-induced changes in the particle distribution of each of the beams, resulting in a modified overlap integral. In the first approximation, with the linearized force, it can be described as the dynamic-β change at the IP after propagation throughout the magnetic lattice:

$$\frac{\beta^*}{\beta_0^*} = \frac{1}{\sqrt{1 - 4\pi\xi\cot(2\pi Q) - 4\pi^2\xi^2}}. \tag{3.43}$$

It is shown in dependence of a transverse tune Q in Fig. 3.20 for the typical vdM and physics operation beam-beam parameters. The LHC colliding horizontal tune is marked with the blue dashed line indicating the decrease in β^* which results in the focusing of the observed beam size. In case another tune configuration was used with $Q < \frac{\pi}{2}$, the net effect would be the increase, meaning defocusing. It is also worth emphasizing that a set-point close to $\frac{\pi}{2}$ gives a small change in β^* with any tune shifts (independently on the cause) due to the flattening gradient visible in Fig. 3.20. The dynamic-β effect is non-static as the beams collide at varying transverse separation, and the force cannot be described with ξ.

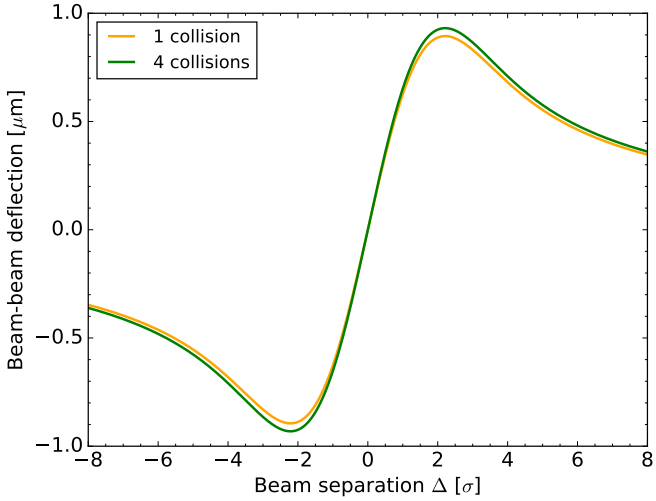

Figure 3.19: Single beam orbit displacement resulting from the beam-beam interaction as a function of total beams separation in the units of beam size σ. The single collision case is compared to the case with additional tune shift corresponding to four collisions, in the vdM conditions are shown with $\xi = 4 \times 10^{-3}$.

The effect on the witness beam particles has to be evaluated taking into account not only the distance between the distribution centroid (point-like treatment), but also taking into account the amplitude of a particle within the bunch distribution. The complete effect is known as the amplitude-dependent beta-beating. This is graphically shown in Fig. 3.21 - the two Gaussian distributions are shown with one of them placed at the example 3σ distance. The force gradient in the separation plane (defined in Eq. (3.28), here denoted with k_x) is shown along the distributions. It is clear that each of the particles within the distribution probes a different part of the force, and it is different for the two transverse planes. It is worth emphasizing that the beam-beam force includes the coupling terms for the transverse planes when the full dynamics is considered, and these are not present in the linear approximation. The optical effect manifests itself in the transverse shape and the resulting size of the beam being notably altered in a non-linear fashion. This effect can be studied by means of simulation, for example, COMBI [77], B*B [89], and XSUIT [90] models.

Detuning with amplitude

As a bunch is composed of single particles with a given spatial distribution that is not point-like, each of the particles probes different part of the non-linear beam-beam force depending on its amplitude in the distribution, according to Eq. 3.16. This is shown in the example scheme in Fig. 3.21, where the gradient of the force from the source bunch k_x in the scanning direction is shown for the particles within the transverse bunch distributions of the witness bunch at head-on collision and at 3σ separation. It is clear that different parts of the distributions are affected in a non-linear, amplitude-dependent manner. Additionally, assuming the separation is present in a single transverse direction, some of the particles can probe oppositely signed parts of the force in the two transverse directions. The average effect on the bunch RMS width can be approximated with point-like treatment with a linear model, the example is shown in the following Sec. 3.5.3. However, if the two distributions shown in Fig. 3.21 are treated as

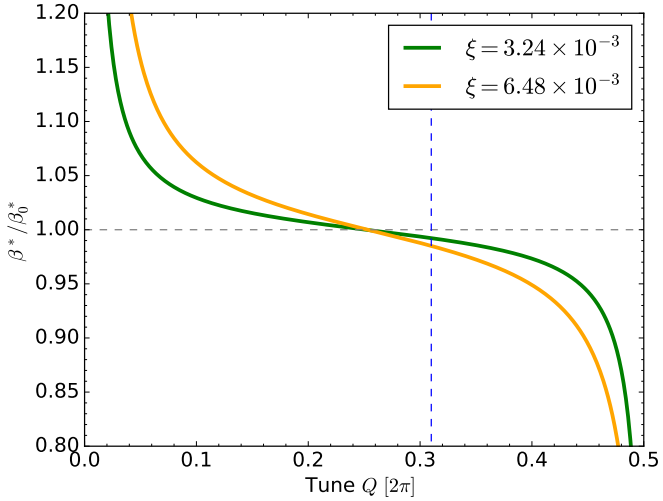

Figure 3.20: Change in β^* as a function of the machine tune Q, for two example beam-beam parameters ξ.

belonging to opposing bunches, the maximum contribution to the overlap area is found at $\Delta/2$. Thus, the effect on σ is not representative of the final effect on luminosity. Comparisons of models using different approaches of estimating the beam-beam effects on the luminosity are shown in the next section (see Fig. 3.26).

Simplified solutions of Eq. (3.26) can be found for a zero-amplitude particle in a head-on configuration. The resulting β-beating in each transverse plane, averaged over the particle distribution assumed to be Gaussian results in:

$$\frac{\overline{\Delta\beta}}{\beta} \approx 0.633 \frac{\Delta\beta_0}{\beta}, \tag{3.44}$$

where $\Delta\beta_0$ describes the linear beating (at $J_x = J_y = 0$). Combining the beating of the same magnitude in the two transverse planes gives the estimation of the relative impact on the luminosity:

$$\frac{\Delta L}{L} \approx -\frac{1}{2}\frac{\Delta\beta_0}{\beta}. \tag{3.45}$$

In the vdM conditions, the effect is the increase in luminosity, in the order of 0.5-1%. The negative correction can be applied at each separation step to remove this beam-beam induced component.

3.4.3 Observables relevant for vdM-calibration

As discussed in Sec. 1.2.1, the calibration constant σ_{vis} is a detector-specific value measured in the dedicated vdM scans. Without knowledge about the specific luminometer system, it is impossible to study it in terms of absolute value. Therefore, in the following sections, the beam-beam-induced bias is always presented in the relative form, so that it can be applied to any luminometer. It is based on the proportionality of the σ_{vis} to the observables:

$$\sigma_{\text{vis}} \sim \mu_{pk}\Sigma_x\Sigma_y. \tag{3.46}$$

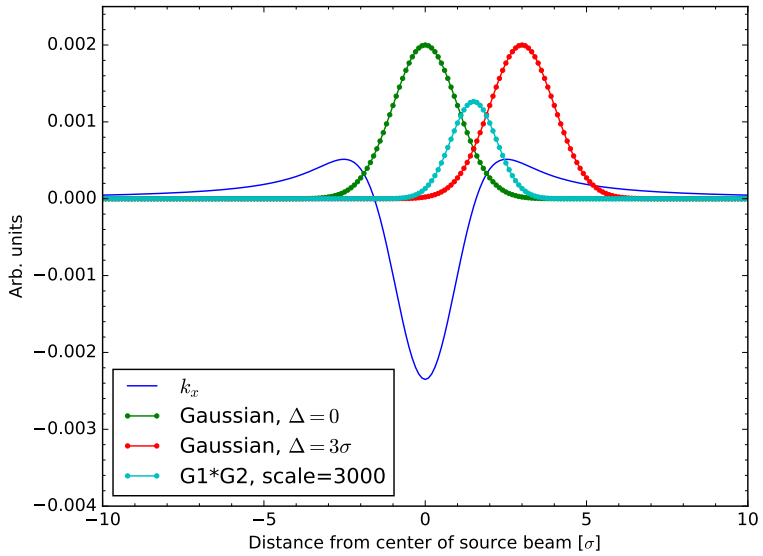

Figure 3.21: The beam-beam force gradient k_x (dark blue) as a function of the distance from the center of the source beam. Two Gaussian distributions are shown with means at different distances - at head-on collision (green) and at 3σ separation (red), and $G1 * G2$ represents their product (light blue).

This formula is equivalent to Eq. 1.16, skipping the constant values. The Σ_x, Σ_y can be calculated with the vdM-method, as in Eq. 1.14, based on the luminosity calculated analytically as defined for Gaussian distribution in Eq. 1.12 or numerically for any particle distribution. However, μ_{pk} is not accessible in analytical models, but the proportionality to the luminosity (Eq. 1.17) can be used to obtain the fundamental relationship between σ_{vis} , and the beam-separation dependence of the luminosity or measured collision rate [24, 25]:

$$\sigma_{\text{vis}} \sim \frac{1}{\mathscr{L}(0,0)} \int \mathscr{L}(x,0)dx \int \mathscr{L}(0,y)dy. \tag{3.47}$$

The constant factors are omitted. This allows defining the relative σ_{vis} bias, caused by the beam-beam-induced changes to the luminosity:

$$\frac{{\sigma_{\text{vis}}}^{\text{BB}}}{{\sigma_{\text{vis}}}^{0}} = \frac{\mathscr{L}_0(0,0)}{\mathscr{L}_{\text{BB}}(0,0)} \frac{\int \mathscr{L}_{\text{BB}}(x,0)dx \int \mathscr{L}_{\text{BB}}(0,y)dy}{\int \mathscr{L}_0(x,0)dx \int \mathscr{L}_0(0,y)dy}, \tag{3.48}$$

where subscript 0 denotes the reference value, and BB indicates the inclusion of the beam-beam interaction under study. This expression allows to derive corrections directly on the visible cross section, but its components can be also used separately to study contributions from the change at the peak and to the convoluted bunch widths.

3.5 Transfer Matrix model

A linear model based on transport matrices can be used to study qualitatively the beam-beam effects on the vdM calibration. The one-turn analytical model was built for a synchrotron magnetic lattice with the beam-beam interactions included [73, 91]. The coherent beam-beam kick has been extended to account for interactions with an offset [77]. The resulting one-turn matrix has been generalized to evaluate the effect on $\mathscr{L}_{inst}$ and σ_{vis} .

3.5.1 Beam-beam interaction

To obtain global properties for a Gaussian distribution of particles going through the beam-beam force of the counter-rotating beam the coherent beam-beam kick is used in the transport matrix. The description of that interaction for a Gaussian particle distribution is obtained from Poisson's equation, by integrating the single-particle kicks over the transverse-density distribution of the source beam:

$$\begin{aligned} k_s(u) &= -\frac{2Nr_p}{\gamma}\frac{e^{-u^2/4\sigma^2}}{2\sigma^2u^4}\left(u^4 - 2u^2\sigma^2(e^{u^2/4\sigma^2}-1)\right) \\ k_{non-s}(u) &= -\frac{2Nr_p}{\gamma}\frac{e^{-u^2/4\sigma^2}}{2\sigma^2u^4}\left(2u^2\sigma^2(e^{u^2/4\sigma^2}-1)\right), \end{aligned} \tag{3.49}$$

where $u = x$ or y, and k_s (k_{non-s}) refer to the kick in the scanning (non-scanning) plane during a separation scan. These formulas represent the averaged kick received by all particles in the witness bunch and can be used as an approximation of all single-particle interactions [91]. The comparison of the effect of a coherent kick in the scanning direction to the single-particle (incoherent) kick (as in Eq. 3.18) as a function of the separation of the beams is shown in Fig. 3.22. The ratio of the two is also plotted, which shows that the effect from the coherent kick is approximately twice smaller than the effect estimated using the incoherent one.

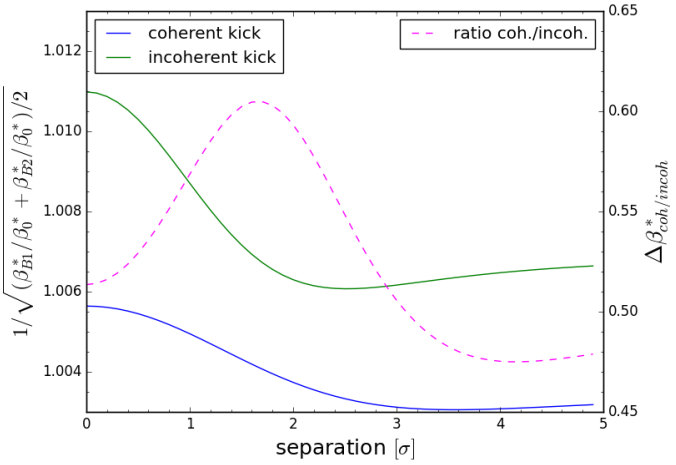

Figure 3.22: The luminosity-equivalent effect on β^* (left-side axis) in the scanning direction as evaluated from the coherent and incoherent beam-beam kicks. On the right-hand axis, the ratio of the magnitudes of the two kicks is shown.

3.5.2 vdM transfer matrix model

The full turn matrix is built from Eqs. (3.2), (3.3) and (3.7) in an example configuration with two collisions at different locations around the ring (2 IPs). The dynamic of a single beam in one of the transverse directions at the interaction point is described by:

$$\begin{pmatrix} \cos 2\pi(Q+\Delta Q) & \beta^* \sin 2\pi(Q+\Delta Q) \\ -\frac{1}{\beta^*} \sin\, 2\pi(Q+\Delta Q) & \cos 2\pi(Q+\Delta Q) \end{pmatrix} = \\ \begin{pmatrix} 1 & 0 \\ -k & 1 \end{pmatrix} \begin{pmatrix} \cos\mu_1 & \beta_0^* \sin\mu_1 \\ -\frac{1}{\beta_0^*} \sin\mu_1 & \cos\mu_1 \end{pmatrix} \begin{pmatrix} 1 & 0 \\ -k & 1 \end{pmatrix} \begin{pmatrix} \cos\mu_2 & \beta_0^* \sin\mu_2 \\ -\frac{1}{\beta_0^*} \sin\mu_2 & \cos\mu_2 \end{pmatrix}, \tag{3.50}$$

where β_0^*, β^* are the original and new beta-function at the IP, and ΔQ is the total change in tune. The phase advances in the two sections of the ring are μ_1, μ_2, between each of the interactions described with the gradient k.

3.5.3 Dynamic-beta and tune shift

The resulting beta-beating depends on the total number of collisions, their strength, and the associated tune shift. At the scanning IP, in the example case of the 2-IPs configuration, it is given by:

$$\frac{\beta^*}{\beta_0^*} = \frac{\sin 2\pi Q - k_0 \beta_0^* \sin 2\pi\mu_1 \sin 2\pi(Q-\mu_1)}{\sin 2\pi(Q+\Delta Q)}, \tag{3.51}$$

with phase advance μ_1 between the two IPs, and k_0 denoting the coherent kick caused by head-on collisions at the non-scanning IP. The formula contains an explicit dependence on the phase advance between the two IPs. The tune shift for the configuration with a single collision ΔQ^w is obtained from the eigenvalues of the one-turn matrix:

$$\cos 2\pi(Q+\Delta Q^w) = \cos 2\pi Q - \frac{k_0 \beta_0^*}{2} \sin 2\pi Q. \tag{3.52}$$

With an additional collision at a different location, the expression is recalculated. In the case of a scanning IP in transverse plane u, the beam-beam interaction impact is different in the scanning and in the non-scanning plane, as $k(u)$ depends on the plane of interest (Eq. 3.49).

$$\cos 2\pi(Q+\Delta Q^{w+s}) = \left(1 - \frac{k(u)k_0(\beta_0^*)^2}{4}\right) \cos 2\pi Q \\ -\frac{\beta_0^*}{2}(k(u)+k_0) \sin 2\pi Q + \frac{k(u)k_0(\beta_0^*)^2}{4} \cos 2\pi(Q-2\mu_1). \tag{3.53}$$

While the expression 3.52 is independent of the phase advance between the IPs, it is introduced with the second beam-beam interaction in 3.53. In the latter case, a slight modulation of the tune shift ΔQ^{w+s} is present with a half-period (π) that depends on the phase advance μ_1 between the IPs and the strength of both collisions. It is compared in Fig. 3.23 to the case of a single head-on collision, that produces a constant tune shift.

This tune shift is propagated to the beta-beating, according to Eq. 3.51. The additional phase-dependent term causes the ratio of the beam envelope changes to be non-constant when different numbers of collisions are compared. The combined effect of the two beams, expressed in a form that contributes

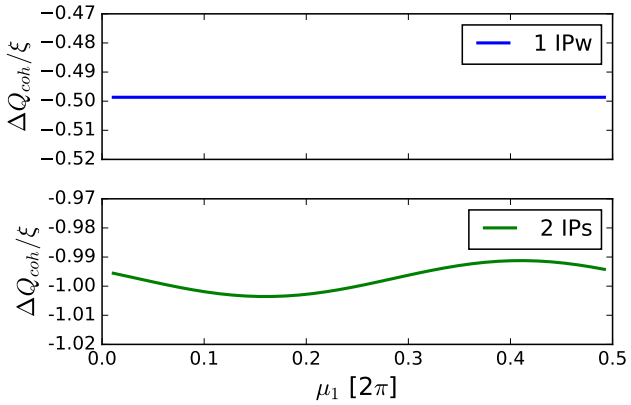

Figure 3.23: Beam–beam tune shift caused by a single (1 IPw) and by two (2 IPs) head-on collisions, as a function of the phase advance between the two collision points.

to the convoluted beam width is shown in Fig. 3.24. The beating as observed at a given location, from a single collision at another location appears in phase with the 2 IPs configuration. In the ratio, however, an additional, residual phase dependence becomes apparent. The dependence of a beam width σ changes over a separation scan is additionally presented in Fig. 3.25, compared to COMBI simulations for a Run-2 nominal lattice, showing a very good agreement.

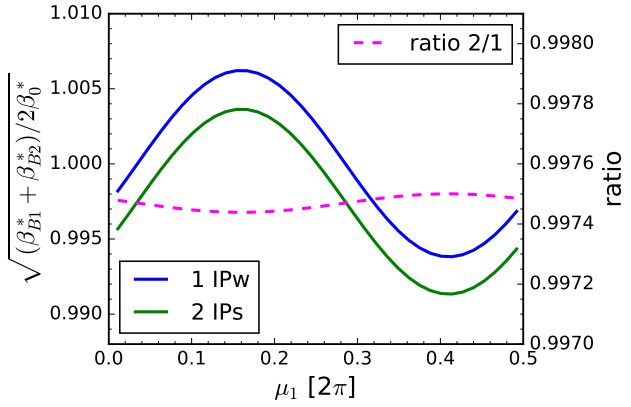

Figure 3.24: Combined β-beating of two beams for head-on collisions, as a function of the phase advance between the two IPs, as measured at the scanning IP. Shown for collisions at the non-scanning IP only (1 IPw), and for collisions both at the non-scanning IP and at the scanning IP (2 IPs).

3.5.4 Luminosity

The obtained beta-beating as well as the calculated orbit shift Δ^{BB} (Eq. 3.15) are subsequently used to estimate the full beam-beam induced bias on the luminosity at each separation step using the Gaussian-beams approximation (Eq. 1.12). The effect on the convoluted beam width cannot be calculated directly, as it includes beta-function changes from each of the beams separation steps:

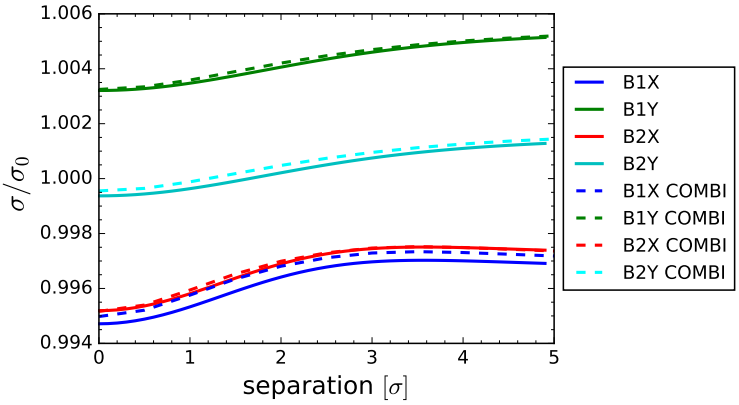

Figure 3.25: Beam-separation dependence of the dynamic-beta effect, calculated analytically (solid curves) and simulated using COMBI (dashed lines).

$$\Sigma_x \sim \sqrt{\sigma^2_{x,B1}(0,0)+\sigma^2_{x,B2}(0,0)}\sqrt{\sigma^2_{y,B1}(0,0)+\sigma^2_{y,B2}(0,0)}\int_{-\infty}^{\infty}\mathscr{L}(\Delta_x,0)d\Delta_x, \tag{3.54}$$

where each of the bunch widths includes the calculated head-on β-function change $\sigma^2(0,0) = \Delta\beta^*/(0,0)\sigma_0^2$. The same expression holds for Σ_y, with integral over the luminosity $\mathscr{L}(0,\Delta_y)$ from the scan in the corresponding plane. The luminosity in the integral is calculated from:

$$\begin{aligned}
\mathscr{L}(\Delta_x,0) &\sim \frac{W\left(\Delta_x+\Delta^{\mathrm{BB}}_{x,B1}+\Delta^{\mathrm{BB}}_{x,B2},\sqrt{\sigma^2_{x,B1}(0,0)+\sigma^2_{x,B2}(0,0)}\right)}{\sqrt{\sigma^2_{x,B1}(\Delta_x,0)+\sigma^2_{x,B2}(\Delta_x,0)}\sqrt{\sigma^2_{y,B1}(\Delta_x,0)+\sigma^2_{y,B2}(\Delta_x,0)}} \\
\mathscr{L}(0,\Delta_y) &\sim \frac{W\left(\Delta_y+\Delta^{\mathrm{BB}}_{y,B1}+\Delta^{\mathrm{BB}}_{y,B2},\sqrt{\sigma^2_{y,B1}(0,0)+\sigma^2_{y,B2}(0,0)}\right)}{\sqrt{\sigma^2_{x,B1}(0,\Delta_y)+\sigma^2_{x,B2}(0,\Delta_y)}\sqrt{\sigma^2_{y,B1}(0,\Delta_y)+\sigma^2_{y,B2}(0,\Delta_y)}},
\end{aligned} \tag{3.55}$$

where W is the reduction factor from Eq. 1.13, and the bunch width in the denominator includes the separation dependent β^* -change. The propagated luminosity bias is shown in Fig. 3.26b, denoting the difference in results when beam-beam interaction is included with reference to no beam-beam kick present. Comparison to COMBI is shown, where the density profiles are described with macro-particles that receive an amplitude-dependent kick, and the resulting overlap is more accurately evaluated. A cross-check for the luminosity calculation was done in the single collision configuration, a comparison to COMBI and MADX is shown in Fig. 3.26a. It is clear that the model works well at the head-on step, where the beam distribution cores are in full overlap. It diverges from COMBI calculation with separation, when the luminosity is a product of the tail particles.

Based on Eq. (3.48) the bias on σ_{vis} is evaluated and is shown in Fig. 3.27. The absolute value differs from the one defined by COMBI, in Fig. 4.23, which is discussed in the following Chapter 4.5, due to approximations used in the calculation, that are valid only in the Gaussian-bunch limit. This inconsistency is a direct result of the significant differences presented in Fig. 3.26b, which are unavoidable in the analytical calculation, and are not aimed at reproducing the COMBI results completely. To improve the results, the linearized model would have to be extended with a beam-beam kick description more appropriate for particles in the tails of beam distribution, that determine the luminosity bias at high

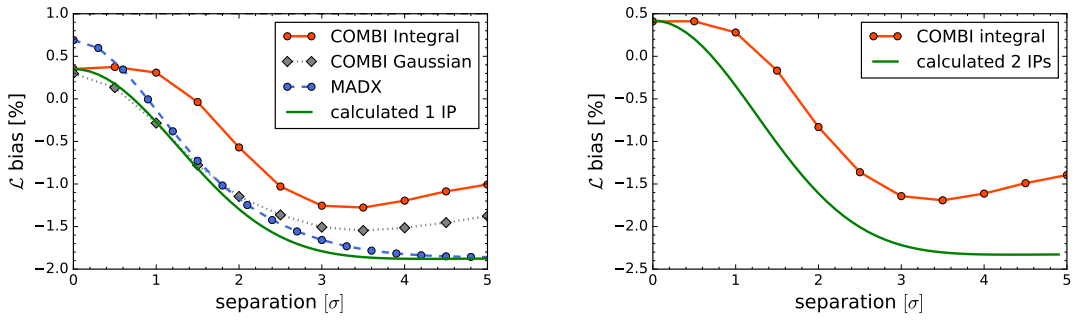

(a) 1 IP

(b) 2 IPs

Figure 3.26: Beam-beam bias on the luminosity as a function of separation as calculated using the Gaussian distribution-based luminosity formula compared to COMBI and MADX simulations in the single IP (3.26a) and 2 IPs configurations (3.26b).

beam separation. Nevertheless, it is shown that the σ_{vis} periodicity with phase advance can be reproduced. The multi-IP tune shift dependence on the phase advances, and hence also the beta-beating, scales with the non-linear beam-beam kick at each separation step. This effect does not vanish in the integrated bias over a full separation scan, moreover, no phase advance configuration cancels it completely.

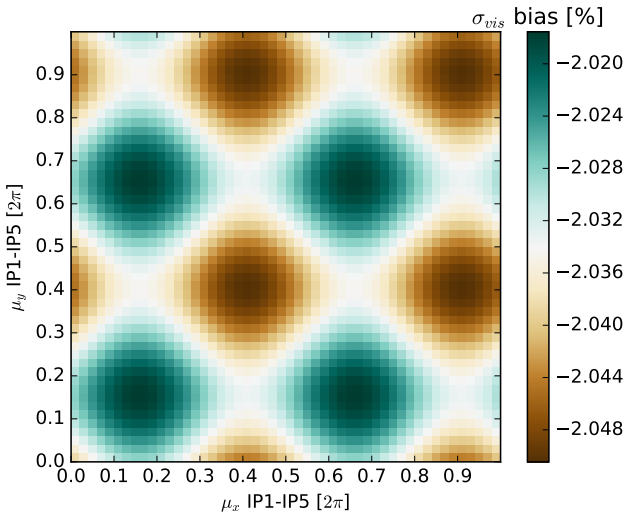

Figure 3.27: Bias on σ_{vis} as a function of phase advances between the two IPs, as obtained analytically.

Conclusions

Analytical calculations are essential in the qualitative understanding of the underlying phenomena of the beam-beam-induced biases. Whereas the impact on beam size is reproduced very well, the linear

approximation oversimplifies the impact on the luminosity for separated beams. Therefore, the impact on the visible cross section cannot be evaluated accurately in this way. Thus, tracking simulations are needed with numerical luminosity estimation to obtain accurate results. This approach (introduced in Sec. 3.3) is employed in the next sections.

4 Beam-beam-related systematic effects in vdM calibration

The LHC particle-physics program requires that the delivered luminosity be measured to an absolute accuracy in the 1% range. To this effect, the absolute luminosity scale at each interaction point (IP) is calibrated by scanning the beams across each other according to the van der Meer method. During such scans, the systematic effects have to be studied in detail, and corrected. One of the most significant beam-related systematic effect is caused by the beam-beam interaction. The orbit and the shape of the colliding bunches are significantly distorted by their mutual electromagnetic interaction; the resulting biases, if left uncorrected, would absorb a major fraction of the systematic uncertainty budget on the luminosity calibration.

This chapter starts with describing typical beam conditions during a vdM calibration session. Further, a summary of the recent studies of such biases in the single-IP configuration is presented, laying the groundwork for the subsequent exploration of beam-beam interaction-related investigations. In the following sections, the beam-beam interaction-related studies are presented based on the simulations carried out with the COherent-Multibunch Beam-beam Interaction multiparticle code (COMBI). Firstly, the generalization of the single-IP parametrization is discussed in the more typical case where bunches collide not only at the scanning IP but also experience additional head-on encounters at up to 3 locations around the ring. The scaling law is derived that relates the multi-IP case to the simpler and better-understood single-IP configuration. Thus, allowing for the correction of the multi-collision beam-beam effects in the vdM calibrations. Further, studies related to the crossing-angle presence during vdM calibrations and related systematic uncertainty are discussed. Lastly, the dependence of beam–beam-induced luminosity-calibration biases on the phase advance between the interaction points is characterized. The other sources of the beam-beam interaction induced systematic uncertainties are considered in Sec. 6.4 for the case of 2022 calibration.

4.1 Beam conditions

The operational conditions for the vdM calibration differ significantly from the standard physics data-taking conditions. The beam parameters have to be optimized, in order to minimize the luminometer and beam systematic effects. The main requirements are: Firstly, the beams have to be as stable and factorizable as possible. The long-range beam-beam interactions are avoided by separating the bunches longitudinally, typically to 525 ns. In this way, there is only a single bunch pair present in the common vacuum chamber of the experimental area at a given time. This creates a limit to the maximum number of bunches that can fit of approximately 150, based on the limited LHC length of almost 27 km. Moreover, this setup eliminates the need for the crossing angle at the IP, hence removing the associated systematic effects. However, at IP2 and IP8 the crossing-angles are always present. The beam size at the IP is increased with a large β^* value to increase the transverse luminous region, allowing for a precise luminosity measurement at each beam separation. This adjustment also provides a lower pile-up for the luminometers, close to 0.5, diminishing the impact on the calibration from the intrinsic detector non-linearities. The per-bunch charge is significantly reduced, to limit the beam-beam effects and the background contribution to the detector signal. The beam-beam effects can also be diminished by increasing the beam emittance from the injector chain. It is crucial for the beam to be well bunched, with minimized fractions of satellite charge around the bunch, and ghost charge in the orbit.

In Table 4.1 the LHC parameters are summarized, typical for the vdM sessions. The reference parameter set is shown, which is used in most of the COMBI simulation results shown in the following sections unless specified otherwise. In some examples, the intensity or emittance is adjusted to scan a wider range of the beam-beam parameter. This set is compared to the typical parameters present in the LHC Run 2 and Run 3 vdM calibrations.

	vdM reference parameter set	LHC Run 2	LHC Run 3 (2022, 2023)
E_B [TeV]	6.5	6.5	6.8
N_p/bunch	7.8×10^{10}	$0.7 - 1.0 \times 10^{10}$	$0.7 - 1.0 \times 10^{10}$
β^* [m]	19.2	19.2	19.2
ϵ_n [μmrad]	3.0	$2.2 - 3.5$	$1.8 - 2.9$
ξ	3.2×10^{-3}	$2.2 - 5.6 \times 10^{-3}$	$2.9 - 5.5 \times 10^{-3}$
Q_x, Q_y	63.310, 60.320	64.310, 59.320	64.310, 59.317

Table 4.1: Beam and machine parameters for the vdM scans, the reference COMBI parameter set is shown compared to LHC Run 2 [21] and Run 3 conditions.

4.2 Correction model

If the beam-beam-induced bias on luminosity is left uncorrected, it can have a significant impact on the calibration results. The difference with respect to an example Single Gaussian (SG) fit (as in Eq. (1.11)) as estimated from the COMBI simulation is shown in Fig. 4.1. Differences between the horizontal and vertical residuals come from the differences in betatron tunes applied, which reflect the LHC case.

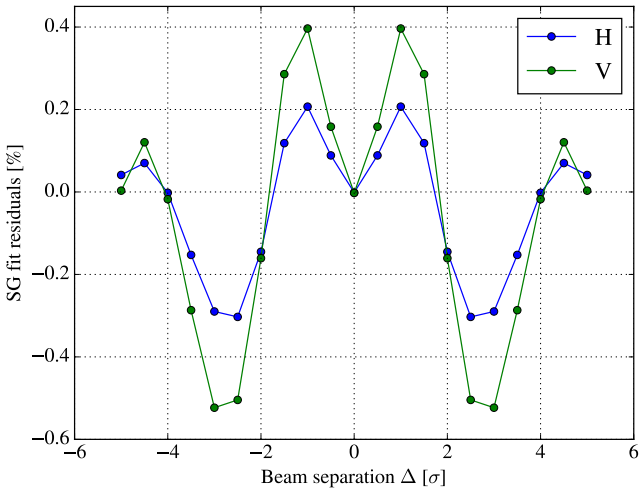

Figure 4.1: Single Gaussian fit residuals, calculated as the difference between the COMBI simulated luminosity to the fitted Gaussian curve. The residuals are shown separately for the scan in horizontal (blue) and vertical (green) directions.

The beam-beam effects correction procedures have been specifically developed to account for the two distinct ways in which the BB interaction affects vdM-based luminosity calibrations: deflection-induced orbit shifts, and optical distortions including the dynamic-β effect, as described in details in Sec. 3.4. The latter can be observed on the transverse-beam profiles, which are distorted in a separation-dependent manner, and therefore affect all observables: μ_{pk}, Σ_x, and Σ_y. The first dynamic-β model [92] was developed to describe the beam-beam-induced distortion during separation scan in a non-static manner. It used the approximation of the beam-beam to a magnetic element, the quadrupole, that can be compared to the phase change and optical error in β^*. It has been extended in [89, 21] to account for the amplitude-dependent nature of the beam-beam effects and the resulting modification of the overlap integral due to the distorted beam shapes. As it was aiming at obtaining high-precision corrections, the overlap integral that defines the luminosity needed to be computed numerically without the assumption of the particle distributions. The polynomial parametrization of the beam-beam effects was derived with the aim of applying per-bunch corrections at any conditions. This is useful in vdM calibration as typically the order of 100 bunches is used, each with distinctive properties. This correction model includes dependence on the nominal tunes as well as the beam-beam parameter $f(Q_x, Q_y, \xi)$. It can be qualitatively understood by comparing to the β-beating induced changes as was shown in Eq. (3.43). It was derived at each separation step with 0.25σ granularity. The corrections account for beam-beam effects both at the IP where the scans are being carried out, hereafter referred to as the "scanning IP", and at the additional IP(s) where head-on collisions are taking place. Details of the multiple collision schemes are discussed in the following Sec. 4.3. A full

description of the correction strategy developed and applied to the vdM-calibration analysis has been described in [21]. A comprehensive list of systematic effects contributing to the final beam-beam interaction uncertainty on σ_{vis} is also listed. In the following sections studies concerning the impact of the crossing angle (Sec 4.4) and phase advances sensitivity (Sec. 4.5) are discussed. The derived strategy of all LHC experiments is to model the beam-beam-induced biases to the luminosity during vdM scans by numerical simulations and apply them to the measured quantities.

The calibration constant σ_{vis} bias is obtained according to Eq. (3.48). In most simulations, total separation range of 5σ is used, as it was shown that the integral converges as this steps, as shown in Fig. 4.2. Thus, the contributions from the beam-beam effects at higher separations can be neglected.

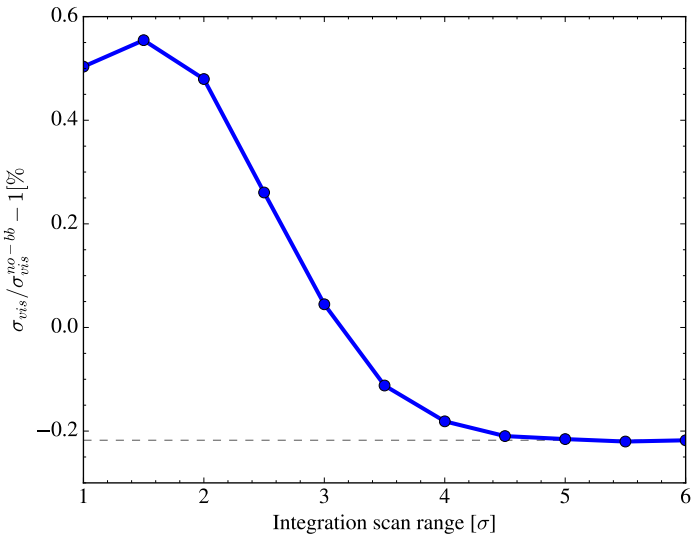

Figure 4.2: Beam-beam induced σ_{vis} bias convergence as a function of the scan range fraction used for integration, normalized with respect to the $\sigma_{\text{vis}}{}^{no-bb}$ without beam-beam effects. A single collision configuration at vdM conditions was used as an example.

4.3 Multiple collision scaling

The correction strategy summarized in the previous section assumes that the beams collide exclusively at the single scanning IP, meaning that they are entirely separated, either in a transverse or longitudinal manner, at the other three IPs of the LHC. Thus, they are assumed to not experience any other beam-beam interactions. In practice this is never true - the machine configuration is optimized to efficiently utilize the beam time at all experiments during luminosity-calibration scans. This practice significantly impacts the unperturbed-tune spectra and, consequently, the extent of biases induced by beam-beam interactions. The whole picture is more complicated due to the multiple beam-beam effects at different locations along the collider.

For a pair of colliding bunches at a particular scanning IP, the quantity referred to as the number of non-scanning interaction points (N_{NSIP}) is defined as the average count of head-on collisions that the two members of the pair undergo at interaction points other than the scanning IP. It is equal to zero when the beams do not collide at any other IPs than the scanning one, and can reach $N_{\mathrm{NSIP}} = 3$ when both bunches in the pair collide at all IPs, as shown schematically in Fig. 4.3. It can also take on fractional values when the two bunches of the colliding pair experience different numbers of additional collisions. For example, for a bunch-pair with the same identification number in the LHC orbit that collides in the two symmetric IPs (IP1 and IP5 from which one is the scanning IP), and one of the bunches also colliding with another bunch at IP8, $N_{\mathrm{NSIP}} = (1+2)/2 = 1.5$.

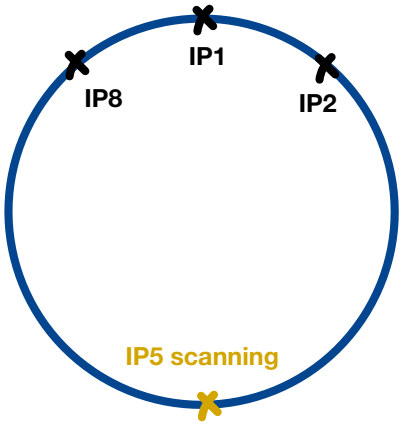

Figure 4.3: The scheme of possible beam-beam interaction along the LHC ring during a separation scan at IP5.

Because of the LHC geometry, with two experiments, ATLAS and CMS, located on the opposite sides of the ring, all the bunches colliding at one of them are also colliding at the second one, unless deliberate transverse separation is applied. This means that for bunches colliding in these experiments, the N_{NSIP} is typically equal to or greater than 1. For the other two experiments, it is more complicated as they are located at $\pm 1/8$th of the ring from IP1. Therefore, the possible values of N_{NSIP} depend on the considered scanning IP. Additionally, the same N_{NSIP} can also be a result of collisions at different locations around the ring. Thus a division into 'bunch families' is used, which refers to a sub-group of bunch pairs, that collide in exactly the same locations, with distinction between the two directions. In the physics operation, the beams filling pattern is optimized to maximize the luminosity, and hence the number of collisions at all IPs. This is not the case in the fills dedicated to the vdM calibrations, but

the mixed bunch families are still present.

The Fourier transform of the bunch centroid motion while undergoing beam-beam collisions gives the coherent tune spectrum. In Figure 4.4, the tune spectra in the case of a single IP ($N_{\mathrm{NSIP}} = 0$) and 2 IPs ($N_{\mathrm{NSIP}} = 1$) configurations are compared. In the former, the tune spread covers the range of roughly the beam-beam parameter $\xi = 3.24 \times 10^{-3}$. Two main peaks are visible that correspond to the coherent modes: σ-mode at the nominal tune ($Q_y = 0.32$) and the π-mode at $Q_y - Y\xi = 0.3164$, where Y is the Yokoya factor [93]. It is typically equal to $Y = 1.1$ for the soft-Gaussian charge distribution. For the LHC case, the tune spread is doubled when there is an additional collision, and the twofold downward shift is observed for the π-mode, as expected [77]. This effect is further enlarged with more additional collisions present.

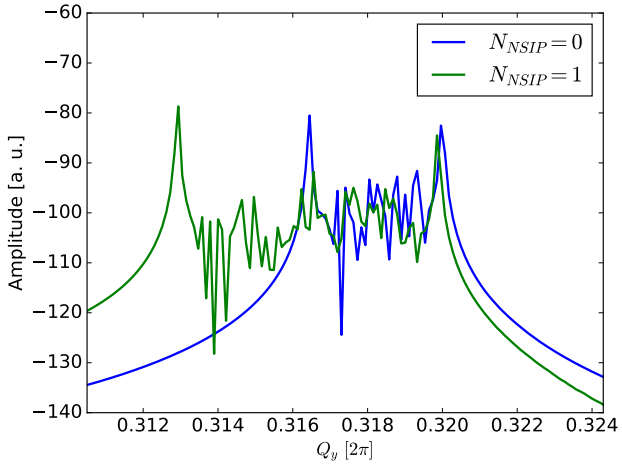

Figure 4.4: Vertical coherent-tune spectra in collisions for different configurations: head-on collisions at the scanning IP only ($N_{\mathrm{NSIP}} = 0$, blue curve), and in the presence of head-on collisions at one additional IP ($N_{\mathrm{NSIP}} = 1$, green curve).

As the beams are transversely separated, the beam-beam force changes and thus the associated tune spectra. This can be observed in Fig. 4.5, separately in the configuration with collision at the scanning IP only (top), and in the presence of head-on collision at one additional IP (bottom), for an example scan in the horizontal plane. For each configuration, the spectra are shown in the horizontal (scanning) plane (first) and the vertical (non-scanning) plane (second). In both cases, the π mode is shifted by the same amount in the two transverse planes. In the first example, the distinction between the scanning (horizontal) and non-scanning plane can be noticed. While in the non-scanning plane (bottom Fig. in 4.5a) the tune spread decreases with increasing separation, in the scanning plane its sign changes from negative to positive between 2 and 3σ separation step. This separation dependence is similar in case a scan with the additional collision is considered, as shown in Fig. 4.5b. But in this case, the π mode is further away from the σ mode, even at a very high separation. Instead, it converges at a frequency that is similar to the single collision tune shift, but it is slightly different in the scanning and non-scanning plane, because of the sign inversion that was observed in the single IP configuration.

The coherent spectra allow to understand how the frequency response of the bunch centroid appears during a vdM scan for different collision configurations in order to compare to the measured tune

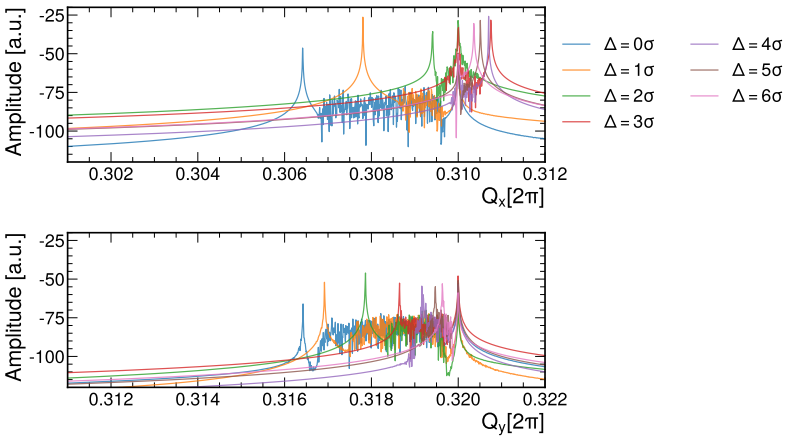

(a) 1 IP configuration - $N_{\mathrm{NSIP}} = 0$

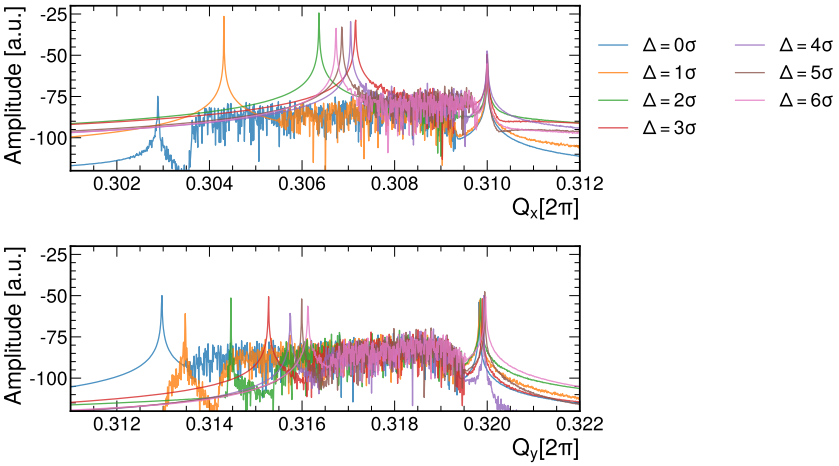

(b) 2 IPs configuration - $N_{\mathrm{NSIP}} = 1$

Figure 4.5: Horizontal (upper) and vertical (lower) coherent-tune spectra in collisions during a separation scan in the horizontal plane, for collisions at the scanning IP only (upper two), and in the presence of head-on collisions at one additional IP (lower two).

spectra of the collider. In a collider only macroscopic effects, as the bunch centroid oscillations can be measured for example with the LHC BBQ systems [94]. A further understanding of what happens to the particles constituting a bunch can be obtained by simulating the impact of the beam-beam force on several test particles with different amplitudes with respect to the opposing beams during a scan. The separation dependence can be more clearly observed from the incoherent spectra, that are based on single-particle oscillations, where the mean tune spread can be extracted, and the coherent modes are not present. The example incoherent spectra for a single bunches, based on the macroparticle positions are shown in Fig. 4.6 for bunches undergoing different numbers of collisions.

The corresponding mean tune shift, extracted as the average of the macro-particle distribution, is shown

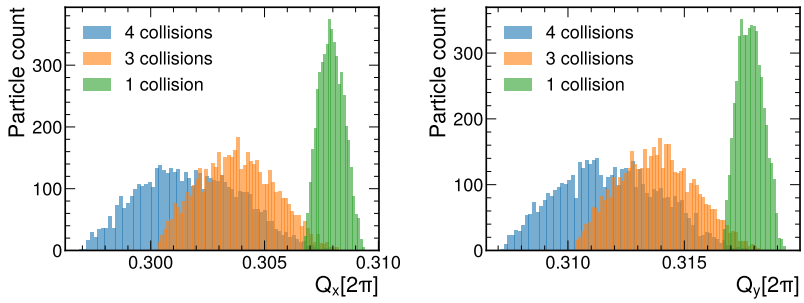

Figure 4.6: Incoherent spectra comparison for bunches with different numbers of collisions, the example is shown in the horizontal plane.

in Fig. 4.7 for bunches with different collision configurations. One of them (in purple) is colliding only at a single non-scanning IP, which corresponds to a shift of the average at approximately $-0.5Y \times \Delta Q/\xi$ in both transverse planes, independently of the separation steps as this bunch does not collide at the scanning IP. For the bunches undergoing the separation scan, the decrease in the mean tune is observed with different separation-step changes in the scanning and non-scanning planes. In the case of N_{NSIP} =3 (in blue), it can be observed that the full separation mean tune shift goes asymptotically to the head-on case of the bunch with N_{NSIP} =2 (in green, orange, and red colors). The disadvantage of using the mean

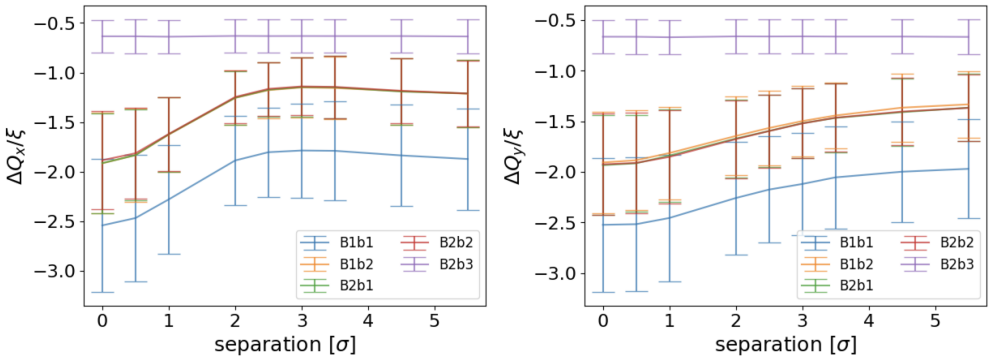

Figure 4.7: Vertical (left) and horizontal (right) incoherent mean tune during a horizontal separation scan, for a different number of collisions: single at non-scanning IP (purple curve), 3 collisions (N_{NSIP} = 2, green, orange and red curves), and 4 collisions (N_{NSIP} = 3, blue curve).

incoherent tune shift is that it cannot be validated with the measurement, where it is not possible to separate the single-bunch contribution. The comparison of the incoherent and coherent tune spectra is shown in Fig. 4.8. In the case of the incoherent tune distribution, the mean tune shift is clearly defined and it is indicated with the vertical line. The coherent spectra were obtained for a configuration including the adiabatic transverse damper (ADT), to remove the coherent modes. However, even in this case, it is not straightforward to define the mean tune shift. In the figure, the weighted mean is indicated with the vertical blue line to show the difference with respect to the incoherent mean tune shift.

An additional beam-beam interaction induces changes to the spectra and this can also be observed on

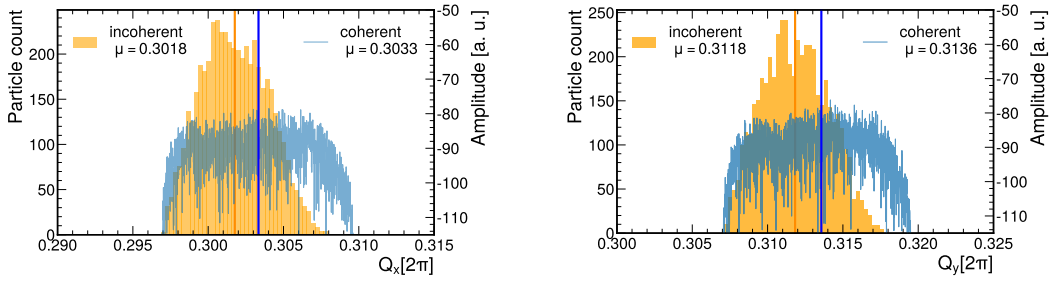

(a) Horizontal tune

(b) Vertical tune

Figure 4.8: Comparison of the coherent (blue) and incoherent (orange) spectra for a bunch colliding at four IPs for a head-on configuration. The estimated mean tune shift is indicated with vertical lines and shown in the legend for both cases.

the luminosity bias. The simplest example is shown in Fig. 4.9, where the luminosity ratio $\mathscr{L}_m$ / $\mathscr{L}_u$ as a function of a separation scan is shown for the case with only one IP scanning $N_{NSIP} = 0$ (light-shaded colors) and when there is another head-on collision is present and $N_{\text{NSIP}} = 1$ (strong colors). The separation dependence is significantly different for both cases shown in the same colors, which indicate scans performed in the same transverse plane. The comparison of the two planes also indicates the high sensitivity to the exact unperturbed transverse tunes values - in the nominal LHC collision setup, there is a very small difference in the fractional tunes of $Q_y - Q_x = 0.01$ $[2\pi]$. In terms of the bias on the calibration constant it corresponds to more than a twofold increase - the second collision adds -0.2% to the simulated bias on σ_{vis} , thus double the correction is needed.

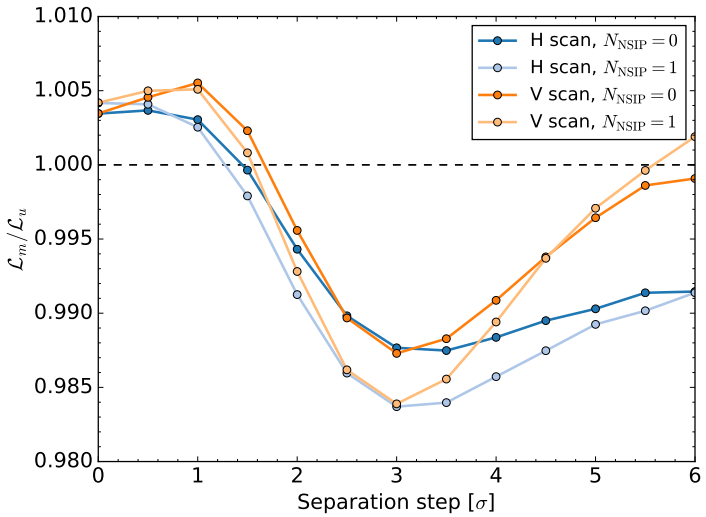

Figure 4.9: The beam-beam induced bias on luminosity during a separation scan in horizontal (blue) and vertical (orange) planes. Two cases are compared: without (darker curves) and with (light curves) an additional head-on collision in another location.

To account for these significant effects, the additional collisions had to be added to the correction model described in the previous section. A simulation campaign has been launched and numerous cases were studied with different combinations of collisions and for a wide range of the beam-beam parameter $0.0027 - 0.01$. The results are summarized in Fig. 4.10, for three beam-beam parameters which are representative of the range of possible conditions during the vdM calibrations and beyond, indicated with different color groups. The simulated multiple-collision cases are shown at $\Delta Q_{\mathrm{mIP}} = 0$, which denotes that nominal tune values and phase advances were used. The increase in the absolute bias can be observed on these points with increasing N_{NSIP} . Starting from the single IP configurations, indicated with dots, the simulated curves are shown with adjusted tune values, symmetrically in both transverse planes, according to x-axis. Due to beam-beam sensitivity to the unperturbed transverse tunes, as discussed in Sec. 4.5, the bigger the tune shift, the bigger the absolute σ_{vis} bias in the range of interest.

With the scaling laws described above, it is possible to reach the multi-collision equivalent bias in σ_{vis} using the single-IP configuration including the mean tune shift from extra collisions - this is indicated with the horizontal lines. The vertical dashed lines correspond to the effective tune shift ΔQ_{mIP} values where an inclined curve associated with a given value of ξ intersects the corresponding horizontal lines. These correspond, from right to left, to $\Delta Q_{\mathrm{mIP}}/\xi = -0.5, -1.0, -1.25$ and -1.5 which happens to be equal to N_{NSIP} /2. The results are organized in a more intuitive manner in Fig. 4.11 where the multi-IP bias-equivalent tune shift is shown as a function of the number of the non-scanning IPs. The linear dependence can be observed with a minor deviation from the straightforward scaling law:

$$\Delta Q_{\mathrm{mIP}} = -0.5 \times \xi \times N_{\mathrm{NSIP}} \, . \tag{4.1}$$

It can be directly related to the previously observed changes induced by additional collisions in the tune spectra. In order to prove the universality of this empirical scaling law, the study was repeated for different possible scanning IPs - the results are shown in Fig. 4.12. For a given scanning IP, there exist several bunch-pairs with different collision locations that yield the same value of N_{NSIP} . The simulation results are compared again to the single-IP configuration with shifted tunes (indicated with a magenta line). While the scaling of the main effect is confirmed, there exists some residual variation to the results at a given N_{NSIP} . This is attributed to the phase-advance fractions, which depend on the collision locations, and can also vary per transverse plane and per beam. The phase advance dependency considerations are addressed in Sec. 4.5.

To summarize, the symmetric transverse tune scan resulted in a very simple empirical scaling law that accounts for the impact of multiple beam-beam interactions on the σ_{vis} bias. For beam-beam parameters up to 0.01, the nominal tune shift in the single collision setup can be changed by $-\xi/2$ per collision to mimic the effect of multiple collisions. For beam-beam parameters higher than 0.01, the behavior of the visible cross section bias is not linear anymore as a function of the tune shift. By combining the parameterization of beam-beam biases for a single interaction point (as detailed in Sec. 4.2) with this scaling rule, a beam-beam correction procedure is established. It is simple to implement, demanding little to no significant computational resources. In many scenarios, it suffices for calculating precise bunch-by-bunch corrections in vdM calibrations or for estimating systematic uncertainties. This approach is particularly valuable when dealing with five to ten vdM-scan pairs involving up to 150 colliding bunches with varying populations and emittances, organized in multiple collision patterns, each requiring distinct multi-interaction point corrections. The computational burden associated with simulating each of these configurations in detail would be substantial. Figure 4.10 gives an overview of the error made in the past calibration that did not include the effect of multiple collisions. Depending

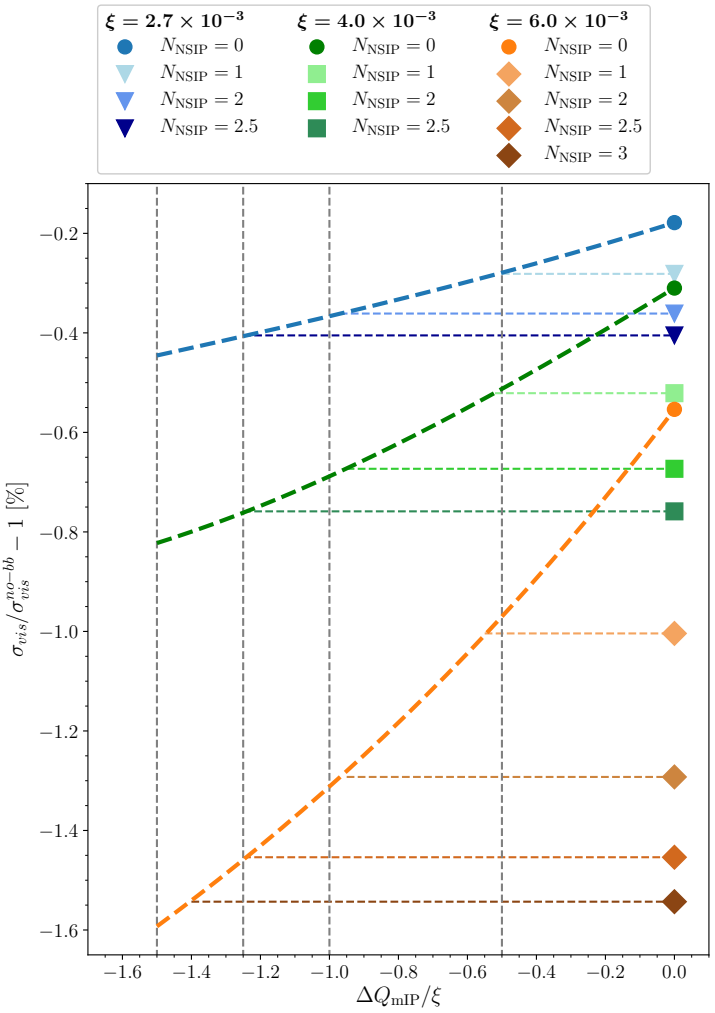

Figure 4.10: Visible cross section bias associated with vdM scans at IP1, for bunch pairs that in addition collide head-on at a fixed number of non-scanning IPs, and with the tunes and phase advances set to their nominal value (markers at $\Delta Q_{\mathrm{mIP}} = 0$). The three sampled values of the single-IP beam-beam parameter ξ are identified by the color groups. Curves starting with circular markers indicate visible cross section bias associated with vdM scans in a single IP configuration ($N_{\mathrm{NSIP}} = 0$), as a function of the multi-IP equivalent mean tune shift ΔQ_{mIP} expressed in units of ξ.

on per bunch ξ and N_{NSIP} the corrections were underestimated from 0.1 up to 1%.

Impact on luminosity while other IPs are scanning

It is also interesting to investigate changes in the absolute luminosity at each of the experiments when the scans are performed at other locations. This is shown in Fig. 4.13 for all four LHC IPs, as the results are very sensitive to the phase-advance set-point. While the absolute changes in the luminosity are very small (< 0.5%), a strong dependence on the separation step can be observed. This reflects the

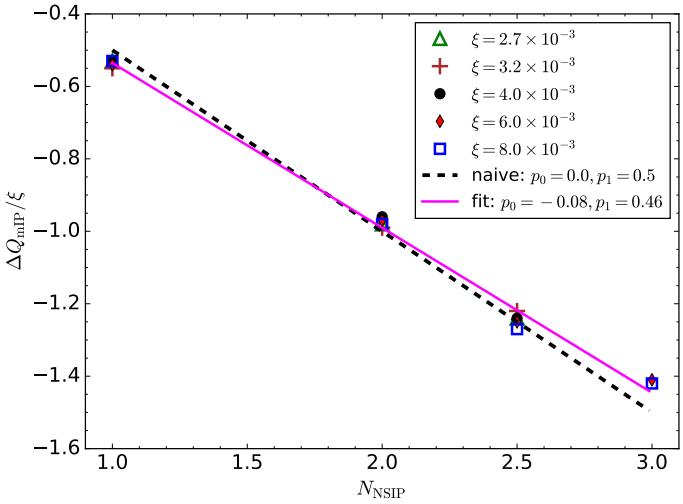

Figure 4.11: Dependence of the normalized multi-IP equivalent tune shift $\Delta Q_{\mathrm{mIP}}/\xi$ on the number of non-scanning IPs N_{NSIP} , for several values of the single-IP beam-beam parameter ξ. The solid magenta line represents a two-parameter linear fit to the points; the black dashed line represents a naive parameterization of the form $\Delta Q_{\mathrm{mIP}}/\xi - 0.5 \times N_{\mathrm{NSIP}}$.

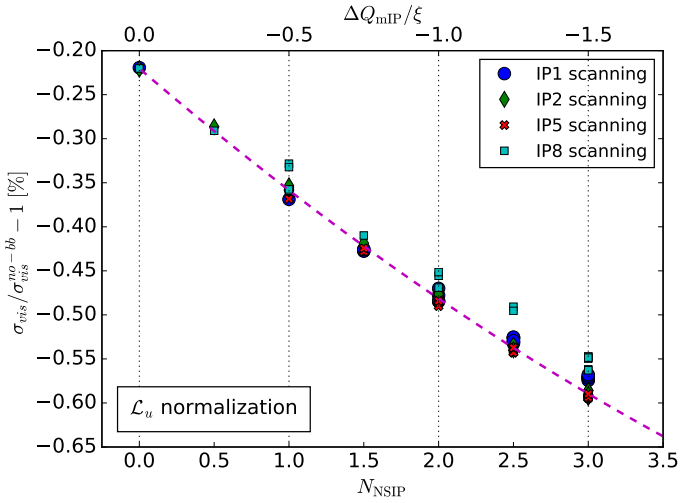

Figure 4.12: Visible cross section bias as a function of the number of non-scanning IPs (lower horizontal axis), for the four possible choices of scanning IP. The curve represents the dependence of the σ_{vis} bias in the $N_{\mathrm{NSIP}} = 0$ case, but with the horizontal and vertical unperturbed tunes shifted (upper horizontal axis).

additional beam-beam bias that would have to be considered if the scans were performed at the same time at both IPs. In the case of symmetrically located experiments, IP1 and IP5, the opposite changes are observed for scans in the horizontal and vertical planes. However, the impact to these IPs from the scans at IP2 and IP8 is almost constant. The luminosity at IP2 is most significantly impacted by a scan at IP5, while at IP8 both IP1 and IP5 give the biggest, non-static changes. These differences are attributed to the phase advances between the IPs.

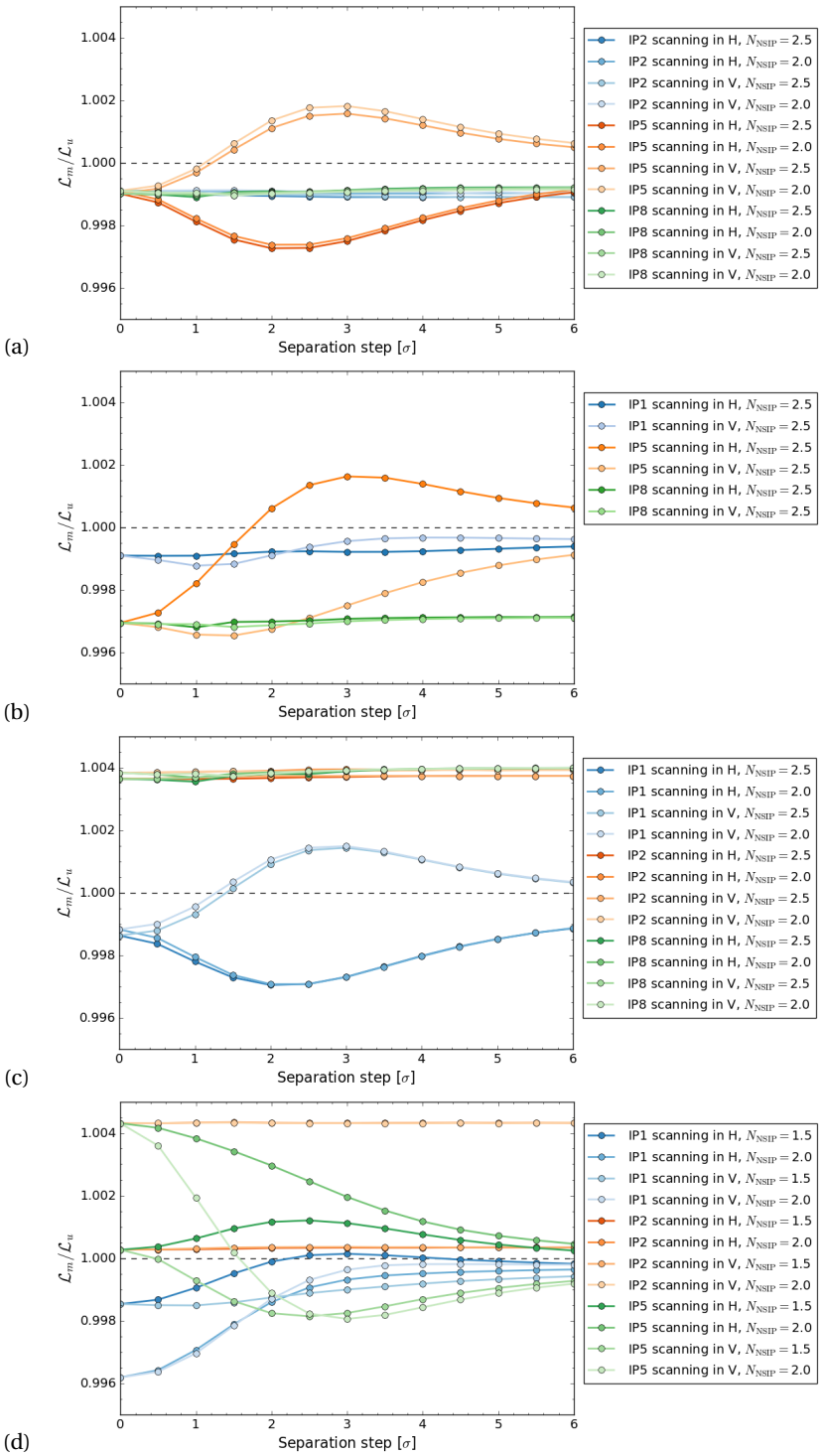

Figure 4.13: The beam-beam induced bias on the luminosity observed at each of the LHC IPs: IP1 (4.13a), IP2 (4.13b), IP5 (4.13c), IP8 (4.13d), while the separation scans are performed at the other IPs either in horizontal (H) or vertical (V) plane, as indicated in the legend. Bunches with different numbers of collisions are presented, indicated with the N_{NSIP} .

4.4 Crossing-angle

As the crossing-angle introduces coupling between transverse and longitudinal planes, it is normally avoided during the vdM calibration to reduce complexity. However, due to the lattice imperfections, a residual crossing-angle of the order of 10 μrad can be present. In addition, there are also experiments or non-standard vdM configurations where the crossing-angle has to be applied, for example at the LHCb experiment.

The main effect of introducing a crossing-angle is the reduction of the absolute luminosity by the factor derived in Eq. (1.21) for the case of Gaussian transverse density profiles. It is a result of the geometrical extension of the overlap size in the crossing-angle plane, that depends on the angle as well as on the bunch length, according to Eq. (1.22). As a result, the luminosity change during a separation scan is expanded in the crossing-angle plane, as was shown in the example in Eq. (1.23). The validation of the COMBI 3D integrator in the vdM configuration is shown in Fig. 4.14 - the geometrical factor obtained numerically is benchmarked against the expected reduction S calculated analytically. The difference between the two curves is well within the expected numerical uncertainty.

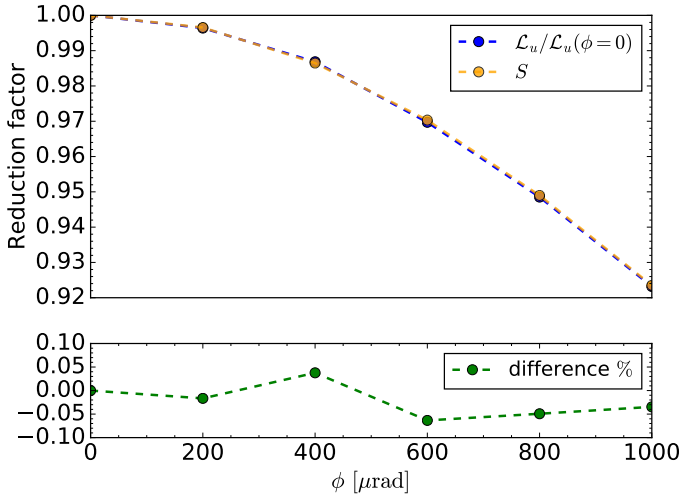

Figure 4.14: Validation for the crossing-angle reduction factor in luminosity. In blue the luminosity defined from the integral is shown, as a ratio to the luminosity calculated for $\phi = 0$. It is compared to the geometrical factor S (in orange) calculated as in Eq. (1.21). The difference between the two curves is plotted below and expressed in [%].

To evaluate the effects of the beam-beam interaction in the presence of a non-zero crossing-angle, the 6D beam-beam kick as described in Sec. 3.3 is used. This approach ensures also an accurate description of the longitudinal dynamics, such as the synchrotron motion and the beam–beam-induced transverse shape variations along the collision path. Furthermore, it takes into account the geometrical effects in the transverse plane associated with the crossing-angle and the bunch length. Thus, the changes in the transverse beam-beam overlap are correctly described, as well as the calculation of the effective strength of the source field experienced by the particles in the witness beam.

The simulated impact on luminosity during separation scans at different crossing-angle configurations is shown in Fig. 4.15. The noticeable change of the curve is observed at a higher angle value, $\phi = 1$ mrad.

As for the bias, it tends to decrease (approaching 1) in the case of the horizontal scan, which also represents the crossing-angle plane in this specific scenario. In contrast, the bias is more pronounced during the vertical scan, leaning towards the negative side ($\frac{\mathcal{L}_m}{\mathcal{L}_u} < 1$).

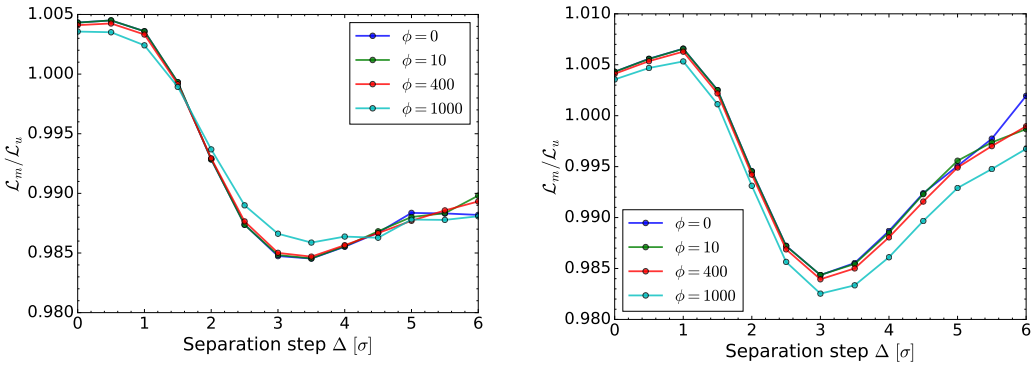

(a) (b)

Figure 4.15: Beam–beam-induced bias on the luminosity during separations scans in (left) horizontal and (right) vertical plane. Different colors correspond to the full crossing-angle used in the horizontal plane - from 0 and residual 10 μm to more typical angles used.

The magnitude of the orbit shift extracted from COMBI simulations with a crossing-angle was found consistent with that computed using the Bassetti-Erskine formula, with the effective convolved beam size as input. The latter is defined differently for the scanning and non-scanning plane, as specified in Eq. (1.22). The comparison of the simulated deflections for the example crossing-angle configuration and corresponding elliptical beam size equivalent is shown in Fig. 4.16. However, if the complete bias on σ_{vis} is evaluated, the two configurations give completely different results, almost twice smaller in the elliptical equivalent case.

The impact of the beam-beam interaction on the visible cross section varying with the full crossing-angle is shown in Fig. 4.17. It was simulated for the typical vdM conditions with $\xi = 3.24 \times 10^{-3}$, where the beam size is approximately 100 μm. In these scenarios, there is a reduction of luminosity up to 10%. This reduction factor is removed from the results by means of normalization to the beam-beam unperturbed luminosity, which already includes this factor. For the residual crossing-angle, smaller than 100 μrad, the impact on the beam-beam bias on σ_{vis} is negligible, remaining below 0.01%. However, for the higher crossing-angle values the σ_{vis} bias increases. For instance, in the case of the largest angle considered, of 1 mrad, the beam-beam induced bias can double, as shown with the orange line in Fig. 4.17. At the same time, the beam-beam parameter calculated using the effective transverse beam size decreases. This observation contradicts the commonly assumed scaling of the beam-beam-induced bias with the beam-beam parameter. This can be understood by observing separate bias contributions to the σ_{vis} coming from the peak and transverse beam size changes, which are shown in Fig. 4.18. The focusing effect on the peak decreases with the crossing-angle as a result of the increase in the effective overlap area and resulting reduction of the beam-beam parameter. This reduction does not affect the Σ_x and Σ_y in the same way as it is measured over the full scan range, the $x-y$ symmetry is changed with the introduction of the crossing-angle. The resulting difference in the

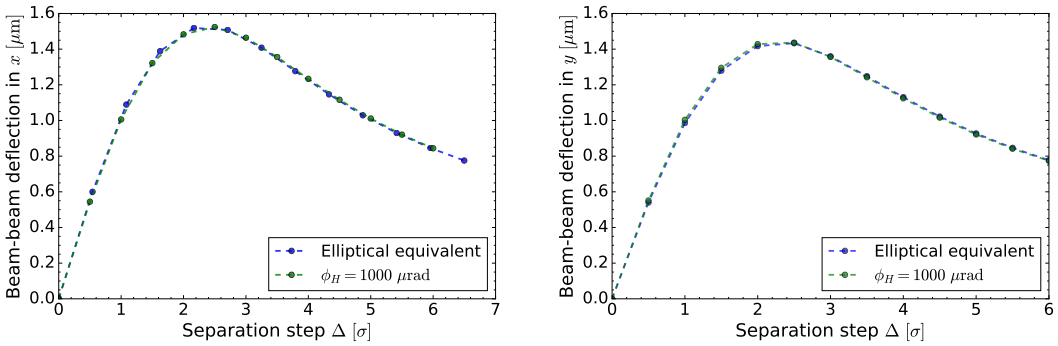

(a) (b)

Figure 4.16: Beam–beam-induced deflection during (left) the horizontal and (right) the vertical separation scan. Two cases are compared: the configuration with crossing-angle (green) and the equivalent elliptical beam size used in the crossing-angle plane (horizontal) instead of the angle (blue). The x axis unit includes the corresponding input beam sizes (different for the two cases in the left figure).

luminosity curves shown in Fig. 4.15 causes the effect on the extracted transverse beam sizes to be slightly more pronounced. However, the negative change observed in the total effect on σ_{vis} is mainly the result of the reduced focusing at the head-on step.

In the figure 4.17, two values of β^* , typical for the vdM configurations are presented, yielding slightly different results. This highlights the sensitivity of the beam-beam-induced bias to β^* in configurations with a crossing-angle, which increases with lower β^* . Additionally, when the same β^* value is considered, the results differ depending on the choice of the crossing-angle plane, as indicated by the blue and orange lines. The only distinction between the two transverse planes, when considering σ_{vis} , is the fractional transverse tunes. Furthermore, it was verified that the results in the vdM configuration remain insensitive to the synchrotron tune and the chromaticity.

In the multi-IP configuration, discussed in Sec. 4.3, it is possible that during a calibration at one of the IPs, the crossing-angle is present at another location. For the case of collisions at IP2 with $\phi_V = 300$ μrad and at IP8 with $\phi_H = -900$ μrad, simulations were also performed with COMBI. The non-negligible impact was found for the bias only at high separation $\Delta > 3\sigma$, which propagated into σ_{vis} bias at the noise level of 0.01%.

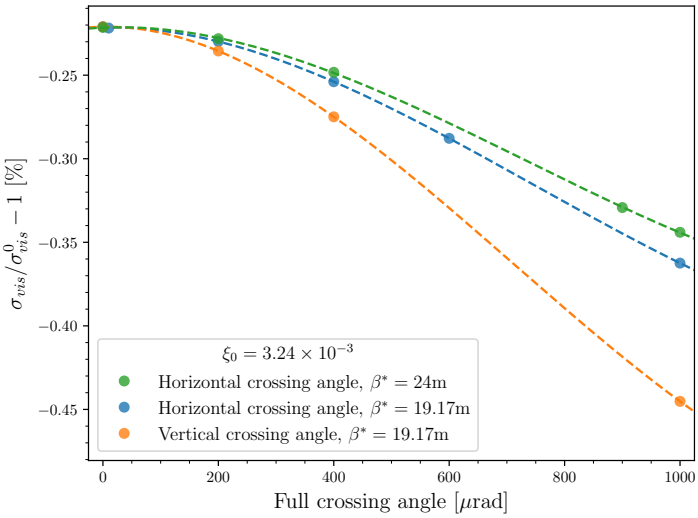

Figure 4.17: Visible cross section bias predicted by COMBI using the 6D kick as a function of the full crossing-angle, for a horizontal (blue) and a vertical (orange) crossing plane at β^* = 19.17 m, and for a horizontal crossing angle at β^* = 24 m (green). The beam-beam parameter value at zero crossing angle is the same in all cases, as indicated in the legend.

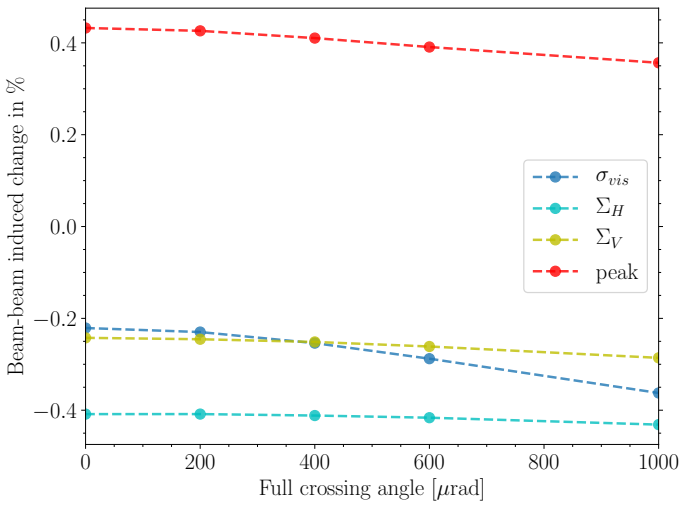

Figure 4.18: Contributions to the visible cross section bias from separate observables.

4.5 Phase advance sensitivity

The phase advance between the points of interest represents the number and fraction of the particle betatron oscillations between these points. The propagation of Courant-Snyder parameters can be described with the linear transport matrix, as discussed in Sec. 3.5. With multiple collisions around the ring, and varying phases per beam and per transverse plane the problem is more complex, with many free parameters. The numerical simulations have been used to study the dependence of the σ_{vis} bias on the choice of phase advance between the IPs.

4.5.1 Single collision configuration

In the single collision configuration, the beam-beam-induced beta-beating is propagated through the whole lattice. The phase advance over one turn is by definition the tune. At the IP the β^* change is directly related to the tune Q and the tune shift ΔQ, as was shown in Eq. (3.43):

$$\frac{\beta^*}{\beta_0^*} = \frac{\sin 2\pi Q}{\sin 2\pi (Q+\Delta Q)} = \frac{1}{\sqrt{1 + k\beta_0^* \cot 2\pi Q - \left(\frac{k\beta_0^*}{2}\right)^2}}. \tag{4.2}$$

The summed effect of the two beams combined in both transverse planes is propagated to the luminosity, as shown in Fig. 4.19a, for the reference vdM parameters (Tab. 4.1). As expected from the formula above, the luminosity tune dependence has π period and since k is negative (Eq. 3.49) it increases infinitely when tune approaches $Q = 0.5 + n/2$. The combination of the beam-beam force and nominal tune can result in a negative or positive impact on the luminosity. Thus, the choice of the tune set-point for the nominal operation can be used to obtain net gain in the absolute luminosity. The impact on the

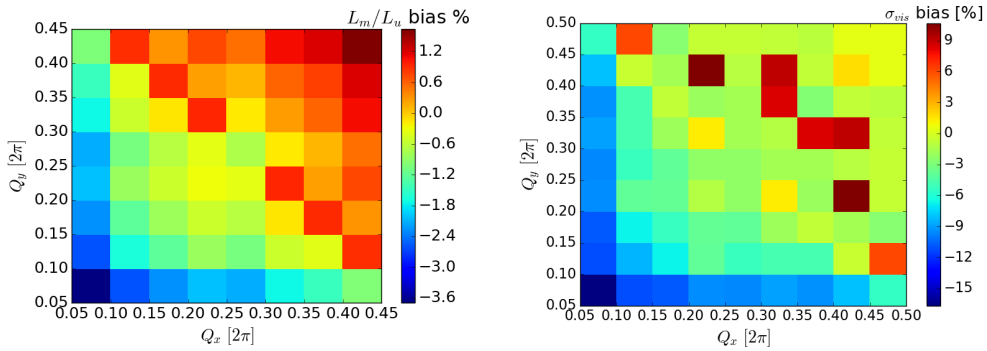

(a) Head-on luminosity

(b) σ_{vis}

Figure 4.19: The luminosity (left) and σ_{vis} (right) beam-beam interaction induced bias in percentage dependence on the nominal betatron tunes Q_x, Q_y.

calibration constant σ_{vis} was calculated according to Eq. (3.48) and is shown in Fig. 4.19b. During a separation scan, the force gradient k in Eq. (4.2) changes magnitude and sign, hence the impact on σ_{vis} is not straightforward to interpret. The current nominal operation tune fractions $Q_x, Q_y = (0.31, 0.32)$, give a very slight net increase in the head-on luminosity of (0.4%), in case of the reference parameters (Tab. 4.1), and result in the small negative bias on σ_{vis} (−0.2%).

4.5.2 Two collisions configuration

In case there is more than a single collision present, the beam-beam-induced luminosity bias exhibits sensitivity not only to the nominal tunes but also to the phase advances between the interaction points. The schematic view of the phase space changes for example due to the beam-beam interaction (red and pink arrows) and their propagation with linear transfer is shown in Fig. 4.20. The orange lines were used to indicate the small amplitude particles that are exposed to the focusing (linearized) force at one of the interaction points and that are observed at different amplitudes after the linear transfer.

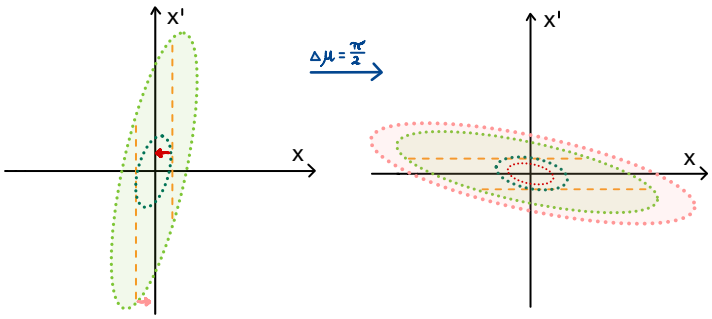

Figure 4.20: Scheme of the beam-beam induced changes to the phase space ellipse rotation in the linear transfer $\Delta\mu = \frac{\pi}{2}$.

This dependency is shown in Fig. 4.21 at different separation steps Δ, separately at the witness and scanning IP. From Fig. 4.21a it is clear that the change with phase and π periodicity are preserved while separating the beams, and the absolute bias diminishes with increasing separation and becomes negligible at $\Delta = 4\sigma$. Thus, it is straightforward to predict the phase advance that can suppress the bias at the witness collision. The picture is more intricate at the scanning IP. Beam–beam-induced bunch-shape distortions from the non-scanning IP(s) propagate around the ring in a manner that depends on that phase advance, thereby making the detailed shape of the $\mathscr{L}_u$ distribution at the scanning IP phase–advance-dependent. In Fig. 4.21b the $\mathscr{L}_u$ normalization is used, which eliminates the effects induced by the head-on collision at the witness IP, thereby accentuating the contribution from the separated interaction at the scanning IP. It becomes evident that in the multi-collision configuration, no phase advance set-point could completely mitigate the effect of the beam-beam interaction. In Figure 4.22 the example projections of the bunch-pair density distributions overlap into single transverse coordinates are shown, at different phase advance settings. The beam-beam-induced bias is shown for the two extreme phase advance set points. It is observed that the head-on beam-beam interaction at the witness is propagated in the phase advance-dependent manner, with focused particles in the core moved to another part of the transverse distributions. As the beam-beam interaction couples the two transverse planes, in the amplitude-dependent manner (as discussed in Sec. 3.2.1), it could lead to the non-factorization of the transverse distributions. At each point in the (μ_x, μ_y) space, the luminosity-bias curves were simulated and the corresponding separation-integrated bias on σ_{vis} was computed. It is shown in Fig. 4.23, where the main phase advance periodicity of π observed on the luminosity is preserved. The phase advance-induced perturbations result in a small modulation of the σ_{vis} around the central value defined by the nominal tunes, variations below 0.1% are observed. To minimize the phase-related errors in the 2 IPs configuration, the phases should be set close to the maximum $\mu = 0.4$ where the related bias gradient is the smallest.

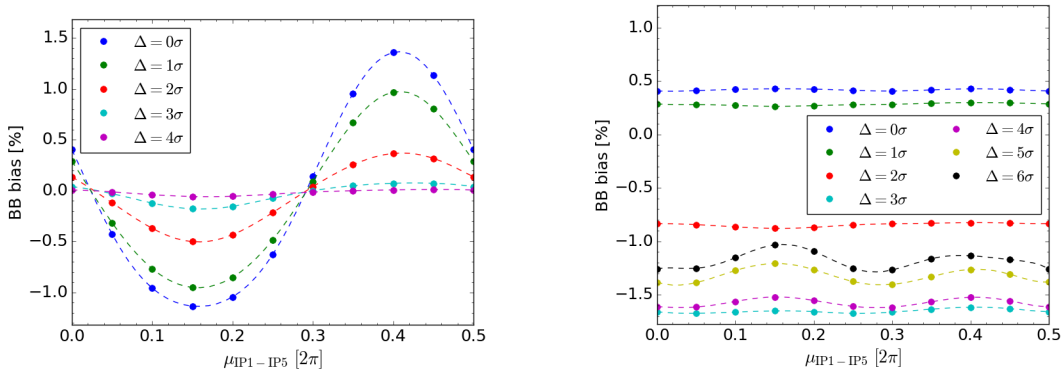

(a) witness IP

(b) scanning IP

Figure 4.21: Luminosity bias induced by the beam-beam interaction as a function of phase advance between the IPs, at various separation steps Δ at the scanning IP. The impact on luminosity is shown on separate figures for the witness (left) and the scanning IP (right).

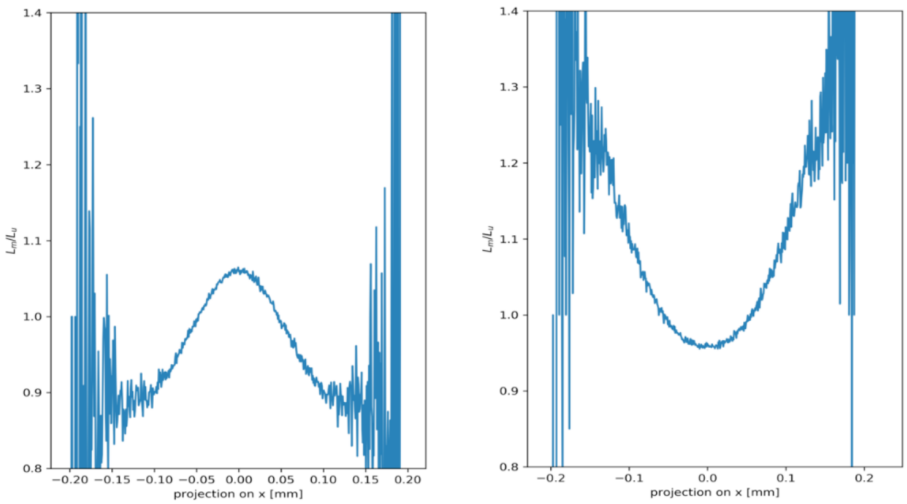

Figure 4.22: Beam-beam induced bias at the witness IP on the projection of the overlap histogram on the x-axis, for the extreme phase effects: maximized (left) positive and (right) negative bias.

4.5.3 More collisions configurations

To assess the impact of more collisions, the above phase scans were repeated for collision patterns with up to three non-scanning IPs, which corresponds to the maximum possible collisions at the LHC. To deal with the increased dimensionality of the problem, the fractional phase advance from IP1 to IP5 was fixed to $\mu_x = \mu_y = 0.405$. With that constraint, and with the nominal tunes and phase advance in the other half of the ring fixed, the horizontal and vertical fractional phase-advance values from IP1 to IP2 were scanned over the range $[0, 2\pi]$, compensating the change IP2-IP5. The results for the bunch-pairs colliding at 3 IPs and 4 IPs are shown in Fig. 4.24. The absolute bias increases with the

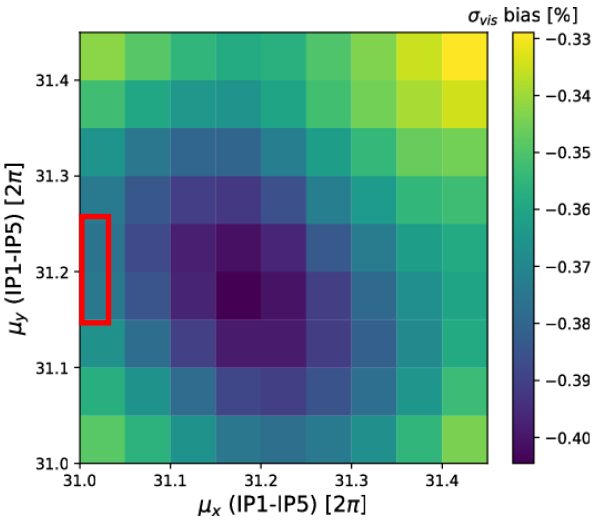

Figure 4.23: Visible cross section bias as a function of phase advance for the 2 IPs configuration from multi-particle COMBI simulations. The LHC nominal values are marked with a red rectangle.

number of collisions, as discussed in Sec. 4.3. The phase advance-related modulation remains below 0.1%.

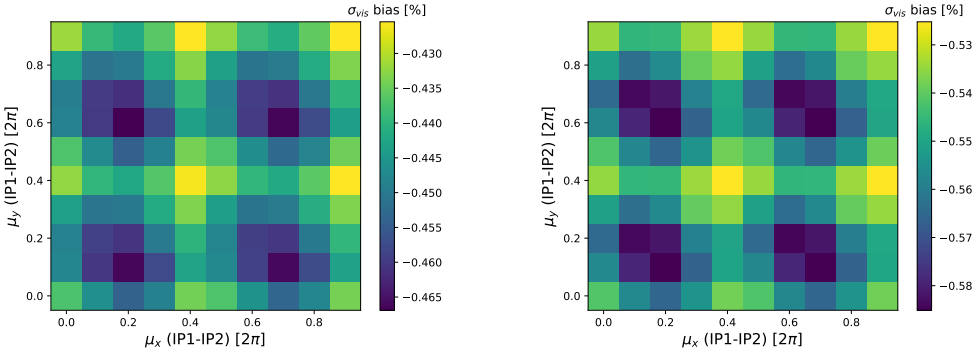

(a) 3 collisions

(b) 4 collisions

Figure 4.24: Visible cross section bias as a function of phase advance between IP1-IP2 for the 3 and 4 IPs configuration from multi-particle COMBI simulations.

The study was then repeated for the other side of the ring, with scanning the phase between IP8-IP1. The results presented in Fig. 4.25 indicate small modulation as in the previous case below 0.1%. It is interesting to notice, that the extreme values are at different phases than in the previously discussed cases.

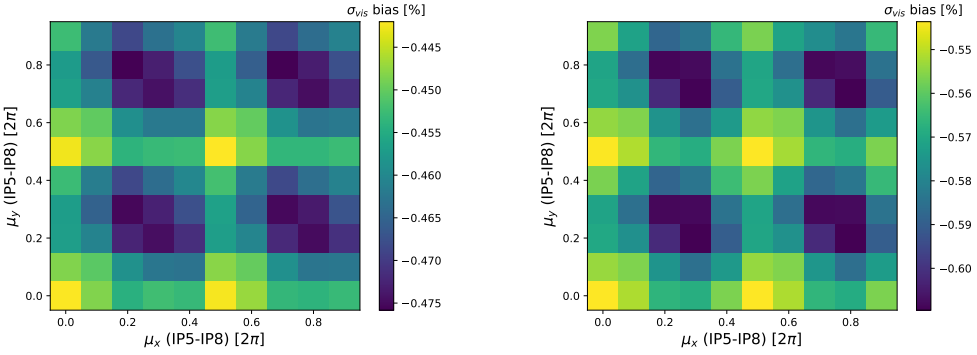

(a) 3 collisions

(b) 4 collisions

Figure 4.25: Visible cross section bias as a function of phase advance between IP8-IP1 for the 3 and 4 IPs configuration from multi-particle COMBI simulations.

4.5.4 Conclusions

Since the phase advances around the LHC can be measured to a few degrees ($\sim 0.015 \times 2\pi$), the lattice "operating point" in phase-advance space is known. Thus only a small fraction of the above-presented scans should be used to define the phase-related uncertainty on σ_{vis} . This shows that the phase advance configuration between the IPs has only a minor impact on beam-beam corrections to vdM calibrations.

In all the above-presented plots in this section, the choice of normalization was made to $\mathscr{L}_u$. However, there is another possibility of $\mathscr{L}_0$ normalization, already discussed in Sec. 4.3. The magnitude of the overall beam-beam correction to the vdM-based absolute luminosity scale was found to depend slightly on the choice of reference normalization. The difference is phase-advance dependent and exhibits a clear periodic structure (Fig. 4.26). The largest absolute difference in σ_{vis} bias between the two reference configurations is bigger than the phase modulation but does not exceed 0.15% (for the high beam-beam parameter $\xi = 0.006$).

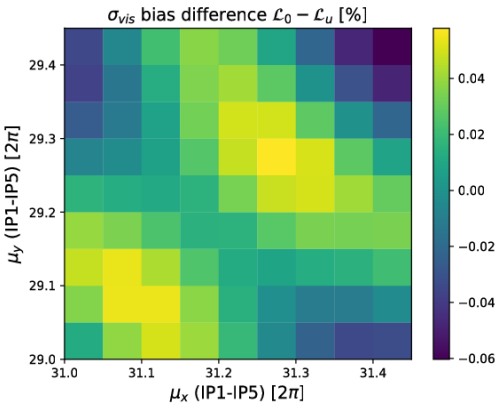

Figure 4.26: Phase-advance dependence of the difference, between the $\mathscr{L}_0$ and the $\mathscr{L}_u$ normalization in the 2 IPs, of the beam-beam induced σ_{vis} bias.

While these scans do not encompass a comprehensive exploration of the entire 12-dimensional phase-advance space (comprising 2 beams, 2 planes, and 3 IP combinations), they do provide an indication that the most significant potential deviation between the $\mathscr{L}_0$ and $\mathscr{L}_u$ normalizations amounts to approximately $0.1-0.2\%$ of σ_{vis} when considering the complete parameter space. The reason behind the nearly identical results of the $\mathscr{L}_0$ and $\mathscr{L}_u$ normalizations lies in the fact that the Run-2 phase-advance between IP1 and IP5 happens to fall within a region of $\mu_x - \mu_y$ where the inconsistency is close to its minimum. Consequently, for cases involving bunches colliding exclusively in these two IPs, the difference in the σ_{vis} bias between the $\mathscr{L}_0$ and $\mathscr{L}_u$ normalizations has been shown to be negligible.

5 Dedicated experiment for model validation

The correction strategy described in the previous Chapter 4 is fully based on the simulation results. The simulation models used for estimating the beam-beam associated luminosity bias were validated with theory, but never with measurements. Thus, a dedicated experiment was designed to prove the accuracy of the simulation results and therefore support the correction strategy employed in the luminosity analysis. The changes to the luminosity induced by the beam-beam interaction cannot be directly separated. As opposed to simulation, there is no access to the unperturbed observables. The configuration with multiple collisions enables the observations of the beam-beam effects at another location as it propagates through the accelerator.

The beam-beam test was performed at the LHC, at the beginning of the Run 3 ramp-up. It was performed at injection energy $\sqrt{s} = 900$ GeV due to an early ramp-up period and withstanding machine limitations. The low energy was chosen because the beam-beam effects are independent of the energy. On the contrary, the total events cross section is lower than at top energy, therefore there was a risk of the measurement being statistically not significant. The beam-beam bias to the single bunch instantaneous luminosity was expected to be at the level of ~ 1%, whereas the preliminary expected luminosity precision was at the level of ~ 0.5%. A solution was found by designing a phase knob, that maximizes the observable beam-beam effects. The dependence on observations of beam-beam effects induced in a head-on collision at another location as a function of the phase advance between the two collision points is shown in Fig. 5.1, as simulated by COMBI. It is important to note that due to the periodicity of this curve, the phase-induced enhancements change the absolute value of luminosities at both interaction points in the same way. The phase adjustment allowed for a threefold enhancement of the effect, the optimal phase is indicated with a green dotted vertical line at $\Delta\mu_{IP1-IP5} = 0.41$ $[2\pi]$. The integer part is irrelevant as the number of full oscillations around the lattice is not important due to periodicity. Applying this phase advance one can obtain an enhancement of the luminosity at both IPs. The net effect mainly depends on the machine tunes. One of the tests was also performed at the minimizing knob, which was designed to reduce the beam-beam bias on luminosity to the minimum, it is marked with a yellow dotted line at $\Delta\mu_{IP1-IP5} = 0.29$ $[2\pi]$. The optics measurements with the knob included in the LHC lattice were necessary, the results are described in Sec. 5.1. The changes in the transverse tune spectra are discussed in Sec. 5.2 with a comparison to COMBI simulation. The emittance measurement for the purpose of precise definition of the beam-beam parameter values across all tests is discussed in Sec. 5.3.

The tests included simplified step-function scans for the measurement of the full beam-beam-induced bias (Sec. 5.4), as well as the full separation scans (as in vdM calibration), for the measured biases at each

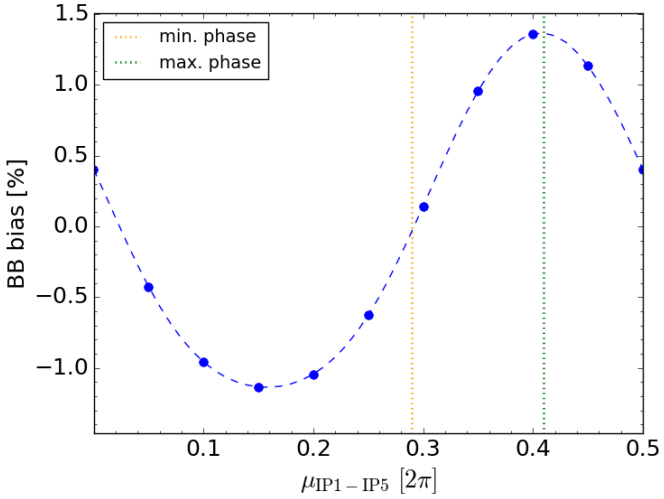

Figure 5.1: Luminosity bias induced by the beam-beam interaction as a function of phase advance between the IPs, at the low beam-beam parameter $\xi = 3.24 \times 10^{-3}$.

separation step (Sec. 5.5). Across the experiment, different filling patterns were used, with 2 (ATLAS and CMS) or 3 (also ALICE) collision points. Only up to four high-intensity bunches ($n = 1.25 \times 10^{11}$ protons) were possible to be injected due to maximum charge limitations. The required emittance was 1.5 μm, or as small as it is possible from the injector chain. These conditions provided the high maximum beam-beam parameter during the experiment, of 0.01 for each interaction. No crossing angles were used for IP1 and IP5, but they were not possible to be removed at IP2 and IP8.

The experiment employed various instruments to measure the beam-beam effects on multiple observables:

- ATLAS and CMS luminometers for the effects on the luminosity. Given that the luminometers were not yet fully calibrated, the relative observations were made during the experiment. To establish a basis for comparison, the luminosity measurements were normalized to the per-bunch charge, defined as specific luminosity. The concept of 'witness' or observer IP was used - while the two beam configuration was changing during the experiment, at one of the IPs the beams were consistently in head-on collision, taking the reference measurement. At IP1, Minimum Bias Trigger Scintillators (MBTs) [95] were used, with per bunch luminosity measurement. It is available per 'Lumi Block' (LB) - whose lengths depend on the data-taking configuration. For each test in the experiment, the LBs were set to correspond to the length of scan steps. The statistical errors (binomial) were defined from raw counts. At IP5, the luminosity was measured with the Hadron Forward Calorimeter, based on the occupancy data (as described in Sec. 2.7). It was chosen out of multiple excellent CMS systems based on its exceptional sensitivity under the beam-beam experiment conditions. The luminosity is published in the periods of four luminosity nibbles - corresponding to 4×4096 LHC orbits, which allows for direct error estimation within each step.
- Synchrotron light monitors (BSRT) [96] were used to measure relative changes in transverse beam sizes as a result of the beam-beam induced β-beating as well as the trends in emittance evolution in time. Additionally, before each test, the wire scanner (WS) was run through the beams, as a

reference for the accurate beam-beam parameter estimation. The cross-check between these measurements is included in Sec. 5.3. The WS raw data was refitted to improve the quality of the measurement. The WS provided the absolute beam size (emittance) measurements for the calculation of the beam-beam parameter.

- Observations on the coherent spectra were made using the LHC Transverse Damper (ADT) [97] and Base-Band Tune (BBQ) [94] systems. Spectrograms with 0.0001 ΔQ resolution are computed using recorded bunch positions at every turn, integrated over the steps used in the experiment (typically 1 min). To mitigate the influence of noises on tune estimation, a median filter is applied with a self-defined local window size as pre-processing. Additionally, the 50 Hz noise lines present in the spectra are masked. The filtered data are fitted by Gaussian functions with a baseline, and the center of the peak is considered as the predicted tune.
- Orbit displacements at each of the IPs were measured with DOROS Beam Position Monitors, which were described in Sec. 2.3.

5.1 Optics measurements

The new lattice parameters including the maximizing phase knob had to be validated with detailed optics measurements.

5.1.1 Phase advance

To measure the phases around the LHC ring, the signal from Beam Position Monitors (BPMs) is used. The expected changes induced with the knob for the main IPs are listed in Tab. 5.1 compared to the measurement, showing a perfect agreement up to 0.01 [2π]. The phase change between IP1 and IP5 was compensated on the other side of the ring so that the total tunes remained unchanged from the nominal values.

	Beam 1		Beam 2	
	$\Delta\mu_x$ [2π]	$\Delta\mu_y$ [2π]	$\Delta\mu_x$ [2π]	$\Delta\mu_y$ [2π]
IP1-IP5	30.977	29.649	31.062	29.762
IP1-IP5 adjusted	30.900	29.900	30.900	29.900
expected change	-0.077	0.251	-0.162	0.138
measured change	-0.076 ± 0.003	0.240 ± 0.002	-0.162 ± 0.002	0.137 ± 0.002

Table 5.1: Phase advances between IP1 and IP5, as in the nominal lattice and required adjusted values. The changes required from the knob and measured after applying the knob are listed.

The change in phase advances was also measured at the BSRT location and it is summarized in Tab. 5.2. There the model diverges more significantly, causing ~ 0.05 [2π] differences. As described in the previous section, the phase adjustments were optimized mainly for the observations at the IPs.

5.1.2 Beta-beating

The beta-beating was measured well within tolerances for the different settings of the knob. The example measurement results with respect to the reference measurements without the full knob are

	Beam 1		Beam 2	
	$\Delta\mu_x$ [2π]	$\Delta\mu_y$ [2π]	$\Delta\mu_x$ [2π]	$\Delta\mu_y$ [2π]
expected change	-0.025	0.251	-0.175	0.072
measured change	-0.073 ± 0.001	0.213 ± 0.001	-0.135 ± 0.001	0.125 ± 0.001

Table 5.2: Phase advance changes at BSRT locations expected from the knob compared to the measured phases after applying the knob.

presented in Figs. 5.2. The biggest difference found was up to 25% around IP5 for Beam 1 in the vertical plane. This kind of big difference around the IPs is expected and can be commonly caused by bad BPMs. Generally, the measurement showed beta-beating was within the acceptable limits, mostly within 10%.

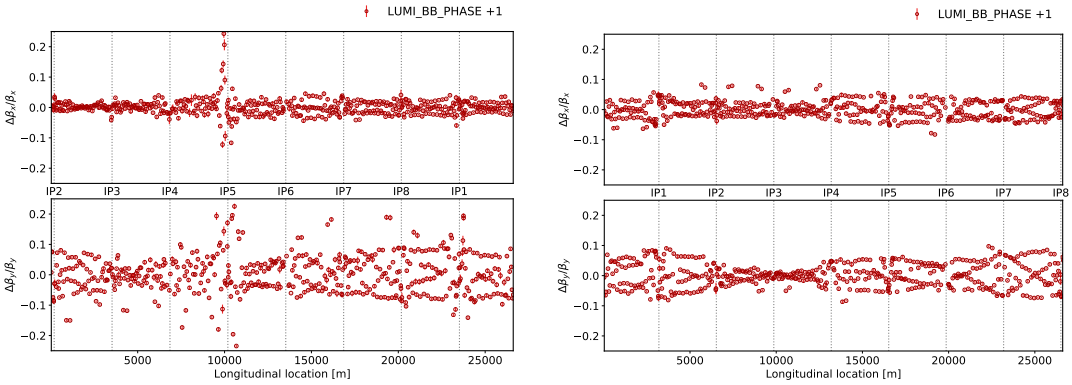

Figure 5.2: Measured beta difference between the lattice with the maximizing (+1) phase knob and nominal lattice along the LHC ring, for Beam 1 (left) and Beam 2 (right).

Differences in the measured β functions were also checked against the MADX LHC lattice model predictions, including the maximizing phase advance knob. Results plotted along the LHC lattice are shown in Fig. 5.3. In this case, the measurements agree with the simulation model within a tolerable level of 10%.

Measured β-functions at the BSRT and WS are summarized in Tab. 5.3, and compared to the MADX model values. The differences between the two are attributed to magnetic imperfections. The measurement error from propagating the beta values along the lattice from BPMs forwards and backward to the interesting location based on the MADX LHC lattice model was estimated up to 3%, which is assigned as the systematic error.

5.1.3 β^* - beta-function waist at the IP

The DOROS BPMs are located at the end of the inner triplets on the experiment side. Due to the phase advance of π between the DOROS on the left and right side, they cannot be used for the precise measurement of the β^* at the IPs. This can only be achieved with a special K-modulation technique [98]

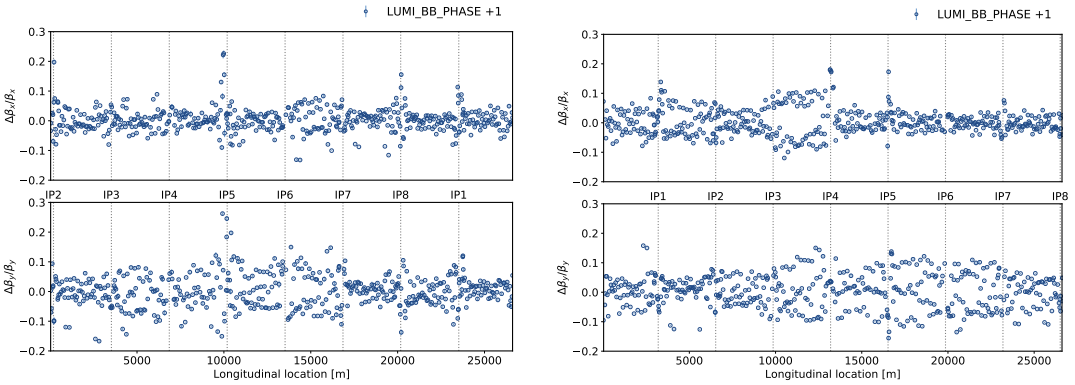

Figure 5.3: Measured beta function differences along the LHC ring with respect to the MADX model with included maximizing (+1) phase knob, for Beam 1 (left) and Beam 2 (right). Error bars include just the errors defined in the measurements (no systematic errors included).

	Beam 1		Beam 2	
	β_x [m]	β_y [m]	β_x [m]	β_y [m]
BSRT	208.7	291.2	214.4	357.6
WS	197.7	350.0	197.3	418.1
BSRT - model	204.9	286.9	196.7	358.1
WS - model	192.7	340.0	185.2	418.2

Table 5.3: Beta functions at the BSRT and WS locations measured with the full knob, compared to the model values.

at the interesting locations. This was performed at the main interaction points in which data were taken during the experiment, the results are summarized in Tab. 5.4 at two different knob settings.

		Beam 1		**Beam 2**	
	knob	β_x [m]	β_y [m]	β_x [m]	β_y [m]
IP1	**+1.0**	10.49 ± 0.01	11.71 ± 0.01	10.11 ± 0.01	11.54 ± 0.01
	-0.7	10.92 ± 0.97	11.89 ± 0.01	10.81 ± 0.01	10.18 ± 0.76
IP5	**+1.0**	11.01 ± 0.01	10.97 ± 0.01	10.20 ± 0.19	11.57 ± 0.10
	-0.7	10.61 ± 0.01	10.76 ± 0.01	9.55 ± 0.01	10.99 ± 0.01

Table 5.4: β^* functions at the IPs measured with K-modulation technique for the lattice at the two opposite knob settings.

5.1.4 Dispersion

It was important to perform dispersion D^* measurements at the IPs, in the configurations with the new optics knob, as it contributes to the measured beam size, according to Eq. (1.29). Assuming the LHC

design value $\frac{\Delta p}{p} = 10^{-4}$, the average dispersion measurement around the IP1 and IP5 was estimated to contribute up to 2% on the observed bunch sizes. It is treated as a static effect during the tests.

5.2 Observations of the effect of the phase knobs

An additional transition between the maximum and minimum knob was tested (within ~ 1 min), with the aim to observe directly the knob induced enhancement of the beam-beam effect on the luminosity. However, during that change a significant momentary decrease in Beam 1 intensity was observed, indicating an instability. Thus, the effect of the knob on luminosity was indistinguishable from the simultaneous change of beam parameters. Nevertheless, it was possible to monitor the coherent transverse tune spectra.

COMBI simulations were performed for the two extreme cases of lattice changes induced by the maximizing and minimizing knobs (Figs. 5.4). For the head-on case (Fig. 5.4a), the coherent modes are suppressed for the maximizing knob, as the phase between the two beam-beam interactions is close to 180 deg. In this configuration, the effect of the first collision is counteracted by the second collision. This configuration is preferable for the spectra observations as the mean tune spread can be fitted. Symmetry in x, y planes is broken during the separation scan. In the separation plane (here X), the coherent modes become visible again at $1.5 \times \sigma$ separation (Fig. 5.4b), at a slightly different frequency than in the non-scanning plane, that depends on the separation (Fig. 5.4c).

These features of the coherent spectra were also observed during the beam-beam experiments. The spectra for different knobs in the head-on configuration are compared in Figs. 5.5, where the suppression of the coherent modes is evident. The comparison of the knobs with separation uses data from separate fills but at very similar conditions. Two example separation steps are shown in Figs. 5.6. The measurements in the non-scanning plane are consistent with the simulation, while in the scanning plane, the reappearing coherent modes were not observed. This can be explained by the presence of a transverse damper in the real machine that reduces the oscillations of two beam centroids independently, which can result in the attenuation of the coherent oscillations linked to beam-beam interactions as previously observed and described in [99].

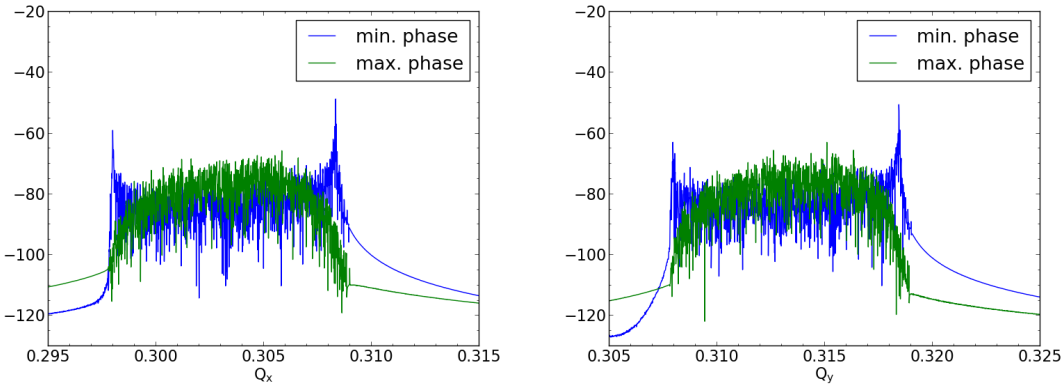

(a) Head-on position

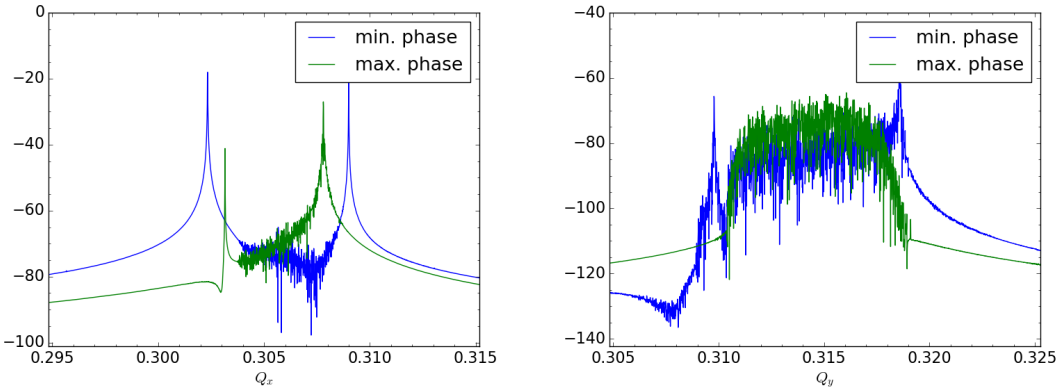

(b) $1.5 \times \sigma$ separation

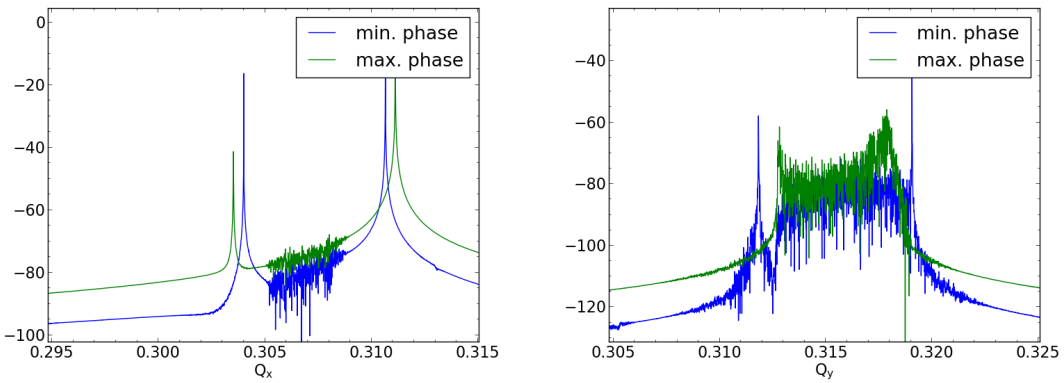

(c) $3 \times \sigma$ separation

Figure 5.4: Comparison of the simulated tune spectra (in the units of $[2\pi]$) for the minimizing (-0.7) and maximizing ($+1$) phase knobs in x-plane (left) and y-plane (right), at different separation steps in the horizontal plane.

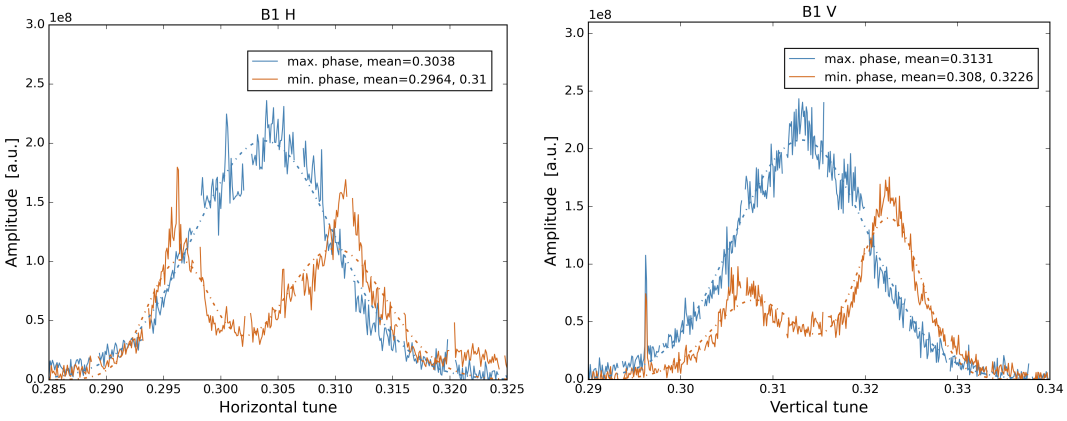

Figure 5.5: Measured beam spectra before and after phase knob change (Beam 1 shown as an example), at the head-on position, for each of the transverse planes.

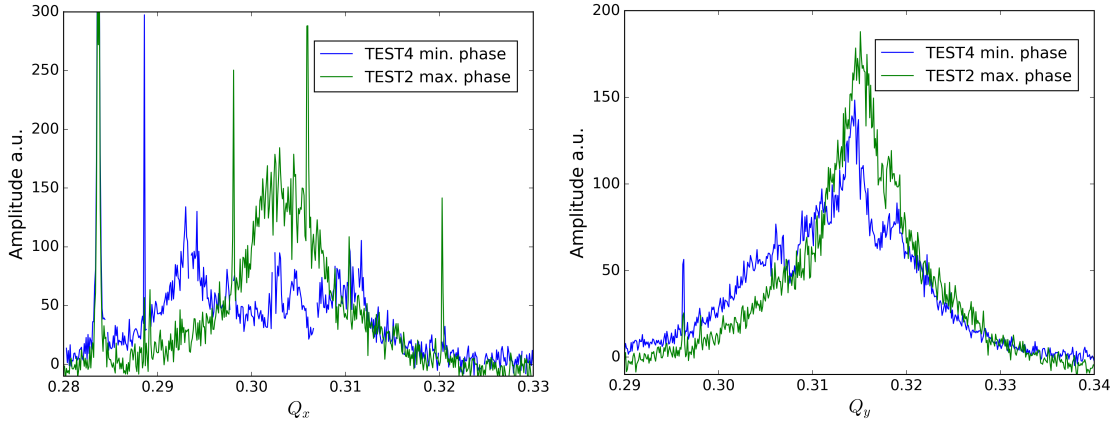

(a) $\Delta = 1.3\sigma$

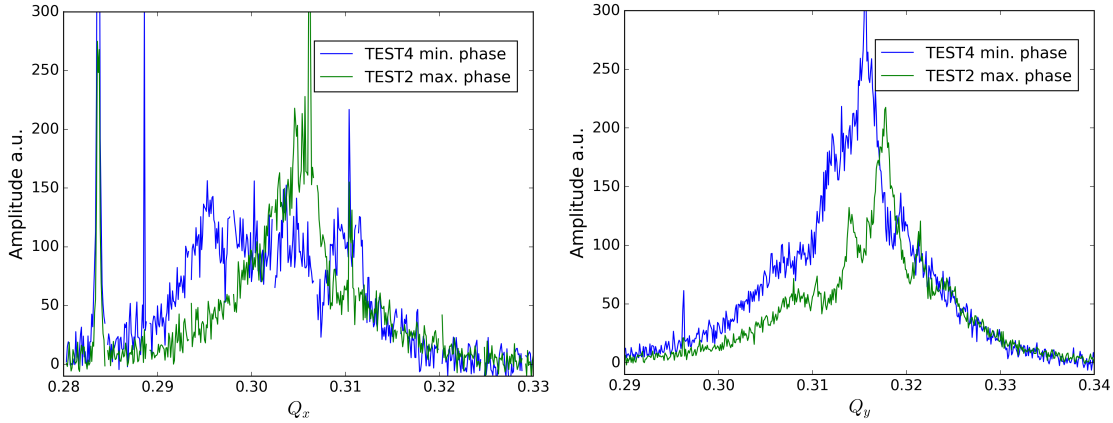

(b) $\Delta = 2.6\sigma$

Figure 5.6: Comparison of the measured transverse spectra at minimizing (TEST4) and maximizing (TEST2) phase knobs with 1.3σ separation (top) and 2.6σ separation (bottom) in the vertical plane.

5.3 Transverse emittance cross-check

For the experiment, it is crucial to estimate the beam parameters well enough to be able to reconstruct the beam-beam parameter with good accuracy. During each of the tests, the wire scanners (WS) were run regularly to check the transverse emittances. The raw data were refitted in the post-processing and scaled with measured β-function (from Tab. 5.3), according to Eq. 1.9. The same procedure was used for emittance measurement at the synchrotron light monitor (BSRT) location, based on the continuous beam size measurement. The errors for both WS and BSRT measurements include the main contribution of 3% systematic uncertainty from the optics measurements. The BSRT data are available every second, but for the purpose of comparison to other measurements, it was averaged per minute. The two-beam average emittance was also extracted from all emittance scans performed both at ATLAS and CMS (as described in Sec. 1.3.2). The accurate β^* measured with the k-modulation technique was used, with reduced uncertainty as summarized in Tab. 5.4. This error was combined with the fit uncertainty. In order to compare all possible emittance measurements, the two beams average is used for the WS and BSRT data. A very good agreement was found for the WS and experiments measurements, as shown in Fig. 5.7.

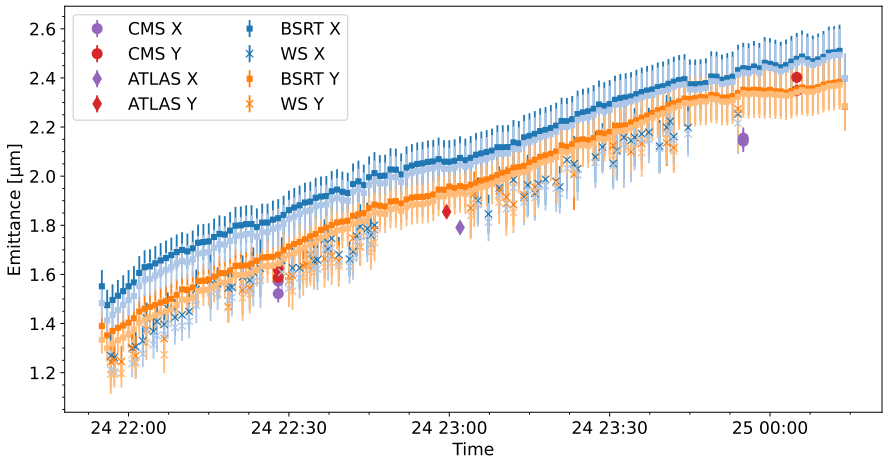

Figure 5.7: Measured normalized average emittance comparison during fill 8037 - time evolution from BSRT, and measurements from wire scanner (WS) and separation scans results at CMS and ATLAS experiments. Different shades of the same color correspond to different bunches, in the case of the measurement at ATLAS, the average of all bunches is shown.

The BSRT is consistent with other measurements in the vertical plane but appears to be significantly overestimated in the horizontal plane. It is expected that the BSRT absolute scale might not be perfect, as the online optical corrections need to be adjusted for the efficiency evolution. Thus, the WS measurements were used throughout the experiment for the calculation of the beam-beam parameter, and BSRT relative changes were used to interpolate in the case of lack of WS measurement.

5.4 Experimental characterization of multi-IP beam-beam effects

To measure the full beam-beam bias induced by a collision, the step-function scan was designed. It consisted of repetitive steps of moving the beams into head-on collision, followed by full separation ($\Delta > 6 \times \sigma$). This test was repeated for two different filling schemes, to observe the effects of single additional collisions (2 IPs configuration, including ATLAS and CMS), as well as the multi-collision beam-beam biases (3 IPs configuration, additionally including ALICE).

5.4.1 Head-on collisions in a two-IP configuration

Each test consisted of four measurements of the full beam-beam effect, and it was performed firstly at CMS, then at ATLAS, and at the end repeated at CMS. The decay of the beam-beam parameter was observed from 0.01 to 0.006 towards the end of the fill. The overview of the two tests performed with the CMS as the observer is shown in Figs. 5.8. The specific luminosity measured at CMS is shown, scaled to the first head-on step, to make the observation of the relative changes easier. The uncertainty was defined from the standard error on the mean of the measurements at each step. The background bandwidths indicate the observed standard deviation. The corresponding measurement is also shown at ATLAS in Fig. 5.9. As foreseen, the distinctive change in the luminosity induced by the beam-beam interaction at another location is observed. The relative luminosity bias values are collected in Tab. 5.5, obtained with reference to the average of the closest head-on points. These values are expected to be the same by design when neglecting the slightly changing beam parameters during each of the tests.

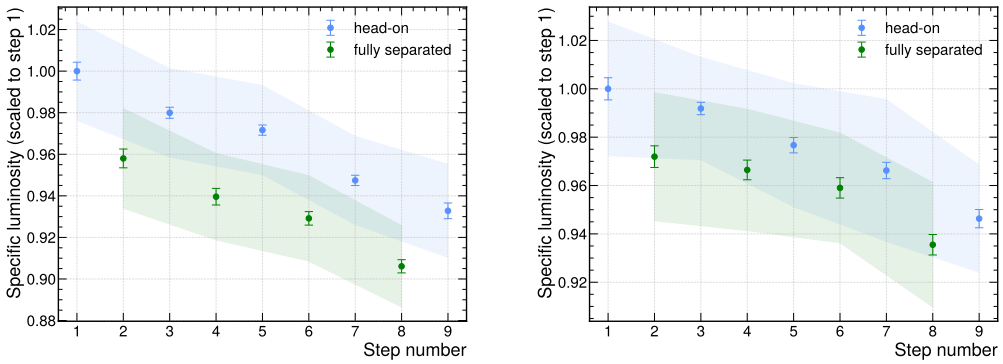

Figure 5.8: CMS specific luminosity during the step-function scans, at high (left), and lower BB parameter (right).

witness	IP5				IP1				IP5			
ξ_{start}	0.0086				0.0067				0.0056			
step #	2	4	6	8	2	4	6	8	2	4	6	8
bias [%]	3.21	3.58	3.01	3.41	2.42	2.64	2.34	1.98	2.46	1.89	1.37	2.23
stat. [%]	0.45	0.35	0.33	0.32	0.34	0.35	0.35	0.35	0.45	0.39	0.46	0.42

Table 5.5: Luminosity bias per full separation step.

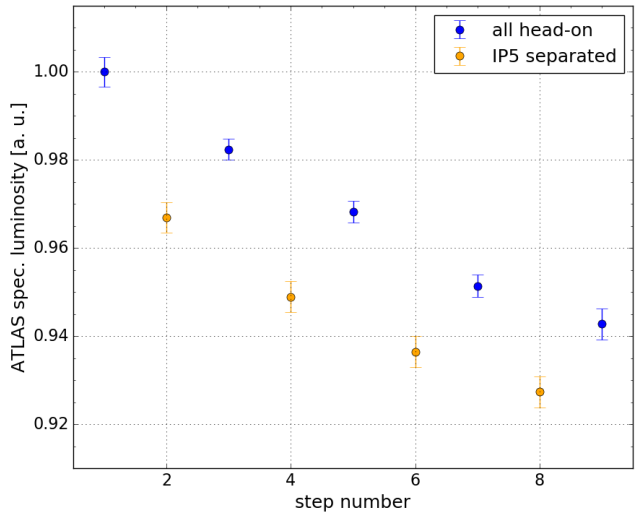

Figure 5.9: ATLAS specific luminosity during the step-function scan.

The comparison of all measurements to the parameterized COMBI simulation predictions is presented in Fig. 5.10, showing an excellent agreement. The results are plotted as a function of the beam-beam parameter, which changes during each of the experiments and was estimated based on the intensity (from FBCT) and emittance (from BSRT) changes. It corresponds to the reverse chronological sequence.

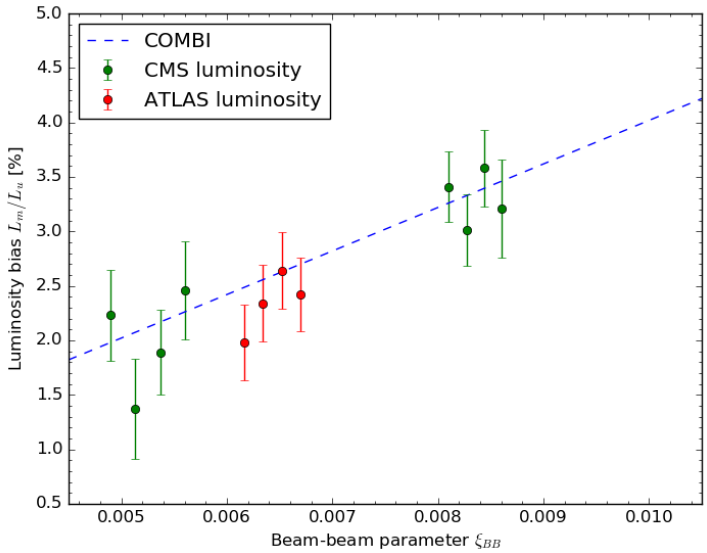

Figure 5.10: COMBI simulated luminosity bias induced by the additional collision as a function of the beam-beam parameter (dashed line), compared to the test results at both ATLAS (red points) and CMS (green points).

The relative changes during the step-function scan on bunch size measured at the BSRT are shown in Fig. 5.11. All the points are normalized to the first head-on measurement, thus the first point in

each plot is always fixed to 1. The linear slope, as estimated from the difference between the last and first measurements head-on, is extracted from all points to remove the effect of the emittance blow-up. A very good agreement with COMBI predictions was observed for the vertical sizes of Beam 2 bunches, where the effect is most pronounced thanks to a favorable phase advance of the beating from the beam-beam interaction to the BSRT location. In contrast, for other cases, the anticipated effect is significantly smaller, less than 1%, and the measurement does not align with the expectations. One of the possible explanations is the discrepancies between the model-predicted and measured phase advances at this location, (as indicated in Tab. 5.1). The biggest observed difference between the measurements and the MADX model of 0.05 [2π] was used to estimate the possible bias on the COMBI predictions, based on Eq. (3.51). It is sensitive to the measured phase advance, and it is indicated in the figures by the blue bands. The vertical plane for Beam 2 (bottom right in Fig. 5.11) gives the possibility of the most accurate predictions. On the measurement side, there is also another possibility, that the effect may be too subtle to detect, potentially being covered by instrumental limitations.

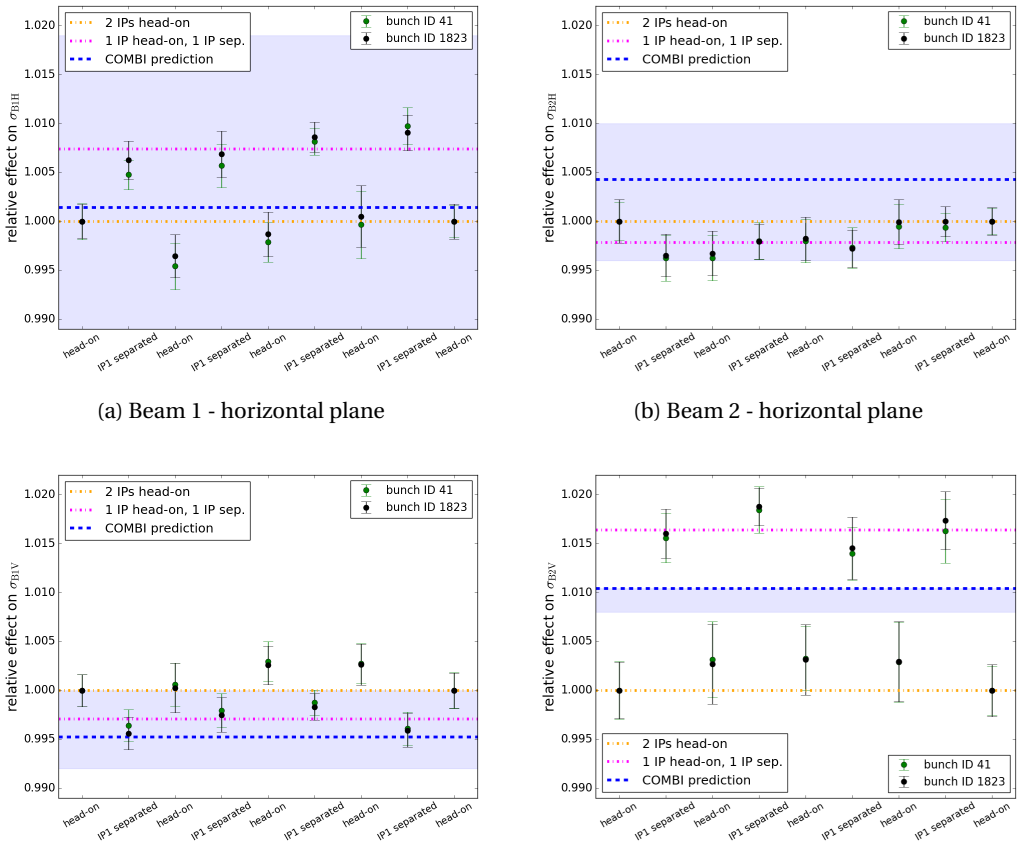

(a) Beam 1 - horizontal plane

(b) Beam 2 - horizontal plane

(c) Beam 1 - vertical plane

(d) Beam 2 - vertical plane

Figure 5.11: BSRT measurements shown per bunch in each beam and plane during step-scan (points), for the first experiment at $\xi = 0.0086$, with IP5 as witness. The yellow and pick lines indicate the average measured effect from the two configuration steps in the test. The blue line indicates COMBI prediction with calculated systematic error indicated by the band.

The example fitted ADT spectra measured during the experiment are shown in Fig. 5.12. Spectrum

profiles do not strictly follow a specific distribution, due to the presence of couplings, noises, and more unknown nonlinear effects. The peak position can be relatively precisely predicted by a Gaussian fit, giving the measurement of the mean tune shift. In each of the step-scans, the single collision tune shift, calculated as twice the mean tune shift, was measured equal to corresponding $\xi \pm 5\%$ for both collision points. As expected, the two collision tune shift was measured to be exactly double that.

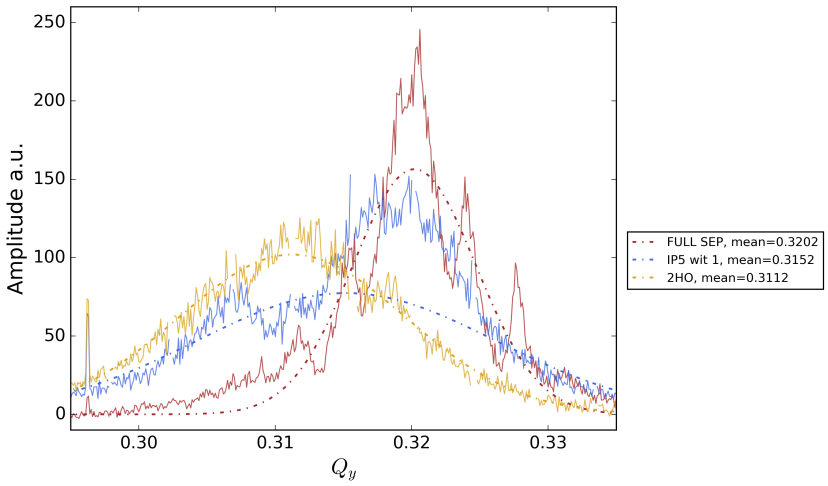

Figure 5.12: Measured changes to the vertical tune spectra depending on the collision configuration during the experiment - reference nominal tune is fitted ('FULL SEP' in red), without the presence of any collisions, compared to changes induced by single collision ('IP5 wit 1' in blue) and two collisions ('2HO' in yellow). The dashed lines in corresponding colors indicate Gaussian fits to the data used to extract mean tunes. [100]

5.4.2 Head-on collisions in a three-IP configuration

Including another collision was only possible with ALICE due to its symmetric location around the LHC ring. The filling pattern where all bunches experience the same number of collisions was used to reduce the statistical uncertainty of the measurement. However, no reliable luminosity measurement was available at IP2. Additionally, the beams collided at the half crossing-angle of 1000 μrad (summing the internal and external angles), causing the geometrical reduction factor of $S = 0.90$. The step-function scan was repeated, with separating or collapsing one IP at a time. The overview of all luminosity measurements at both ATLAS and CMS is shown in Fig. 5.13. In this test very stable beam conditions were observed, providing the measurements at the two experiments at very similar beam-beam parameter. The measured beam-beam-induced biases in all steps during this experiment are summarized in Tab. 5.6 with reference to the interpolated in time head-on specific luminosity (based on 3 head-on points). Very good agreement with simulation was achieved in the case of the 2 IPs. In the case of single-IP biases, the measured effect was smaller than predicted, especially for IP2 separations. The biggest bias is attributed to the imperfect orbit changes, with H-V coupling, displacement knob leakage, and magnetic hysteresis, affecting most significantly the reference head-on points.

The transverse tune spectra were more complicated to analyze in this test as coherent modes were present when separating the IPs as predicted in the simulation studies. In these cases, the maximum tune shift is estimated from the fitted π mode instead of the fit to the incoherent part of the spectrum.

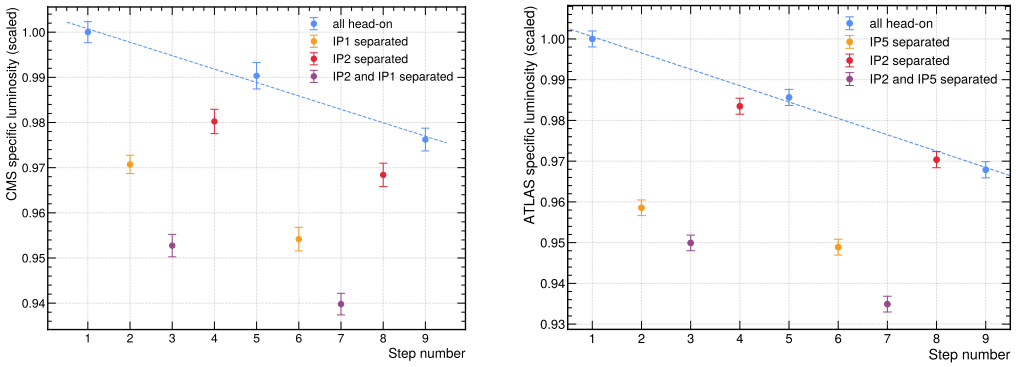

Figure 5.13: Specific luminosity at CMS (left) and ATLAS (right) while separating the other IPs (as indicated in the legend).

witness	IP5			IP1		
ξ_{start}	0.009			0.009		
separation step	IP1	IP1&IP2	IP2	IP5	IP5&IP2	IP2
bias part 1 [%]	-2.67	-4.21	-1.17	-4.02	-4.47	-0.67
stat. [%]	0.21	0.26	0.27	0.20	0.20	0.19
bias part 2 [%]	-3.26	-4.32	-1.06	-3.41	-4.41	-0.26
stat. [%]	0.26	0.24	0.28	0.20	0.20	0.20
COMBI [%]	-3.79	-5.66	-1.74	-3.77	-4.86	-0.99

Table 5.6: Luminosity bias per full separation step. The relative bias per step is calculated as a difference of measured luminosity with respect to the average of the two closest head-on points. The bias was measured twice for each configuration and it is shown in separate rows.

For configurations including all three collisions, the suppression of coherent modes from the symmetry between IP1 and IP5 was still effective. The summary of the measured tune shifts depending on the collision configuration is shown in Fig. 5.14. The conservative estimation of tune uncertainty was used $u(\Delta Q) = 0.002$.

5.5 Measured separation-dependence of the beam-beam bias

The beam-beam corrections are applied separately at each step of a separation scan. Thus, it is crucial to validate the simulated bias dependence on the nominal separation. The full vdM-like scans were performed both at ATLAS and CMS, in the configuration with collisions only at these IPs. The measured luminosity scan curves are fitted with a Gaussian (Figs. 5.15-5.16), as expected from Eq. 3.49. The points are shown from a head-on point just before the beginning of the scan. At the following steps, the beams are fully separated, to $6 \times \sigma_{\text{nom}}$ and scanned across each other in steps of $2 \times 0.43\,\sigma_{\text{nom}}$, each lasting 30 s. The σ_{nom} is defined from the default LHC parameters - which is the limitation of the operational application. It uses a constant emittance equal to $\epsilon_{LHC} = 3.5\ \mu$m, which for the case of the experiment turned out to be overestimated. The local β-function is used from the lattice parameters - $\beta^* = 11$ m

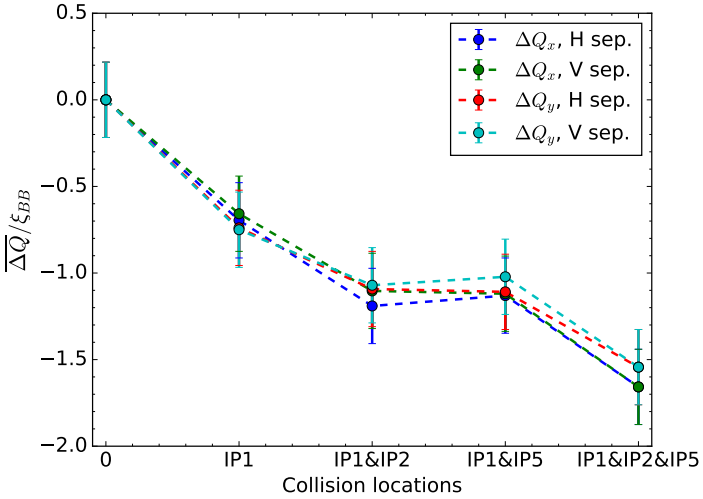

Figure 5.14: Measured mean tune shift as a function of the number of collisions (at various locations), for both transverse planes and both separation (sep.) directions used in the experiment.

for both IP1 and IP5. The middle and the last point also indicate the measurement at the head-on beam position. However, the middle scan point at head-on configuration includes an extra separation, as shown in Fig. 5.17 for an example scan (between 9-10th min.).This effect is causing up to $\sim 15\,\mu$m extra separation between the beams. The measured σ is obtained from the emittance scans, executed just after each of the experiments, separately at each IP. As the σ_{nom} is usually much bigger than the measured σ, the steps were overestimated to $\sim 1.3 \times \sigma_{\text{meas}}$. Thus, many of the high separation points are expected to have a very similar beam-beam bias, as they are already above $6 \times \sigma_{\text{meas}}$ separation, confirming the consistency of the measurement.

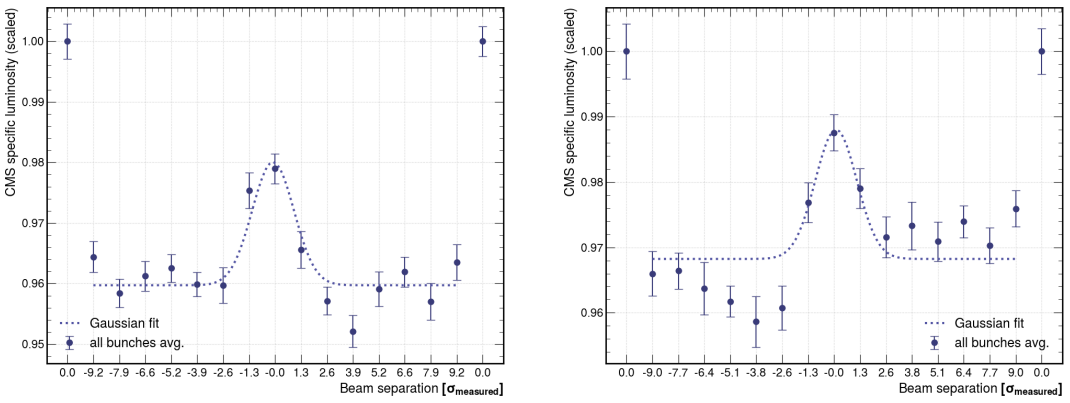

Figure 5.15: CMS specific luminosity relative change during separation scans in x-plane (left) and y-plane (right) at ATLAS, shown with a fitted Gaussian function.

The first and the last head-on points were used to extract the approximately linear decay of specific

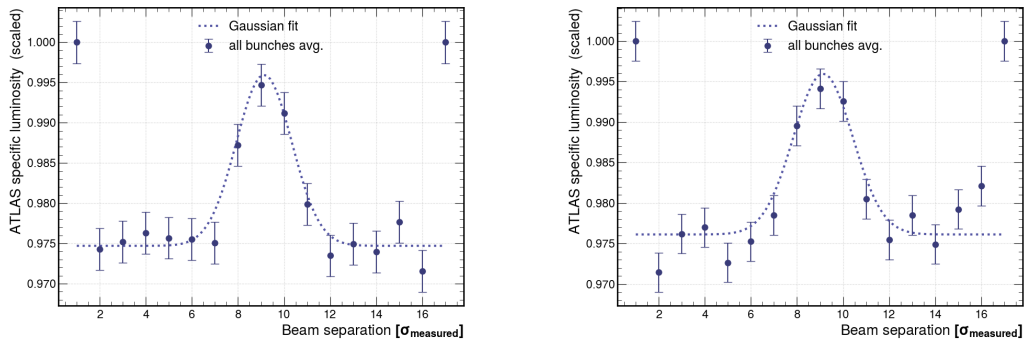

Figure 5.16: ATLAS specific luminosity relative change during separation scans in x-plane (left) and y-plane (right) at CMS, shown with a fitted Gaussian function.

luminosity with time due to the emittance changes, within a single test time span. Thus, the measurement along the separation is shown with reference to the head-on position (fixed at 1). Since the points at high separation in Fig. 5.15 for the scan in y-plane are at different levels for the two directions of the beams' separation (negative or positive separation sign), the assumption on the linear specific luminosity change with time is very likely to be partially wrong for that part of the test.

The results are more consistent for the ATLAS witness observations, at lower beam-beam parameter and more stable beam conditions (see Fig. 5.16) - the full separation points are fitted at the same specific luminosity level. Nevertheless, all four fits indicate the effect of a total specific luminosity change between $4-2.4\%$, which is consistent with the expected range of the total effect change over the time of the experiment (based on ξ_{start}). Fits parameters are summarized in the middle part of the Tab. 5.7. The first two are shown in terms of the relative effect on specific luminosity to the head-on points before and after the scans. For the other two parameters, the assumption of the nominal separation set by the magnets was used. Additionally, the fitted bunch width is translated to units of σ_{meas} , which is extracted from the emittance scans at the observing IP, performed just after each of the experiments. For IP5 as the witness, the results are up to 30% underestimated, but they are improved in the second part for IP1 as a witness - with the agreement within 10%. This indicates that the fit improves with the decreased total scan range (and thus higher scan step granularity). The fitted means are compared in the last row to DOROS measurements of the beams offset in the middle of the scan at the peak measurement, at the scanning IP. These results are not fully consistent with expectations, especially for the first experiment. The improvement is expected if the experiment would be repeated with the increased granularity of scan points, especially in the steep gradient region below $3 \times \sigma_{\text{meas}}$.

Additionally, in Fig. 5.17 the the beam-beam deflection is visible in the scanning horizontal plane at IP1 (blue curve). The linear orbit drift is removed from the DOROS data based on the luminosity optimization position before the scan compared to the positions after the end of the scan. In the next step, the nominal displacements are removed from the DOROS data with a linear fit to all separation steps, which are indicated with the dashed lines. The nominal separation movement in the scanning plane causes the movement in the other plane due to residual coupling (green dashed curve). The non-closure of the orbit displacement bump is also present as the correlated movements at another location, here IP5, are observed. The maximum amplitude of the deflection is consistent with the

witness	IP5		IP1	
plane	H	V	H	V
ξ_{start}	0.010	0.0083	0.0068	0.0062
peak	0.982	0.988	0.997	0.996
constant	0.960	0.968	0.974	0.976
bunch width [σ_{meas}]	0.70	0.76	0.91	1.06
mean [μm]	-79.7	37.4	49.8	35.2
DOROS B1-B2 [μm]	-13.6	-17.5	-9.0	-14.1

Table 5.7: Gaussian-fit parameters of the luminosity bias along the separation steps for each witness IP and each scan in the transverse plane.

analytical prediction from Eq. (3.15), and equals 8 μm after taking into account geometric change from the IP to BPM location at the level of 0.5 μm. However, the change of the deflection sign at high separation should not be present (min. 1-4 and 15-18 in Fig. 5.17). This distortion of the observed beam-beam deflection is partially attributed to the additional non-linear component to the measured orbits from the hysteresis effect in the superconducting corrector magnets, which can be significant at the injection energy [101]. The correction for this effect was not applied.

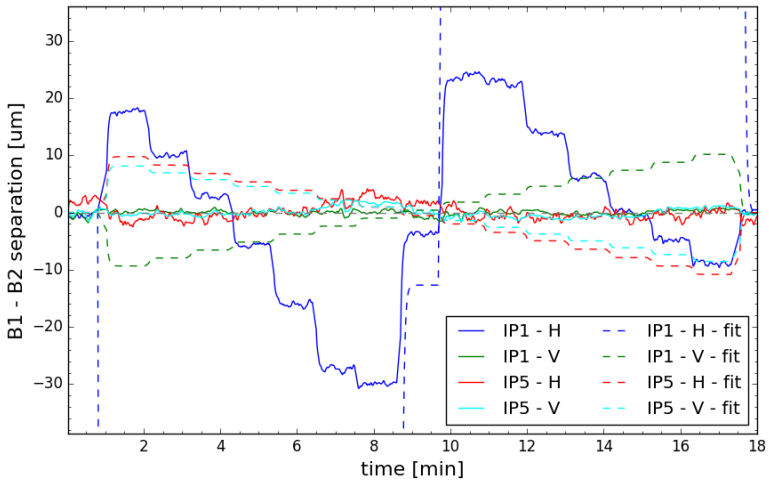

Figure 5.17: Beams separations as measured by the DOROS in transverse planes, at IP1 and IP5 during separation scan in the horizontal plane at IP1, after removing fitted knob displacements and linear orbit drift. Fitted knob displacements are shown with dashed lines.

The distinctive separation-dependent beam-beam interaction-induced changes can be also observed in the beam width measured at the BSRT location. The examples are shown in Fig. 5.18, very good agreement between the separately measured bunches was found.

By extracting the mean transverse tune shift from the ADT-measured spectra, the dependence in the scanning and non-scanning direction was reconstructed. It is presented in Fig. 5.19 for both horizontal and vertical scans, showing a good agreement with the COMBI predicted dependence, shown before in Sec. 4.3 (in Fig. 4.7).

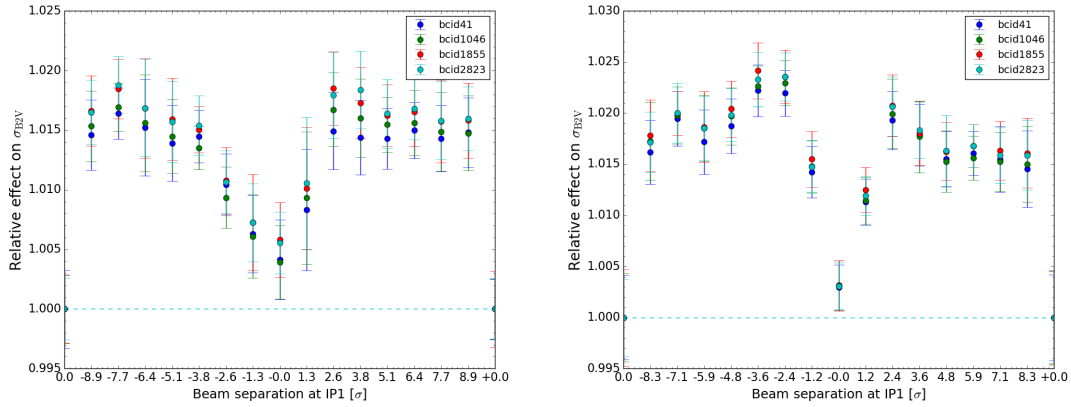

(a) Horizontal scan

(b) Vertical scan

Figure 5.18: Beam 2 size measurement at the BSRT the vertical plane during separation scans at IP1, normalization to head-on points before and after the scan was used to highlight the relative effect.

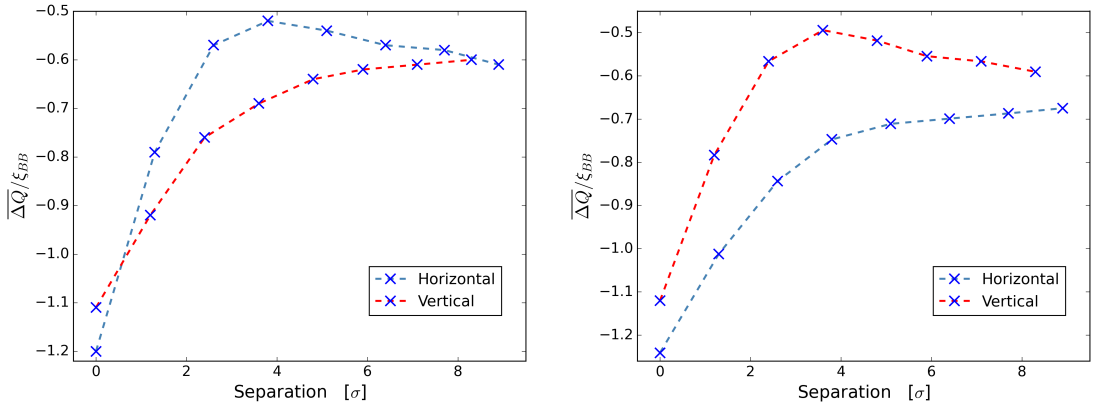

(a) Horizontal scan

(b) Vertical scan

Figure 5.19: Measured tune shift change in units of the beam-beam parameter ξ_{BB} for the horizontal (blue dashed line) and vertical (red dashed line) planes, during a horizontal (left) and vertical (right) separation scans at IP1. Measured points are indicated with the cross symbol, curved are added to guide the eye. [100]

Conclusions

These tests proved the fundamental assumptions in the beam-beam interaction effects modeling to be valid. The impact on the luminosity via the amplitude-dependent beta-beating was measured with very good agreement. The variations induced by the beam-beam interaction were measured on luminosity, betatron tune spectra, and bunch sizes, with a very good agreement with expectations for different collision configurations. The luminosity measurement precision of 0.2-0.3% at low energy conditions was sufficient to measure the beam-beam interaction effects below 0.5% level. The accuracy can still be improved with dedicated corrections. As a result of these beam-beam experiments, some effects

were recognized that might be useful from the diagnostics point of view:

- there is an optimal phase advances configuration between the IPs that can be used to enhance the luminosity,
- suppression of the coherent beam-beam modes allows for a more straightforward tune spectra interpretation with the possibility of more accurate measurement of the mean betatron tunes,
- the phase advances could be further optimized to the BSRT location (IP4) to enhance observation of beam-beam effects and decrease the measurement uncertainties associated with phase advance error sensitivity. The latter can be also profitable for the accurate emittance measurement with BSRT as it requires exact knowledge of the local β-function.

Absolute luminosity calibration Part III

This part brings together all the ingredients discussed in the previous chapters. The first Run 3 absolute luminosity calibration is presented using the vdM method. The data of the recently upgraded BCM1F-μTCA luminometer (discussed in Sec. 2.8) are used. The beam-beam effects studies presented in Chapter 4 are implemented as corrections and to define the related systematic uncertainty. This effort leads to a cutting-edge result of achieving a preliminary luminosity measurement with 1.3% total systematic uncertainty. This opens a way to sub-1% precision in the future results as discussed further in Sec. 8.

6 Beam-related systematic effects

In this section, the first Run 3 luminosity calibration of the proton-proton collisions data set at $\sqrt{s} = 13.6$ TeV recorded in 2022 with the CMS experiment is reported. The BCM1F-μTCA measurement is calibrated with the van der Meer (vdM) method [24, 25], also introduced in Sec. 1.2.1. The analysis techniques were built on the earlier CMS luminosity measurements [33, 102, 103, 104, 105]. vdM and other beam-separation scans were recorded during the November 2022 fills 8379 and 8381. Four standard vdM and two beam-imaging (BI) scans are used to obtain the final BCM1F-μTCA calibration. The complete CMS luminosity calibration using the main CMS luminometer (HFET) and other independent systems is the effort of the whole BRIL project within the Luminosity Physics Object Group (LUM POG), and it is reported separately in [106].

This chapter is structured as follows. Firstly, the BCM1F-μTCA specific beam-induced background corrections in the vdM conditions are discussed in Sec. 6.1. It is followed by the summary of other beams-related biases, coming from their intensities (see Sec. 6.2), the relative positions (see Sec. 6.3), and the non-factorization of the beams transverse distributions (see Sec. 6.5). Further, the beam-beam effects are discussed in detail in Sec. 6.4. The first BCM1F-μTCA calibration performed after applying corrections is presented in Sec. 6.5. In a separate part, the uncertainties related to the transition to physics conditions and long-term stability are discussed (see Chapter 7). Finally, in Chapter 8 the summary of all the systematic uncertainties is presented with the outlook towards high-precision legacy results including combined data sets from multiple years.

6.1 Background

The beam-induced background and detector-specific noise are measured in dedicated super-separation scans. During such scans the beams are separated by 5σ in both transverse planes, resulting in a total of almost 7.1σ separation. This is done to ensure that there is no transverse overlap of the two beams, and thus no luminosity. BCM1F-μTCA has a very good sensitivity to the backgrounds, and it is also used to provide online background measurement to the CMS and the LHC (as discussed in detail in Sec. 2.8.8). The signal measured in two such periods during the 2022 calibration, is shown in Fig. 6.1. The measurement statistical uncertainty is minimized by extending the super-separation periods to 5 min. However, there is still a significant uncertainty that is a result of the very low particle rate. Thus, the average of all collidable bunches is used as the background that is subtracted directly from all BCM1F-μTCA rates measured during separation scans. The observed change in the background levels during the fill with decaying per-bunch intensities was close to -5%, which is very close to the average

change of the total beam currents. This change is approximately twice as small as the uncertainty on the background measurement. The total correction from the background measurement to σ_{vis} was on average $-1.5 \pm 0.1\%$.

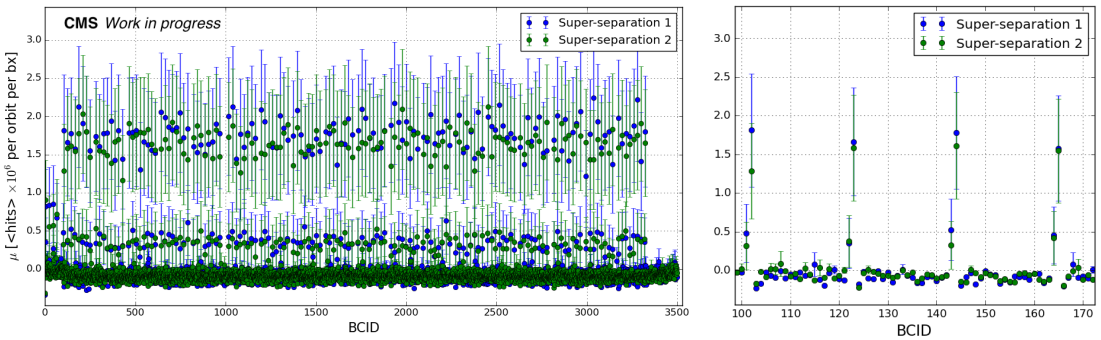

(a) Full orbit

(b) Zoom-in

Figure 6.1: Per-bunch rates measured by the BCM1F-μTCA during two super-separation scans in vdM fill. The top band points correspond to the collidable bunches that were used for collision background estimation. There are only four non-colliding bunches at the beginning of the orbit. The lower band points above the noise level around zero correspond to the incoming beam-induced background (that is measured 12.5 ns ahead of the collision signal) - clearer visible in the zoom-in (right side).

6.2 Bunch charge

The single bunch-pair charge normalization of the BCM1F-μTCA rates measured during vdM scans is required before the fitting is done, in order to remove dependence on the intensity decay with collisions. It is performed using the well-established procedures: the relative per-bunch intensity differences are obtained from the FBCT measurement [37], and these are scaled to the absolute beam current from much more accurate DCCT measurement [38] in order to establish the correct absolute luminosity scale. The number of protons per bunch is estimated with the formula documented in previous CMS calibrations [33].

Further, the corrections for ghost and satellite charges are applied [107]. The former corresponds to the charges that are trapped in the non-colliding part of the LHC orbit, while the latter corresponds to the charges within each of the BCIDs used in the calibration, but outside of the central RF bucket (1 BCID = 10 RF buckets). These charges are primarily measured by the BSRL monitors, and the results for 2022 vdM fill were presented in Ref. [108]. The ghost and satellite charge fractions were all found to be between 0.1% and 0.4%. These results were additionally confirmed with preliminary LHCb ghost-charge measurements using the Beam Gas Imaging (BGI) [109]. The average effect on the visible cross section in terms of correction was estimated to be 0.43%.

To account for the precision of the DCCT measurement [38], 0.2% uncertainty was assigned. Additionally, the maximum difference of 0.15% between the two methods of measuring the ghost charge was assigned as an uncertainty, giving a total of 0.25% uncertainty on the bunch current normalization.

6.3 Beam position

The movement of the beams during any separation scan is induced by a local change of the closed orbit. It is caused by a combination of the change of currents in the 5 dipole magnets located just outside the experimental cavern. This defines the nominal separation value Δx_{nom}.

The beam position analysis for the vdM scans has three separate components:

- Length scale calibration - the scale of the nominal positions Δx_{nom} set by the corrector magnets can differ slightly from the real one Δx_{real}, which can be expressed via the length scale factor α_{LS}:

$$\Delta x_{\text{real}} = \alpha_{\text{LS}} \Delta x_{\text{nom}}. \tag{6.1}$$

  It is obtained separately for each beam and each plane. The measurement of such a first-order scale factor was performed by analysing the constant separation scans. In this procedure, both beams are moved simultaneously over a distance of $4/5\sigma_{\text{nom}}$ in parallel to each other, keeping a constant displacement between them of $\Delta = \sqrt{2}\sigma_{\text{nom}}$. During such movement, the beam spot is displaced, which can be measured with the CMS Tracker. These data are fitted with a linear function to extract the length scale α_{LS}. This is repeated in the two possible beam directions. Although the results differ slightly for each beam, each plane, and the movement direction, in all cases the final length scale was found to be close to $\alpha_{\text{LS}} = 0.995$. It is expected that this parameter is rather stable over time, which was confirmed by the results that considered constant-separation scan data from three different fills (~ 2 months apart). Thus, the weighted average of all these scans was used to define the final length scale, and the error on the mean and the weighted spread were combined to assign the uncertainty. This was used to estimate the effect on σ_{vis} , resulting in the final correction of $-1.00 \pm 0.12\%$.

- Linear orbit drift (LOD) during a scan can cause the beams to move with respect to each other, beyond the desired nominal separation. This change is measured by comparing the positions between the two head-on steps: before and after the scan. A linear interpolation is used to apply a correction at each separation step, which is then added to the nominal separation. This correction is different for each scan-pair and spans the range of a -0.3% to 0.3% correction on σ_{vis} . The uncertainty is defined from the comparison to the effect of the correction based on the LHC arc BPMs data, which yields a difference of 0.1%.

- Residual orbit drift (ROD) includes the non-linear orbit drifts, excluding the length scale and beam-beam deflection discussed in the next section (Sec. 6.4), but including the possible magnetic hysteresis effects. This is studied using the DOROS data (all measurements within a scan), which are fitted per scan with a non-linear model. The model has three separate components: linear DOROS length scale with respect to the nominal separation, displacement in the non-scanning plane, and beam-beam deflection with varying amplitude. While the per scan correction is typically bigger than LOD, the effect on the final average is negligible, equal to 0.02%. However, it provides a significant, twofold improvement in the per-scan RMS of the visible cross section. The uncertainty is estimated as the combination of the uncertainties of the fit model parameters, equal to 0.35%.

The complete analysis is described in detail in [110].

6.3.1 Towards per-bunch orbit correction

An alternative method was also used to verify the linear orbit drift correction. The displacement of the orbit centroid from the mean was measured from the calibration fits, as described in Sec. 2.8.9. This measurement has a very good agreement (~ 0.1 μm) between different luminometers as shown in Tab. 6.1 for BCM1F-μTCA and HFET. The standard deviation σ shows the bunch-to-bunch differences that are the result of the orbit bump leakage of the small displacements from other IPs than the CMS. This is shown in Fig. 6.2, for the scan with the biggest σ. The data are grouped by the bunch family - depending on the number of collisions each bunch in measured bunch-pair undergoes. A significant difference is observed for the bunches colliding at IP2, especially for Beam 1. This is caused by the significant separation and crossing angle at that IP, causing a deflection that is propagated through the LHC lattice to CMS. The DOROS-measured orbit drifts are based on the full-orbit signal, which is sensitive to each bunch's distance and charge (not a simple average of all bunches), hence it is not straightforward to compare. However, assuming the bunches are well centered before each scan thanks to the luminosity optimization, a cross-check can be performed. A good agreement between the measured means before applying the correction with OD was found for most of the scans, the comparison is shown in Tab. 6.2 - differences smaller than 1 μm were marked in green. The OD values in grey cannot be verified (non-scanning direction). There are two scans (BI1 in X and vdM2 in X) where the magnitude of the correction appears to be underestimated and was marked in orange. There are also a few cases (vdM1 in Y, vdM3 in X and Y) where the sign of the correction is wrong, causing the displacement to be bigger after applying the correction (marked in yellow). The results are very different with residual corrections applied, but only slight improvement was observed for nominal residuals, hence it is not included.

The measured per BCID displacement could be used in the future to apply the per-bunch orbit correction, as in some cases the displacement can be significantly different (> 1 μm) from all bunches' average orbit. A residual change (0.1 μm) in the displacement is expected during the scan from the beam-beam orbit effect propagation.

		HFET [μm]		BCM1F-μTCA [μm]		**BCM1F-μTCA /HFET**	**difference [μm]**
		av. Fit Mean	σ	av. Fit Mean	σ		
vdM1	**X**	2.991	0.946	2.863	0.968	0.96	0.128
vdM1	**Y**	1.617	0.479	1.646	0.572	1.02	-0.029
BI1	**X**	-3.984	0.933	-4.078	0.971	1.02	0.094
BI1	**Y**	-0.589	0.389	-0.627	0.442	1.07	0.038
BI2	**X**	-1.611	0.876	-1.600	0.895	0.99	-0.011
BI2	**Y**	0.331	0.366	0.286	0.405	0.86	0.046
vdM2	**X**	-8.293	1.013	-8.281	1.063	1.00	-0.012
vdM2	**Y**	-1.589	0.425	-1.589	0.534	1.00	-0.001
vdM3	**X**	0.337	0.986	0.411	1.011	1.22	-0.075
vdM3	**Y**	1.065	0.405	1.036	0.466	0.97	0.028
vdM4	**X**	-1.588	0.945	-1.614	1.028	1.02	0.026
vdM4	**Y**	-0.727	0.414	-0.662	0.488	0.91	-0.065

Table 6.1: Average orbit centroid displacements as extracted from the vdM fits to HFET and BCM1F-μTCA measured rate. The standard deviation σ indicated the bunch-to-bunch differences. The comparison between the detectors in the last column shows very good agreement.

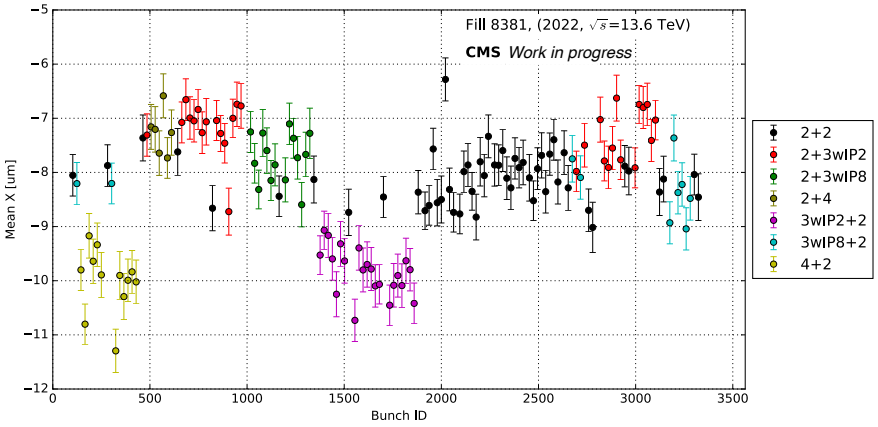

Figure 6.2: Per bunch fitted Gaussian mean for the scan in X plane during vdM2 as extracted from BCM1F-μTCA measurements. Colors were used to differentiate between bunch-pair families - the black points correspond to the reference bunches with a minimum number of collisions (2) at CMS and ATLAS. The labels indicate the number of collisions for different beams with + sign between them (Beam 1 bunch on the left of +, and Beam 2 bunch on the right side of + sign). In cases where the bunch collides in 3 locations, the specific IP is indicated after 'w' (short for 'with'). This is not done in cases of 4 collisions as it includes all possible LHC IPs.

		av. Fit Mean [μm]	**OD X [μm]**	**OD Y [μm]**	**difference [μm]**
vdM1	**X**	2.99	-2.21	0.55	0.78
vdM1	**Y**	1.62	0.45	0.25	1.86
BI1	**X**	-3.98	2.27	0.72	-1.72
BI1	**Y**	-0.59	-1.66	0.61	0.02
BI2	**X**	-1.61	0.67	0.50	-0.94
BI2	**Y**	0.33	-0.54	-1.13	-0.80
vdM2	**X**	-8.29	3.16	-0.90	-5.13
vdM2	**Y**	-1.59	2.87	1.69	0.10
vdM3	**X**	0.34	0.30	1.02	0.64
vdM3	**Y**	1.06	0.24	0.51	1.57
vdM4	**X**	-1.59	1.80	0.25	0.22
vdM4	**Y**	-0.73	-0.90	0.61	-0.11

Table 6.2: Average orbit centroid displacements as extracted from the vdM fits by HFET compared to the middle point of the linear orbit drift correction. Colors indicate agreement between the measurements, from good (< 1 μm, green), worse (≥ 1 μm, yellow) and completely opposite sign (orange). The non-scanning plane orbit drift is grayed out.

6.4 Beam-beam effects

The beam-beam effects during the vdM scans are corrected in a twofold way, as discussed in detail in Chapter 3.4. The deflection induced by the accumulated force of the counter-rotating beams is calculated, based on the Basetti–Erskine formula [74]. The calculated average displacement for the first scan in fill 8381 is shown in Fig. 6.3 (top). The correction is made by adding these values to the nominal separation of the two beams. The second correction, for the optical distortion, is applied directly to the measured rates. The parameterization is used (described in Sec. 4.2) to evaluate the beam-beam induced luminosity bias at each separation step for any desired beam-beam parameter and transverse tunes $f(\xi, Q_x, Q_y)$ [21]. The example results of this calculation for the first vdM scan in fill 8381 are shown in Fig. 6.3 (bottom). Both corrections are calculated for each bunch individually, the sidebands indicate the spread of the per-bunch results.

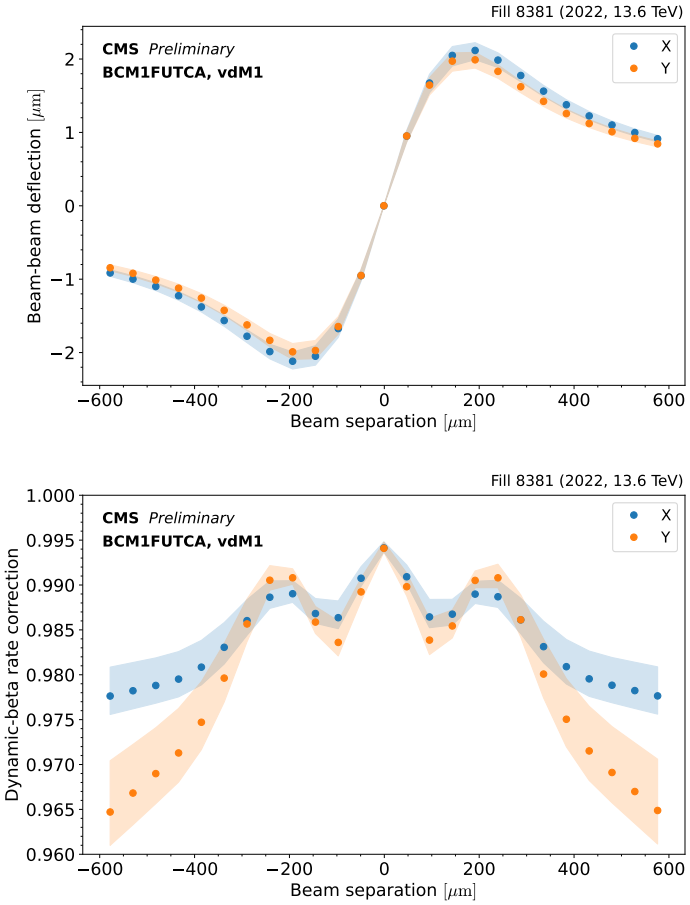

Figure 6.3: Beam-beam deflection (top), and Dynamic-beta corrections (bottom) are shown for the first scan-pair (in X and Y planes) in fill 8381 with input from the BCM1F-μTCA measured Σ_x, Σ_y. The average effect is indicated with dots and sidebands covering the minimum and maximum values used for the per-bunch correction.

In order to mimic the bias induced by the beam-beam collisions at non-scanning IPs, the tune shift is applied, which is proportional to the number of additional collisions at the non-scanning IPs (as discussed in Sec. 4.3). The full beam-beam corrections calculated per bunch during one of the 2022

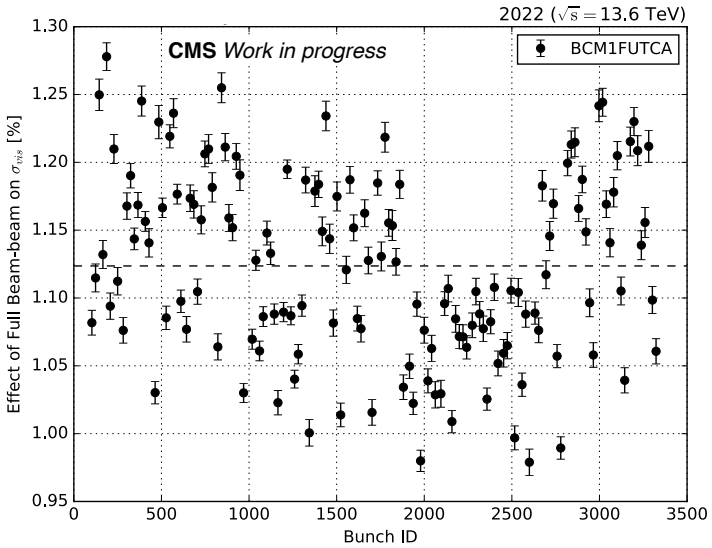

Figure 6.4: The full beam-beam bias on BCM1F-μTCA σ_{vis} , shown for the last VdM scan. The group of bunches between BCIDs 2000–2500 can be distinguished, corresponding to bunches with the least number of collisions (only CMS and ATLAS) and hence resulting in the systematically smaller correction.

vdM scans is shown in Fig. 6.4. The average effect of the total correction on the σ_{vis} is +1%. The separate averages per scan are summarized in Table 6.3. The two corrections are anti-correlated, hence their effect is significantly bigger when considered separately. In the example scan, the total correction consists of 2.36% correction from the beam-beam deflection and −1.35% correction from the dynamic-beta distortions.

	VdM1	**BI1**	**BI2**	**VdM2**	**VdM3**	**VdM4**	**Average**
BCM1F-μTCA	0.90%	0.93%	0.96%	1.01%	1.00%	1.03%	0.97%

Table 6.3: Impact of the combined beam-beam corrections on the σ_{vis} value obtained for BCM1F-μTCA detector and scans with the DG fit, for scans in fill 8381. This is calculated as the σ_{vis} value after applying the full beam-beam corrections compared to the σ_{vis} value without applying these.

The observed increase in the total correction throughout the fill is attributed to the increase of the beam-beam parameter due to strongly damped beam size in the y plane. This is visible in Fig. 6.5a, for elliptical and round beam-beam parameters from Eqs. (3.23) and (3.22). In the correction calculation the latter is used. Significant differences up to 10% were also observed in the per bunch beam-beam parameter. The regular pattern of a lower value was observed in approximately every 4^{th} bunch. This was linked to the patterns in the measured per bunch charge.

The measured emittances and their ratio evolutions during all scans in fill 8381, including all 6 main scan-pairs, are shown in Fig. 6.5b. The decrease in vertical emittance was estimated to be 0.045 μm/h, giving the total change of −20% over the two scanning blocks in fill 8381 (∼11 h). The damping was also observed in the horizontal plane, with a smaller change of about −7%, as it is convoluted with emittance increase due to intra-beam scattering.

The biggest beam-beam parameter measured in fill 8381 was 5.5×10^{-3}; significantly higher than the typically assumed vdM conditions value (as indicated in Tab. 4.1).

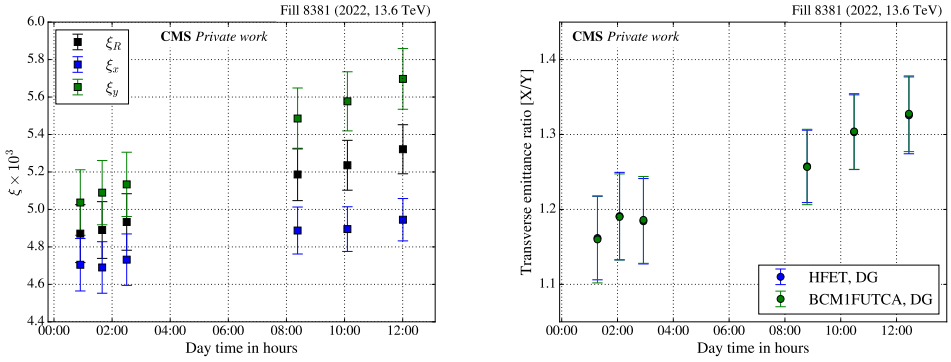

(a) Beam-beam parameter

(b) Transverse emittances ratio

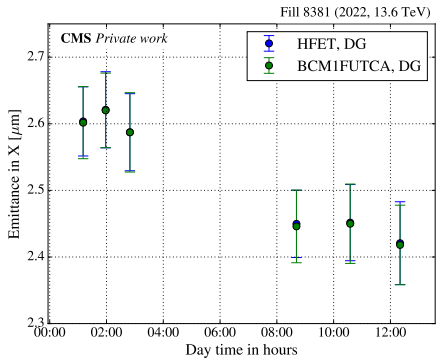

(c) ϵ_x

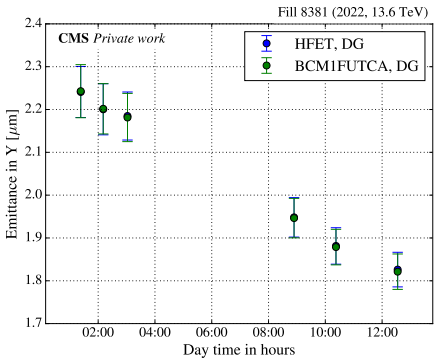

(d) ϵ_y

Figure 6.5: Evolution of the average beam-beam parameter and transverse beam emittances (convoluted for the two beams), and their ratio during vdM session in fill 8381, as measured by the CMS luminometers (HFET measurement added for validation). Double Gaussian (DG) fit was used (see Sec. 6.6) to extract convoluted widths from the scans. The spread in per-bunch values is indicated with error bars.

In Figure 6.6 the distributions of Σ_x, Σ_y are presented (diagonal subplots) as well as their correlation (off-diagonal subplots). Each of the set of four plots corresponds to a single scan-pair, arranged in chronological order, additionally, the color code is used to indicate different bunch families. In both planes, the family-dependent groups become more clearly separated with time (most clearly visible in Fig. 6.6f). This dependence is not removed fully with the described correction. Thus indicating additional beam-beam interaction-induced bias that has an impact on the per bunch widths that is not included in the correction model.

The systematic uncertainty is evaluated by taking into account various contributions to cover the correction model imperfections. These can result directly from the lattice uncertainties; on the nominal LHC tunes, which have the uncertainty of $u(Q) = \pm 0.002$ $[2\pi]$, and the nominal β^* value at CMS. In order to reduce uncertainty attributed to the latter, the 2022 measurements of the vdM optics were used [111], using the K-modulation technique [98]. The results are summarized in the Tab. 6.4. The

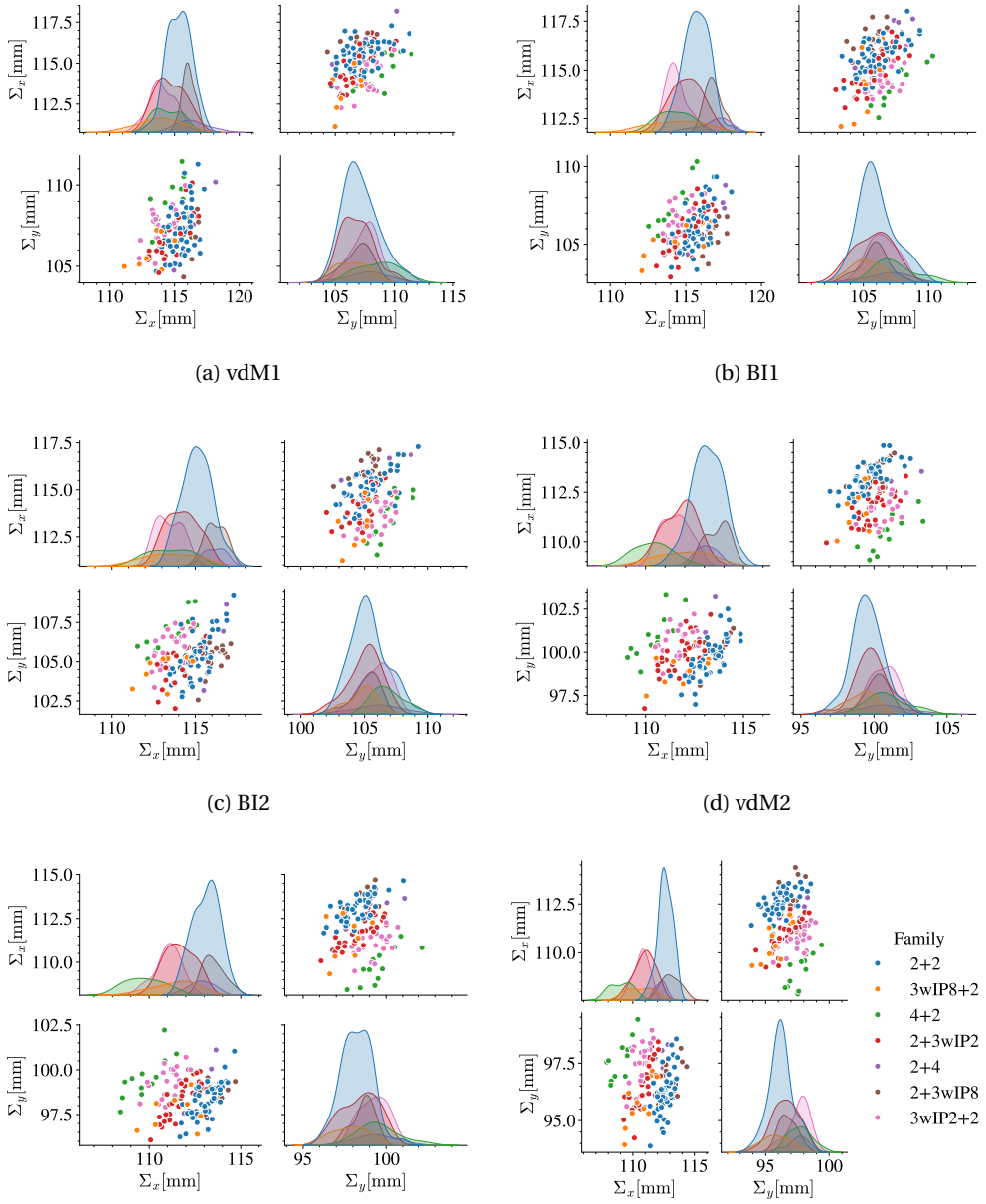

Figure 6.6: Per vdM scan-pair distributions of BCM1F-μTCA measured bunch widths in the two transverse planes (subplots on diagonal) and their correlation (off-diagonal). The color-code is used to separate the bunch families and the plots are shown in chronological order.

assigned systematic uncertainties include the measurement, reproducibility, and tune errors, however, these are much smaller than the difference between the β^* values for the two beams. As the corrections are based on the measured convoluted beam size of the two beams, the uncertainty has to be defined from the biggest difference between the two beams $u(\beta^*) = \pm 1.16$m ($\sim 6\%$). The propagation of these

uncertainties to σ_{vis} is evaluated using the parametrization. The biases from non-Gaussian tails of

Beam	Plane	β^* [m]	error [m]
B1	H	19.46	0.30
B1	V	19.22	0.27
B2	H	18.3	0.26
B2	V	18.08	0.27

Table 6.4: β^* measurements and systematic uncertainties in the vdM configuration for IP5, as measured by the OMC team in 2022 [111].

the transverse beam profiles and the beam-to-beam imbalance are also considered. Additionally, the polynomial parametrization has an attributed uncertainty, as well as the multi-IP tune-shift model, including the phase advance-related uncertainty.

Considering that the beam-beam parameter during the vdM session was evaluated to 5.5×10^{-3} or lower, the upper boundary is used to estimate the final uncertainties. The number of total collisions from the filling scheme is shown in Fig. 6.7, indicating that most of the bunch-pairs had 1 or 1.5 (on average) additional collisions. The effect on σ_{vis} was evaluated and all contributions are summarized in Tab. 6.5. The last three entries in the table were estimated with dedicated simulations [21]. The total uncertainty is estimated to be 0.37%.

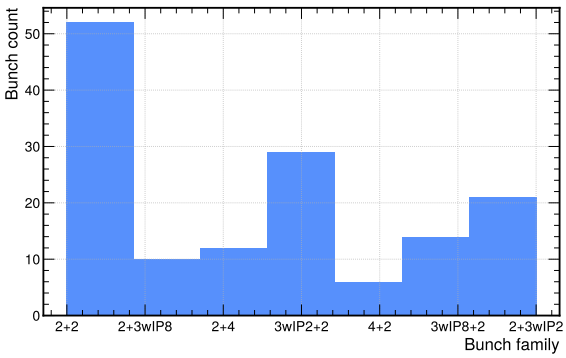

Figure 6.7: Bunch count per family, depending on the number and location of collisions, based on the filling scheme. Family labels are showing collisions per bunch separately for Beam 1 and 2 (in a form B1+B2). In case collisions are taking place just in CMS and ATLAS or all IPs just the numerical labels are used - correspondingly 2 and 4. In case of ambiguous 3 collisions - the IP number per beam is specified.

6.5 Non-factorization

The vdM calibration method includes the assumption on factorizable beam distributions in the transverse planes, as the luminous area is expressed as a product of the x- and y-dependent functions (as introduced in Sec. 1.2.1). In reality, there is always a correlation between the two planes that causes the non-factorization and thus a bias to the vdM calibration method. To estimate this bias, the transverse proton densities of the two beams are reconstructed. The true overlap product gives the luminous area

Source	Uncertainty
Nominal tunes	0.24%
Phases & multi-IP	0.20%
β^* at CMS	0.11%
Non-Gaussian tails	0.10%
BB imbalance	0.10%
Polynomial	0.10%
Total	0.37%

Table 6.5: Contributions to total beam-beam systematic uncertainty.

that can be compared to the expectation for the vdM scans.

The CMS luminosity measurements employ two methods to asses the non-factorization [33, 102, 103, 112]:

- The beam-imaging method [113, 114, 115], where the reconstructed vertices [116] measured during a set of four beam-imaging scans are simultaneously fitted to extract the two transverse proton densities.

- The simultaneous analysis of standard vdM, and vdM with an offset in the non-scanning plane, or diagonal scans. In the latter, the beams are moved simultaneously in x and y, such that the scan axis is rotated by 45 deg with respect to a standard vdM scan. The combination of the data from all these scans allows to probe different parts of the luminous area. The simultaneous fit of rate information from more than one type of scan allows for evaluation of the non-factorization.

The second method proved to be more accurate in estimating the correction for 2022 vdM scans. The full analysis was presented in [117], resulting in the correction of $0.98 \pm 0.35\%$ with additional model uncertainty of 0.7%. Thus, the final uncertainty of 0.8% on σ_{vis} was assigned.

6.6 Calibration

After all the possible corrections discussed in the previous sections are applied, the normalized BCM1F-μTCA rates with the measured per bunch current, in order to obtain the so-called specific luminosity, are fitted as a function of the beams separation. The double-Gaussian (DG) function was chosen as the fit model, after checking multiple models. It is defined as:

$$f_{\text{DG}}(\chi) = \frac{r_\chi}{\sqrt{2\pi}} \left[\frac{\epsilon_\chi}{\sigma_{1\chi}} \exp\left(-\frac{(\Delta\chi - \mu_\chi)^2}{2\sigma_{1\chi}^2} \right) + \frac{1-\epsilon_\chi}{\sigma_{2\chi}} \exp\left(-\frac{(\Delta\chi - \mu_\chi)^2}{2\sigma_{2\chi}^2} \right) \right], \tag{6.2}$$

where $\Delta\chi$ ($\chi = x, y$) is the beam separation, r_χ is the peak rate, μ_χ the peak position parameter, and ϵ_χ is the weight between 0 and 1 of the first Gaussian in the sum. The effective value of the "width" of the fit model Σ_χ is then calculated from the two fitted widths $\sigma_{1\chi}, \sigma_{2\chi}$ as [33]:

$$\Sigma_\chi = \frac{\sigma_{1\chi}\sigma_{2\chi}}{\epsilon_\chi\sigma_{2\chi} + (1-\epsilon_\chi)\sigma_{1\chi}}. \tag{6.3}$$

The results have good convergence and fit quality, very similar to those obtained from a single-Gaussian (SG) plus 4^{th}- or 6^{th}-order polynomial models, within 0.2%. Example final fit results are shown in Fig. 6.8. The simplest SG model overestimates the final calibration by 1% due to high values at high separation, which can be attributed to either the bunch distribution being over-populated at the tails or poor statistical precision

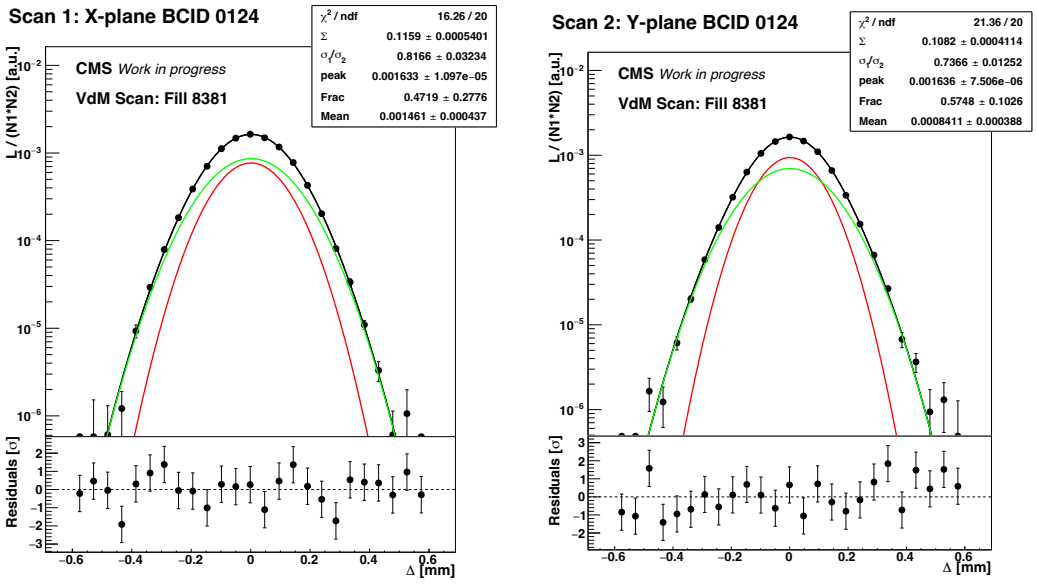

Figure 6.8: Example DG fits to the BCM1F-μTCA rates normalized with per bunch intensities during the first vdM scan pair in x (left) and y (right) for BCID 124.

The convoluted beam widths measured with BCM1F-μTCA and compared to the main CMS luminometer HFET are shown in Fig. 6.9-6.11. In Fig. 6.9 the overview of measured per-bunch widths along the LHC orbit is shown. In the x plane, distinctive groups can be noticed, which correspond to 'bunch family' (indicated also in Fig. 6.2 and discussed in Sec. 6.4) dependent bunch size changes. In the y-plane the Σ spread is similar, but the pattern is associated with the injector chain-induced structures, as it is every 8th bunch that has the biggest or the smallest size. This period is equal to the number of bunches injected into LHC at the same time for 2022.

The time dependence of the distributions of the scan parameters for each of the scans can be observed in Fig. 6.10. Two clearly separated clusters are visible which correspond to the two scanning blocks, separated by almost 6 h. The overall increase in the peak rates is measured with time, which is strongly correlated to the damping of emittances measured on Σ_x, Σ_y. This observation proves the stability of the vdM fill setup, these observations would not be possible in the physics data-taking when the beam lifetime is much worse and emittance changes involve many more components (e.g. long-range beam-beam interactions). The per-scan correlations of all these parameters are summarized in Tab. 6.6. While a very strong correlation is observed for the fitted peaks measured in the x- and y-plane, this is not the case for the transverse bunch widths, which show a small correlation in the first scan-pair, evolving towards no correlation in the last scan-pair. This could potentially be linked to the transverse emittances evolution in a synchrotron. As the LHC lattice is not symmetric in the transverse planes, different effects have to be considered. Coulomb scattering of particles within a bunch causes the

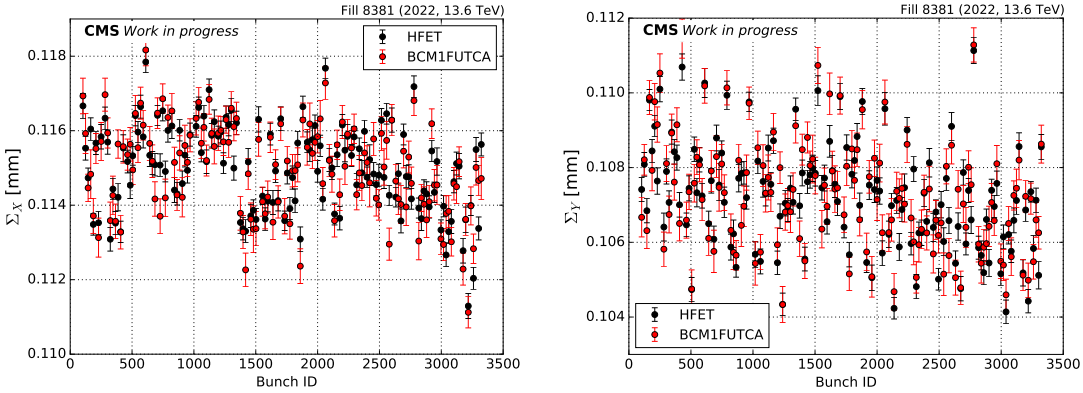

Figure 6.9: Overview of the per-bunch Σ results measured during the first vdM scan-pair in fill 8381 by BCM1F-μTCA in x- (left) and y-plane (right), compared to the main CMS luminometer HFET.

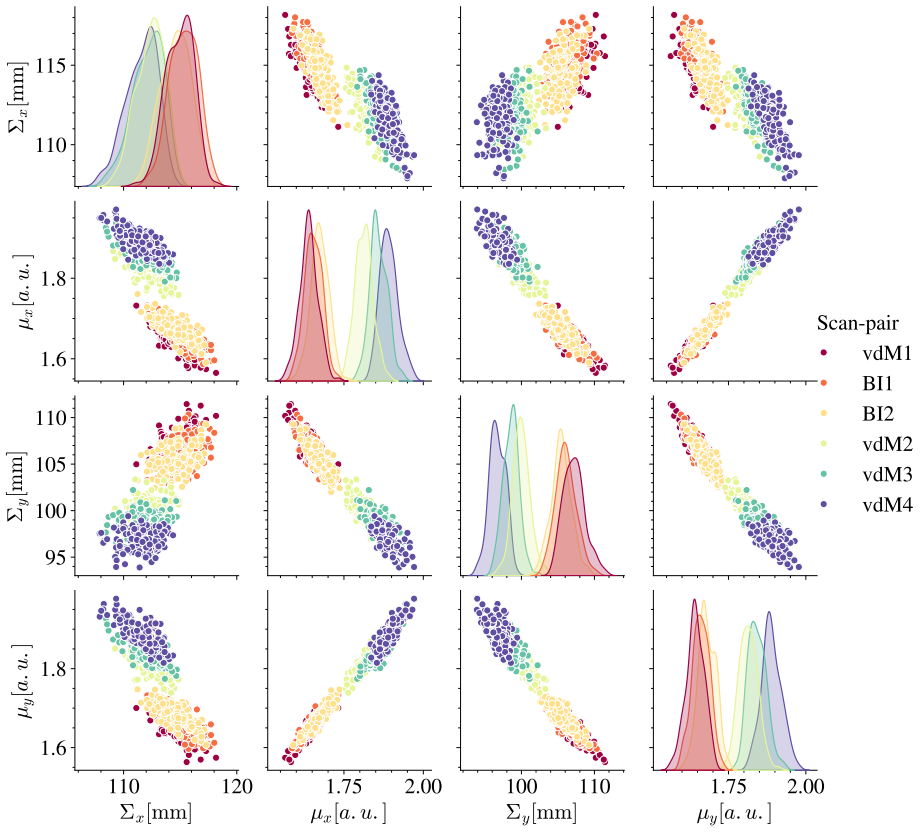

Figure 6.10: Overview of the BCM1F-μTCA measured vdM scan parameters - normalized distributions are shown on diagonal and their correlation on off-diagonal subplots. The color code is used to separate the vdM scan pairs and highlight the changes in time.

momentum exchange in the transverse and longitudinal planes, causing the emittance to increase with time [3], especially in the horizontal plane, where the dispersion is much higher. The momentum offset can be also caused by synchrotron radiation. As it is a statistical quantum mechanical process it could lead to a reduction of the correlations between planes.

	vdM1	BI1	BI2	vdM2	vdM3	vdM4
$\rho(\Sigma_x, \mu_x)$	-0.78	-0.78	-0.76	-0.76	-0.71	-0.74
$\rho(\Sigma_x, \Sigma_y)$	0.43	0.40	0.33	0.20	0.09	0.01
$\rho(\Sigma_x, \mu_y)$	-0.68	-0.73	-0.72	-0.68	-0.74	-0.73
$\rho(\mu_x, \Sigma_y)$	-0.77	-0.79	-0.77	-0.66	-0.58	-0.54
$\rho(\mu_x, \mu_y)$	0.88	0.92	0.92	0.88	0.84	0.85
$\rho(\Sigma_y, \mu_y)$	-0.86	-0.84	-0.81	-0.76	-0.60	-0.54

Table 6.6: Per scan correlations (ρ) of the BCM1F-μTCA measured scan parameters - bunch widths Σ_x, Σ_y and the fitted rate at the peak μ_x, μ_x.

The evolution of all bunches average Σ_x, Σ_y is shown in Fig. 6.11. The BCM1F-μTCA is compared to HFET measurements, showing a very good agreement. The systematic change in time can be observed in the y-plane. In both planes, the step between each 3 scan-pairs is present due to damping during the time gap (~ 6 h).

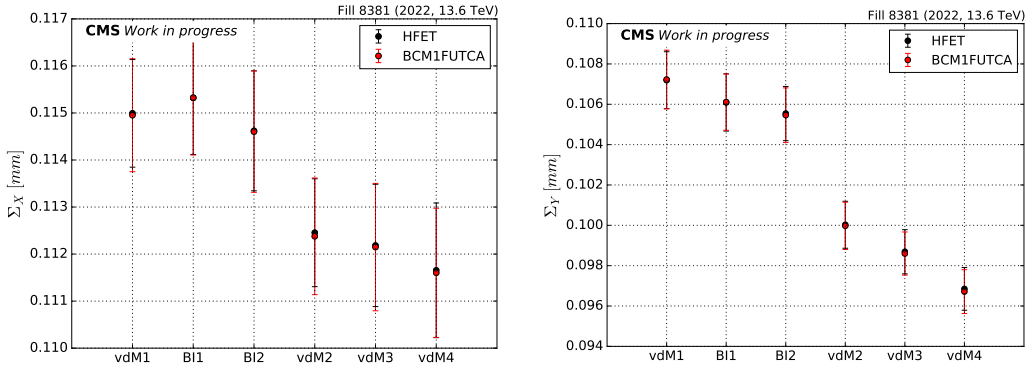

Figure 6.11: Overview of the full beams average Σ results measured during all vdM scan-pairs by BCM1F-μTCA in x- (left) and y-plane (right), compared to the main CMS luminometer HFET. The errors describe the spread in per-bunch Σ per scan.

The overview of the per-bunch measurements within a single scan pair is shown in Fig. 6.12a, indicating no colliding-pattern related dependence, that is present in Σ_x, Σ_y. Thus, the bunch-by-bunch variations are purely statistical and are estimated using the standard error on the weighted mean, resulting in 0.1%. This was validated with combined data from all scans and all detectors to improve the statistical error and is shown in Fig. 6.12b. Instead, the two bandwidths of data are emerging, with a period of 2 bunches, which could indicate a sensitivity to the formation of bunches in the injector chain. The overview of per-vdM-scan average results is shown in Fig. 6.13b. A good fit quality was obtained for all scans and all bunches, which is shown in Fig. 6.13a with χ^2 distributions. The model performs slightly better in the vertical plane. The final value is calculated as the weighted mean of all these results.

The BCM1F-μTCA visible cross section after applying corrections is 129.05 μb. To consider the step in the results from the two scanning blocks, the uncertainty related to the scan-to-scan variations is calculated from the RMS of all scans, resulting in 0.4% on σ_{vis} . The impact of the emittance evolution during a single scan-pair scan is expected to be included in this uncertainty. The calibration results were validated with consistency check by comparing the absolute luminosity throughout the vdM fill - the BCM1F-μTCA is in agreement with the main luminometer within 0.2%. If other independently calibrated systems (total of 5) are taken into account, the consistency is still very good, at the level of 0.4%.

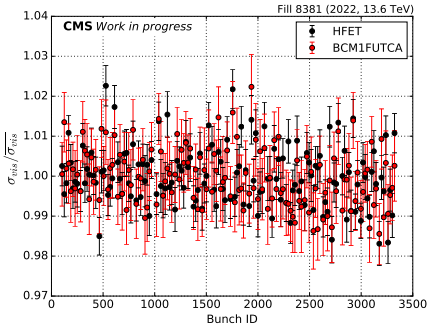

(a) Per-bunch σ_{vis} results from vdM1 normalized to all bunches average. Comparison of BCM1F-μTCA to HFET.

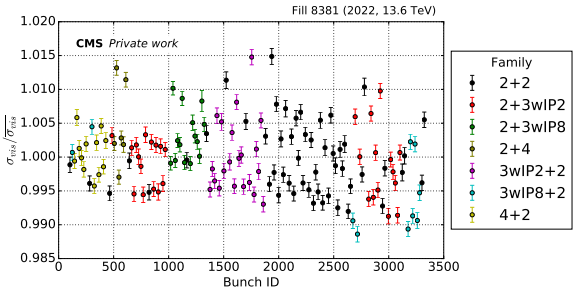

(b) Combined σ_{vis} results from all scans and all CMS luminometers normalized to all bunches average. Different colors are used for bunch-pairs belonging to the same family.

Figure 6.12: Normalized visible cross section results as a function of bunch ID.

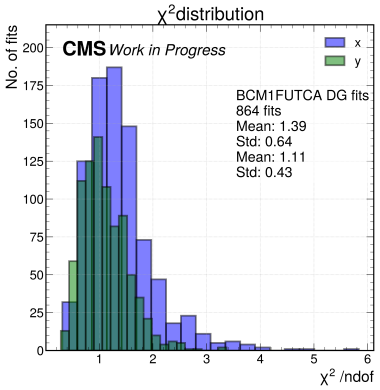

(a) χ^2 distributions of fits to each bunch data and all vdM scans, shown separately for the two scanning planes [66].

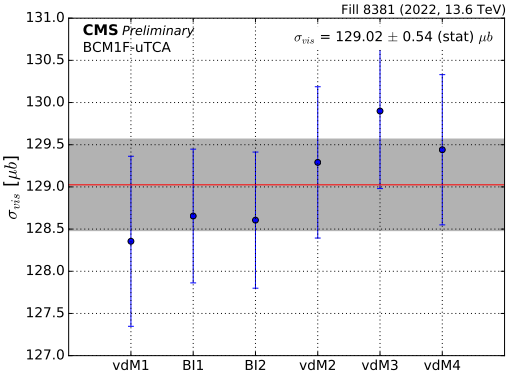

(b) Overview of the per-scan average σ_{vis} for all scans used in the final calibration.

Figure 6.13: Final BCM1F-μTCA σ_{vis} results.

7 Transition to nominal physics conditions

The vdM calibration presented in the previous chapter is meant to be used for the total integrated luminosity of 2022. This implies that the additional contributions from the detector performance throughout the year have to be considered. Firstly, the performance of the BCM1F-μTCA afterglow correction is shown in Sec. 7.1 and the residual uncorrected fractions are estimated to assign the corresponding systematic uncertainty. This is followed by the measurement of stability in Sec. 7.2 to correct for time-dependent inefficiencies. The outlook towards the post-2022 Run 3 data is also included as more dedicated data are available to study the detector performance. Lastly, the BCM1F-μTCA response linearity is discussed in Sec. 7.3, in terms of cross-checks with other CMS systems to estimate the related systematic uncertainty. Additionally, a preliminary study with dedicated beam-beam corrections is shown as an example of the cross-detector independent non-linearity measurement.

7.1 Afterglow correction residuals

The BCM1F-μTCA afterglow model is described in detail in Sec. 2.8.5. The full 2022 data sample was reprocessed applying the afterglow correction. The example fill is shown in Fig. 7.1 in terms of the visible cross-section-equivalent measured during an emittance scan. In the online data, the systematic difference is visible for the first bunches in each of the trains, as these are the least affected by the afterglow hits. After the activation fractions from each previous colliding bunch are subtracted in the reprocessing, the systematic difference is removed.

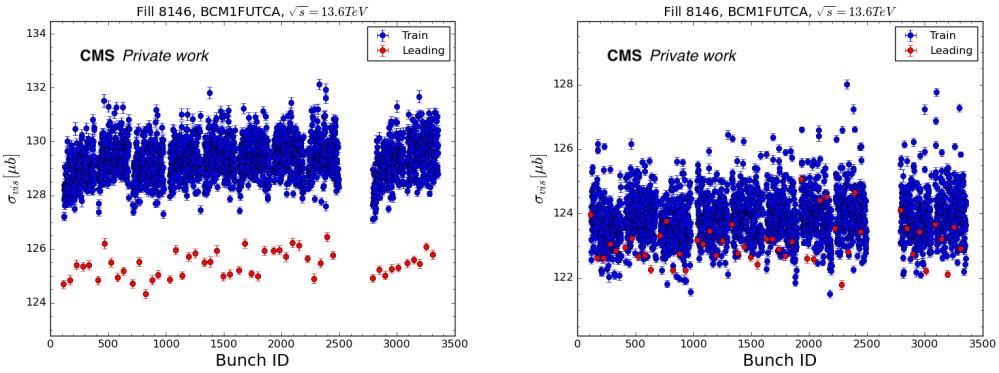

Figure 7.1: Per-bunch visible cross-section-equivalent measured during the emittance scan in one of 2022 fills before the afterglow correction (left) and after (right). The first bunch in each train is plotted in red.

The applied correction depends on the train length as well as on the total SBIL, thus ranging from -1 to -3%. The correction residuals were estimated based on the leftover rate fractions in the bunch-crossings following each of the trains with the LHC orbit. One hour of integrated data was used to estimate the average fractions per fill. The data are shown in Fig. 7.2, indicating the fractions to be below 0.1%. This is assigned as the systematic uncertainty of the afterglow correction.

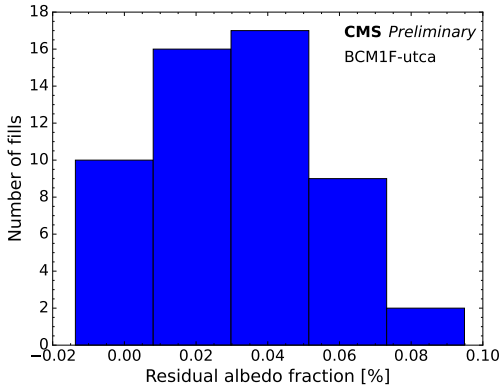

Figure 7.2: Afterglow correction residuals, calculated throughout 2022 fills, each entry includes 1 h of integrated BCM1F-μTCA rates.

7.2 Stability measurement and correction

The stability correction for the 2022 dataset is determined by monitoring changes in the emittance scan results throughout the operation. The reference point for the correction factor is the vdM session period, to correct for differences present before or after the vdM calibration. The results are shown in Fig. 7.3, with the vdM fill marked with the vertical green dashed line.

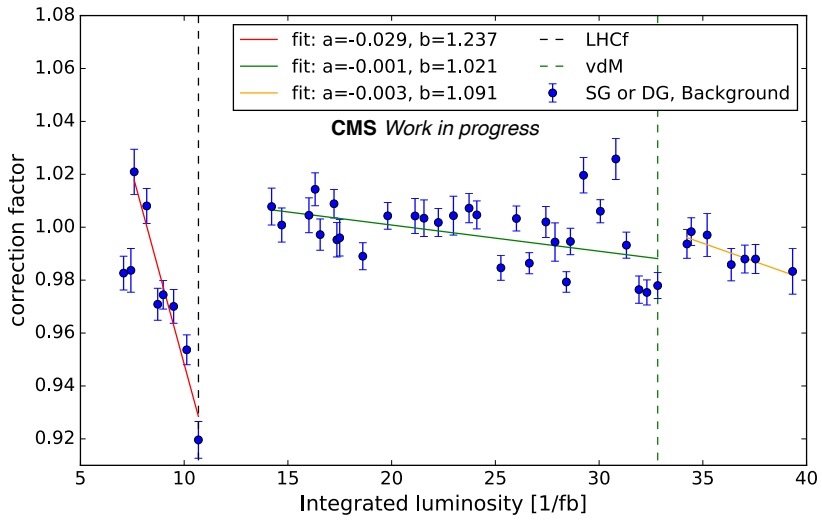

Figure 7.3: The stability correction factor was obtained from emittance scans throughout the year. The vdM period is taken as a reference (==1). Three periods were distinguished for a separately fitted correction: demarcated by the LHCf and vdM run periods.

The emittance scan data were corrected for the beam-induced background based on the non-colliding bunch signal. It is fitted using either a single Gaussian or double Gaussian function to obtain the relative constant (σ_{vis} equivalent). The per-fill beam-related systematic effects are not corrected leading to some variation between scans. Nevertheless, their impact is minimized by restricting the data sample to the scans performed at similar beam conditions. The outliers in the data can be attributed to short-term fluctuations in the average detector efficiency caused by multiple channels dropping out, owing to the sensor stability issue described in Sec. 2.8. This issue was present in a few fills during the data taking of the last 15 fb^{-1} of data in 2022. The data selection was based on the χ^2 of the fits to use only good-quality fits and with additional cuts based on the standard deviation of all results per scan.

The BCM1F-μTCA measurements were fitted separately for three distinctive periods. The main degradation in efficiency was observed after the technical stop (before the LHCf run marked with the vertical black dashed line). It was attributed to the evolution of the effective doping concentration and thus the increase in the full depletion voltage with accumulated fluence. In parallel, there was also a degradation in the efficiency of optical converters. Their configuration was adjusted and the high voltage set-point was increased to enhance the efficiency. The subsequent periods were fitted with two linear functions separately, before and after vdM scans fill (indicated by the dashed green line). Some outliers are observed at the end of the second period (fitted with a green curve), attributed to multiple overlapping issues. During this period, a new detector operation-related challenge emerged with an abruptly increasing leakage current with prompt radiation on some of the channels, up to the protection limit. Moreover, the cooling temperature had to be temporarily increased, potentially

affecting the sensor performance. All these factors could have an impact on the overall stability. For the vdM session the detector configuration was carefully optimized, justifying the separate treatment of the last fitting period (yellow curve). The early Run 3 period between 7-10 fb^{-1} was further excluded due to the previously mentioned issues, as well as the unavailability of the raw data in the central luminosity DAQ as BCM1F-μTCA integration into the data processing system was not complete at the time. Further studies are necessary to derive dedicated corrections for this period to include it in the luminosity dataset and ensure the accuracy of the legacy results. For the other two periods, the fitted efficiency correction in Fig. 7.3 is used to scale the BCM1F-μTCA data separately in each fill.

To quantify the systematic uncertainty associated with the BCM1F-μTCA stability in 2022, after applying all the corrections, other reliable luminometers were used. This uncertainty is measured as the width of the total integrated luminosity ratios (BCM1F-μTCA to other systems, mainly HFET and DT) distribution in the 2022 data set, shown in Fig. 7.4, thus 0.45% is assigned. The agreement of the central value of the luminosity is further confirmed based on the mean of the ratio histogram - different detectors agree on the level of 0.3% through the year of 2022.

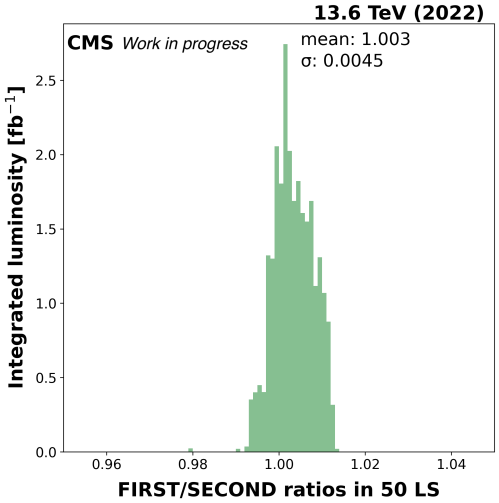

Figure 7.4: The distribution of the luminosity measurement ratio in 2022 data sample - BCM1F-μTCA is compared to any other available secondary CMS luminometer, in each integrated 50 LS (~19 min) [66].

The excellent performance of BCM1F-μTCA is additionally confirmed with preliminary 2023 vdM scan results showing a -0.5% change in the calibration constant after the second year of operation. This comparison does not include all necessary corrections for systematic effects.

As mentioned in Section 2.8.3 during the 2022 operation new features were implemented that provide more insight into the detector performance. Based on the amplitude spectra analysis, the per fill efficiency can be measured more accurately, based on the changes of each BCM1F-μTCA channel, as was shown in Sec. 2.8.5.

7.3 Non-linearity measurement

The expectations on high BCM1F-μTCA linearity were discussed in Sec. 2.8.6. The regular linearity checks with respect to other luminometers throughout 2022 have shown an excellent performance of the BCM1F-μTCA . The example cross-checks against REMUS and HFET have shown less than 0.1% [Hz/μb] (per SBIL) relative non-linearity, the example of the former is shown in Fig. 7.5.

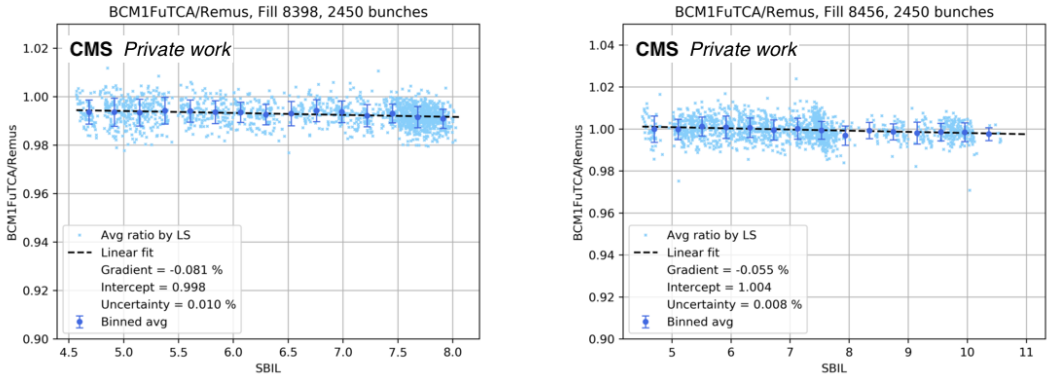

Figure 7.5: Linearity cross-checks for BCM1F-μTCA with respect to REMUS for two nominal fills in 2022 [66].

The overall linearity cross-checks to other systems are summarized in histograms in Fig. 7.6, in terms of fitted slopes to all 2022 data. The contribution of each measured slope is scaled with the total integrated luminosity within each fill. The mean slopes indicated at the top of each subfigure confirm the non-linearity to be at a maximum of 0.1% [Hz/μb]. This measurement is relative to other systems, thus the extracted slope is not used as the correction as it is impossible to claim that one of the systems has a perfectly linear response. Instead, this value is used to assign the systematic uncertainty, for average single bunch instantaneous luminosity measured in 2022 of $\overline{SBIL} = 5.4$ [Hz/μb] it results in 0.54% uncertainty.

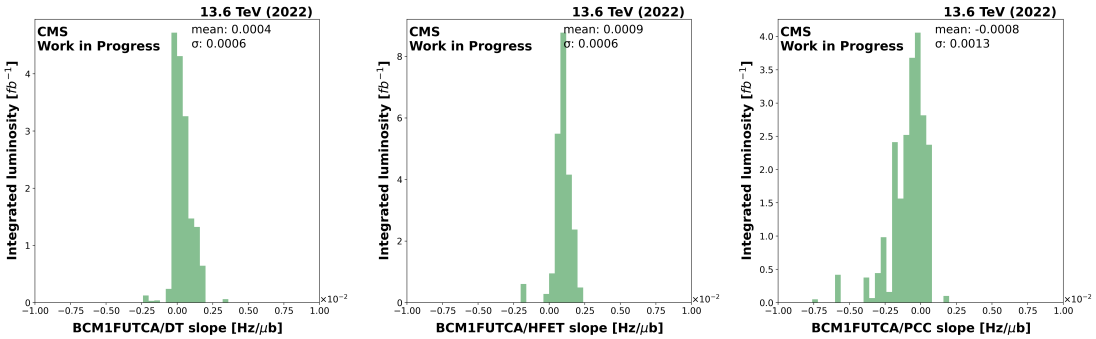

Figure 7.6: The distribution of the response slopes as a function of SBIL, for BCM1F-μTCA with respect to other luminometers, measured for all 2022 data [66].

7.3.1 Towards independent non-linearity measurement

As shown in the preceding section, the assessment of luminometer non-linearity primarily relies on cross-detector comparisons. This method requires an assumption of one of the reference systems to be completely linear. Thus, the measurement can be underestimated in case the compared systems are co-linear. This creates the necessity for a reference detector-independent method to measure the non-linearity. In this section, the method based on luminosity scans with dedicated beam-beam corrections is discussed.

The emittance scans (introduced in Sec. 1.3.2) or so-called μ-scans, which are designed to change the pile-up (and SBIL) using the beam separation steps, can be also used to study the luminometer response across a wide SBIL range. From the emittance scans, an equivalent of the calibration constant σ_{vis} can be extracted to study the SBIL dependence, as was shown in [118]. However, the data recorded in physics conditions are challenging to correct for the beam-related systematic effects as it is done from vdM conditions. These could potentially bias the extracted non-linearity slopes.

The correction strategy discussed in Chapter 4 is not suited for the standard physics data-taking conditions, as there are several key differences. Firstly, the single bunch instantaneous luminosity (SBIL) [1] is much higher, approximately $\times 100$. At the same time, there is a twofold increase in the beam-beam parameter compared to the vdM regime. It is not directly proportional, as can be understood when comparing Eq. 3.22 and 1.7. The main difference comes from the SBIL quadratic dependence on intensity, while it is linear in the case of the beam-beam parameter. The parasitic beam-beam (long-range) interactions have to be taken into account, present in the common vacuum chamber area around the IP due to the compact spacing of bunches. Additionally, the presence of a non-zero crossing-angle introduces coupling between the transverse and longitudinal planes. Moreover, the focusing at the IP is sufficiently strong (β^* reached 30 cm in Run 3) for it to result in variations of the transverse beam size along the collision.

Understanding the beam-beam-induced biases under these conditions is essential for gaining insights into the underlying detector-specific effects. To accurately simulate these intricate effects, the COMBI model with a 6D lens (described in Sec. 3.3) was extended to include a sliced luminosity integrator to provide a comprehensive description of the transverse overlap throughout the collision. This enables the possibility to generate dedicated corrections, to eliminate the beam-beam-induced biases and thereby minimize the associated systematic uncertainty.

Individual bunches

This procedure was applied to a dataset from a special physics fill, prepared for the Beam Synchrotron Radiation Telescopes (BSRT) calibration, encompassing a wide range of per bunch emittances and thus yielding a wide SBIL range. In total six scans were performed at CMS, at different β^* leveling steps. One of the scans performed after the last leveling step at $\beta^* = 30$ cm, with the longest integration time per step of 40 s was found particularly useful as it provided the best statistical precision. The measured transverse profiles from that emittance scans are shown in Fig. 7.7, for all colliding bunches at the CMS. One of them was a pilot bunch with low intensity, and thus much worse statistical error, that was excluded from the study. Due to operational limitations, the scan range is set the same for all bunches, thus covering a small range $< 3.5\sigma$ for the widest bunches. This was estimated to cause an extra systematic error of approximately 1-2% on the measured bunch width. Thus, only 5 bunches

[1] Pile-up (PU) = $\sim 7 \times$ SBIL

could be used.

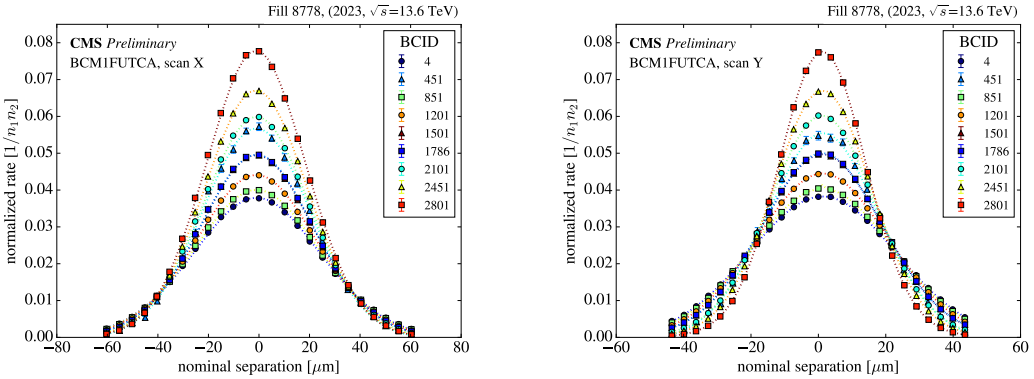

Figure 7.7: Bunch overlap profiles for 9 bunches in fill, with various emittances resulting in the difference in the rate at the peak. Two scans, separately in x (left) and y (right) planes are shown. Scan points measured by BCM1F-μTCA were fitted with the double Gaussian function, and they are indicated with dotted lines. The Bunch IDs (BCIDs) are indicated in the legend. BCID 451 is a pilot bunch (lower intensity) with the bigger statistical error, excluded in the study.

A special setup with individual, well-separated bunches was used, with no long-range beam-beam interactions. The measured convoluted bunch widths were used to estimate the emittances (from Eq. 1.24). The reconstructed average bunch length from BSRL and crossing-angle measured by DOROS were used to remove their contribution to the overlap width in x-plane. The results are summarized in Fig. 7.8a. These values, along with other parameters measured with LHC instrumentation were used to set up the simulation. The COMBI simulated bias on the $\sigma_{\text{vis}}^{\text{emit}}$ for all the considered bunches is summarized in Fig. 7.8b as a function of the corresponding beam-beam parameter. The linearized dependence would indicate the bias slope of -0.25%/$\xi \times 10^3$. These values were used as corrections to the emittance scan data.

Consequently, the measured change of $\sigma_{\text{vis}}^{\text{emit}}$ across SBIL is shown in Figs. 7.9, separately for two example CMS luminometers. The original data ('Uncorrected') are compared to the results including dedicated corrections. The fitted linear dependence on SBIL is indicated in the legend. The 'Uncorrected' slopes are assumed to result from two primary contributions. Firstly, the apparent beam-beam-induced slope - which is removed with COMBI-produced corrections, and measured to be approximately -0.2% [1/(Hz/μb)]. It originates from the increasing ξ, and thus beam–beam-related bias with SBIL. Secondly, there are intrinsic detector response inefficiencies. In the case of a perfectly linear luminometer, the COMBI-corrected slope should be flat across SBIL. For the BCM1F-μTCA system (Fig. 7.9a), the final red slope aligns closely with zero, at -0.14%, confirming its good performance. There was no dedicated optimization of the detector setup for this fill, which would be recommended in future measurements. The same measurement was also performed on each single channel data, indicating small variations in the observed non-linearity. The second independent system, PLT is shown for comparison (Fig. 7.9b), with distinct behavior and a known issue of excessive accidental hits in the luminosity signal (non-corrected data used to highlight non-linearity). The positive non-linearity is observed with SBIL of 0.52%, verifying the method sensitivity. The HFET measured non-linearity

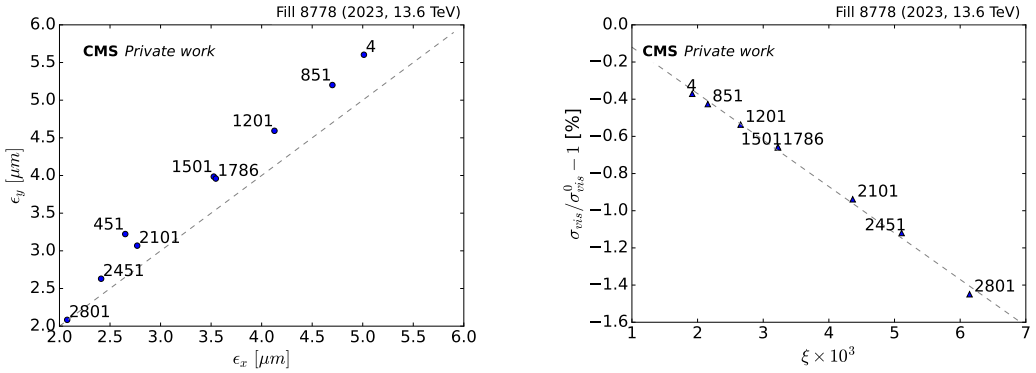

(a) Per bunch emittances measured in the emittance scan. The gray dashed curve on the diagonal indicates a round shape.

(b) COMBI estimated per-bunch σ_{vis} bias as a function of beam-beam parameter. The gray dashed curve indicates the linear fit.

Figure 7.8: The CMS measured input emittances (left) in fill 8778 for the dedicated COMBI simulation-based beam-beam corrections (right).

with SBIL (Fig. 7.9a) is also very close to 0, the slightly positive slope was observed after applying a correction of 0.09%. This can be used as a valuable verification of the absolute values on non-linearities as a function of SBIL, without the risk of excluding the co-linear contributions.

However, to use this measurement as a correction factor to the measured rate, it is necessary to take into account that the non-linearity measured on σ_{vis} includes the contributions from changing SBIL during a scan. In the simplest case, of a standard horizontal and vertical scan pair, and assuming the Gaussian transverse distributions, it can be shown that the measured non-linearity is more than twice smaller than the rate non-linearity as a function of SBIL:

$$\sigma_{\text{vis}}{}^{\text{M}} = \sigma_{\text{vis}}{}^{\text{T}} + (\sqrt{2}-1)\alpha \times \text{SBIL} \times (\sigma_{\text{vis}}{}^{\text{T}})^2, \tag{7.1}$$

where superscripts M and T denote correspondingly the measured and true value. The non-linearity correction is calculated using the additional factor $\alpha = 1/(\sqrt{2}-1) \times \text{slope}^{\text{M}}$. The effect of choosing SBIL^M or SBIL^T as a reference is negligible for non-linearity close to or smaller than 1%.

It is worth noting that additional systematic errors stemming from non-factorization can bias the results and could not be considered in these studies. Another source of bias arises from the challenging fit quality, a result of the operational limits of the scan range for multiple bunches with varying transverse emittances. This uncertainty is incorporated into the errors based on the multiple fit models used for the scan data, and it was reduced by removing the widest bunches from the fit. This leads to the systematic uncertainty at the level of ±0.15% on the extracted slopes.

While there is room for data quality improvement in future measurements, this approach shows promise as a means of independently measuring non-linearity. This might become especially useful in the future, at the HL-LHC, as the non-linearity is expected to be a prominent issue due to significantly higher pile-up.

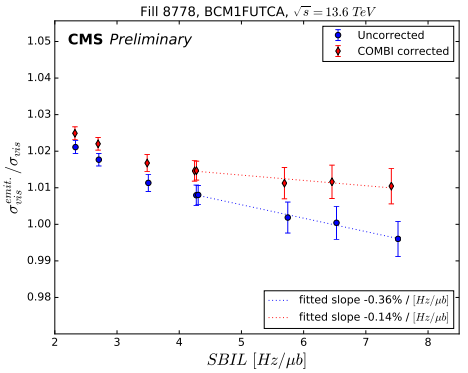

(a) BCM1F-μTCA

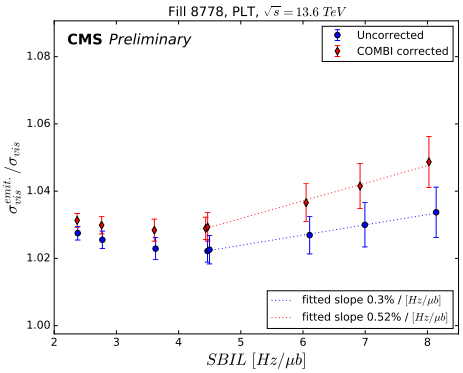

(b) PLT

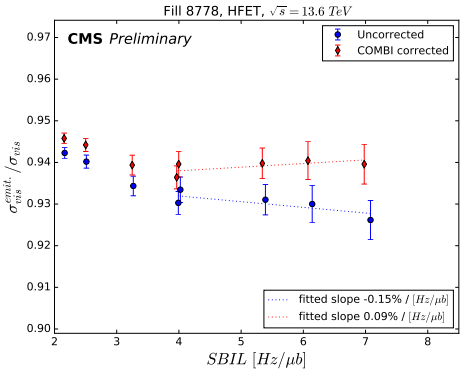

(c) HFET

Figure 7.9: Measured non-linearity slopes from the emittance scan results along a wide range of SBIL for different CMS luminometers. Two types of data are shown in each of the figures - uncorrected (blue) and beam-beam bias-corrected (red).

Trains of bunches

To repeat the non-linearity measurement in the standard emittance scans the systematic effects have to be understood in the complex scenario, including trains. As shown in Figs. 7.10a and 7.10b the distinctive patterns dependent on the main collisions as well as the number of long-range interactions can be observed from the displacements at the IP. In the example measurements from fill with 36-bunches long trains are presented. In the Figures, color code is used to indicate the bunch family that describes just the IPs where each bunch in the measured bunch-pair is colliding. It can be noticed that the displaced collisions for one of the families shown with pink dots cause the main positive displacement for all the bunches and additional displacements depending on the position in a train are present from long-range interactions. While a similar spread is observed in the measured σ_{vis} in Fig. 7.10c as in the vdM conditions, there is not enough evidence that it can be caused by the long-range beam-beam interactions.

With the new luminosity integrator implemented in COMBI, all the elements are available to study the long-range interactions' impact on the emittance scan measurements.

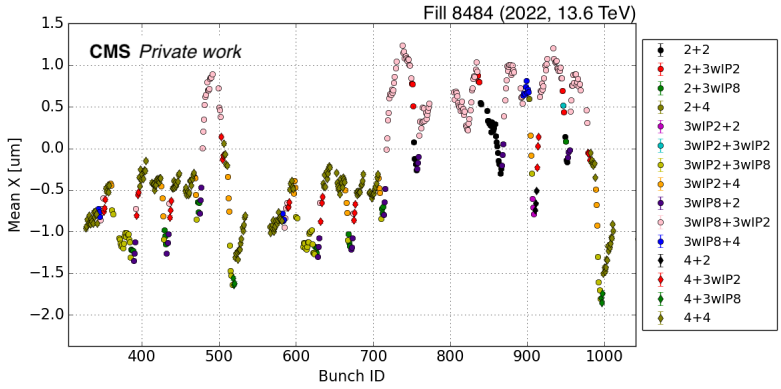

(a) displacement in x

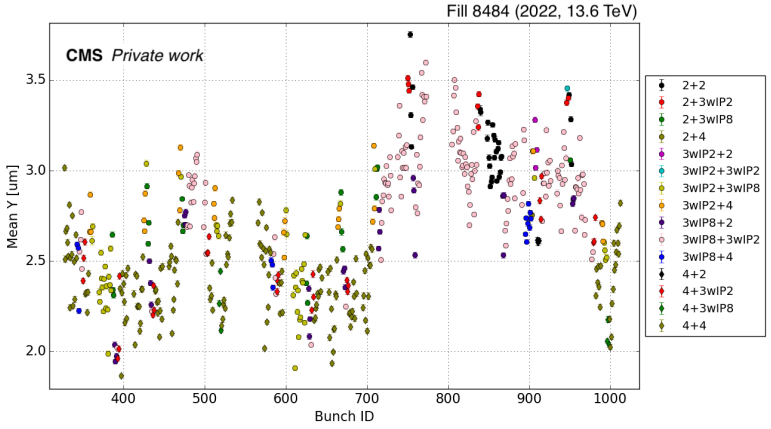

(b) displacement in y

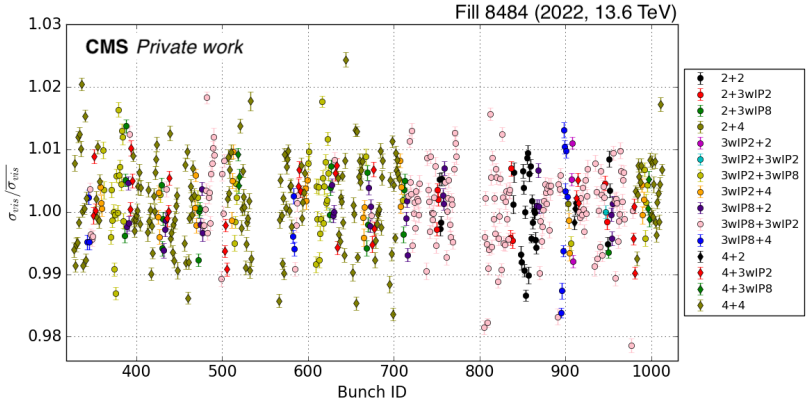

(c) per bunch σ_{vis} variation from full beam average

Figure 7.10: BCM1F-μTCA measured transverse displacements from the fitted Gaussian mean to the luminosity scan and the spread in per bunch σ_{vis} (bottom plot) for a fraction of the LHC orbit. Color code was used to indicate the main bunch families.

8 Overall systematic uncertainty

The process of calibrating and measuring the integrated luminosity of proton-proton collision data at $\sqrt{s}$ = 13.6 TeV, which was recorded by the CMS experiment in 2022, has been completed. The calibration was executed using the vdM scan method, and various systematic effects were taken into account during this procedure. The integration of the full-year data was carried out using the BCM1F-μTCA detector. This detector was not the primary luminometer of the CMS experiment, as the system was only fully commissioned after the start of Run 3, thus only 84% of the full-year data is available. Nevertheless, this summary aims to prove that BCM1F-μTCA is an excellent candidate for the main CMS luminometer in the coming years of Run 3, as equal precision can be achieved when compared to the current main luminometer.

The sources of systematic uncertainty that affect the measurement are concisely outlined in Table 8.1. To determine the total uncertainty, these individual contributions are combined in quadrature. The separate contributions from the calibration method and detector data integration are shown. The most significant contribution comes from the systematic uncertainty on the non-factorization correction or rather the lack of knowledge of the true bunches shape. Moreover, the results included in the table are based exclusively on the data from the 2nd scanning block and might not be correct with the same accuracy for the data coming from the first scanning block, as the non-factorization is possible to change with time (this was reported previously by CMS [49] and ATLAS [119]). Thus, conservative systematic uncertainty is necessary until further results from beam-imaging scans are available.

Towards legacy results

In case the results from the non-factorization analysis summarized in Sec. 6.5 are confirmed, the calibration systematic uncertainty would be reduced to 0.98%. What is more, the improved corrections are expected to reduce the scan-to-scan variations. The new detector data versions aim to improve cross-detector consistency which would ultimately give the systematic uncertainty ~ 0.7% on calibration. The overall 2022 stability and afterglow residuals are also expected to be smaller after the data are reprocessed with improved detector-specific corrections, reducing the systematic uncertainty to ~ 0.6%. As more than one reliable luminometer is available, the data samples could be combined to significantly reduce the detector-specific instabilities. Combining all these improvements will lead to a total systematic uncertainty at the level of 0.9% for the legacy 2022 results. These results are also already on a similar quality level as the Run 2 results and thus could be combined into a common sample with reduced total uncertainty.

Source	**Uncertainty** (%)
Calibration	
Background*	0.1
Bunch current	0.3
Beam positions	0.3
Beam-beam effects	0.4
Length scale	0.1
Factorization bias	0.8
Scan-to-scan variation*	0.4
Bunch-to-bunch variation*	0.1
Cross-detector consistency*	0.2
Integration	
Afterglow corrections*	0.1
Cross-detector stability*	0.5
Cross-detector linearity*	0.5
Calibration	1.1
Integration	0.7
Total	1.3

Table 8.1: Summary of uncertainty contributions with total value indicated in the last row. The * symbol was used to indicate differences with respect to the CMS 2022 luminosity calibration [106], as a result of different choice of the main luminometer.

Part IV Conclusions and outlook

The goal of building a cutting-edge luminometer at the Compact Muon Solenoid (CMS) experiment was achieved. The Fast Beam Conditions Monitor upgraded for Run 3 (BCM1F-μTCA) has shown an excellent performance in the first year of operation in 2022. The new silicon sensors and careful detector optimization provided a stable measurement throughout the year. The upgraded firmware with an advanced peak finder algorithm guaranteed very good noise separation, leading to state-of-the-art response linearity in the function of increasing particle rate with single bunch instantaneous luminosity (or pileup). Dedicated corrections were derived to improve the data quality and separation of the afterglow background that depends on the bunch spacing from the collision products. The multifunctional capacity of BCM1F-μTCA was demonstrated with possible measurements in addition to the luminosity. Extreme sensitivity and strategic location enable the separation of the background signals induced by the beam. High-precision measurements of the beam properties can also be performed in the separation scans. The work presented in this thesis shows that BCM1F-μTCA is a perfect candidate for the main CMS luminometer. Nevertheless, outstanding performance is not guaranteed in the coming years of Run 3 as it requires a careful understanding of the detector performance changes, which cannot be fully automatized. It also provides the first insight into the future luminometer performance, the Fast Beam Conditions Monitor in the High-Luminosity Large Hadron Collider (HL-LHC) era (FBCM), as the same sensor technology is being considered.

In the context of precise calibration of the BCM1F-μTCA luminometer, the beam-beam interaction effects were studied. The extension of the single-IP correction model to a more realistic scenario, where collisions occur not only at the scanning IP but also involve additional head-on encounters at multiple locations around the ring, was successful. An empirical scaling law was derived from an extensive numerical simulation study, supported by a clear understanding of the underlying beam dynamics, which establishes a connection between the multiple-IPs and the simplest single-IP configurations, enabling the per-bunch correction of multi-collision beam-beam effects in the luminosity calibration with the van der Meer (vdM) method. Furthermore, the studies concerning the presence of crossing angles at the location of the vdM calibration were carried out and quantified the associated systematic uncertainties. The characterization of luminosity-calibration biases induced by beam-beam interactions, with their dependence on the phase advance between interaction points, was addressed.

The necessity to validate experimentally the extensive simulation studies for precise luminosity calibration was addressed with a novel test. The experiment at the LHC was proposed with a strategical selection of the phase advances for amplification of the beam-beam interaction-induced effects, to provide statistically significant evidence supporting the correction model. The fundamental dependence of the instantaneous luminosity enhancement by the beam-beam interaction was measured as a function of the beam-beam parameter with a clear linear dependency as assumed in the correction model. The changes to the luminosity were studied as a function of the number of collisions as well as during a separation scan, which was made feasible by adopting the concept of an extra collision point employed as an observation point. Additionally, measurements on the transverse tune spectra were performed, showing the distinctive changes in the scanning and non-scanning planes. The tune shift dependence on the number of collisions was measured. The evidence for the beam-beam effects was also shown in the bunch size changes at the synchrotron light monitor (BSRT) location as well as by measuring the deflection during a separation scan at the closest beam position monitors (DOROS BPMs). All measurements agree with the COherent Multibunch Beam-beam Interaction (COMBI) simulation predictions. The phase advance used for the validation experiment has a more general application since it can be used also in physics fills for the luminosity enhancement at all experiments in the LHC and HL-LHC era. The net increase could be of the order of 7-8% depending on the collision set-up of LHCb and ALICE. Some limitations were recognized in the experiment that could be improved

in future validations, including a more precise characterization of the dependence during a separation scan to compare with the correction model. Collectively, both simulation and experimental findings contribute to a comprehensive understanding of the complexities surrounding beam-beam effects in the context of luminosity calibration and beyond.

The first calibration of the BCM1F-μTCA luminometer was performed. After applying all possible correction factors the calibration constant σ_{vis} was obtained with the vdM method. A complete assessment of the systematic uncertainties arising from beam-beam interactions was performed. Other sources of systematic uncertainties in the vdM scans were also considered. The overall performance of BCM1F-μTCA during 2022 data-taking was characterized. The reprocessing of the full 2022 data sample with per-channel calibration factors and afterglow corrections led to very good measurement stability and linearity. The possibility of the reference-detector independent non-linearity measurement was studied with dedicated beam-beam effects corrections. The measurement confirmed the very good BCM1F-μTCA linearity response but was limited by the lack of a full description of the systematic effects. The opportunity of performing such measurements in all operational scans was considered but requires further studies of the impact of beam-beam long-range interactions on luminosity. Although the presented luminosity calibration is only preliminary, the final systematic uncertainty of 1.3% is already at the level of the previous legacy results. The luminosity measurement results presented in this thesis prove that CMS is ready to achieve the 1% HL-LHC integrated luminosity precision target.

A An appendix

A.1 Integrals

$$\int_{-\infty}^{\infty} e^{-at^2}\,dt = \sqrt{\pi/a} \tag{A.1}$$

$$\int_{-\infty}^{\infty} e^{-(at^2+bt+c)}\,dt = \sqrt{\pi/a}\exp\left(\frac{b^2}{4a}-c\right) \tag{A.2}$$

A.2 Phase advances

	Beam 1		**Beam 2**	
	$\Delta\mu_x\ [2\pi]$	$\Delta\mu_y\ [2\pi]$	$\Delta\mu_x\ [2\pi]$	$\Delta\mu_y\ [2\pi]$
IP1-IP2	9.064	7.831	7.969	8.035
IP2-BSRT	15.302	14.206	15.484	14.243
BSRT-IP5	7.610	7.612	7.609	7.483
IP5-IP8	23.295	22.552	23.081	22.674
IP8-IP1	8.038	8.119	9.167	7.884
	63.31	**60.32**	**63.31**	**60.32**

Table A.1: Nominal LHC phase advances extracted from MADX LHC lattice model.

Bibliography

[1] C. Bernardini. “AdA:The first electron-positron collider”. In: *Phys. Perspect.* 6 (2004), pp. 156–183. DOI: 10.1007/s00016-003-0202-y.

[2] O. S. Brüning et al. “LHC Design Report”. In: (2004). Publisher: CERN. DOI: 10.5170/CERN-2004-003-V-1.

[3] A. W. Chao et al. *Handbook of Accelerator Physics and Engineering*. 2nd. WORLD SCIENTIFIC, 2013. DOI: 10.1142/8543.

[4] ATLAS Collaboration. *The ATLAS Experiment at the CERN Large Hadron Collider: A Description of the Detector Configuration for Run 3*. 2023.

[5] CMS Collaboration. *Development of the CMS detector for the CERN LHC Run 3*. 2023.

[6] A. A. Alves Jr. et al. “The LHCb Detector at the LHC”. In: *JINST* 3 (2008), S08005. DOI: 10.1088/1748-0221/3/08/S08005.

[7] ALICE collaboration. “The ALICE experiment at the CERN LHC. A Large Ion Collider Experiment”. In: *JINST* 3 (2008). Also published by CERN Geneva in 2010, S08002. DOI: 10.1088/1748-0221/3/08/S08002.

[8] FASER Collaboration et al. *Technical Proposal for FASER: ForwArd Search ExpeRiment at the LHC*. Dec. 21, 2018.

[9] C. Ahdida et al. *SND@LHC - Scattering and Neutrino Detector at the LHC*. Tech. rep. Geneva: CERN, 2021.

[10] CMS Collaboration. “Measurements of the W boson rapidity, helicity, double-differential cross sections, and charge asymmetry in pp collisions at $\sqrt{s}$ = 13.6 TeV”. In: *Physical Review D* 102.9 (Nov. 2020). DOI: 10.1103/physrevd.102.092012.

[11] A. Tumasyan et al. “Measurement of the mass dependence of the transverse momentum of lepton pairs in Drell-Yan production in proton-proton collisions at $\sqrt{s}$ = 13 TeV”. In: *Eur. Phys. J. C* 83.7 (2023), p. 628. DOI: 10.1140/epjc/s10052-023-11631-7.

[12] CMS Collaboration. “Measurement of differential $t\bar{t}$ production cross sections in the full kinematic range using lepton+jets events from proton-proton collisions at $\sqrt{s}$ = 13 TeV”. In: *Physical Review D* 104.9 (Nov. 2021). DOI: 10.1103/physrevd.104.092013.

[13] CMS Collaboration. "First measurement of the top quark pair production cross section in proton-proton collisions at $\sqrt{s}$ = 13.6 TeV". In: *Journal of High Energy Physics* 2023.8 (Aug. 2023). DOI: 10.1007/jhep08(2023)204.

[14] CMS collaboration. "Combined measurements of Higgs boson couplings in proton–proton collisions at $\sqrt{s}$ = 13 TeV". In: *The European Physical Journal C* 79.5 (May 2019). DOI: 10.1140/epjc/s10052-019-6909-y.

[15] *CMS Luminosity - Public Results*.

[16] CMS Collaboration. *The Phase-2 Upgrade of the CMS Beam Radiation Instrumentation and Luminosity Detectors*. Tech. rep. This is the final version, approved by the LHCC. Geneva: CERN, 2021.

[17] O. Aberle et al. *High-Luminosity Large Hadron Collider (HL-LHC): Technical design report*. CERN Yellow Reports: Monographs. Geneva: CERN, 2020. DOI: 10.23731/CYRM-2020-0010.

[18] X. Buffat et al. "Results of β^* luminosity leveling MD". In: (2012).

[19] V. Petit. "Beam screen surface studies". LHC Performance Workshop Chamonix 2023.

[20] *Electron-Ion Collider website*.

[21] Babaev, A. et al. "Impact of beam–beam effects on absolute luminosity calibrations at the CERN Large Hadron Collider". In: *Eur. Phys. J. C* 84.1 (2024), p. 17. DOI: 10.1140/epjc/s10052-023-12192-5.

[22] W. Herr and B. Muratori. "Concept of luminosity". In: (2006). DOI: 10.5170/CERN-2006-002.361.

[23] R. L. Workman et al. "Review of Particle Physics". In: *PTEP* 2022 (2022), p. 083C01. DOI: 10.1093/ptep/ptac097.

[24] S. van der Meer. *Calibration of the effective beam height in the ISR*. Tech. rep. Geneva: CERN, 1968.

[25] C. Rubbia. *Measurement of the luminosity of $p-\overline{p}$ collider with a (generalized) Van der Meer Method*. Tech. rep. Geneva: CERN, 1977.

[26] M. Ferro-Luzzi. "Proposal for an absolute luminosity determination in colliding beam experiments using vertex detection of beam-gas interactions". In: *Nucl. Instrum. Methods Phys. Res., A* 553.3 (2005), pp. 388–399. DOI: 10.1016/j.nima.2005.07.010.

[27] LHCb collaboration. "Precision luminosity measurements at LHCb". In: *JINST* 9.12 (Dec. 2014), P12005. DOI: 10.1088/1748-0221/9/12/P12005.

[28] P. Grafström and W. Kozanecki. "Luminosity determination at proton colliders". In: *Prog. Part. Nucl. Phys.* 81 (2015), pp. 97–148. DOI: 10.1016/j.ppnp.2014.11.002.

[29] S. Jadach. *Theoretical error of luminosity cross section at LEP*. June 10, 2003.

[30] A. Hayrapetyan et al. "Luminosity determination using Z boson production at the CMS experiment". In: *The European Physical Journal C* 84.1 (Jan. 10, 2024), p. 26. DOI: 10.1140/epjc/s10052-023-12268-2.

[31] M. H. et al. “Operational beta* levelling at the LHC in 2022 and beyond”. English. In: *Proc. IPAC’23* (Venice, Italy). IPAC’23 - 14th International Particle Accelerator Conference 14. JACoW Publishing, Geneva, Switzerland, May 2023, pp. 642–645. DOI: 10.18429/JACoW-IPAC2023-MOPL045.

[32] R. Tomas Garcia et al. *HL-LHC Run 4 proton operational scenario*. Tech. rep. Geneva: CERN, 2022.

[33] A. M. Sirunyan et al. “Precision luminosity measurement in proton-proton collisions at $\sqrt{s}$ = 13 TeV in 2015 and 2016 at CMS”. In: *Eur. Phys. J. C* 81.9 (2021), p. 800. DOI: 10.1140/epjc/s10052-021-09538-2.

[34] ATLAS collaboration. “Luminosity determination in pp collisions at $\sqrt{s}$ = 13 TeV using the ATLAS detector at the LHC.” In: *Eur. Phys. J. C* 83.10 (2023), p. 982. DOI: 10.1140/epjc/s10052-023-11747-w.

[35] V. Ziemann. “Comparison of non-linear effects from the electric field of several current distributions”. In: *Nuclear Instruments and Methods in Physics Research Section A: Accelerators, Spectrometers, Detectors and Associated Equipment* 556.1 (2006), pp. 45–51. DOI: https://doi.org/10.1016/j.nima.2005.10.121.

[36] H. Wiedemann. “Resonances”. In: *Particle Accelerator Physics*. Ed. by H. Wiedemann. Graduate Texts in Physics. Cham: Springer International Publishing, 2015, pp. 539–564. DOI: 10.1007/978-3-319-18317-6_16.

[37] G. Anders et al. *Study of the relative LHC bunch populations for luminosity calibration*. Tech. rep. CERN-ATS-Note-2012-028 PERF. 2012.

[38] C. Barschel et al. *Results of the LHC DCCT calibration studies*. Tech. rep. CERN-ATS-Note-2012-026 PERF. 2012.

[39] M. Gąsior et al. “First Operational Experience with the LHC Diode ORbit and OScillation (DOROS) System”. In: (2017), MOPG07. DOI: 10.18429/JACoW-IBIC2016-MOPG07.

[40] M. Krupa et al. “HL-LHC BPM System Development Status”. In: *JACoW IBIC* 2022 (2022), pp. 408–412. DOI: 10.18429/JACoW-IBIC2022-WEP12.

[41] H. S. Matis et al. “The BRAN luminosity detectors for the LHC.” In: *Nucl. Instrum. Methods Phys. Res., A* 848 (2017). 22 pages, 32 Figures, pp. 114–126. DOI: 10.1016/j.nima.2016.12.019.

[42] S. Mazzoni et al. “A New Luminosity Monitor for the LHC Run 3”. In: *JACoW IBIC* 2022 (2022), pp. 163–167. DOI: 10.18429/JACoW-IBIC2022-MOP45.

[43] P. Hopchev. “Absolute luminosity measurements at LHCb”. Presented 25 Nov 2011. U. Grenoble Alpes, 2011.

[44] R. Aaij et al. “Searches for low-mass dimuon resonances”. In: *JHEP* 10 (2020), p. 156. DOI: 10.1007/JHEP10(2020)156.

[45] F. R. Kassel. “The rate dependent radiation induced signal degradation of diamond detectors”. Presented 27 Jan 2017. KIT, Karlsruhe, 2017.

[46] S. Orfanelli et al. “Design of a novel Cherenkov detectors system for machine induced background monitoring in the CMS cavern”. In: (2013).

[47] G. Segura Millan, D. Perrin, and L. Scibile. “RAMSES: the LHC radiation monitoring system for the environment and safety”. In: *Proc. 10th International Conference on Accelerator and Large Experimental Physics Control Systems (ICALEPCS 2005): Geneva, Switzerland, October 10–14, 2005*. 2005.

[48] J. Mans et al. *CMS Technical Design Report for the Phase 1 Upgrade of the Hadron Calorimeter*. Tech. rep. 2012.

[49] CMS collaboration. “Precision luminosity measurement in proton-proton collisions at $\sqrt{s}$ = 13 TeV in 2015 and 2016 at CMS”. In: *Eur. Phys. J. C* 81.9 (2021), p. 800. DOI: 10.1140/epjc/s10052-021-09538-2.

[50] E. Ayala et al. “The Pixel Luminosity Telescope: a detector for luminosity measurement at CMS using silicon pixel sensors”. In: *The European Physical Journal C* 83.7 (July 2023). DOI: 10.1140/epjc/s10052-023-11713-6.

[51] J. Wanczyk. “Measurements and estimates of the radiation levels in the CMS Experimental Cavern using Medipix and RAMSES monitors, and the FLUKA Monte Carlo code”. Presented 31 Jul 2019. AGH-UST, Cracow, 2019.

[52] R. Hall-Wilton et al. “Fast beam conditions monitor (BCM1F) for CMS”. In: *2008 IEEE Nuclear Science Symposium Conference Record*. 2008, pp. 3298–3301. DOI: 10.1109/NSSMIC.2008.4775050.

[53] J. L. Leonard et al. “Fast Beam Condition Monitor for CMS: performance and upgrade”. In: *Nucl. Instrum. Methods Phys. Res., A* 765 (2014), pp. 235–239. DOI: 10.1016/j.nima.2014.05.008.

[54] A. Dabrowski. *Upgrade of the CMS instrumentation for luminosity and machine induced background measurements*. Tech. rep. Geneva: CERN, 2016. DOI: 10.1016/j.nuclphysbps.2015.09.180.

[55] D. Przyborowski, J. Kaplon, and P. Rymaszewski. “Design and Performance of the BCM1F Front End ASIC for the Beam Condition Monitoring System at the CMS Experiment”. In: *IEEE Trans. Nucl. Sci.* 63.4 (2016), pp. 2300–2308. DOI: 10.1109/TNS.2016.2575781.

[56] J. L. Leonard et al. “Upgraded Fast Beam Conditions Monitor for CMS online luminosity measurement”. In: *PoS* TIPP2014 (2014), p. 346. DOI: 10.22323/1.213.0346.

[57] M. Guthoff. “The new Fast Beam Condition Monitor using poly-crystalline diamond sensors for luminosity measurement at CMS”. In: *Nuclear Instruments and Methods in Physics Research Section A: Accelerators, Spectrometers, Detectors and Associated Equipment* 936 (2019). Frontier Detectors for Frontier Physics: 14th Pisa Meeting on Advanced Detectors, pp. 717–718. DOI: https://doi.org/10.1016/j.nima.2018.11.071.

[58] Y. Otarid. “Qualification of the BCM1F detector for luminosity measurement in the CMS experiment”. Presented 06 Sep 2019. Telecom Physique Strasbourg - University of Strasbourg, 2019.

[59] CMS collaboration. *The Phase-2 Upgrade of the CMS Tracker*. Tech. rep. Geneva: CERN, 2017. DOI: 10.17181/CERN.QZ28.FLHW.

[60] J. Rubenach. “Search for heavy Higgs bosons in conjunction with neural-network-driven reconstruction and upgrade of the Fast Beam Condition Monitor at the CMS experiment”. Presented 30 Mar 2023. Hamburg U., 2023.

[61] H. Bichsel. “Straggling in Thin Silicon Detectors”. In: *Rev. Mod. Phys.* 60 (1988), pp. 663–699. DOI: 10.1103/RevModPhys.60.663.

[62] *CAEN V895 Leading Edge Discriminator*.

[63] M. Penno. “A Real-time Histogramming Unit for Luminosity Measurement of each Bunch Crossing at CMS”. In: Topical Workshop on Electronics for Particle Physics, Perugia (Italy), 23 Sep 2013 - 27 Sep 2013. 2013.

[64] A. A. Zagozdzinska. *The CMS Fast Beams Condition Monitor Backend Electronics based on MicroTCA technology*. Tech. rep. Geneva: CERN, 2016. DOI: 10.1109/NSSMIC.2015.7581987.

[65] A. J. Ruede. “New Peak Finding Algorithm for the BCM1F Detector of the CMS Experiment at CERN”. Presented 19 Mar 2018. Ernst Abbe Hochschule Jena, 2018.

[66] Courtesy of BRIL.

[67] G. Auzinger. “Silicon Sensor Development for the CMS Tracker Upgrade”. Presented 20 Nov 2013. TU Vienna, 2013.

[68] S. Müller. “The Beam Condition Monitor 2 and the Radiation Environment of the CMS Detector at the LHC”. Presented on 14 Jan 2011. Karlsruhe U., 2011.

[69] P. Baldi and K. Hornik. “Neural networks and principal component analysis: Learning from examples without local minima”. In: *Neural Networks* 2.1 (1989), pp. 53–58. DOI: https://doi.org/10.1016/0893-6080(89)90014-2.

[70] M. Guthoff. *Instrumentation for beam radiation and luminosity measurement in the CMS experiment using novel detector technologies*. Tech. rep. Geneva: CERN, 2017. DOI: 10.1016/j.nima.2016.06.028.

[71] S. Y. Lee. *Accelerator Physics*. 3rd. WORLD SCIENTIFIC, 2011. DOI: 10.1142/8335.

[72] A. W. Chao. “Beam-beam instability”. In: *AIP Conf. Proc.* 127 (1985). Ed. by M. Month, P. F. Dahl, and M. Dienes, pp. 201–242. DOI: 10.1063/1.35187.

[73] E. Keil. “Beam-beam effects as a function of the tunes”. In: (1995).

[74] W. Kozanecki, T. Pieloni, and J. Wenninger. *Observation of beam-beam deflections with LHC orbit data*. CERN Accelerator Note CERN-ACC-NOTE-2013-0006. 2013.

[75] T. Pieloni et al. “Dynamic beta and beta-beating effects in the presence of the beam-beam interactions”. In: (2016), MOPR027. DOI: 10.18429/JACoW-HB2016-MOPR027.

[76] D. Brandt et al. “Is LEP beam-beam limited at its highest energy?” In: (1999).

[77] T. Pieloni. “A study of beam-beam effects in hadron colliders with a large number of bunches”. CERN-THESIS-2010-056, THESE-4211-2008. PhD thesis. École Polytechnique Fédérale de Lausanne, 2008. DOI: 10.5075/epfl-thesis-4211.

[78] M. Bassetti and G. A. Erskine. *Closed expression for the electrical field of a two-dimensional Gaussian charge*. Tech. rep. Geneva: CERN, 1980.

[79] R. Tomás et al. “Beam-beam amplitude detuning with forced oscillations”. In: *Phys. Rev. Accel. Beams* 20 (10 Oct. 2017), p. 101002. DOI: 10.1103/PhysRevAccelBeams.20.101002.

[80] L. Barraud and X. Buffat. “Mode coupling instability of colliding beams in the HL-LHC”. In: (2019).

[81] X. Buffat et al. “Stability diagrams of colliding beams in the Large Hadron Collider”. In: *Phys. Rev. Spec. Top. Accel. Beams* 17.11 (2014), p. 111002. DOI: 10.1103/PhysRevSTAB.17.111002.

[82] F. W. Jones, W. Herr, and T. Pieloni. “Parallel Beam Beam Simulation Incorporating Multiple Bunches and Multiple Interaction Regions”. In: *Conf. Proc. C* 070625 (2007). Ed. by C. Petit-Jean-Genaz, p. 3235. DOI: 10.1109/PAC.2007.4440383.

[83] X. Buffat. “Transverse beams stability studies at the Large Hadron Collider”. In: (Jan. 20, 2015). Publisher: Lausanne, EPFL. DOI: 10.5075/EPFL-THESIS-6321.

[84] Open MPI website.

[85] S. V. Furuseth. “Transverse Noise, Decoherence, and Landau Damping in High-Energy Hadron Colliders”. presented 21 May 2021. Ecole Polytechnique, Lausanne, 2021. DOI: 10.5075/epfl-thesis-9330.

[86] W. Herr, M. P. Zorzano-Mier, and F. Jones. “Hybrid Fast Multipole Method Applied to Beam-Beam Collisions in the Strong-Strong Regime”. In: *Phys. Rev. Spec. Top. Accel. Beams* 4 (2001), p. 054402.

[87] M. Placidi and J. Wenninger. “Interaction region diagnostics in e^+e^- ring colliders”. In: (1998).

[88] P. Bambade et al. “Observation of beam-beam deflections at the interaction point of the SLAC Linear Collider”. In: *Phys. Rev. Lett.* 62 (25 June 1989), pp. 2949–2952. DOI: 10.1103/PhysRevLett.62.2949.

[89] V. Balagura. “Van der Meer scan luminosity measurement and beam-beam correction”. In: *Eur. Phys. J. C* 81 (2021), p. 26. DOI: 10.1140/epjc/s10052-021-08837-y.

[90] G. Iadarola et al. *Xsuite: an integrated beam physics simulation framework*. Tech. rep. 2023.

[91] X. Buffat. “Coherent Beam-Beam Effects”. In: *CERN Yellow Rep. School Proc.* 3 (2017). Ed. by W. Herr, p. 391. DOI: 10.23730/CYRSP-2017-003.391.

[92] W. Herr. “Beam-beam and dynamic beta. LHC Lumi Days 2012”. In: (2012).

[93] K. Yokoya et al. “Tune shift of coherent beam-beam oscillations”. In: *Part. Accel.* 27 (1990), pp. 181–186.

[94] A. Boccardi et al. *First Results from the LHC BBQ Tune and Chromaticity Systems*. Tech. rep. Geneva: CERN, 2009.

[95] ATLAS Collaboration. “Luminosity determination in pp collisions at $\sqrt{s} = 7$ TeV using the ATLAS detector at the LHC”. In: *The European Physical Journal C* 71.4 (Apr. 2011). DOI: 10.1140/epjc/s10052-011-1630-5.

[96] G. Trad. “Development and Optimisation of the SPS and LHC beam diagnostics based on Synchrotron Radiation monitors”. Presented 22 Jan 2015. U. Grenoble Alpes, 2014.

[97] M. Söderén et al. “ADT and Obsbox in LHC Run 2, Plans for LS2”. In: (2019), pp. 165–171.

[98] F. C. et al. “Challenges of K-modulation measurements in the LHC Run 3”. English. In: *Proc. IPAC’23* (Venice, Italy). IPAC’23 - 14th International Particle Accelerator Conference 14. JACoW Publishing, Geneva, Switzerland, May 2023, pp. 531–534. DOI: 10.18429/JACoW-IPAC2023-MOPL014.

[99] R. Calaga et al. *Coherent beam-beam mode in the LHC*. en. 2014. DOI: 10.5170/CERN-2014-004.227.

[100] J. W. et al. *Beam-beam tests at the LHC*. Tech. rep. To be submitted. CERN, 2024.

[101] A. Chmielińska et al. *Magnetization in superconducting corrector magnets and impact on luminosity-calibration scans in the Large Hadron Collider*. 2023.

[102] CMS collaboration. *CMS luminosity measurement for the 2017 data-taking period at* $\sqrt{s} = 13$ TeV. Tech. rep. Geneva: CERN, 2018.

[103] CMS collaboration. *CMS luminosity measurement for the 2018 data-taking period at* $\sqrt{s} = 13$ TeV. Tech. rep. Geneva: CERN, 2019.

[104] CMS collaboration. *Luminosity measurement in proton-proton collisions at 5.02 TeV in 2017 at CMS*. Tech. rep. Geneva: CERN, 2021.

[105] CMS collaboration. *CMS luminosity measurement using nucleus-nucleus collisions at* $\sqrt{s_{\mathrm{NN}}} = 5.02$ *TeV in 2018*. Tech. rep. Geneva: CERN, 2022.

[106] CMS collaboration. *Luminosity measurement for the 2022 pp data-taking period at* 13.6 *TeV*. Tech. rep. CERN, 2024.

[107] A. Alici et al. *Study of the LHC ghost charge and satellite bunches for luminosity calibration*. Tech. rep. CERN-ATS-Note-2012-029 PERF. 2012.

[108] M. Gonzales Berges and S. Mazzoni. *Preliminary BSRL data analysis for 2022 VdM fills*. LLCMWG meeting. 23 Jan 2023.

[109] N. McHugh. *Preliminary LHCb November 2022 ghost charge measurements*. LLCMWG meeting. 13 Feb 2023.

[110] M. D. Coen. *Studying beam position measurements for the luminosity calibration at CMS*.

[111] T. Persson. *Measuring VdM optics β^**. LLCMWG meeting. 13 Feb 2023.

[112] CMS Collaboration. *Nonfactorization in Van der Meer scans in Run 2*. CMS Detector Performance Note CMS-DP-2019-019. 2019.

[113] M. Klute, C. Medlock, and J. Salfeld-Nebgen. "Beam imaging and luminosity calibration". In: *JINST* 12 (2017), P03018. DOI: 10.1088/1748-0221/12/03/P03018.

[114] J. Knolle. "The factorization bias in the Van der Meer method: Run 2 experiences at the CMS experiment". In: *Proc. LHC Lumi Days 2019: Prévessin, France, June 4–5, 2019*. 2019.

[115] J. Knolle. "Measuring luminosity and the $t\bar{t}Z$ production cross section with the CMS experiment". Presented 25 Jun 2020. Hamburg U., 2020.

[116] S. Chatrchyan et al. "Description and performance of track and primary-vertex reconstruction with the CMS tracker". In: *JINST* 9 (2014), P10009. DOI: 10.1088/1748-0221/9/10/P10009.

[117] CMS collaboration. *XY-factorization correction for luminosity calibration using off-axis scans for 2022 pp data at 13.6 TeV*. Tech. rep. CERN, 2022.

[118] Karacheban, Olena, Tsrunchev, Peter, and on behalf of CMS. "Emittance scans for CMS luminosity calibration". In: *EPJ Web Conf.* 201 (2019), p. 04001. DOI: 10.1051/epjconf/201920104001.

[119] ATLAS collaboration. "Luminosity determination in pp collisions at $\sqrt{s}$ s = 8 TeV using the ATLAS detector at the LHC". In: *The European Physical Journal C* 76.12 (Nov. 2016). DOI: 10.1140/epjc/s10052-016-4466-1.